



Vol. No. Class Mark 7

FOR REFERENCE ONLY

[illegible]

Environmental Influences on the Performance of Thin Film Solar Cells

by

Ralph Gottschalg


Doctoral Thesis

Submitted in partial fulfilment of the requirements
for the award of

Doctor of Philosophy of Loughborough University

September 25th, 2001

© by Ralph Gottschalg 2001

 Loughborough University P.O. Box 3300, Leicestershire LE11 3TU, UK
Date Sept 02
Class
Acc No. 040258988

Abstract

The response of thin film photovoltaic devices to changes in the environment is not well understood. There are a large number of conflicting reports, reflecting largely the superimposed nature of the environmental effects. A separation of the effects is not often attempted mainly because of the lack of appropriate spectral data.

An experimental system has been designed and operated to facilitate the separation of the environmental effects, including spectral effects. This involves measurements in a controlled laboratory environment as well as outdoor monitoring. Furthermore, a number of analysis tools have been developed and tested for their suitability. In order to develop a system model, the applicability of parametric models for thin film devices is probed. The thermal variation of the underlying physical parameters is investigated and problems of describing thin film devices with parametric models are discussed.

It is shown that the magnitude of the spectral effects for thin film devices is potentially much more significant than for conventional crystalline silicon devices. This analysis is centred on the primary spectral effect, i.e. it is conducted purely on the basis of available light and does not consider any absorption profiles or device structures. It is also shown that there is a strong daily and seasonal variation in the fraction of the useful light for devices employing a larger band gap.

Environmental effects are observed directly from outdoor measurements. It is

apparent that many of the reported idiosyncrasies occurring during the operation of thin film devices can be explained simply by including spectral effects. It is possible to show the secondary spectral effect for multi-junction devices, i.e. an effect that depends on the composition of the solar irradiance and not purely on the magnitude of spectrally useful irradiance. This effect impacts mainly on the short circuit current and to some extent on the fill factor.

Finally, the findings of this work are brought together in a simulation code for thin film photovoltaic devices. It is shown that it is possible to simulate such a photovoltaic system using parametric models, as long as the spectrum is considered. This is used to investigate the operational losses for one particular device.

Acknowledgements

This work was aided by many people and their support is gratefully acknowledged. The number is possibly too great to mention here. I want to express my appreciation for all the support I got during this work.

The samples were supplied by Jutta Beier of Antec GmbH, Robert Gay of Siemens Solar, Ersin Öszan and Tim Bruton of BP Solar, Horst Schade of PST, Philip Stillman of Intersolar Group and Andrea Zavaczki of Dunasolar. I am thankful for their support and helpful discussions.

I want to thank Mathias Rommel in the Electron Devices research group at the University of Erlangen for all the support in the early stages of the work, especially for letting me use their solar simulator and dark measurement arrangements. The collaboration in the fitting work was a pleasure.

Jenny Nelson allowed me to use the equipment at Imperial College, for which I am grateful.

Steve Ransome and Ricardo Rüther were a great help in the interpretation of the outdoor measurements and their comments were very much appreciated.

Tom Betts' support in patiently reading all these pages is greatly appreciated.

I am very grateful for the support I got from my supervisors David Infield and Michael Kearney.

Last but not least, I want to thank my wife Elke for support and distraction.

Contents

1	Introduction	1
2	Influence of Operating Conditions on the Performance of Solar Cells	4
2.1	Performance Parameters	5
2.2	Thermal Effects	7
2.3	irradiance Effects	9
2.4	Spectral Effects	10
2.5	Degradational Effects	10
3	Parametrisation of Thin Film Solar Cells	12
3.1	Standard Diode Models	12
3.2	Modifications for a-Si Devices	18
3.3	Modifications for CIGS and CdTe	25
4	Extraction of Physical Parameters	32
4.1	Introduction	32
4.2	Fitting of I-V Characteristics	34
4.2.1	Identification of Starting Values	36
4.2.2	Error Criteria	40
4.3	Test of Existing Methods	44
4.3.1	Test Approach	44

4.3.2	Applied Evaluation Methodology	45
4.3.3	Tests and Results	48
4.4	Final Algorithm	60
5	Experimental Methods	62
5.1	Introduction	62
5.2	Solar Simulator	63
5.2.1	Illumination	64
5.2.2	Temperature Control	65
5.2.3	Electric Measurement System	67
5.2.4	Computer Control	68
5.3	Outdoor Measurements	69
5.3.1	Spectroradiometer	69
5.3.2	Outdoor System	71
5.3.3	Computer Control	73
5.4	Samples Tested	76
6	Influence of Operating Temperature	77
6.1	Introduction	77
6.2	Measurements	81
6.3	Thermal Variation of Parameters	88
6.3.1	Series Resistance	88
6.3.2	Parallel Resistance	92
6.3.3	Diode Ideality Factor	96
6.3.4	Diode Saturation Current	100
6.4	Hysteresis Effects	105
6.5	Repeatability of Measurements	108
6.6	Devices with Back Diode	113

6.7	Conclusions	117
7	Spectral Effects for Outdoor Operations	120
7.1	Introduction	120
7.2	Spectral Effects of Weather and Air Mass	123
7.3	Daily Cycle	127
7.4	Seasonal Variations	131
7.5	Conclusions	135
8	Outdoor Performance	137
8.1	Introduction	137
8.2	Measurement Environment	140
8.3	Stability of Measurements	142
8.4	Short Circuit Current	147
8.5	Fill Factor	161
8.6	Open Circuit Voltage	175
8.7	V_{MPP} to V_{OC} Ratio	185
8.8	Efficiency	191
8.9	Conclusion	198
9	Simulation of the Outdoor Performance	200
9.1	Introduction	200
9.2	Model	203
9.2.1	Thermal Model	205
9.2.2	Optical Model	207
9.2.3	Cell Model	209
9.3	Seasonal Performance	211
9.4	System Losses	212
9.5	Conclusions	216

10 Conclusions and Recommendations for Future Work	217
10.1 Conclusions	217
10.2 Recommendations for Future Work	220
A Mathematical Formulae for the Fitting	221
A.1 One Diode Model	222
A.2 Two Diode Model	223
A.3 Crandall Model	224
A.4 Merten Model	225
A.5 Backdiode Model	227
B Simulation of Environmental Conditions	229
B.1 Position of the Sun	229
B.1.1 Notation	231
B.1.2 Solar Time	232
B.1.3 Position of the Sun	233
B.2 Separation of Beam and Diffuse Irradiance	236
B.3 Reflection on the Surface of a PV Module	239
B.4 Operating Temperature of the PV Module	242
B.4.1 Energy Balance	242
B.4.2 Convective Coefficient of Module Top Surface	244
B.4.3 Convective Coefficient of Module Bottom Surface	245
B.4.4 Sky Temperature	247
C Publications and Presentations Arising from this Work	248
C.1 Conference Publications	248
C.2 Journal Publications	250
C.3 Oral Presentations	250

Chapter 1

Introduction

Recent years have seen a steady increase in the use of photovoltaic devices for the production of electric power. A major obstacle for faster deployment is the high cost of energy generated by these devices. These costs can be reduced in two ways, either by lowering the cost of production or increasing the efficiency of the devices. A lot of research has been conducted on thin film solar cells, leading to a significant increase in efficiencies achieved, as shown in figure 1.1¹. This increase in efficiency makes thin film devices valid contenders, considering that some are competing with large-grain polycrystalline silicon devices.

Thin film solar cells, which are commercially available or becoming close to commercialisation, promise a major reduction in production cost because a higher degree of mechanisation can be achieved as well as thinner cells (leading to reduced material costs). This is normally achieved by accepting lower material qualities, resulting in a lower efficiency than the more expensive crystalline devices but significantly cheaper cost per installed capacity.

However, these new technologies do show some differences in the response to environmental conditions compared to commercially available crystalline Silicon

¹Data compiled from Zweibel [Zweibel 95], Guha et al. [Guha 00] and past issues of the solar cell efficiency tables published in the journal Progress in Photovoltaics.

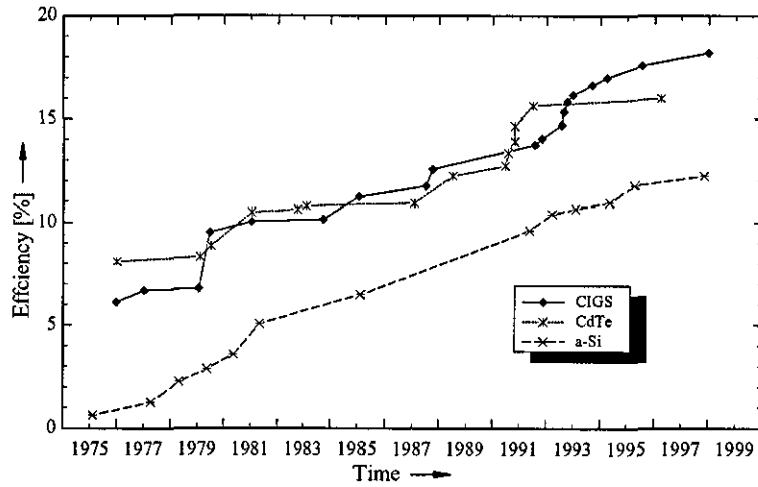


Figure 1.1: *Development of Achieved Efficiencies for Thin Film Solar Cells¹*. All devices have achieved efficiencies of 10% with CIGS approaching 20%.

(c-Si) devices. Differences have been reported in the seasonal performance of amorphous Silicon (a-Si). Explaining these is the major aim of this study, since this a prerequisite for accurate performance prediction and a successful market introduction of these technologies. Kleiss et al. [Kleiss 94] attempted to model the performance, which includes environmental data as input for a simulation code. This published model can predict only the output at the maximum power point while the approach given in this work predicts the overall I-V characteristic.

Amorphous silicon was the only thin film technology commercially available at the beginning of this study, with two more technologies on the verge of commercialisation, Cadmium-Telluride (CdTe) and Copper-Indium/Gallium-Diselenide (CIGS), and thus the work was extended to include the behaviour of these devices as well. Solar cells are commonly calibrated at standard test conditions (STC) and efficiency is stated at these conditions. However, these are rarely seen in outdoor operation and thus performance variations need to be investigated and modelled. A very general introduction to performance effects is given in chapter 2, where

terms used throughout this work are defined.

The most accurate approach to system performance modelling for c-Si is to apply a parametric model and include the thermal variation of the underlying parameters [Coors 97]. The model commonly used for c-Si is the two diode model. It is of limited applicability for thin film cells, as will be shown in chapter 3. Thus, more suitable models are identified in that chapter. The standard parametric model, in its most general form, does not model the thermal behaviour of the short circuit current I_{SC} and the open circuit voltage V_{OC} realistically, and the variation of the underlying parameters needs to be included. There is, however, hardly any data available in the literature and thus the dependence of these parameters on temperature is investigated in chapter 6. This required the development of a method for the accurate determination of these parameters. The necessary software development is given in chapter 4. The hardware used for this as well as for the other experiments is described in chapter 5.

Under real operating conditions the devices also will be exposed to changes in the incident solar spectrum [Rüther 94, Kleiss 92]. The significance of this is investigated in chapter 7.

The significance of environmental effects on the performance of thin film devices is then investigated in chapter 8, analysing outdoor measurements for a-Si, CdTe and CIGS technologies.

The information gained is then used for developing a system model that allows the systematic investigation of the importance of environmental factors on the performance of thin film solar cells. This is done in chapter 9.

Chapter 2

Influence of Operating Conditions on the Performance of Solar Cells

This study was initiated because of reports of a significant seasonal difference in behaviour of a-Si photovoltaic (PV) devices by R  ther and Livingstone [R  ther 94]. The aim was to understand this behaviour and investigate these effects for the particular location of Loughborough, UK. Two further materials were close to market introduction, CdTe and CIGS, and it was decided to include them in the study as well.

This chapter gives a short introduction to the influence of the operating conditions on solar cells as it is commonly observed. A much more detailed analysis follows in chapter 3, where the device physics is considered. Here, the intention is to introduce the standard performance parameters and illustrate the expected influence of the operating conditions. These will be investigated on the basis of experimental results in chapter 6.

The influence of environmental factors on the performance of PV cells can be separated into four effects: temperature, magnitude of irradiance, spectral composition of the light and time of light exposure. These effects will be discussed in

Temperature	25°C
irradiance	1000 W/m ²
Spectrum	AM1.5

Table 2.1: Standard Test Conditions for Solar Cells.

the following sections of this chapter. These effects generally can be superimposed except for the degradational effects, because it is known that degradation depends on temperature and irradiance [Kondo 97, Cueto 99].

2.1 Performance Parameters

Solar cells are commonly tested under Standard Test Conditions, which are summarised in table 2.1. Such a measurement does not describe the outdoor performance well, because the operating temperature is typical of the winter months whilst the irradiance intensity is observed in the summer. The spectrum is more applicable to the spring/autumn period.

Thus, it is important to investigate the influence of deviations from these standard conditions on the device performance.

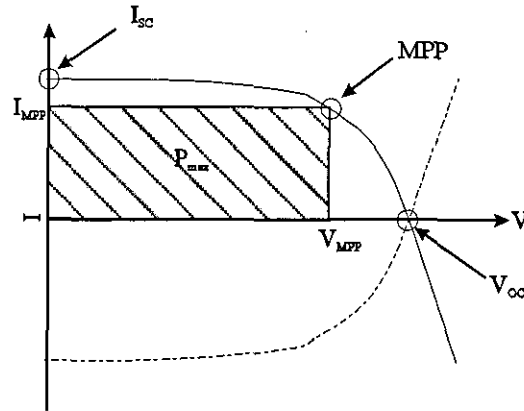


Figure 2.1: *Illustration of Common Performance Indicators.* The graph compares physical (dashed line) and engineering sign convention (full line) and illustrates the performance indicators in the engineering convention.

The device performance is commonly described using the short-circuit current I_{SC} , the open circuit voltage V_{OC} , the maximum power point MPP, and the fill factor FF, which is a measure of the "squareness" of the I-V characteristic. These are illustrated in figure 2.1. The FF is defined as:

$$FF = \frac{V_{MPP} \cdot I_{MPP}}{V_{OC} \cdot I_{SC}} \quad (2.1)$$

where V_{MPP} and I_{MPP} represent the voltage and the current at the maximum power point. This relates directly to the efficiency η as:

$$\eta = \frac{V_{OC} \cdot I_{SC} \cdot FF}{P_i} = \frac{P_{MPP}}{P_i} \quad (2.2)$$

where P_i is the power of the incident irradiance and P_{MPP} is the electrical power at the maximum power point. A very important factor for understanding the influence of temperature and irradiance is the band gap of the material. It directly determines the theoretical maximum efficiency and its influence is two-fold. Firstly, it determines the number of electrons that are generated by the incident light because this is the minimum energy required for generating an electron-hole pair and only photons with an energy equal to or higher than the band gap can generate an electron-hole pair, i.e. a lower band gap will result in a larger current. Secondly, the operating voltage is related approximately linearly to the band gap, i.e. a larger band gap results in a larger open circuit voltage. These two facts are contradicting themselves. Obviously, power is current times voltage which results in a zero power for a zero bandgap or an infinitely large band gap because either the voltage or the current will be zero. Clearly, there will be a maximum between the two extremes, as illustrated in figure 2.2. The maximum theoretical

efficiency is dependent on the spectrum, for the AM1.5 spectrum the ideal band gap is around 1.4 eV.

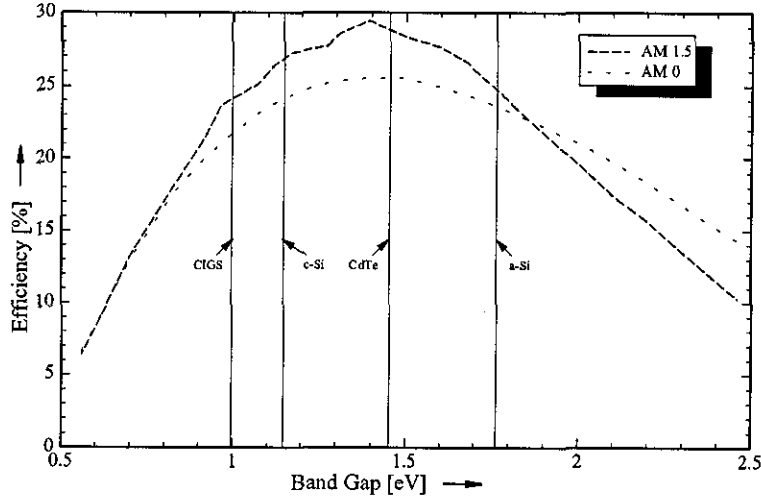


Figure 2.2: *Dependence of the Theoretical Device Efficiency on the Band Gap.* The figure illustrates the position of the band gap for materials investigated in this study relative to the theoretical maximum efficiency using the data presented in [Green 92].

I_{SC} and V_{OC} are thus given by device physics, although they can be adversely affected by device engineering issues. The FF, and thus the MPP, is dependent on the amount of recombination occurring within the device as well as the series and shunt resistance.

2.2 Thermal Effects

The effect of temperature results from a reduction of the band gap with increasing temperature and an increase of recombination. This decrease in the band gap will have a direct impact on the open circuit voltage. A smaller band gap also means that less energy is needed for the generation of an electron hole pair, thus the short circuit current will increase. This behaviour is illustrated in figure 2.3. The

effect on the I_{SC} is considered to be small and linear in most cases, while the effect on V_{OC} depends logarithmically on the ratio of photocurrent and recombination current.

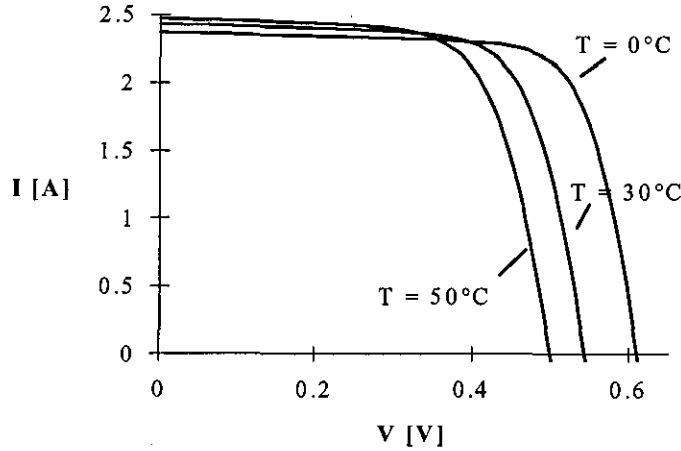


Figure 2.3: *Illustration of the Temperature Dependence of a Solar Cell.* The curve is plotted using standard parameters for c-Si solar cells.

The overall effect is a reduction in the peak theoretical efficiency, which is easily explained with reference to figure 2.2. In the case of CIGS and c-Si the band gap moves away from the theoretical maximum, leading to a reduction in efficiency. CdTe will show a less severe impact because the variation is in the flat region of the curve shown in figure 2.2. However, a-Si will move towards the maximum and thus temperature may have a positive influence, depending on the magnitude of recombination, though. The commonly reported slight decrease in efficiency in a-Si devices, e.g. see [Schade 98], is not due to the apparent reduction of the band gap, but due to an increase in recombination which dominates the device behaviour.

It is a well known fact that devices tend to operate at temperatures which are elevated with respect to the ambient temperatures, e.g. see [Fuentes 85, Koltay 98]. However, the magnitude for the investigated materials may differ from the com-

mon c-Si devices, mainly due to the different band gaps of the devices and different device structures.

2.3 irradiance Effects

The photocurrent is commonly assumed to superimpose on the effects of operating conditions, i.e. to be independent of the operating conditions [Tarr 80]. This principle of superposition is in fact a crucial assumption, because it allows the use of Shockley's theory of diodes [Shockley 49] and the modelling of the influence of illumination with a voltage-independent photocurrent. The magnitude of the photocurrent varies linearly with intensity and shows a small linear temperature dependence, as explained in more detail in chapter 3. The open circuit voltage varies logarithmically with illumination. This behaviour is illustrated in figure 2.4.

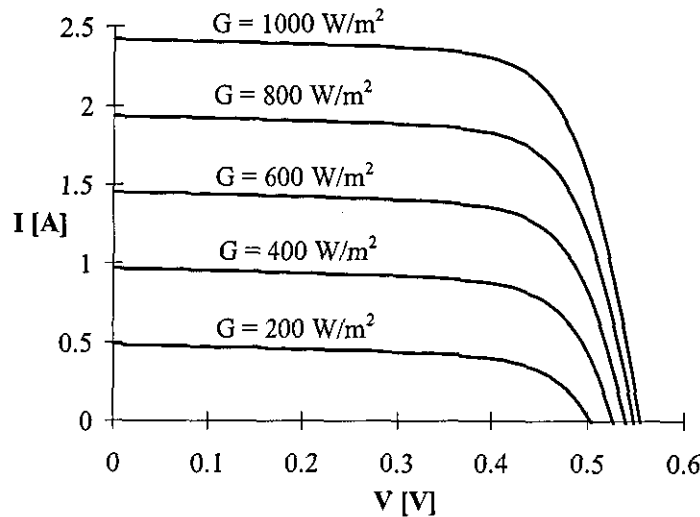


Figure 2.4: *Influence of the Irradiance Intensity of the I-V Characteristic.* The effect is considered to be a linear relationship on the light intensity.

Engelhardt [Engelhardt 96] investigates this for CIGS, showing that the assumption of a linear dependence on the photocurrent is sufficient, which is confirmed for

different CIGS devices investigated by Nishitani et al. [Nishitani 98]. No such investigation is known to the author for the other materials. However, these results cannot completely be reproduced in this work, as shown in chapter 8.

2.4 Spectral Effects

The spectrum directly influences the magnitude of the photocurrent. It may vary due to changes in air mass, weather, humidity or particles in the air. This has been modelled e.g. by Nann [Nann 92a] and Chen [Chen 94]. A shift in the spectrum towards higher photon energies, i.e. the blue spectrum, for lower air masses, i.e. towards noon (daily cycle) and towards summer (seasonal cycle), has been predicted. However, the investigation of such spectral effects is not commonly done and nothing is known about the magnitude of these effects in the UK. The UK presents a different climate from the sites where investigations of such spectral effects have been carried out to date. It is a maritime climate in contrast to e.g. Stuttgart, Germany or Golden, USA, for which data exists. Thus, a spectroradiometer was installed at the Centre for Renewable Energy Systems Technology (CREST) in Loughborough and an investigation of apparent spectral effects was carried out. The results are presented in chapter 7.

2.5 Degradational Effects

There is a minor degradation during operation for all kinds of materials, including c-Si, but the strongest known effect is for a-Si. In the case of a-Si it is known that the device performance reduces over a continued period of exposure, eventually reaching a stable value after roughly 6 months. The final efficiency strongly depends on the material and the newer multi-junction devices show less degradation than the first generation single junction devices [Wagner 95]. It is difficult to

determine exactly how much a device deteriorates in outdoor operation because other environmental effects such as temperature and irradiance level have a significant influence on the overall degradation. Thus, a thorough understanding of the other environmental effects is needed before any serious attempt of modelling degradation can be carried out.

Chapter 3

Parametrisation of Thin Film

Solar Cells

An accurate understanding of the environmental effects is only possible if the individual effects can be modelled. Thus, the effects can be separated and quantified. It has been shown for c-Si that the most accurate method of performance modelling is by means of a model based on the device physics [Coors 97]. It was decided to follow this route in order to model thin film devices.

This chapter reviews the literature on this topic, starting with the well documented model for c-Si, the two diode model. The applicability of this model is investigated for the case of thin film devices on the basis of available literature. It transpires that the two diode model is not applicable and necessary improvements are presented.

3.1 Standard Diode Models

In the most general case, solar cells are described by a set of coupled, non-linear differential equations. These are given here following the description of Wagemann and Eschrich [Wagemann 94].

The first formula needed is the Poisson equation, the Maxwell equation that relates the divergence of the electric field E to the space charge density:

$$\nabla \cdot \overline{E} = \frac{e}{\epsilon_0 \epsilon_r} (p - n + N_D^+ - N_A^- \pm N_{rec}^{+,-} \pm N_{trap}^{+,-}) \quad (3.1)$$

where e is the positive elementary charge of an electron, ϵ_0 is the permittivity in the vacuum, ϵ_r the dielectric constant, p the density of the positive charge carriers (i.e. holes), n the density of the electrons, N_D (N_A) are stationary ionised donor (acceptor) concentrations acting as disturbance centres, $N_{rec}^{+,-}$ and $N_{trap}^{+,-}$ are the densities of recombination centres and traps.

The overall current is formed by the partial currents of the electrons and the holes. The current densities for the electrons j_e and the holes j_h become:

$$\begin{aligned} j_e &= e\mu_e n \overline{E} + eD_e \nabla n \\ j_h &= e\mu_h p \overline{E} - eD_h \nabla p \end{aligned} \quad (3.2)$$

where μ_e , μ_h represent the mobility of the electrons and holes, and D_e and D_h are the corresponding diffusion coefficients.

Finally, the continuity equations are needed:

$$\frac{\partial p}{\partial t} = -\frac{1}{e} \nabla \cdot \overline{j_h} - \frac{\Delta p}{\tau_h} + G_{opt} \quad (3.3)$$

and

$$\frac{\partial n}{\partial t} = +\frac{1}{e} \nabla \cdot \overline{j_e} - \frac{\Delta n}{\tau_e} + G_{opt} \quad (3.4)$$

where G_{opt} represents the optical generation rate, which depends on the frequency and intensity of the light and τ_h and τ_e are the lifetimes of the holes and electrons respectively. The mobility of the electrons and the holes, the diffusion coefficients and the lifetimes are connected through the Einstein relation for non-degenerate statistics:

$$D_{h,e} = \frac{kT}{e} \mu_{h,e} \quad (3.5)$$

and the diffusion length $L_{h,e}$:

$$L_{h,e} = \sqrt{D_{h,e} \tau_{h,e}} \quad (3.6)$$

where T is the device temperature in [K] and k is the Boltzmann constant.

This set of equations can only be solved in general by means of numerical integration, which is certainly not appropriate for the case of system modelling, both because of its high complexity and the lack of material parameters for specific devices. Thus, in order to obtain a closed form analytical solution, several assumptions and simplifications have to be made. The main assumption is about the electric field across the device, which is assumed to be restricted to the space charge region (SCR) of the device, which stretches from x_p to x_n in figure 3.1. In a p-n junction, the SCR accounts for only a minimal part of the overall thickness of the device. It is, in order to maximise the charge separation, close to the top of the cell, as the largest amount of the absorption occurs close to the top surface. However, the majority of the carrier generation happens far away from the junction and in the absence of an electric field. In order to contribute to the generated current, the charge carriers must be separated by a potential difference, which is

implemented by the p-n junction. It is assumed that the area outside the junction is field free, as illustrated in figure 3.1. This certainly is a significant simplification but valid for high quality material. As only charge carriers that reach the junction will contribute to the overall current, the generated electron-hole pairs will have to separate in space. Without this separation, the generated electron-hole pair would simply recombine and would be lost. There is no field present for the majority of charge carriers, thus any movement is simply driven by charge carrier concentrations, the mechanism for the charge separation is diffusion.

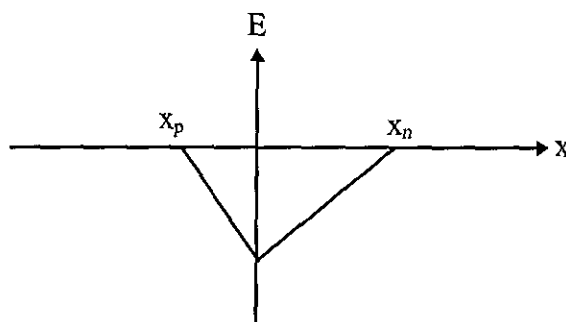


Figure 3.1: *Assumed Electric Field over the Space Charge Region.* The electric field within the device is assumed to be restricted to the SCR and to be negligible outside it.

Carrier generation within the junction, i.e. in the presence of the field, the so-called drift current, is neglected in the standard approach, albeit in principle being a significantly more efficient mechanism of charge separation. The current through the whole device is then assumed to be the sum of the minority carrier currents. Using these assumptions and solving above equations yields the so-called one diode model, which is described as:

$$I = -I_{ph} + I_{01} \left[\exp \left(\frac{eV_j}{n_1 kT} \right) - 1 \right] \quad (3.7)$$

This is the standard diode equation shifted by the photogenerated current I_{ph} . I is the current through the device in [A], I_{01} is the saturation current of the diode in [A], V_j is the voltage across the junction and n_1 is the ideality factor of the diode. The ideality factor is introduced to compensate for the fact that the assumption of pure diffusion driven currents is not always exact. The ideality factor should be between one, which indicates pure diffusion in the cell, and two, which indicates a completely drift driven device [Jia 87].

The voltage at the junction normally varies from the voltage at the nodes because there is a potential drop due to the resistance of the contacts and the path through the semiconductor material etc. It can be modelled simply as:

$$V_j = V - IR_S \quad (3.8)$$

where R_S is a lumped series resistance in $[\Omega]$. Furthermore, not all the current goes across the junction - due to the size of these devices there is always some shunting at the cell boundaries or due to imperfections at the junctions. This shunt current I_{sh} can be described as:

$$I_{sh} = \frac{V_j}{R_P} \quad (3.9)$$

where R_P is the parallel or shunt resistance.

As mentioned, the one diode model given so far neglects completely any recombination within the SCR of the device. However, recombination will occur within the SCR, despite the presence of an electric field which drives the charge carriers. This can be modelled as the current of a second diode I_{D2} which is given as:

$$I_{D2} = I_{02} \left[\exp \left(\frac{eV_j}{n_2 kT} \right) - 1 \right] \quad (3.10)$$

The ideality factor in this case should be close to two.

The model is thus given as:

$$I = -I_{ph} + I_{01} \left(\exp \left(\frac{eV_j}{n_1 kT} \right) - 1 \right) + I_{02} \left(\exp \left(\frac{eV_j}{n_2 kT} \right) - 1 \right) + \frac{V_j}{R_p} \quad (3.11)$$

This model is referred to as the two diode model. The equivalent circuit representing this is shown in figure 3.2.

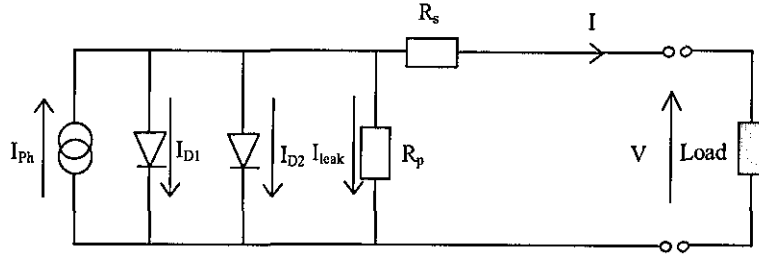


Figure 3.2: *Electrical Representation of a Solar Cell.* The cell is represented by the four partial currents: photogeneration, first diode, second diode and shunting.

The parameters needed for the description of the two diode model are I_{ph} , I_{01} , n_1 , I_{02} , n_2 , R_s and R_p . Choosing a realistic set of parameters (the values for parameters used for this graph are given in chapter 4) then allows one to investigate the contributions of the partial currents, as done in figure 3.3 for constant irradiance and temperature. It is apparent that different regions are dominated by different partial currents.

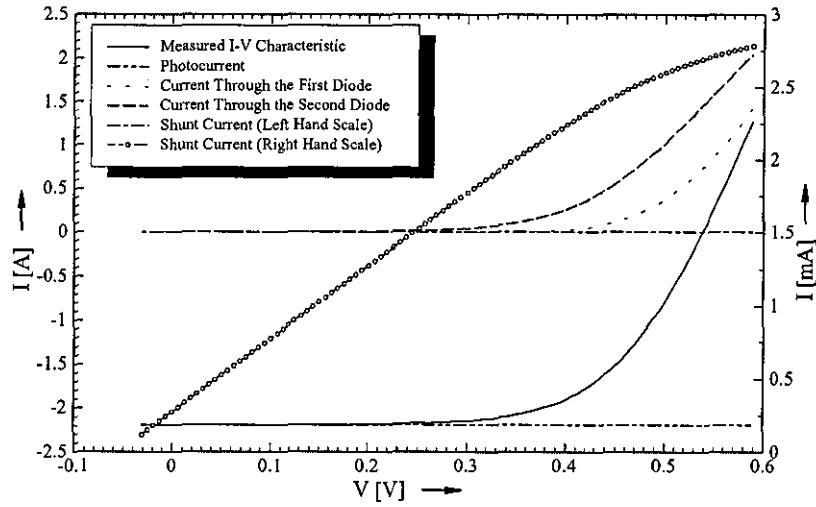


Figure 3.3: *Contributions of the Partial Currents to the Overall I-V Characteristic.* The graph shows the partial currents through the electric devices representing the equivalent circuit, which are calculated as described in the text. The contribution of the shunt is diminishingly small, thus it was plotted a second time on another scale.

3.2 Modifications for a-Si Devices

Amorphous silicon devices deviate from the model given in equation 3.11 in the key aspect that they show a voltage dependent photocurrent as shown in figure 3.4, where the same module is measured under illuminated and dark conditions at the same temperature. The principle of superposition, i.e. that the photocurrent is independent of operating voltage, is violated and another model has to be applied. The reason for this behaviour is that a-Si devices are dominated by drift currents, i.e. charge separation occurs due to an electric field. This is caused by the different device structure, which is illustrated in figure 3.5. The main difference is the introduction of an intrinsic layer between the n and the p layer.

The introduction of an intrinsic layer, the so called p-i-n structure, extends the SCR over the whole i-layer, as shown in figure 3.6. The i-layer takes up the vast majority of the cell volume. Thus nearly all carriers are generated in the

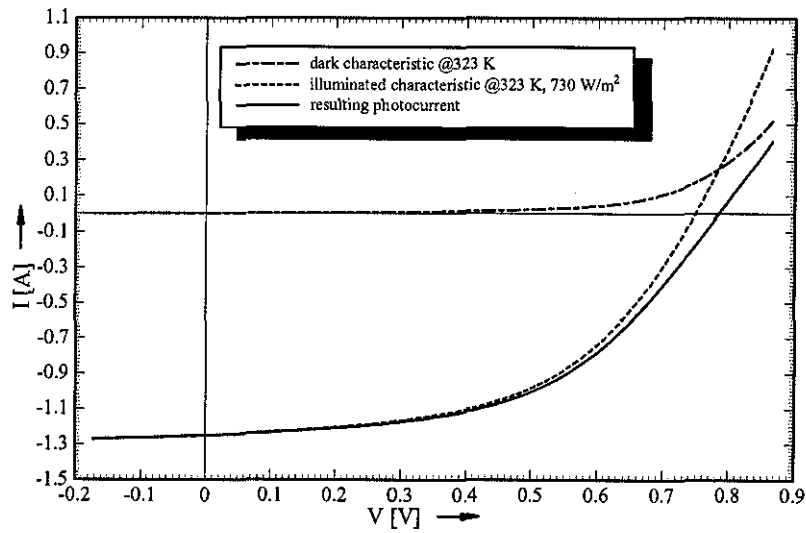


Figure 3.4: *Photocurrent of a New a-Si Module.* The measurement shown here was taken at an irradiance of 730 W/m^2 and at a temperature of 323 K . It is obvious that the assumption of a constant photocurrent is not applicable to a-Si devices.

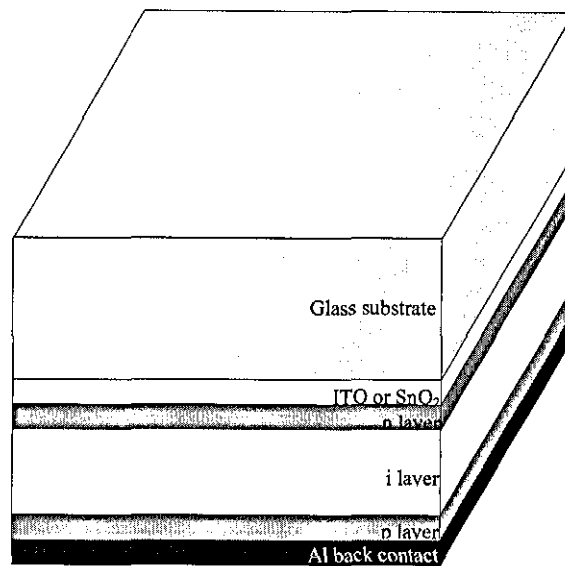


Figure 3.5: *Structure of a Single Junction a-Si Cell.* The back contact of this superstrate structure is typically realised by aluminium, which is followed by the semiconductor layers, front contact and glass cover.

presence of an electric field. This enhances the charge separation and is a much more efficient process than diffusion, which dominates c-Si devices. The presence of the field allows the use of lower quality semiconductor materials. It has also been shown that the voltage across the device has an influence on the degradation, which led to the production of same-bandgap multijunction devices. This increases the potential across the width of the cell and thus reduced electronic properties are felt less than for a lower potential.

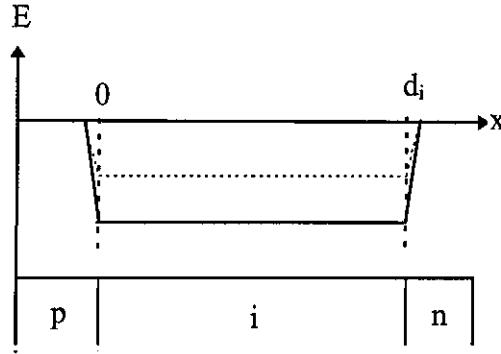


Figure 3.6: *Structure of the Electric Field within the p-i-n Solar Cell.* For the sake of orientation the diode structure is sketched below the field. The zero point of the x-axis is the p-i junction, d_i is the thickness of the i-layer. For an applied forward bias the magnitude of the electric field will decrease as indicated with the dashed lines.

The first closed form solution for the I-V characteristic of this device structure was given by Crandall [Crandall 83]. This method was first used by Smeets et al. [Smeets 86] for the modelling of a-Si solar cells. It is the commonly used method for the parametrisation of a-Si devices [Wagemann 94, Hegedus 97].

The photocurrent is modelled as:

$$I_{ph} = I'_{ph} (V_{bi} - V_j) \frac{\mu\tau}{d_i^2} \left[1 - \exp \left(-\frac{1}{\frac{\mu\tau}{d_i^2} (V_{bi} - V_j)} \right) \right] \quad (3.12)$$

where I'_{ph} is the irradiance dependent saturation current of the photocurrent, d_i is the thickness of the i-layer, $\mu\tau$ given in $\left[\frac{cm^2}{V}\right]$ is called the effective lifetime of the charge carriers albeit strictly speaking it does not have the units of a life time. V_{bi} is the built in voltage.

However, this method was criticised on the basis of numerical simulation by Hack and Shur [Hack 85]. A possible explanation for the deviations found between the numerical and the analytical solution is believed to be due to the fact that the main contributor to the recombination, the dangling bonds, have three charge states and not two as used by Crandall. This amphoteric nature is well accepted nowadays, and used for modelling purposes (see e.g. Rubinelli and Schropp [Rubinelli 98]). Subsequently, the recombination function is different. Fischer and Shah [Fischer 94] suggested a new recombination function in order to allow for the amphoteric influences on the recombination. This was used by Hubin and Shah [Hubin 95] for a model of the drift component of the photocurrent. Merten et al. [Merten 98b] use this function to model the behaviour of an a-Si solar cell as:

$$I = -I'_{ph} \left(\frac{1}{\frac{\mu\tau}{d_i^2} (V_{bi} - V_j)} - 1 \right) + I_0 \left(\exp \left(\frac{eV_j}{nkT} \right) - 1 \right) + \frac{V_j}{R_p} \quad (3.13)$$

The ratio in the first term of equation 3.13 is the term calculated by Hubin and Shah [Hubin 95], which describes the photocurrent produced under drift conditions assuming weak absorption. The remaining two terms in equation 3.13 are phenomenologically identical with the one diode model. The additional loss term in equation 3.13 shows a relatively small influence for high $\mu\tau$ products, i.e. long drift distances. On the other hand, a short drift length means that there will be hardly collection of photocurrent. The voltage dependence of the photocurrent

explains the apparent decrease of shunt resistance, i.e. slope around I_{sc} , for illuminated devices, as shown in figure 3.8, which is frequently reported in the literature e.g. by Alonso et al. [Alonso 94] or by Protogeropoulos et al. [Protogeropoulos 91]. This also explains the decrease in shunt resistance with increasing degradation, as observed in our laboratory [Gottschalg 98], because any degradation will adversely affect the drift length and thus increase the impact of the voltage dependence around I_{sc} .

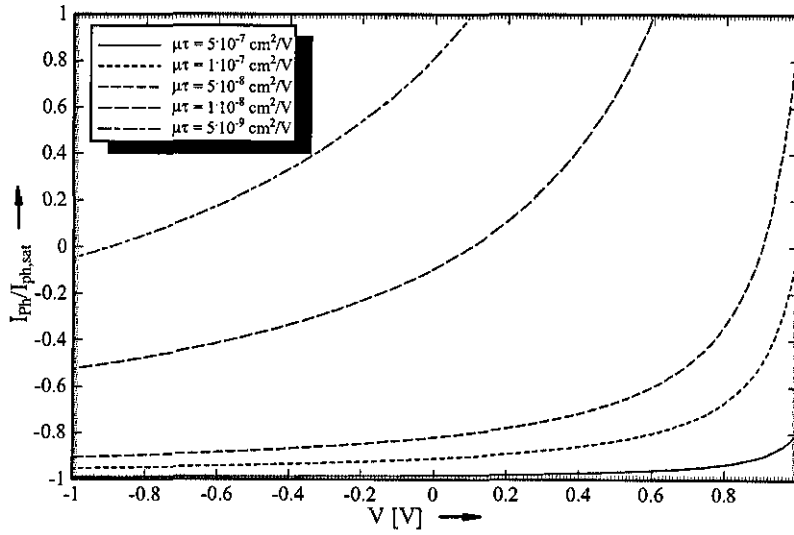


Figure 3.7: *Influence of the $\mu\tau$ -Product on the Photocurrent.* The photocurrent is calculated assuming a flatband voltage of 1.1 V and a normalised saturation current of the photocurrent. The order of magnitude of the $\mu\tau$ -product is in accordance with Schiff [Schiff 91].

A test for the applicability of both models was conducted [Gottschalg 98] in order to decide between the two models. It was found that for devices tested in this study, the Shah-Merten model as given by equation 3.13 delivers the more realistic results. Illuminated I-V measurements were taken for temperatures ranging from 293 to 348 K. Both theoretical models were then fitted and the results were compared with the expectations.

The investigation used two indicators for the appropriateness of the model. Firstly,

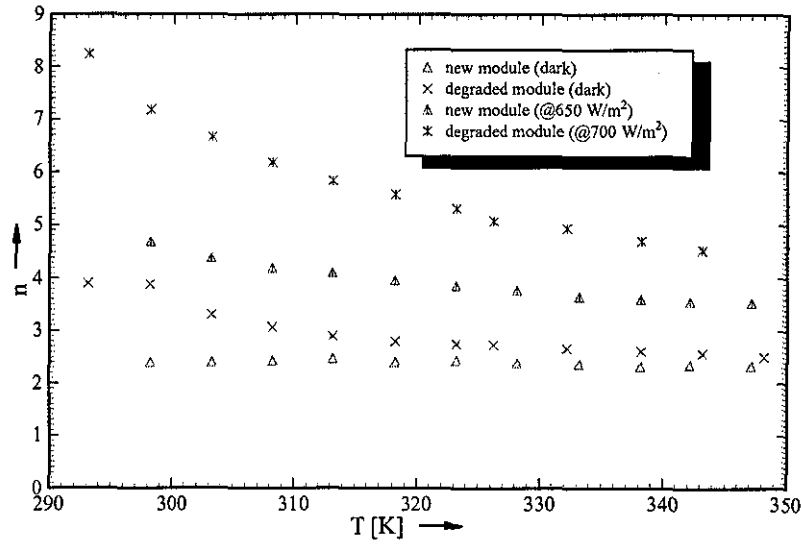


Figure 3.8: *Thermal Behaviour of the Diode Ideality Factor of Modules.* Values extracted in the dark are high and were investigated further. Values obtained in the illuminated case show the inappropriateness of the voltage independent photocurrent model to describe a-Si devices.

the diode ideality factor should theoretically be less than two and a valid model should give values in this order of magnitude. Secondly, values for the flatband voltage and $\mu\tau/d_i^2$ should give sensible results.

The diode ideality factor appears to be problematic, as it seems to be very high, even in the dark case. As stated above, it should be below two, higher values are unphysical. However, these values are not uncommon. A possible explanation is a distributed series resistance, which was shown to have an impact on these properties with c-Si devices (e.g. [DeVos 84, Araujo 86]). It was shown by Eisgruber and Sites [Eisgruber 94], that a high diode ideality factor of thin film solar cells can be the result of a distributed series resistance. Decreasing the size of the cell should then give values below two. This was then investigated by cutting a small single cell out of one of the modules. The cell was then edged at all four sides in order to eliminate any damage done by cutting the module and measured again. The result, which is shown in figure 3.9 for two samples, shows that the diode

ideality factor is indeed below two, supporting this theory. Thus, a geometric factor will need to be introduced when looking at modules.

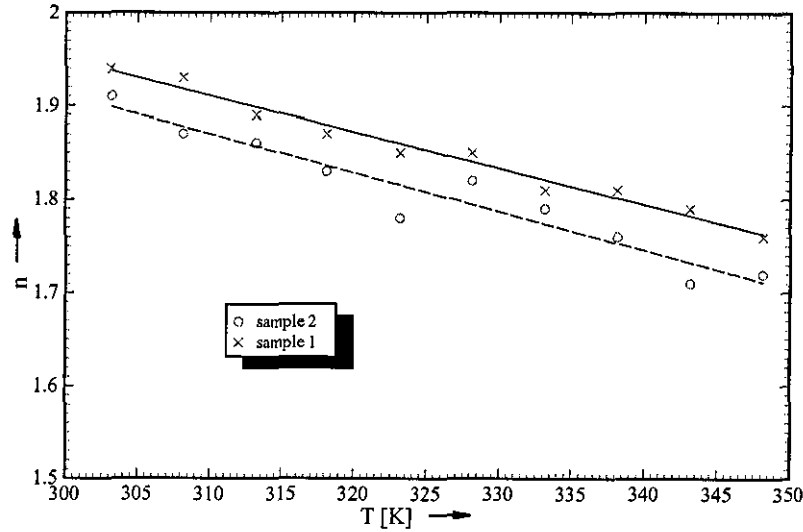


Figure 3.9: *Diode Ideality Factor of a Smaller Cell.* Both samples were cut out of a full size module which exhibited a diode ideality factor above two. The lower values of the diode ideality factor of these samples indicate that the high diode ideality factors shown for full size modules are due to geometric effects.

The flatband voltage should be around 1.1 to 1.2 for a-Si devices [Wagemann 94].

This value was indeed found for both models.

The $\mu\tau/d_i^2$ -product, as shown in figure 3.10, gave an indication for a preferred model. In order to investigate the appropriateness of the $\mu\tau/d_i^2$ -product it is necessary to estimate the physical range of these parameters. According to Wagemann and Eschrich [Wagemann 94], values of these properties can be expected as: $\mu \approx 0.1 \text{ cm}^2\text{V}^{-1}\text{s}^{-1}$, $\tau \approx 10^{-8}..10^{-6} \text{ s}$ and $d_i \approx 10^{-6} \text{ m}$. In this context, the values obtained with Crandall's model appear to be too high. The values extracted for this model are shown for a degraded module in figure 3.10. They would correlate with a thickness of the i-layer between 10^{-10} m and 10^{-8} m , which is too thin. Thus, the Shah-Merten Model would appear to be more realistic and is used in the further investigations.

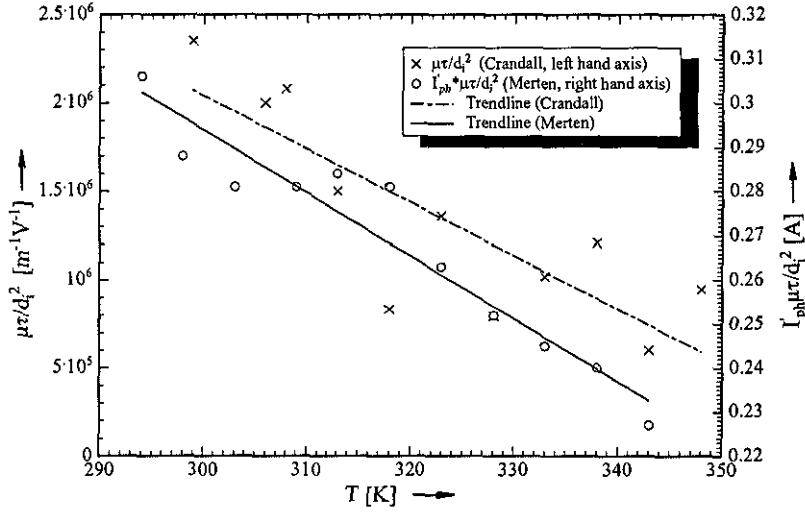


Figure 3.10: Variation of the $\mu\tau/d_i^2$ -Product. The thermal behaviour is rather similar for both models. The absolute values are more realistic for the Merten model.

3.3 Modifications for CIGS and CdTe

CIGS and CdTe solar cells are polycrystalline heterojunction devices, produced as p-n junctions. Thus, there is no obvious reason why the Shockley model should not apply. However, measured I-V characteristics show a forward current limiting effect, which is temperature dependent as shown in figure 3.11. This gives a clear indication that the standard model needs to be modified.

The roll-over effect observed in figure 3.11 can be attributed to the device structure illustrated in figure 3.12. The CdTe layer forms a Schottky barrier with the back contact which is reverse biased, thus creating the current limiting effect shown in figure 3.11.

A back diode was reported for both materials, e.g. by Bowron et al. [Bowron 91] and Engelhardt [Engelhardt 96] for CIGS, and Stollwerck [Stollwerck 95] and Niemegeers and Burgelmann [Niemegeers 97] for CdTe. It can be reasoned as a lowering of the bands at the metal-semiconductor contact as illustrated in figure

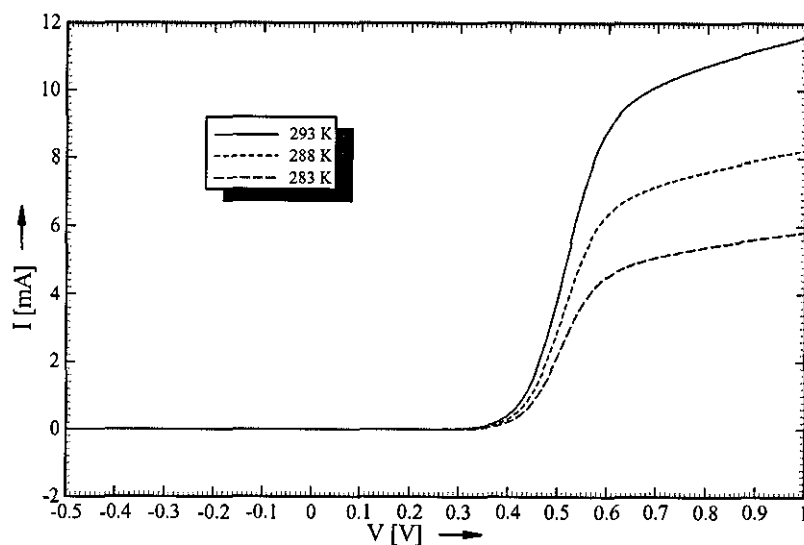


Figure 3.11: *Measured I-V Dark Characteristic of a CdTe Solar Cell.* There is a temperature dependent, forward current limiting effect, which can not be explained by the standard theory.

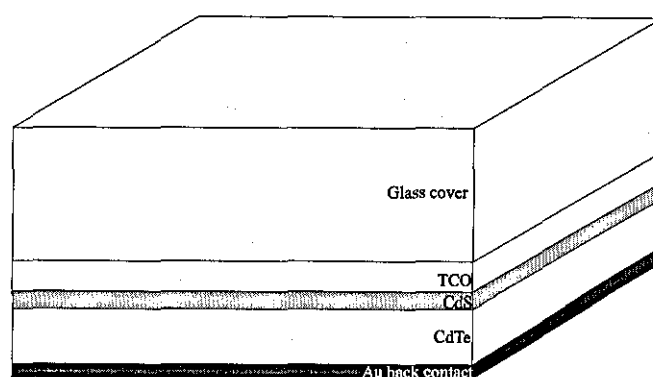


Figure 3.12: *Structure of a CdTe Cell.* The device shown here is manufactured using a glass superstrate with the layers deposited as indicated in the graph.

3.13 for a CdTe device. This back contact manifests itself by two effects: firstly, a roll over effect (i.e. the I-V characteristic saturates for voltages above the open circuit voltage for low operating temperatures) and secondly a cross-over effect (i.e. the illuminated and dark characteristic intersect).

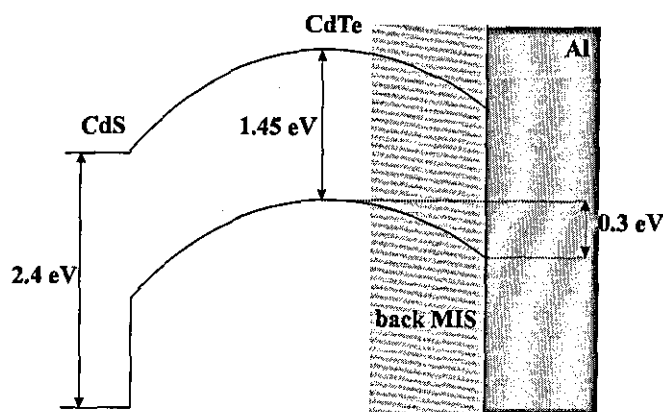


Figure 3.13: *Schematic Band Diagram of a CdTe Cell.* The graph illustrates the band bending towards the back Al-contact and the formation of a back metal-intrinsic-semiconductor junction that is opposite to the main junction (after [Stollwerck 95]).

This Schottky diode influences the device behaviour more significantly at lower operating temperatures, as seen in figure 3.11, which would agree with a back diode. However, this diode is not part of the photovoltaically active material. Thus, its influence is on the apparent series resistance yielding the equivalent circuit shown in figure 3.14.

When allowing for a modified series resistance, the mathematical representation given in equation 3.11 is still applicable. However, the voltage at the junction has to be calculated differently. In addition to the voltage drop over the series resistance, a voltage drop occurs across the Schottky diode. The voltage at the junction can then be calculated as:

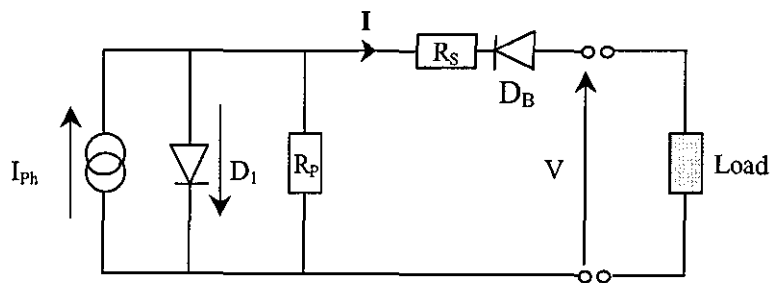


Figure 3.14: *Electrical Representation of a CdTe Solar Cell.* The equivalent circuit is essentially identical to the standard representation except for the added backdiode D_B . It is obvious that this diode influences the voltage apparent at the main junction but, in this picture, does not have any other effects.

$$V_j = V - IR_S - V_{BD} \quad (3.14)$$

Here V_{BD} represents the voltage drop across the back diode.

The Schottky diode is in reverse bias but, as Niemegeers and Burgelmann suggest [Niemegeers 97], should not be in breakdown for normal operating conditions. This assumption is reasonable because the voltages involved in operating such devices are well below one volt per cell at the point of connection, while typical breakdown voltages are in the order of several volts. The overall voltage drop is split between the back diode, the series resistance and the main junction. Thus, the voltage drop across the Schottky diode is relatively small and no breakdown can be expected. The voltage drop across the back diode can thus be modelled as a normal Schottky diode in the generation/recombination mode, which is given as:

$$V_{BD} = \frac{kT}{e} \left[\ln \left(\frac{I}{I_{BD}} + 1 \right) \right] \quad (3.15)$$

Here I_{BD} is the saturation current of the back diode which depends exponentially on temperature. The influence of the back diode and the band diagram given in figure 3.13 indicate that the influence of the metal-semiconductor structure is dominated by the hole current. Thus, a good approximation to the voltage drop across the back diode can be given by modelling the hole current only. The voltage drop then is given as:

$$V_{BD} = -\frac{kT}{e} \left[\ln \left(-\frac{I}{I_{BD}} + 1 \right) \right] \quad (3.16)$$

A crude investigation of the influence of the back diode is now possible. Assuming that the current mechanism of the back diode is thermionic emission allows an investigation of its thermal influence. The thermal behaviour of the saturation current of the Schottky barrier dominated by thermionic emission can be modelled as [Sze 81]:

$$I_{BD} = A^{**} T^2 \exp \left(\frac{-e\phi_{BD}}{kT} \right) \quad (3.17)$$

Here A^{**} is the effective Richardson constant and ϕ_{BD} is the barrier height of the back diode. This temperature dependence was implemented in the sketch in figure 3.15, where the overall impact of this model is shown. It is important to note that only the thermal dependence of the back diode height is considered which leads to a misrepresentation of the thermal behaviour of the solar cell, but this will be investigated separately in chapter 6. The values used for this plot were chosen in order to represent a typical silicon solar cell with a back diode added. The back diode was estimated as I_{BD} equal to 1A for a temperature of 300 K. This is an estimation made on the basis of measurements presented by other groups, e.g. by

Stollwerck [Stollwerck 95]. The back diode barrier height was assumed to be 0.3 eV.

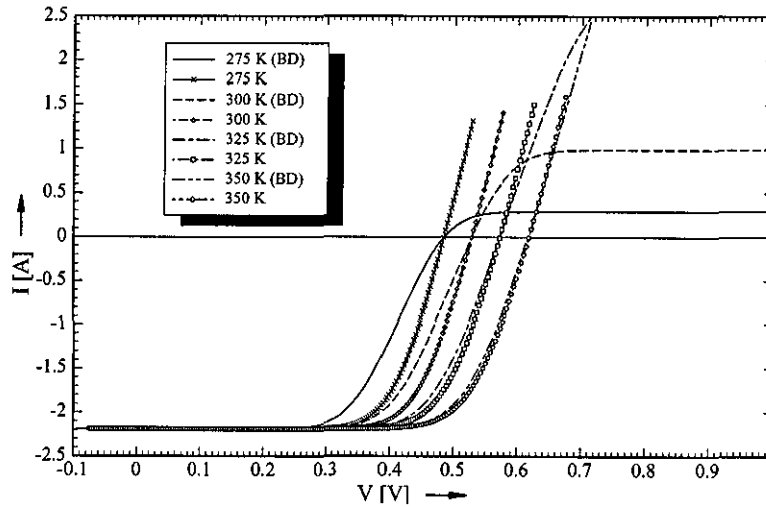


Figure 3.15: *Influence of the Back Diode on the Device Behaviour.* The curves were simulated by exclusively using the thermal dependence of the back diode, which explains the uncommon behaviour of I_{SC} and V_{OC} . The qualitative influence of the backdiode can be seen, though.

It can be seen, though, that the general trend is well in accordance with measurements reported e.g. by Stollwerck [Stollwerck 95]. The magnitude of the effect obviously depends on the actual barrier height, but it is interesting to see that the back diode effectively minimises the effect of extreme forward biasing, as can happen when a string in a parallel connection gets shaded.

Shafarman and Phillips [Shafarman 96] performed direct measurements on a CIS-Molybdenum contact and could not confirm the presence of a Schottky-like behaviour. Thus it is questionable that the observed diode originates from this contact. Topic et al. [Topic 97] investigated the behaviour of devices with such a blocking diode by means of numerical simulation, attributing any deviations to an increase in acceptor like states, though failing to explain why this should occur. Niemegeers et al. [Niemegeers 98] argue that the cross-over is due to effects in the

bulk. This contradicts the model of a nonlinear series resistance put forward by Topic et al. [Topic 97].

Thus, in the case of CIGS it is questionable if a back diode always exists. It may vary due to the many different production technologies. The applicability of the back diode model will be investigated in chapter 6, where the influence of temperature is investigated.

The method developed in this section certainly provides the expected trends. It obviously simplifies the picture significantly to assume a pure hole current and thermionic emission as a current mechanism. However, this avoids the necessity of further numerical analysis while being able to describe the cell behaviour. The applicability of this model will be discussed in more detail in chapter 6.

Chapter 4

Extraction of Physical Parameters

4.1 Introduction

It was established in the previous chapters that a parametric approach promises to be the most accurate method of I-V curve translation. However, in order to ensure the accuracy of the given models it is necessary to identify the parameters for a given device. Unfortunately, these are not easy to measure and have to be extracted from measured I-V characteristics. In all cases the quality of the model depends crucially on the appropriateness of the parameters used. It is therefore important to identify the most accurate method of determining such parameters. Different methods have been suggested for the extraction of parameters. These methods tend to give a relatively wide spread of extracted parameters which then lead to deviations for translated conditions [Herrmann 97]. Some methods, e.g. the one used by Wolf and Rauschenbach [Wolf 63], depend on the use of a multiplicity of measurements at different environmental conditions. The disadvantage of this approach is that in certain cases the parameters might not be independent

of those environmental conditions, i.e. they vary with temperature and irradiance [Veissid 91, Gottschalg 97]. Thus, this method can be expected to generate a significant error if any of the parameters changes its value due to the variation in measurement conditions.

Simplified, so-called direct, approaches have been suggested [Phang 84, Enebish 93, Craparo 95, Sharma 93], in which the equivalent circuit parameters are identified from particular features of the data, such as intercepts on the I and V axes and gradients at these points. For the unrealistic case of error free measurements and a perfect model, direct calculation is the most accurate method [Phang 86]. The disadvantage of such methods, though, is that they depend on the accuracy of the points chosen for the calculation. Should any of these points be erroneous, this will have a significant effect on the calculated parameters. It is not uncommon to obtain a negative shunt resistance when using these methods, which clearly is not a physical result. Thus, such methods were not considered for this work and instead the focus was put on the use of different fitting algorithms, as suggested by many workers [Charles 81, Araujo 82, Polman 86, Phang 85, Burgers 96].

Fitting algorithms are numerical methods to "fine tune" a given set of estimated parameters with respect to a user defined error function. This definition indicates that the quality of the result depends on three things: the initial estimation of the parameters, the error function and the applied algorithm.

Investigations published so far, e.g. [Phang 85, Appelbaum 93], have dealt with the influence of the error criterion used in the fitting process, assuming that all algorithms are equally good in optimising the values and that measurement strategy, accuracy and stability of the measurements do not have an influence on the overall accuracy. Prior to this work, the influence of the latter factors has not been systematically investigated.

This chapter investigates the influence of different extraction methods on the

overall quality of resulting parameters. In the second part it will then describe the algorithm used in the remainder of this work. This investigation concentrates on the two diode model, as it has a high number of parameters to be determined and thus represents a challenge for the extraction method. Hence, the quality of results obtained for this model should be surpassed by potentially simpler methods.

The investigation of the error criteria involves solving equation 3.11 repeatedly (or the appropriate equation for the extended models). This function is unfortunately implicit. It can not be calculated directly and thus needs to be iterated. The iteration process used in this work is to minimise the difference between the left and the right side of equation 3.11. The method used for this was the Van-Wijngaarden-Dekker-Brent algorithm as given by Press et al. [Press 89], as it is up to 15 times faster than other techniques such as binary search or golden section search.

4.2 Fitting of I-V Characteristics

Fitting is, as stated above, the fine tuning of estimated parameter values as illustrated in figure 4.1. The measurements are used as a starting point to estimate the initial values, which are subsequently adjusted until there is sufficient agreement between measurements and theory. The complexity of the fitting process increases with the number of parameters, because it increases the likelihood of local minima in the error function. These cause nearly all fitting algorithms to stop prematurely. Unfortunately, the diode model for solar cells shows a high number of local minima, as shown by Beier [Beier 92] and Knaupp [Knaupp 97]. The adjustment may be a blind 'trial and error' based approach, in which a new set of parameters is determined. This set is then tested, i.e. utilised to calculate synthetical measurements, which are then used to calculate the error. If the

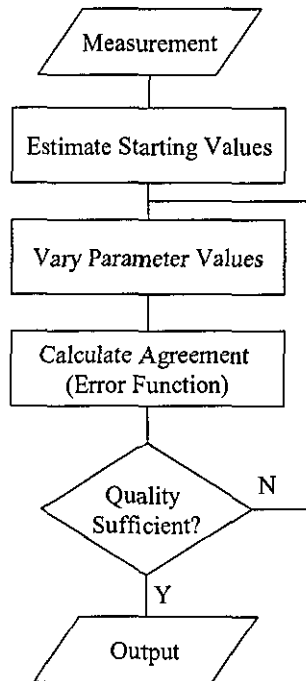


Figure 4.1: *Illustration of a General Fitting Process.* Using the measurements for comparison, a set of parameters is estimated and adjusted until the result is satisfactory.

calculated set is better than the previous set, the algorithm continues to search in this direction, if it is worse it changes direction. A typical representative of such an approach is the Simplex algorithm given by Caceci and Cacheris [Caceci 84]. It does not use any information contained in the error function.

A second class uses the error function by calculating the gradient of this function in the multi-dimensional space. This gradient is then evaluated and the algorithm follows the direction with the steepest reduction in the error function. A typical algorithm for this class is the Marquardt-Levenberg algorithm as given by Press et al. [Press 89].

If the function to be fitted is linear, it is possible to determine the parameters by simple matrix operations, thus reducing the problems of non-linear fitting. Unfortunately, the theoretical models to be fitted in this work are highly non-

linear and thus not suitable for such an approach. It is however possible to separate the fitting processes of linear and non-linear parameters. Such a method was developed for this work, because it promises to simplify the fitting process. The approach is explained here for the two diode model but the principle is the same for other models.

The idea of separating in linear and non-linear parameters was first published by Nguyen et al. [Nguyen 82]. Several such approaches have been published (e.g. [Araujo 82], [Obst 94]) so far but all of them have been limited to constant diode factors, thus fitting only one single non-linear fitting parameter. Investigation of the I-V relationship reveals that the parameters R_S , n_1 and n_2 are non-linear with respect to the fitting. The parameters I_{ph} , I_{01} , I_{02} and $\frac{1}{R_p}$ can be calculated using a linear approach.

Following the approach of separating linear and non-linear parameters for the fitting, a hybrid algorithm was developed. The non-linear fitting is performed using a Simplex algorithm, using the fact that this algorithm does not need any information on the error function except for the error for one set of parameters. The simplex determines the next combination of R_S , n_1 and n_2 to be tested. The corresponding linear parameters are then determined using a Singular-Value-Decomposition (SVD), which, according to Press et al. [Press 89], is the ideal solution for such a matrix based solution.

An additional benefit of the hybrid algorithm is that it only needs starting values for the non-linear parameters, thus minimising the problems of obtaining values for the diode saturation currents.

4.2.1 Identification of Starting Values

It will be shown that the estimation of good starting values can be crucial for the determination of sensible parameters. This section introduces the methods used

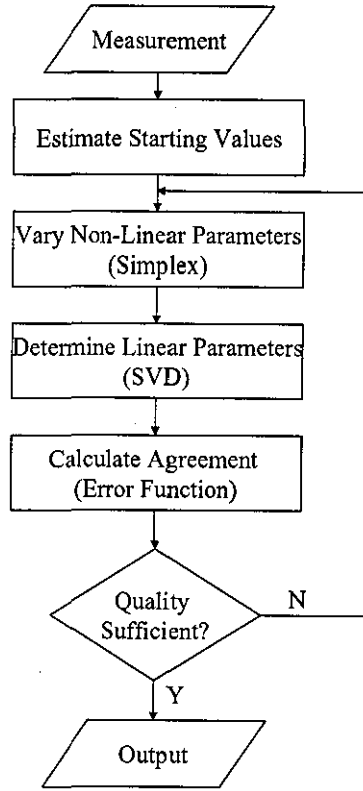


Figure 4.2: *Flow Chart of the Hybrid Algorithm.* The graph illustrates the splitting of the actual fitting process into two steps, a non-linear and a linear step.

and developed in this work. Formulae 4.1 to 4.3 are used for the calculation of the series and parallel resistance and the photocurrent using the method given by Craparo and Thatcher [Craparo 95]. They determine the series resistance as:

$$R_s = \frac{kT}{e} \frac{1 - \frac{I'_{SC}}{I'_{OC}}}{I_{SC} + V_{OC}I'_{SC}} - \frac{1}{I'_{OC}} \quad (4.1)$$

where I'_{SC} and I'_{OC} are the slopes at short circuit and open circuit respectively, these values have the units [A/V]. The parallel resistance is then determined as:

$$R_P = \frac{1}{I_{SC}} - R_S \quad (4.2)$$

The short circuit current is then used to calculate the photocurrent as:

$$I_{ph} = \left(1 + \frac{R_S}{R_P}\right) I_{SC} \quad (4.3)$$

One Diode Model

The one diode model was investigated by Phang et al. [Phang 84]. They assume that $\exp\left(\frac{eV_{oc}}{nkT}\right) \gg \exp\left(\frac{eI_{SC}R_S}{nkT}\right)$ and $R_S \ll R_P$, which avoids having to determine the parameters through an iteration. The error is supposedly less than 10%. The formula for the estimation of the diode ideality factor then becomes:

$$n = \frac{\frac{e}{kT} \left(V_{mpp} + \frac{I_{mpp}}{I_{SC}} - V_{OC} \right)}{\ln \left(I_{mpp} + V_{mpp} * I'_{OC} - I_{SC} \right) - \ln \left(V_{OC} I'_{OC} - I_{SC} \right) + \frac{I_{mpp}}{I_{SC} - V_{OC} * I'_{OC}}} \quad (4.4)$$

The diode saturation current can then be calculated as:

$$I_{01} = \frac{(V_{oc} I'_{oc} - I_{SC})}{\exp\left(\frac{eV_{OC}}{nkT}\right) - 1} \quad (4.5)$$

Two Diode Model

A method using direct calculation was given by Sharma et al. [Sharma 93]. The diode ideality factors in this work are taken as the theoretical values of one and two for the ideality factors n_1 and n_2 respectively. The remaining parameters are then calculated as [Sharma 93]:

$$I_{01} = \frac{I_{ph} \left[\exp \left(\frac{e(V_{MPP} + I_{MPP}R_S)}{2kT} \right) - 1 \right] - (I_{ph} - I_{MPP}) \left[\exp \left(\frac{eV_{oc}}{2kT} \right) - 1 \right]}{Z} \quad (4.6)$$

$$I_{02} = \frac{(I_{ph} - I_{MPP}) \left[\exp \left(\frac{eV_{oc}}{kT} \right) - 1 \right] - I_{ph} \left[\exp \left(\frac{e(V_{MPP} + I_{MPP}R_S)}{kT} \right) - 1 \right]}{Z} \quad (4.7)$$

the subscript MPP indicates values at the maximum power point. The letter Z in above equations abbreviates the following:

$$Z = \left[\exp \left(\frac{eV_{oc}}{kT} \right) - 1 \right] \left[\exp \left(\frac{e(V_{MPP} + I_{MPP}R_S)}{2kT} \right) - 1 \right] - \left[\exp \left(\frac{eV_{oc}}{2kT} \right) - 1 \right] \left[\exp \left(\frac{e(V_{MPP} + I_{MPP}R_S)}{kT} \right) - 1 \right] \quad (4.8)$$

This method was used for the initial test of fitting algorithms presented in section 4.3. It has, however, the distinct disadvantage that it neglects the shunt resistance, which is a good assumption for high quality cells but not necessarily appropriate for less ideal devices. Thus a method was needed to remedy this. It is suggested in this work to use a singular value decomposition as given by Press [Press 89]. This still leaves a problem with estimating the starting values for the remaining non-linear parameters (n_1 and n_2 in the case of the 2 diode model), but allows the accurate determination of the linear parameters (I_{01} and I_{02}).

Crandall and Merten Model

The Crandall model, as well as the Merten model, introduces two additional parameters with respect to the one diode model. Unfortunately, both are non-linear. Additionally, the diode ideality factor does not have a clear theoretical

value. It is a lumped parameter, which accounts for mixed charge separation methods. Hence the simple assumption of a definite theoretical value is no longer possible. The diode ideality is estimated as the diode ideality of the standard one diode model. The additional parameter $\frac{\mu\tau}{d_i^2}$ is estimated based on literature values given in [Wagemann 94] as $1 \cdot 10^{-6} \text{ m}^{-1}\text{V}^{-1}$ and the flatband voltage as 1.1 V.

Backdiode Model

The difference in this model is the forward current limitation and the subsequent reduction in the fill factor. The saturation current of the back diode is estimated as the highest forward current in the measurements.

4.2.2 Error Criteria

Minimax (Tchebyshev)

This is the simplest error criterion possible. The error simply is the maximum deviation from the measurements to the fitted curve. The main flaw is that one has to know the overall average error of the measurement in order to make sure that the selected criterion for the termination of the fitting process is above this uncertainty because otherwise obviously no solution can be found. Furthermore, it will favour a certain region of the I-V characteristic, i.e. the area of large currents, and thus was ruled out for further investigation.

Standard Deviation

The standard deviation σ is probably the best known error criterion. In the case of I-V characteristics, it can be defined as:

$$\sigma = \frac{1}{N} \sqrt{\sum_{n=1}^N (I_{meas} - I_{calc})^2} \quad (4.9)$$

Here N is the number of measured data points, I is the current, the subscripts "meas" and "calc" indicate measured and calculated values respectively.

The main problem, however, is its dependence on the distribution of measured points: e.g. in the illuminated case, points in the region around the short circuit current contribute more to overall measurement error. Additionally all values are treated equally, independent of their measurement accuracy. A change in measurement accuracy is important, because many measurement devices switch automatically according to the measurement range.

For fitting purposes mostly the square of the standard deviation is used, the variance. That has the advantage that the values the computer deals with are much larger and hence further away from the round-off error of the computer. However, it is not used here as it has been superseded by the chi-squared criterion.

Chi-squared

The Chi-squared method is the standard approach nowadays for problems with variable errors, e.g. due to changes in the measurement aperture. For using this criterion, a standard deviation σ_i has to be associated with each point, i.e. the measurement error at each point. If these are not known, and the values are assumed to be equal to one, the chi squared algorithm is identical to the standard deviation. It is defined as:

$$\chi^2 = \frac{1}{N} \sqrt{\sum_{n=1}^N \frac{(I_{meas} - I_{calc})^2}{\sigma_i}} \quad (4.10)$$

This method takes care of variable measurement accuracy but does not tackle the main problem of the dependence on the point distribution.

Furthermore, there is a problem with the calculation of the standard deviation at point i . It is not appropriate to use the measurement uncertainty of the current only because this does not take into account the error in voltage, irradiance and temperature measurements and gives, according to Veissid et al. [Veissid 90], in the special case of the I-V characteristic, statistically impossible probabilities for the fitted parameters. The standard deviation at point i should be calculated for the function to be fitted depending upon the measurement uncertainties S of the measured quantities, in our case current S_I , voltage S_V , irradiance S_G and device temperature S_T . This can be expressed as:

$$\sigma_i = S_I \frac{\partial f(I, V, G, T)}{\partial I} + S_V \frac{\partial f(I, V, G, T)}{\partial V} + S_G \frac{\partial f(I, V, G, T)}{\partial G} + S_T \frac{\partial f(I, V, G, T)}{\partial T} \quad (4.11)$$

The calculation of above deviations is tedious, but can be done in straightforward calculations, the results of these are given in appendix A. σ_i is also dependent on the parameters and thus changes the error function. This leads to unpredictable results and it was found in tests that it often upsets the fitting algorithm. Thus this extension was not pursued any further for the fitting process but should be applied when the error associated with the parameters is to be calculated.

Relative Standard Deviation

This method was presented by Araujo et al. [Araujo 82] in order to overcome the distribution dependency of the fitting process. The authors define their error criterion as:

$$\sigma = \frac{1}{N} \sum_{n=1}^N \sqrt{\left(\frac{I_{meas} - I_{calc}}{I_{meas}} \right)^2} \quad (4.12)$$

This method supposedly works well for the examples given in above publication but still has the problem that different measurement errors are disregarded. These obviously could be included but the disadvantage of this method is that round-off errors can be crucial and the whole fitting is much less robust. It was therefore not investigated any further.

Area Criterion

All the above algorithms (except for the minimax criterion) have the problem that the quality of the fitting process depends on the point distributions. The fit will be performed mainly for the well represented parts of the curve. To overcome this problem Phang and Chan [Phang 85] suggested using the difference of the areas under the curves. They calculate the area difference ΔA as:

$$\Delta A = \left| \frac{(V_{meas,m+1} - V_{meas,m}) ([\Delta I_m]^2 + [\Delta I_{m+1}]^2)}{2 (|\Delta I_m| + |\Delta I_{m+1}|)} \right| \quad (4.13)$$

$$+ \sum_{i=1, i \neq m}^{N-1} \left| \frac{(\Delta I_i + \Delta I_{i+1}) (V_{meas,i+1} - V_{meas,i})}{2} \right|$$

Between the points m and $m+1$ the sign of the current difference changes as indicated in figure 4.3. ΔI is an abbreviation for the current difference of the calculated current at point i and the measured current at point $i+1$:

$$\Delta I = I_{calc,i} - I_{meas,i+1} \quad (4.14)$$

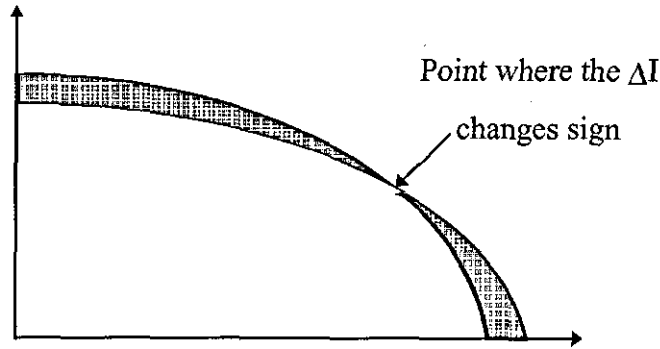


Figure 4.3: *Sketch of the Area Differences.* Between the points m and $m+1$ the ΔI changes sign.

The advantage of this criterion is that it is much less susceptible for uneven point distributions. Its applicability is tested in the following section.

4.3 Test of Existing Methods

The appropriateness of existing fitting methods was investigated in order to evaluate the most suitable approach for this work. This testing work was done in collaboration with Mathias Rommel at the Chair of Electron Devices at the University of Erlangen, Germany. This collaboration added the implementation of the area error criterion for the Marquardt-Levenberg algorithm and the Simplex algorithm to the list of available fitting methods, as well as a second implementation of the hybrid algorithm for control purposes.

4.3.1 Test Approach

This investigations concentrates, for the reasons given above, on the two diode model. The I-V characteristic was given in chapter 3 as:

Parameter	Value
I_{ph}	$2.19 \cdot 10^{-3} Am^2/W$
R_S	$2.5 \cdot 10^{-2} \Omega$
n_1	0.99
I_{01}	$2.4 \cdot 10^{-9} A$
n_2	1.9
I_{02}	$5.5 \cdot 10^{-5} A$
R_P	$2 \cdot 10^2 \Omega$

Table 4.1: Parameters Used for the Simulation.

$$I = -I_{ph} + I_{01} \left[\exp \left(\frac{eV_j}{n_1 kT} \right) - 1 \right] + I_{02} \left[\exp \left(\frac{eV_j}{n_2 kT} \right) - 1 \right] + \frac{V_j}{R_p} \quad (4.15)$$

with

$$V_j = V - IR_S \quad (4.16)$$

Variations in the irradiance influence only the photocurrent, but this is neglected in the remainder of this chapter as we deal exclusively with single I-V measurements taken under constant conditions.

The parameters assumed for the following simulations were chosen in order to represent a typical crystalline silicon cell (in this case one manufactured at the University of Erlangen, Germany). The parameters used in this plot are used throughout this chapter. These model parameters are given in table 4.1.

4.3.2 Applied Evaluation Methodology

A common approach for testing the quality of the extracted parameters is to compare selected measured points with points calculated on the basis of the extracted parameters. Points commonly chosen for this task are the V_{OC} , MPP and I_{SC} .

This approach has two distinct disadvantages. First, it does not consider explicitly any inaccuracies in the measurement and can thus be misleading. Second, it is possible to obtain an excellent description of these particular points despite significant flaws in the sets of fitted parameters. Thus the measurement of distinct points on the I-V characteristic and recalculating them with the extracted parameters is not a good measure of the accuracy of the extracted parameters.

In order to avoid these problems, simulated data were used in this study. Data sets were generated by calculating the desired voltage or current values and calculating the corresponding I-V values to a relative accuracy of 10^{-9} , i.e. until the relative change from old to new values was smaller than the given accuracy. This way one knows the inaccuracy of the 'measurement' as well as the ideal set of parameters. These data were used as input to commonly used fitting algorithms.

Two examples of the main classes of fitting algorithms were chosen, in order to give a representative picture. The algorithms tested are the Simplex algorithm (SI), the Marquardt-Levenberg (ML) algorithm and the hybrid algorithm (HA) described in section 4.2.

These three methods cover the most common means employed for parameter identification. For each of these the influence of the measurement conditions on the accuracy of the yielded parameters has been investigated.

Most fitting algorithms require starting values for all the parameters to be fitted. The influence of these on the final values is illustrated in figure 4.4, where the Simplex algorithm is started with values which are ideal except for the series resistance which is given a known error. The ε -value used for the evaluation is described in equation 4.17 below. Even small variations of the initial value of the series resistance lead to poor fitting.

It is obviously not realistic to use the ideal parameters as an input. In order to represent real situations, the initial values were estimated using available techniques,

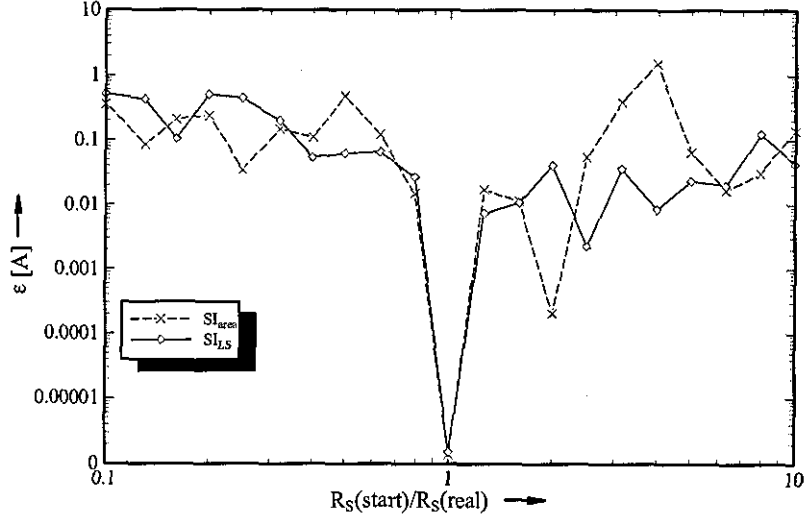


Figure 4.4: *Dependence of the Accuracy of the Simplex Algorithm on the Starting Value.* It is obvious that, in order to deliver good results, the Simplex needs starting values that are better than usually estimated for both tested error criteria (least square (LS) and area).

as given in section 4.2.1.

The error associated with a given set of parameters is defined as:

$$\varepsilon = \sum_{i=1}^7 |(P_{i,fit} - P_{i,real}) w_i| \quad (4.17)$$

where P_i represents the seven parameters to be extracted. The indices 'fit' and 'real' indicate the extracted and the real (i.e. simulated) value, respectively. The weighting factor w_i is defined in relation to the maximum power point as:

$$w_i = \left. \frac{\partial I}{\partial P_i} \right|_{MPP} \quad (4.18)$$

This means that the error has the units of [A], which is unusual but not undesirable. It emphasises the fact that all errors impact directly on current mea-

surements. It has the further advantage that it is independent from any fitting criterion, and is thus an 'impartial' assessment of the quality of the fit. Moreover, this weighting scheme is beneficial in that it tends to preclude any single parameter going completely out of range whilst the other parameters remain close to ideal. It could happen, for example, that the shunt resistance might be assigned a value of the order of $10^{13}\Omega$, but, despite this, all the other parameters would be returned close to their ideal values. Use of this weighting scheme helps to minimise the effect of such error on the overall measure of goodness of fit. It is judged here that such a result is preferable to a fit in which all parameter values are significantly wrong.

The definition of the weighting factors w_i given in equation 4.18 was also motivated by the importance of examining the region of normal operating conditions, i.e. around the MPP, as for some devices the essential principle of superposition is not necessarily valid.

In this work ε -values of less than 0.01A correspond to a good fit, ε -values of less than 0.001A to a nearly ideal fit. The relative errors between extracted and modelled parameters are typically well below one percent.

4.3.3 Tests and Results

The graphs presented throughout this chapter were generated by using the same set of data as given in section 4.3.1. The reason for doing so is for the sake of consistency. The results are comparable with those obtained from other sets of data and show some typical idiosyncracies. Other sets of data were tested as well, showing no significant differences, thus the decision to present results using these values is purely arbitrary. Only when a diode ideality factor was given unrealistic values, thus diminishing the influence of that particular diode or making the two diodes mathematically indistinguishable from each other (i.e. their contributions

to the overall current had a similar shape), was a decrease in the accuracy of the extraction of the parameters observable.

The environmental conditions assumed are an operating temperature of 328K and an irradiance level of 1000 W/m^2 , with the irradiance being proportional to the photocurrent. The irradiance correlates with standard measurement conditions while the temperature was chosen to represent a realistic operating temperature. Variations in these external constants have no significant effect on the accuracy of the process.

Influence of the Number of Measurement Points

The first investigation carried out was to assess the influence of the number of measurement points. Certain parameters dominate the characteristic in particular regions, as discussed in section 4.3.2. Hence it is necessary to identify sufficient data to cover all regions adequately.

This sufficiency obviously depends on the distribution of data points as well as the total number. Here we only investigate measurements taken at regular voltage intervals. Other measurement strategies are investigated in section 4.3.3.

It appears from figure 4.5 that the total number of points has only a minor impact on the overall accuracy of the parameter extraction. Apart from one bad fit in the Marquardt-Levenberg algorithm using the area criterion, all extracted values are more or less ideal. This bad fit is surprising and was thus further investigated. It showed that it is due to a basic problem of the Marquardt-Levenberg algorithm, which has the potential to cause significant problems. The method used here utilises a Gauss-Jordan elimination in order to calculate the eigenvalues. During this process a matrix may come close to being singular, causing a problem with round-off errors. This typically happens with the values describing the shunt resistance, when the corrected values lead to a very large increase in the parameter,

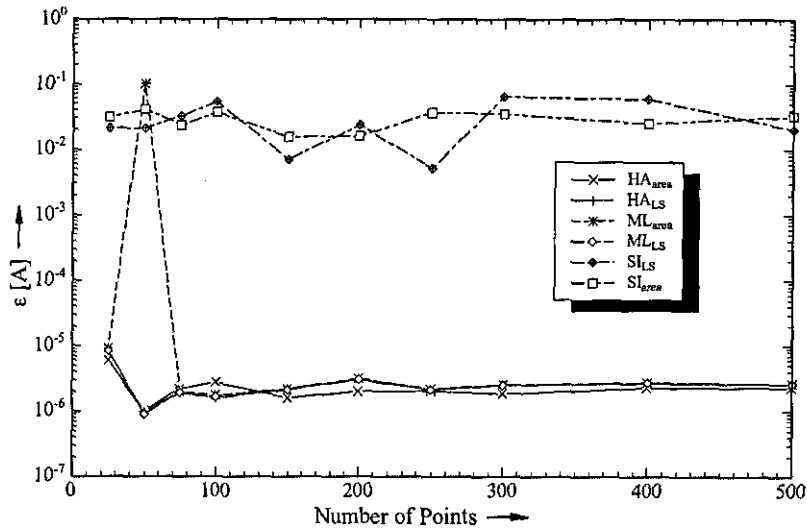


Figure 4.5: *Accuracy for Measurements with Evenly Distributed Voltage Steps.* It appears that in this case the point number only has a minor influence. The hybrid algorithm and the Marquardt-Levenberg recover the parameters very well while the Simplex struggles for all numbers of measurement points.

driving it to unrealistically high values. Graphically, one could imagine the algorithm following a winding valley to its minimum. At some stage it would reduce the affected values again but due to the round-off error during the calculation, the calculated new values do not create a sufficient improvement. The main effect of the round-off error is then essentially to prevent the final 'homing-in' of the algorithm. The other parameters tend to be close to their ideal values in such a case.

Minor variations are due to the selected stopping criterion. The accuracy can generally be improved by reducing the tolerable variation of the yielded parameters between each optimising step. This would, however, significantly increase the calculation time. The slightly improved accuracy at 50 points is not significant because it could not be reproduced with other sets of parameters. It appears that all algorithms are very robust for total point numbers above 150.

The Simplex algorithm seems to have the most difficulty in recovering the real

values. This is somewhat surprising as this algorithm is the most commonly used one and should be able to identify the minimum correctly. As this was generally observed it was investigated in detail. It showed that the explanation lies with the specification of the starting value: The Simplex algorithm delivered very good values for nearly ideal starting values but as soon as the starting values were less ideal it quickly deteriorated. This is shown clearly in figure 4.4 for the case of varying series resistance. This graph considers variations in a single parameter, the situation deteriorates as soon as more parameters are varied. The problem is due to premature stopping, i.e. stopping at non-ideal values. Premature stopping is caused by the high number of local minima. Beier [Beier 92] showed in her work that there are many local minima due to the implicit definition of equation 4.15. The variation in the quality of the results presented in figure 4.5 is due to frequent restarts of the algorithm, which were performed following the recommendation given by Press et al. [Press 89]. This introduces an arbitrary element which allows a significant increase in accuracy of the overall algorithm, but is still far from ideal.

It can be concluded that for this particular measurement procedure, the number of measurements does not significantly influence the accuracy as long as it is greater than 25. Increasing the number of points above 150 results in only a minor improvement.

Influence of the measurement procedure

There are three standard measurement strategies for measuring the I-V characteristics of solar cells. One can apply the voltage in regularly distributed steps (as in section 4.3.3), control the current in regularly distributed steps, or measure with a variable resistive load. All three strategies have been simulated. The simulated measurement strategies with equal current steps and with passive load lead to

a lower concentration of points around short circuit conditions and an increased point density towards higher voltages. The equal current step strategy yields a point distribution which is more biased towards higher voltages than the resistive load. Employing the resistive load strategy restricts the measurements to the 4th quadrant only, i.e. between open circuit and short circuit condition.

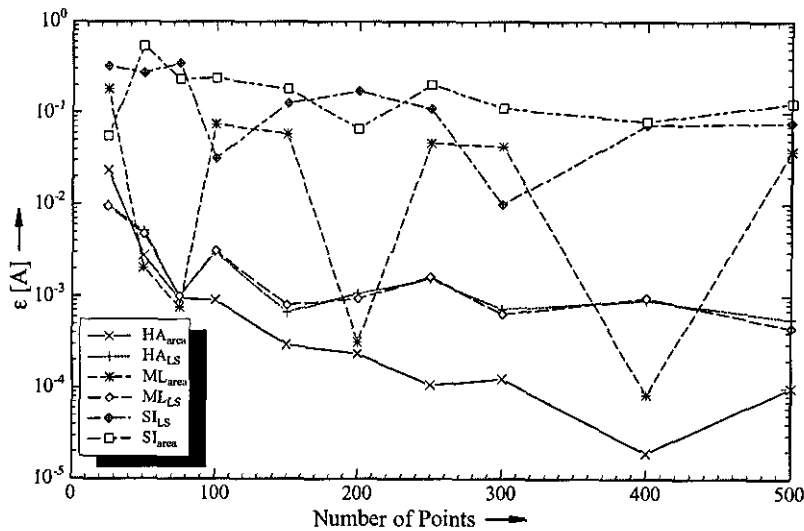


Figure 4.6: *Accuracy for Measurements with Evenly Distributed Current Steps.* It is obvious that a higher point density leads in most cases to a higher accuracy. The Simplex is inaccurate as in the other simulations. The idiosyncrasies of the Marquardt-Levenberg algorithm employing the area criterion are explained in the text.

The results of the tests using the equal current step strategy, as shown in figure 4.6, show a clear trend: increasing the number of points improves the accuracy in most cases. The Simplex algorithm still has problems regarding the starting values, while the hybrid algorithm and the Marquardt-Levenberg algorithm perform quite well for measurements with 150 points or more. The sub-optimal fits of the Marquardt-Levenberg algorithm using the area criterion may be caused by difficulties in implementing the first derivative of the area criterion for a given point. Thus they cannot be attributed to influences of the measurement con-

ditions. The sub-optimal fits are mainly produced by faulty fitting of the shunt resistance which could probably be controlled by penalising extreme values within the error criterion.

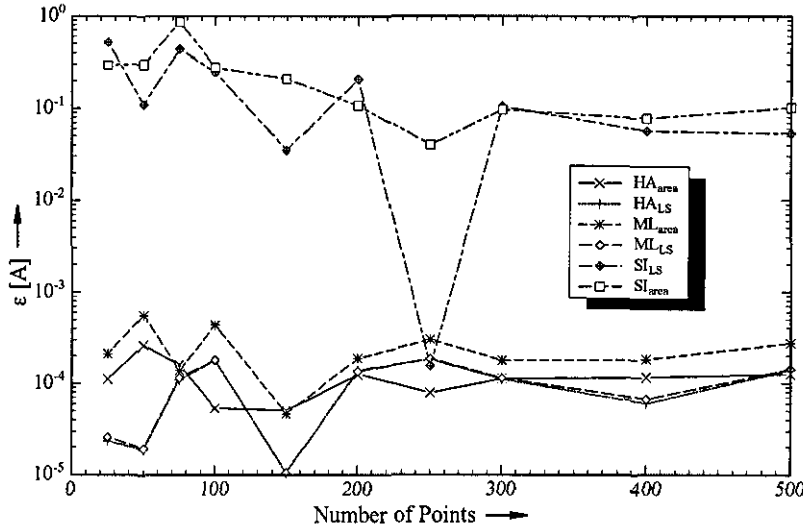


Figure 4.7: *Accuracy for Measurements for the Passive Loading Strategy.* No clear trend is obvious. The Simplex is as inaccurate as in the other simulations, with the single exception using the least squared criterion in the case of 200 measurement points. It can be assumed to be fortuitous that the Simplex had extremely good starting values in one of the restarts.

The passive load strategy, as shown in figure 4.7 yields much better results. There is no obvious trend in the graph, except that minor deviations are possible for measurements with less than 75 points. Once again the Simplex algorithm suffers from the variations in the input values.

Comparing the different measurement strategies clearly shows that it is preferable to measure devices with constant voltage steps. The passive method yields reliable results as well, but in general the errors are slightly higher than for the constant voltage step strategy. The constant current strategy performs quite badly in comparison. This is mainly due to the fact that the region around the short circuit condition is dominated by the shunt resistance and the influence of this

parameter is underestimated due to the measurement procedure.

Influence of the Measurement Error

Questioning the influence of the measurement error could appear to be quite unnecessary because it is obvious that better measurement accuracy will yield better results. However, solar simulators are quite costly and the question should therefore be phrased as 'what inaccuracies can be tolerated'. In this section we used sets of data with 200 points and the preferred constant voltage measurement procedure. Three levels of random measurement errors were generated which can be attributed to good (level 1), average (level 2) and cheap (level 3) systems. Systematic errors were not investigated because these have a very predictable influence, e.g. systematic measurement errors in the current will lead to a different photocurrent.

Several sets of data were generated in order to assess the influence of errors in one particular measurement and the accumulated influence of all errors being non-ideal. The measurements needed to describe an I-V measurement are voltage, current, temperature and irradiance. It is assumed for each point that all four measurements are taken. Gaussian errors of the following error levels were assumed: G (1, 5 and 10 W/m²), T (0.1, 0.5 and 1K), I (0.1, 1 and 10 mA) and V (0.1, 1 and 10 mV). The error was calculated for each point separately and in the first instance the error was added to one measurement only, yielding the sets G1, G5, G10, T01, T05, T1, V01, V1, V10, I01, I1 and I10 which are used in figure 4.8 and correspond to the previously given error levels. Additionally sets called L1, L2 and L3 were created where all measurements were affected by errors, again in the order given above.

The measurement error has, as shown in figure 4.8, a major influence on the accuracy. The results shown here are typical results, which were not significantly

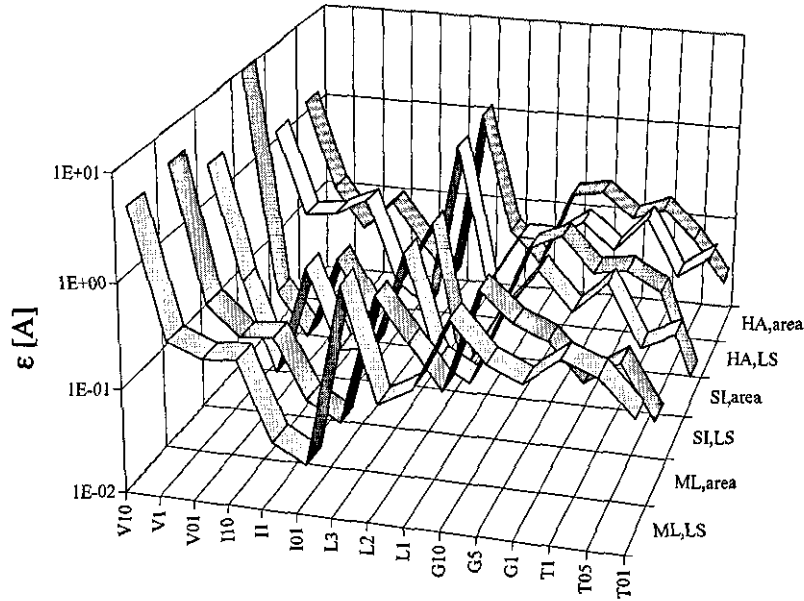


Figure 4.8: *Influence of the Measurement Error on the Accuracy of the Extracted Parameters.* The letter indicates the affected measurement and the number gives the level as $[mV]$ for V , $[mA]$ for I , $[W/m^2]$ for G and $[K]$ for T . The sets marked with L are erroneous in all measurements in the same extent as the corresponding level for the single measurements. The result that a higher measurement accuracy yields more accurate parameters was somewhat predictable. However the difference between the average and the good system is surprisingly small.

different when using different sets of data. The set-up that allows the most accurate extraction of the parameters is the good system, as could be expected. However, the difference between the average and the good system is surprisingly low. The slight decrease in the accuracy from the error level 2 to error level 3 in the fits using the least square criterion for the hybrid algorithm and Marquardt-Levenberg algorithm can be reasoned with unusual contributions of the simulated errors. It is quite possible that a random error has by chance only a minor impact on the overall results. If e.g. the voltage has a strong variation at values close to short circuit, it will lead to hardly any error in the current, while around the open voltage condition it would have a significant impact. Following this approach allows the construction of data sets with the same error width, but having very

different impacts on the extraction process. Additionally, it is possible that errors in two different variables cancel (e.g. a high current is offset by too high an irradiance reading).

The results of this experiment are idiosyncratic in the case of Simplex algorithm. Values delivered can be closer to the original (i.e. simulated) values than the otherwise more efficient fitting algorithms although the value of the internal error criterion used in the fitting process is larger than the values yielded by the otherwise more efficient algorithms. This can be explained as follows: a general problem for the Simplex algorithm in the previous experiments was being prone to premature stopping; but this can become beneficial when large errors in the measurements occur. In these apparently paradoxical cases, the Simplex algorithm starts with good initial values and merely preforms minor adjustments. It thus stays close to the original values, whilst the other algorithms find the minimum according to the chosen internal error criterion which is mathematically better, but in this instance less effective in terms of the heuristic error norm ϵ .

It is obvious that errors in different variables have different influences on the overall accuracy. The voltage has the most influence, while the impact of the current is surprisingly moderate. The influence of measurement accuracy in the temperature and the irradiance is somewhere in between. The magnitude of the inaccuracy of the sets of data where all measurements contain error is dominated by the influence of the voltage. This suggests that it is very important to measure the devices using a four probe measurement, as it is shown by Heidler [Heidler 93] that measuring with two wires introduces a significant error.

The influence of errors in the temperature and irradiance measurements can, however, be minimised by averaging over all measured values, as shown in figure 4.9. Here it was assumed that the set of data was measured effectively instantaneously, so that a drift in the measurement conditions could be neglected. The results for

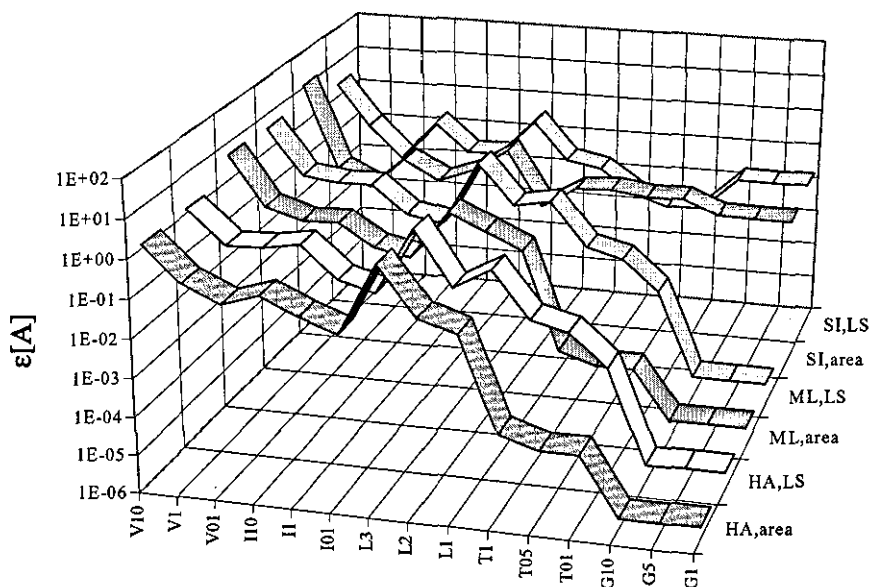


Figure 4.9: *Influence of Measurement Error When the G and T Values are Averaged.* It is apparent that the results are much more accurate than for unaveraged values (figure 4.8). This indicates that fast measurements with small thermal drifts are advisable.

the sets where the error was introduced in the temperature and the irradiance are nearly ideal, as could be expected by the nature of the added error.

Influence of the Stability of the Measurement Conditions

In a final test the influence of unstable measurement conditions was investigated. In real measurements, it is often found that the irradiance is not completely stable mainly due to instabilities in the power supply used to power the solar simulator lamps or due to weather changes in the case of outdoor measurements. This can significantly change the applicability of different extraction methods, especially when only selected points are used for the extraction of the parameters. This is because typical time constants for reaction to changes in environment are a few microseconds. Commercial simulators are classified according to the size of variations around an average irradiance level. For internationally agreed classes,

there are three categories of instability: $\pm 2\%$, $\pm 5\%$ and $\pm 10\%$ [IEC 94].

Temperature will also vary in practice particularly if the device is kept in the dark prior to measurement (e.g. to avoid degradation of the sample or excessive heat loads on the cooling equipment). In order to simulate common experimental arrangements, the thermal drift was chosen as 0.1, 0.5 and 1K over the measurement. Only positive drifts were considered because under normal operation, the device temperature will increase. The data used in this section do not have any added error.

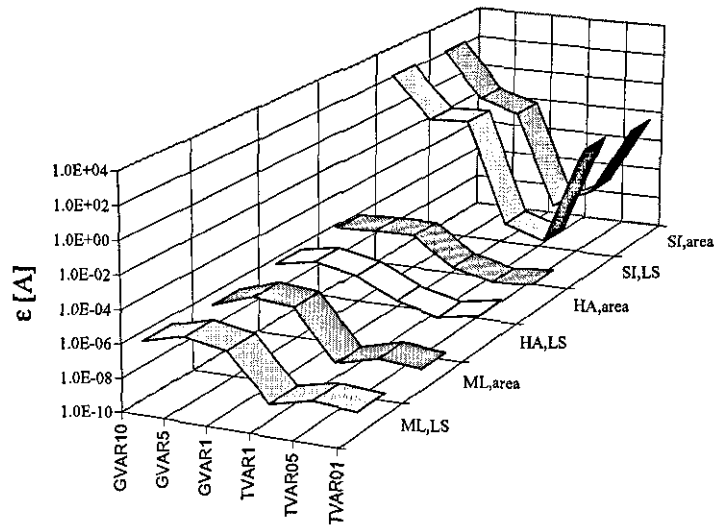


Figure 4.10: *Influence of Instable Measurement Conditions.* Neither hybrid algorithm nor Marquardt-Levenberg have problems with instable measurement conditions. In contrast, the Simplex does have significantly more problems than in the constant case.

The results from these tests are shown in figure 4.10. It appears that the overall accuracy is hardly influenced by this drift in measurement conditions. The behaviour of the different algorithms is not significantly affected, compared to the stable conditions.

If the variability is not accounted for, e.g. when the averaged, starting or end value is used, it does have a significant influence on the overall accuracy, as could

be expected.

Here, for the first time in the whole test, the Simplex occasionally yielded a better fit with respect to equation 4.17. In the pure mathematical sense the fits were always worse, because the final residues were higher than for the hybrid algorithm and Marquardt-Levenberg. This did not change even for ideal starting values. The Marquardt-Levenberg and the hybrid algorithm stumbled over their own efficiency and found a minimum in a corner of the space that was not wanted. Here a more controlled non-linear fitting algorithm in the hybrid algorithm would be of great advantage.

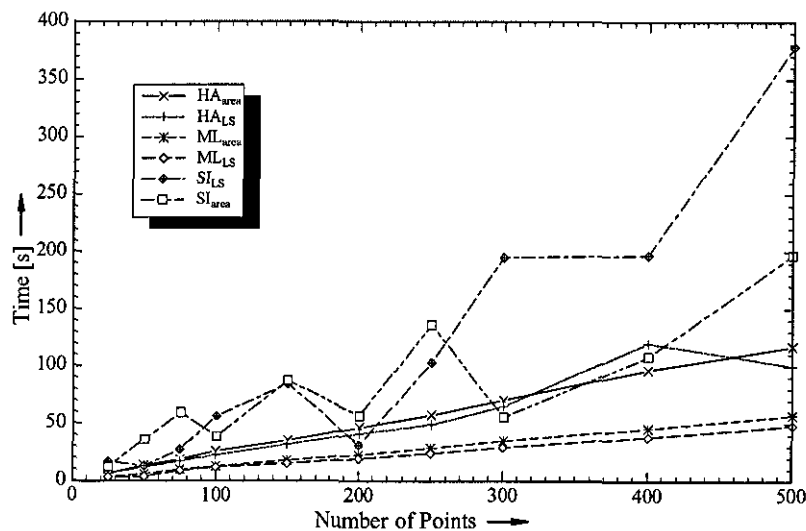


Figure 4.11: *Speed of the Algorithms Using Different Error Criteria.* The Marquard Levenberg algorithm nearly always outperforms the other options.

Speed

Speed is only a minor issue but still can be crucial in some applications, like the continuous evaluation of I-V curves. Figure 4.11 illustrates the results obtained for most tests. The algorithm using the area criterion is slightly slower for a low number of points but sometimes faster for a high number of points. The speed of

the search algorithms nearly always showed that the ML was the fastest and the SI the slowest algorithm.

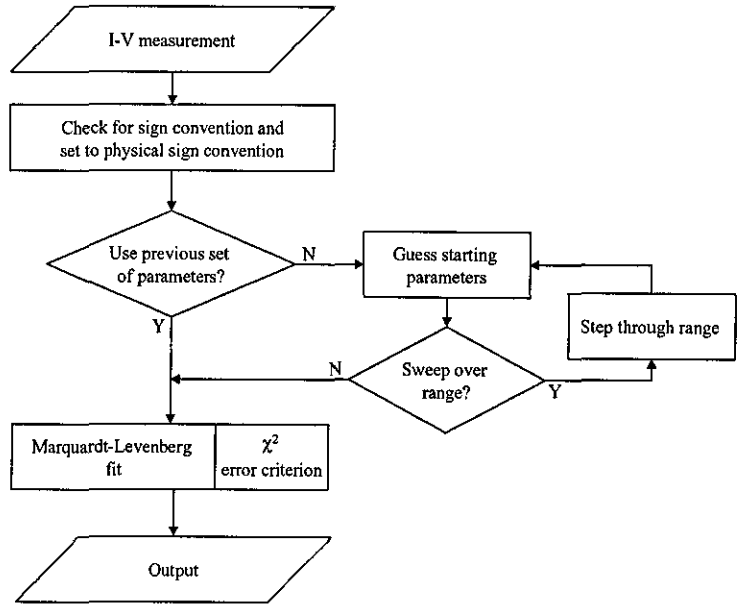


Figure 4.12: *Flowchart of the Final Fitting Program.* The Marquardt-Levenberg algorithm employing the χ^2 -error criterion is used. The emphasis is put on obtaining appropriate starting parameters.

4.4 Final Algorithm

The tests in the previous section were used for the design of the final fitting algorithm. The importance of having a good initial estimate of the parameters to be extracted was clearly shown and thus a variety of options is provided, as shown in figure 4.12. The fitting algorithm chosen from now on is the Marquardt-Levenberg employing the χ^2 error.

The algorithm was chosen because of its speed and reliability. It appeared to be the best choice, despite the advantage of the simplex algorithm in the presence of measurement errors. The hybrid algorithm was used in cases when the Marquardt-

Levenberg algorithm experienced problems with identifying the shunt resistance, which was found to be a good indicator of problems in the fitting process when using the Marquardt-Levenberg algorithm.

The starting values for the fitting process were calculated using measured points from the curve. In some cases the fitting process is started with the results of the previous fit. This option is used when a dependence on an input parameter is to be investigated. Furthermore, the starting value can be tested by stepping through a given range relative to the initial non-linear parameter and calculating the linear parameters with a Singular-Value-Decomposition as given by Press et al. [Press 89].

Chapter 5

Experimental Methods

5.1 Introduction

The analysis of environmental influences on the performance of thin film photovoltaic devices needs to be supported by experiment. Two distinct approaches have been taken in this work.

First, the response of devices to different environmental conditions can be investigated by direct control of the relevant external factors. The solar simulator system, described in section 5.2, was designed and built specifically for this purpose.

Second, the variation of outdoor conditions and device response can be measured simultaneously using the system described in section 5.3. For this approach it is important to ascertain the exact environmental conditions affecting the device. This is, in part, covered by standard meteorological measurements. However, since no data is available for the spectral effects across the UK, a comprehensive approach for the characterisation of this aspect of the operational environment, and the response of the cells, was developed as described below.

5.2 Solar Simulator

A solar simulator consists of three main components. These control incident irradiance, device temperature and electrical loading respectively. All components were chosen to ensure a high repeatability of the associated measurements. The system is shown schematically in figure 5.1. The system is fully enclosed in order to minimise disturbances from the surrounding environment.

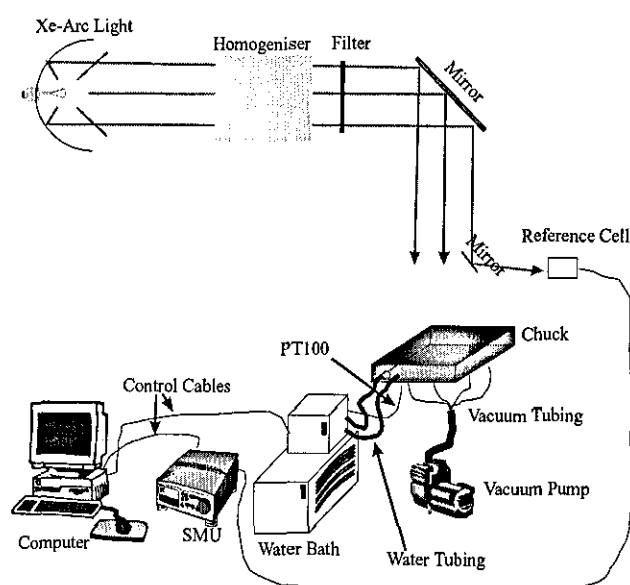


Figure 5.1: *Sketch of the Solar Simulator.* Most of the components are computer controlled, resulting in a high repeatability of measurements.

The objective of high repeatability was achieved by computer control of the entire measurement process with the exception of the irradiance, which is controlled manually as described below. When a measurement is to be conducted, the computer adjusts the cell temperature to the target temperature and forces the user to wait for a minimum of 5 minutes after having achieved a stable target temperature. This ensures an even temperature distribution across the device. Then the shutter is opened and the measurements are taken.

	Class A	Class B	Class C
Inhomogeneity	< 2%	< 5%	< 10%
Stability	< 2%	< 5%	< 10%
Spectral Match	0.75 – 1.25	0.6 – 1.4	0.4 – 2.0
Angle of Incidence	< 5°	< 5°	< 5°

Table 5.1: Classification of Light Sources.

5.2.1 Illumination

The quality of the illumination has an immediate effect on the quality of the measurements, even small variations distort the I-V characteristic. The requirements set out in the international standard [IEC 94] are summarised in table 5.1. It was decided to purchase a system that should meet Class B specifications, since this would give a high degree of confidence in the results while still being affordable. A ScienceTech solar simulator SS1kW was purchased in order to meet these requirements. The components of this system are illustrated in figure 5.1. The light source itself is mounted in a frame as shown in figure 5.2. An electronic shutter allows measurement of the devices in the dark as well as excluding light from the measurement area without having to switch off the light. This is important in order to avoid possible degradation of the devices during the measurements while maintaining the life time of the bulb, which is reduced by frequent starts. Irradiance control is achieved by introducing appropriate neutral density filters. The system is shown in its frame in figure 5.2.

The solar simulator chosen assures a high degree of repeatability for the measurements. It consists of a Xe-Arc lamp with a stabilised power supply and appropriate filters to obtain AM0, AM1 and AM1.5G. The beam is then homogenised by a beam conditioner. As described above, the intensity is regulated by manually introduced reflective neutral density filters within the beam homogeniser. This minimises the number of moving parts which results in a high reliability.

The light intensity is measured with a silicon diode, which allows detection of any

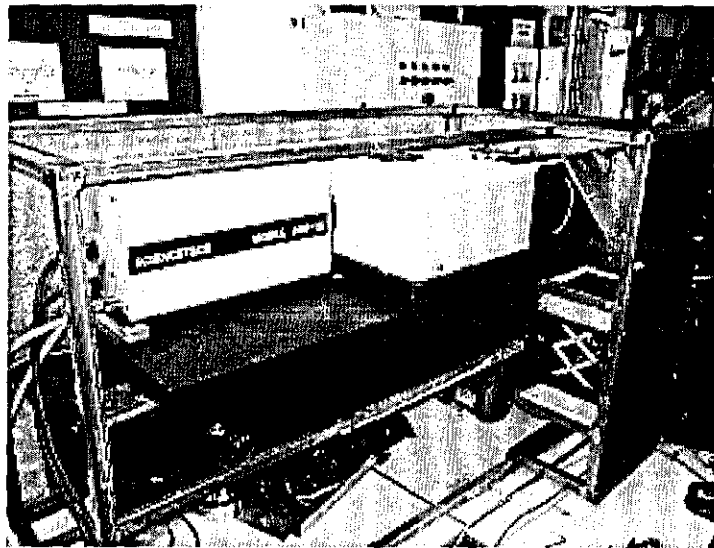


Figure 5.2: *Photo of the Solar Simulator.* The casing was removed for the purpose of this picture so that the electric, thermal and illumination components are visible.

variation in the intensity. This diode is not fixed to the measurement chuck in order to limit variation in its temperature. Light is guided to this device by a small mirror and the intensities are calibrated against measurements taken on the chuck.

Due to technical problems with the light source itself, it was not possible to commission the irradiance control in the course of this work and thus no illuminated analysis of I-V characteristics is presented.

5.2.2 Temperature Control

The thermally controlled chuck, which is shown in figure 5.3, was designed to allow cells or modules up to a size of 10 cm by 10 cm to be contacted both at the front and back whilst minimising thermal variation across the device. For back contacting, two grooves are cut into the front of the chuck which allow small contact pieces to be inserted at any location on a cell or module and at any distance from each other. The remaining parts of the grooves are fitted with

aluminium pieces to ensure thermal uniformity.

In order to ensure that the mini-modules are brought into good thermal contact with the chuck, small holes are drilled through the aluminium which are connected to a vacuum pump. The suction ensures that good thermal contact is maintained and also serves as a clamp so that the test module does not move during the experiment.

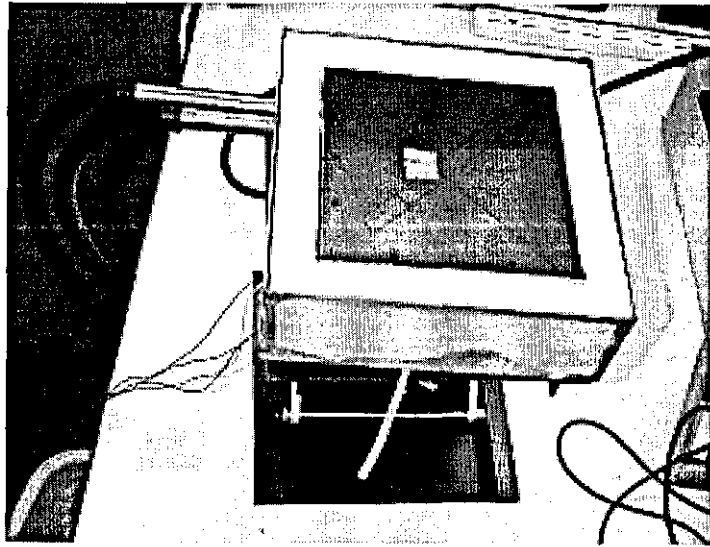


Figure 5.3: *Photo of the Measurement Chuck.* The tubes seen on the left are connected to the water bath. The chuck itself is embedded in insulation and mounted on a jack.

Cooled or heated fluid is pumped through pipes in the chuck to control its temperature. The temperature control is performed by a Julabo F32HD waterbath unit, which also pumps heated/cooled liquid through the chuck. The temperature in principal can range from -25°C to 200°C but is normally limited to 90°C in order to avoid damage to the devices. Illuminated measurements are taken only at temperatures above 10°C in order to avoid problems due to condensation on the devices. The temperature is controlled through the feedback given by a PT100 resistor fitted to the chuck, as illustrated in figure 5.3. Alternatively,

a PT100 mounted within pre-manufactured module can be connected instead of the one positioned within the chuck when necessary. The temperature is kept within $\pm 0.1^{\circ}\text{C}$ and varies less than $\pm 0.5^{\circ}\text{C}$ across the chuck area, as shown by Elsworth [Elsworth 98]. The system is thus suitable for class A testing. The complete system is shown in figure 5.4.

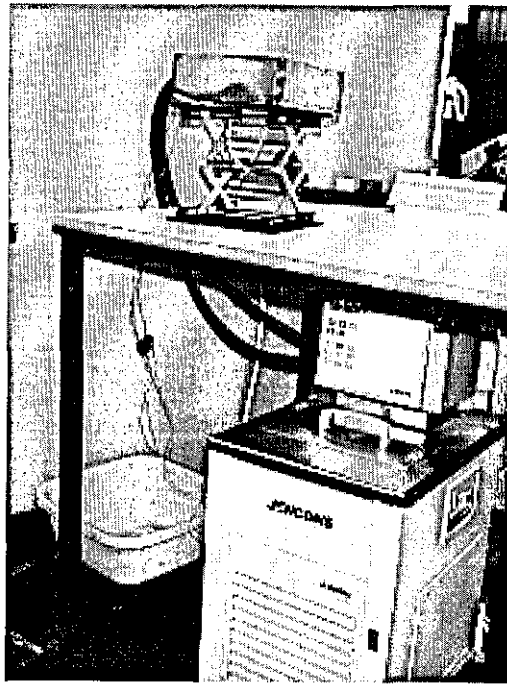


Figure 5.4: *Photo of the Thermal Control System.* The water bath is located under the table. It is connected to the chuck through the tubing. Also visible are the four wires connecting the PT100 to the controller.

5.2.3 Electric Measurement System

Electrical measurements and cell loading are carried out using a source-measure-unit (SMU), a Keithley 2420 SourceMeter, which has the capability to source and sink current at a controlled voltage, as well as to measure the voltage and current respectively via a 4-probe measurement set-up. The necessity of using a 4-probe measurement arrangement was emphasised by Heidler [Heidler 93]. He

demonstrates that using a 2-probe measurement will result in overestimation of the cell's series resistance. The SMU has a built-in capability to sweep the current or the voltage through any given region, which lends itself to I-V curve determination.

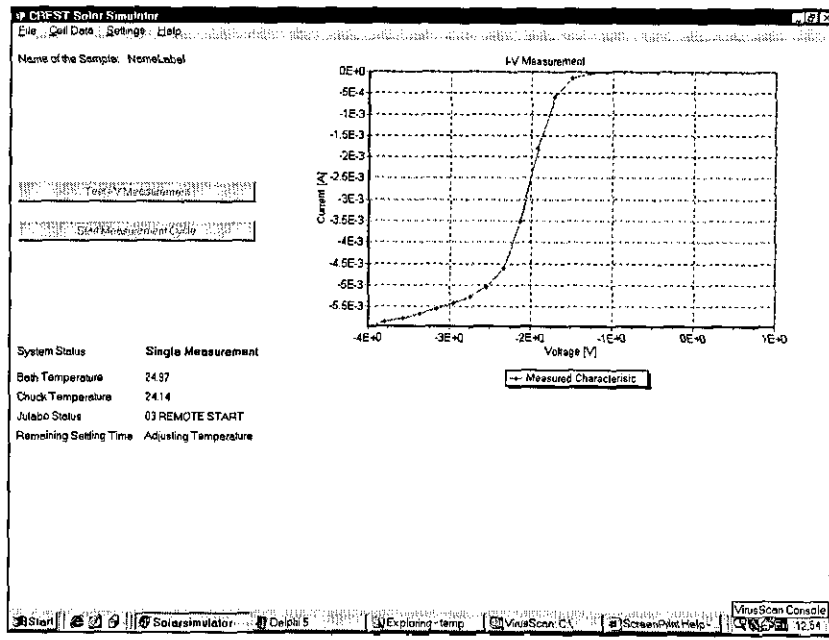


Figure 5.5: *Screen Shot of the Solar Simulator Control Program.* The program displays the state of the thermal system as well as the last I-V measurement. The details of the measurements are determined in the main menu.

5.2.4 Computer Control

The overall system is controlled using a PC. The control routines are written using Borland Delphi. It can be seen from figure 5.5, which depicts the window seen during a measurement, that the state of the system can be observed graphically at all times. Every second the system monitors the state of the waterbath and checks the chuck temperature, bath temperature and status of the unit. There are two measurement options available, a test measurement, which uses a lower number of measurements and a lower accuracy and does not consider the temperature, and a normal measurement, which checks the temperature and uses a higher

measurement accuracy.

The chart shows the last measurement taken by the system, the case illustrated in figure 5.5 is a test measurement used to identify if the device has been contacted correctly. The measurement environment is controlled through the menu bar, which allows device data, electrical measurement boundaries and compliance (i.e. maximal current permissible) and thermal settings to be set. It is possible to conduct a whole series of measurements at different temperatures or single measurements, both are fully computer controlled. No user interaction necessary after contacting the device and starting the measurement cycle.

5.3 Outdoor Measurements

The second strand of the experimental work aims at investigating the behaviour of the devices under real operating conditions. This also serves to clarify the meaning of the term 'real operating conditions' in the context of a maritime environment such as the UK is. This involved two separate measurement systems being operated by a PC. These two control systems resided in reality on a single PC which performed these two programmes as separate tasks. The spectroradiometer came with its proprietary software. Therefore, it appeared sensible to use this control software rather than writing a new set of control algorithms, which would have resulted in the duplicity of control programs. The following sections describe the two separate measurement systems and the linking computer control in more detail.

5.3.1 Spectroradiometer

To date, all published investigations of incident radiation spectra known to the author have been conducted using silicon detectors. This limits the spectrum to

those wavelengths to which crystalline silicon devices can respond, i.e. up to 1100 nm. This means that parts of the spectrum of relevance for CIGS devices lie outside the measurement range, since CIGS devices respond to irradiance up to 1360 nm [Gay 96]. In contrast, the system installed at Loughborough utilises two detectors, a Si detector which is used for the spectral range up to 1000 nm and an InGaAs detector for the region up to 1700 nm.

The incident spectral solar irradiance at Loughborough has been measured using this spectroradiometer. The spectroradiometer was commissioned in April 1998 and has been in continuous operation at CREST since May 1998. The complete system including integrating sphere and fibre optics was supplied and calibrated by Instruments SA, UK. The integrating sphere faces due south with an inclination of 52° (the latitude at Loughborough) which is also the inclination of adjacent roof mounted PV systems and test cells.

Each characterisation of the spectrum used for this work comprises 141 spectral measurements at 10 nm steps, across the spectral range from 300 to 1700 nm. The integration time was chosen to be 0.1 s.

Measurements of the incident spectrum are taken every 10 minutes over the day. The scanning time to complete each run is of the order of 1.5 minutes. This rather long measurement time does lead to some distortion of the spectrum, especially for days with rapidly moving clouds. Such distortion will be averaged out to a significant extent by the large number of data sets used.

The measured data is then analysed. Data sets with an overall irradiance of less than 10 W/m^2 are ignored, because they exhibit a poor signal to noise ratio. Furthermore, they will contribute insignificantly to the overall energy yield. Total irradiance is calculated by integrating over the whole measured spectrum. Thus, the term total irradiance in this work always refers to the integrated irradiance in the range from 300 to 1700nm, reflecting the response of the combined detectors.

The energy within this spectral range is more than 94% in the standard AM1.5 spectrum, thus the difference to the overall total irradiance is very small. Furthermore, the irradiance outside this range does not contribute to the operation of any of the solar cells investigated in this study.

5.3.2 Outdoor System

The devices were sealed and framed with a thermocouple at the back and the samples are mounted on a frame facing due south with a tilt angle of 52°. Simultaneously to the spectral measurements, I-V scans are carried out every ten minutes.

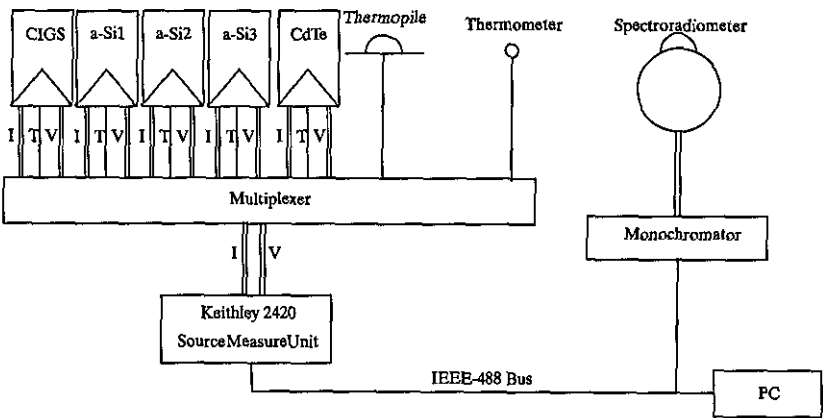


Figure 5.6: *Set-up of the Outdoor Measurements.* The measurements were carried out by a Keithley 2940 unit, which did measure the I-V values as well as the currents determining the temperature and the irradiance. The spectroradiometer was connected separately.

A measurement series consists of irradiance, ambient temperature, wind speed and device temperature plus a complete I-V characteristic for each sample. The program controlling the Keithley captures the data saved by the spectroradiometer and stores the complete measurements.

The measurements of the I-V characteristic are carried out, as in the case of the indoor arrangement, using a Keithley 2420 SourceMeter (SMU). The SMU

also deals with the measurements of the device temperature by measuring the resistance of the PT100 sensors through a 4 wire connection.

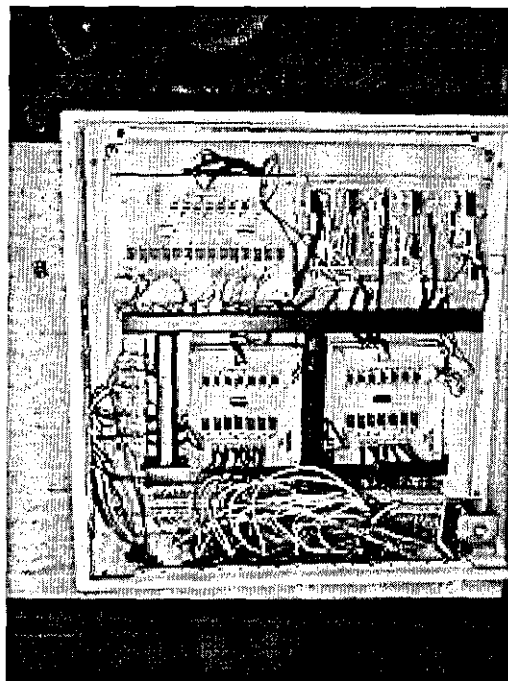


Figure 5.7: *Photo of the Outdoor Switching System.* The main control board can be seen in the top right corner. The other three stacked sets of boards are the relays for the voltage and the temperature respectively. A heater (lower right corner) is used to avoid condensation on the boards.

The different modules are accessed via a multiplexer unit which utilises the four digital output lines of the SMU. It is housed close to the test side on the roof of the AMREL building. All communications between the SMU and the devices employ the four probe approach. The multiplexer unit is shown in figure 5.7. In the bottom right corner of this unit, one can see a small heating unit, which was installed in order to reduce the likelihood of condensation in the environmentally sealed metal box. All connections to the multiplexer unit are installed at the bottom of the unit in order to avoid water ingress due to water running along the cables.

Except during the measurement sequence, the circuit is inactive. The different

measurement states of the unit are controlled via the digital output of the SMU, which provides the possibility for a 4 bit control through 4 switchable channels or lines. Line 1 is used as a clock impulse, placing an on/off pulse on this line takes the circuit out of stand-by mode and activates the first channel. Setting line 2 to 'on' (high) enables the current/voltage measurement. Finally, an 'on' impulse is applied to line 3, enabling the temperature measurement. Then the next module is set up by sending another on/off pulse on line 1. Thus all panels are measured in a cyclic fashion. The ambient temperature can be accessed by applying an 'on' impulse to the lines 1, 2 and 3. The global irradiance is measured by a pyranometer by setting line 4 to 'on'. Finally the measurement-cycle is concluded by deactivating the whole unit again. This is done by applying an 'on' impulse to all four lines, taking the circuit back into the idle state.

5.3.3 Computer Control

The computer control is crucial, as two different systems need to be accessed. A program was written using Borland Delphi, which controls the I-V measurements and is able to capture the spectral measurements. The main window of this is shown in figure 5.8.

The program presents all relevant information of the last measurement (or current measurement when measuring) in graphical form. As apparent from figure 5.8, the I-V characteristics of all devices to be tested are displayed as well as their maximum power points. Figure 5.8 displays a different set of modules from the ones tested in this work. The samples measured here are full size modules which were installed for the follow-up project. To date, the system allows for 20 devices to be tested. Together with their I-V characteristics, the irradiance immediately before and after the measurement, ambient and device temperature are displayed graphically. The program also captures the spectrum as measured by the spec-

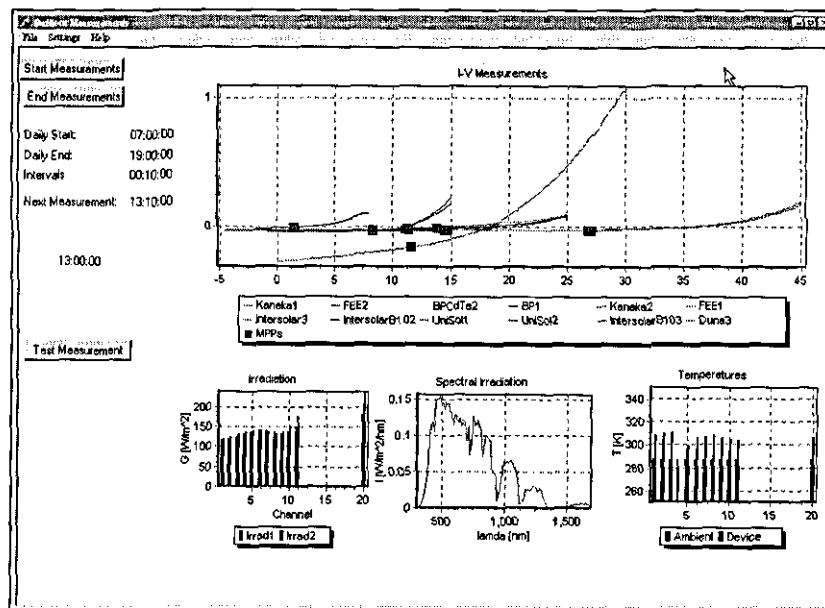


Figure 5.8: *Main Window of the Outdoor Measurement System.* The system currently allows to investigate up to 20 samples. The Irradiance before and after each measurement, the incident spectrum, ambient and device temperature and I-V characteristics are measured and plotted for each measurement step.

roradiometer and displays this data graphically in the centre of the bottom row of charts.

A measurement cycle is started by measuring the ambient global conditions, i.e. global irradiance and ambient temperature. This is followed by the device measurements, which are carried out by the SMU, applying different voltage ranges for each device as well as different current compliances. The current compliance typically is set to 110% of the short circuit current given by the manufacturer, while the voltage measurements start at a small negative voltage and finish at 110% of V_{OC} . Each measurement consists of 200 points. The measurement sequence is concluded with a second measurement of the global irradiance. Thus measurements with significant changes of irradiance can be detected and discarded. Data sets were rejected if the deviation of the irradiance was more than 5% from the average of all measurements of this particular time step. This threshold was reached

Abbreviation	Technology	N _s	Type
aSi1	double junction aSi/aSiGe	6	mini module
aSi2	single junction aSi	6	mini module
aSi3	double junction aSi	3	mini module
aSi4	single junction aSi	3	mini module
aSi5	double junction aSi	14	module
CdTe1	single CdTe cell	3	mini module
CdTe2	CdTe mini module	8	mini module
CIGS1	CIGS mini module	12	mini module

Table 5.2: Overview of the Samples Tested in this Work.

in the measurement presented in figure 5.8 , as apparent from the lower left chart in this figure.

The electrical measurements are stored together with irradiance and device temperature in one file for each measurement. The spectroradiometer data is stored in separate files, in a *proprietary format of Instruments SA*.

After some initial teething problems, the system has operated well since September 1999. The major problems experienced so far are due to power failures. The control program is in principle able to restart automatically while the spectroradiometer monitoring program needs user interaction. The second problem experienced is the number of files. Due to the high number of files measured and stored, the harddrive filled up very quickly. This problem is amplified by the fact that all files will take up a minimum of space, this minimum space is one block on the harddrive. This means that even if a file is only 1 kB long, it will always take 16 kB of storage space on the harddrive. This problem was circumvented by using the packing program arj each day at midnight, pack all the files measured that day into one single file and deleting the original files. Since the implementation of this, the system has operated very reliably.

5.4 Samples Tested

Samples were supplied by various manufacturers of thin film devices. The aim of this work was comparing the performance of these devices but investigating the key operational effects. The manufacturers are not identified. An overview of the samples used in the tests is given in table 5.2.

The majority of the samples listed in table 5.2 are custom made samples and hence their performance is only partially comparable to modules available commercially. Some were cut out of larger modules in order to create samples of a size that could be measured using the indoor system. It is considered unlikely that this influences the results regarding environmental effects, even though the absolute efficiency will be affected.

Chapter 6

Influence of Operating Temperature

6.1 Introduction

The influence of the operating temperature is important, because devices tend to operate at significantly elevated operating temperatures, compared to STC conditions. Obviously, ambient temperatures can be higher but even at lower ambient temperatures than STC, the devices will operate at significantly elevated temperatures, typically around 25-30 K above ambient. This means that, as shown later when investigating the climate at Loughborough in the UK in figure 8.3, the devices will operate the majority of the time at or above this temperature and thus thermal effects are of vital importance for the overall performance.

The increased operating temperature is due to the thermalisation and non-utilisation of photons. The effect of increasing temperature is twofold: firstly it decreases the apparent band gap slightly and, secondly, it increases recombination. In the illuminated case, this generally reduces the efficiency. However, in the case of a-Si a positive temperature coefficient has been reported [Carlson 00], while other

researchers found a negative temperature coefficient [Schade 98]. Both studies present outdoor measurements, it is most likely that other effects, e.g. spectrum, obscure the results and thus this chapter focuses on measurements in a controlled environment. This chapter concentrates on dark characteristics so that the effects of illumination can be excluded.

All previous investigations on the performance of thin film solar cells were conducted on the basis of performance parameters such as efficiency, open circuit voltage and short circuit current. This is not sufficient for the description of devices in a simulation package, which typically uses parametric models as reviewed in chapter 3.

The variation of the underlying physical parameters has not been published for thin films and is still very much under discussion. This chapter aims at contributing to this discussion and investigating the possibilities for modelling I-V characteristics by parametric models.

There is a significant amount of work published on the variation of the physical device parameters of c-Si, which should be the starting point for any further investigation. When measuring a c-Si cell, this is typically dominated by the variation of the diode saturation current, as this varies exponentially with temperature [Fan 86]. In photovoltaic modules, however, additional effects will also occur to a varying degree. This difference is due to contacting effects, which can be nearly eliminated when measuring a single cell with a four probe measurement arrangement. In a module, however, effects like contacting will have a significant influence on the overall behaviour, especially as a relatively large temperature variation occurs naturally during normal operation which will cause different effects in different materials (solder, wires, terminals), and thus will contribute to the overall power level achievable. These effects were shown e.g. by Veissid and Andrade [Veissid 91]. This should be more pronounced in thin films, as the inter-

connection typically is electrically less efficient than for c-Si devices, as e.g. the laser cutting of the single cells might not remove all material or the TCO layer might be not as homogenous as one would want. In the work below, mini-modules are investigated, which represent an ensemble of cells and interconnections, thus additional effects can be expected to be observed in the variation of the device parameters. The effect of the exponential increase of the diode saturation current with temperature will also be apparent for thin films, thus in the following the common approach for modelling the variation of the diode saturation current given by Fan [Fan 86] and the other parameters of c-Si devices is reviewed.

Araujo et al. [Araujo 82] give a relation for the diode saturation currents. They found that, if the majority of the recombination occurs within the bulk of the material (as it is the case for c-Si) the first diode behaves as predicted by Shockley's diffusion theory. This can be modelled as:

$$I_{01} = C_{01}T^3 \exp\left(-\frac{E_G}{kT}\right) \quad (6.1)$$

where C_{01} is an empirical constant and E_G is the band gap. In all materials investigated in this study, it is not likely that the bulk recombination dominates. In the case of a-Si, there is hardly any bulk material, as the junction essentially stretches across the whole device. Polycrystalline devices, on the other hand, have an area where bulk recombination will occur, but the recombination at the junction will be much more significant, as there are two different lattices in contact, presenting a large number of recombination centres. The recombination at states within the band gap can be calculated as [Wolf 77]:

$$I_{01} = C_{01}T^{\frac{\gamma}{2}} \exp\left(-\frac{E_G}{2kT}\right) \quad (6.2)$$

where γ is an empirical parameter which is typically 5 for c-Si devices. This considers deep traps in the middle of the band gap, hence the activation energy is half that of the band gap and hence the two is introduced. For shallow traps, γ would be three and the overall thermal behaviour of the diode saturation current can be modelled as [Wolf 77]:

$$I_{01} = C_{01}T^{\frac{\gamma}{2}} \exp\left(-\frac{\frac{E_G}{2} - E_t - E_i}{kT}\right) \quad (6.3)$$

where E_t is the energy level of the shallow traps and E_i is the applied potential $-e\psi$. Most likely, a variety of recombination centres will be present in the devices under investigation. A further recombination mechanism is coulombic scattering at grain boundaries or recombination centres. It can be modelled as [Overstraeten 86]:

$$I_{01} = C_{01}T^2 \exp\left(-\frac{V_{GB}}{V_T}\right) \quad (6.4)$$

where V_{GB} is the voltage corresponding to the energy difference at the grain boundaries. Fan [Fan 86] gives a general formula for the variation of the diode saturation current, allowing for different recombination effects, as:

$$I_{01} = C_{01}T^{\frac{3}{n}} \exp\left(-\frac{E_G}{mkT}\right) \quad (6.5)$$

where n and m are empirical parameters depending on the quality of the cell material and the junction type.

The variation of other parameters was investigated by Veissid and Andrade [Veissid 91], giving a relation for the remaining parameters as:

$$n_2 = n_{2,300K} [1 - C_n (T - 300)] \quad (6.6)$$

$$R_S = R_{S,300K} [1 + C_{rs} (T - 300)] \quad (6.7)$$

$$R_P = R_{P,300K} [1 + C_{rp} (T - 300)] \quad (6.8)$$

However, all these linear formulae are limited to c-Si and it will be apparent that they are not necessarily applicable to thin film devices. They are given here to give a base line for the following investigation and to emphasise the differences between different materials.

6.2 Measurements

The thermal variation of the parameters was investigated by conducting dark measurements using the CREST solar simulator set-up at temperatures ranging from 283 to 353 K, thus covering the range in which cells typically operate. A typical measurement series is shown in figure 6.1 for an a-Si double junction sample. Each measurement was repeated 5 times for the calculation of the standard deviation

of the parameters determined. The measurement cycle started with cooling the devices down to 283 K. Whenever the measurement temperature was achieved, a 5 minute thermal settling period was kept in order to guarantee that the whole cell was at the desired temperature. A further 5 minutes settling time was introduced between the 5 measurements for each temperature, in order to guarantee that the measurements were completely independent of each other.

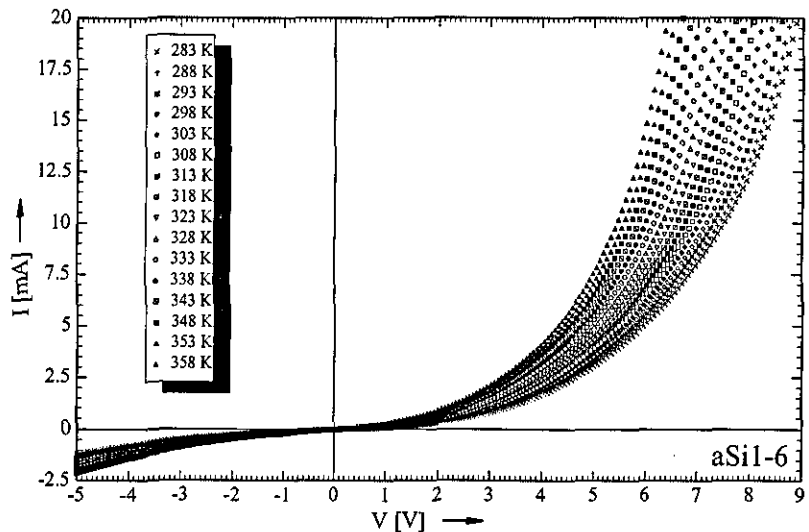


Figure 6.1: *Thermal Measurement Series of Cell aSi1-6.* The graph shows the measurements taken for the 6th cell of the aSi1 technology, which was measured. Only the first measurement measured at each temperature is shown.

The parameters were then extracted using the fitting method described in chapter 4 and the corresponding curves were calculated. The quality of the agreement can be considered to be very good, as indicated for a double junction device in figure 6.2. The measurements shown in this figure represent 10 degree steps, i.e. only half the measurements in this series are shown, and only every fifth point of the measurement is plotted, exclusively to increase the clearness in the graph.

The agreement between fit and measurement is always of similar quality, as long as there are no deviations from the theory. Devices presenting challenges are the

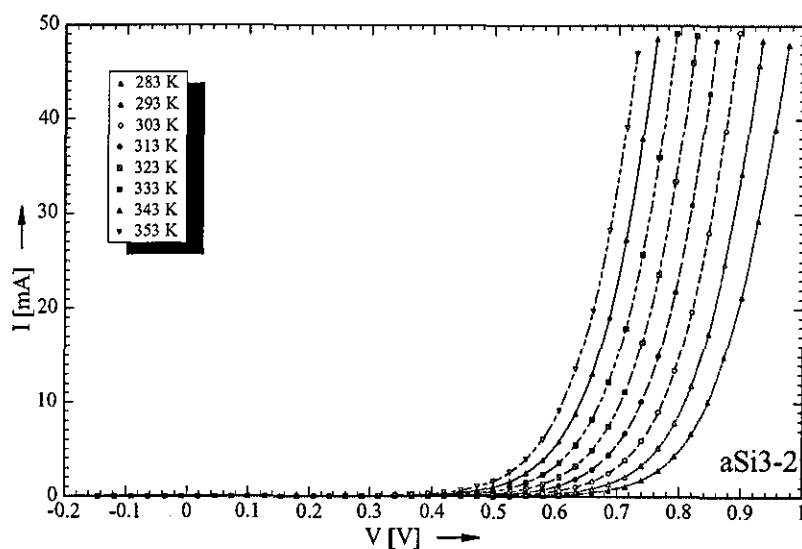


Figure 6.2: *Agreement between Fit and Measurements.* The measurements are represented by the symbols, the fit by the lines. Every 5th point of the measurements is shown.

aSi1 and aSi2 devices, for very different reasons.

The deviations from the theory are in both cases immediately apparent from the I-V characteristics. In order to illustrate this, the double junction devices are compared in figure 6.3. One difference is the point where the impact of the series resistance is visible (the apparent change in the slope of the characteristic towards higher voltages). This phenomenon is due to the contacting of the devices and will be discussed in more detail in section 6.3.1. The interesting bit is, however, the part leading towards this additional bend, which is, in the case of the aSi1 cell, not a straight line (in this semi-logarithmic plot) as it is predicted by the theory and shown by the aSi3 device. This will result in a compensation in the fitting, thereby reducing the physical significance of the fitted parameters is reduced.

The reason for this behaviour is most likely the fact that the aSi1 device is an aSi:H-aSiGe:H double junction device, which requires the contacting of slightly different lattices. Despite the fact that it is the nature of amorphous materials to

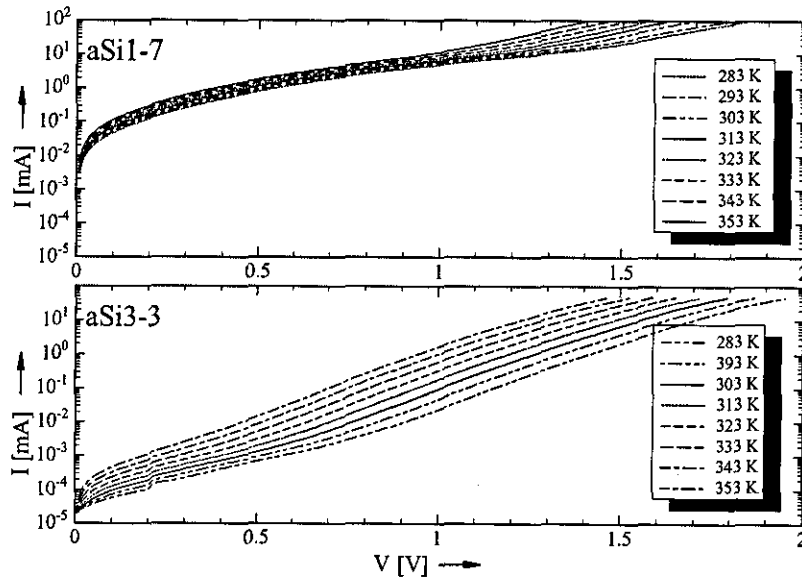


Figure 6.3: *Comparison of the Measurements of aSi1 and aSi3 Technologies.* Both devices are using a double junction technology, but show very different I-V characteristics.

be highly disordered, this will introduce additional effects. The aim of this chapter is to provide the parameter variation for the usage in a simulation tool and not to provide perfect physical modelling. Therefore, the parameters extracted for the aSi1 devices are suitable for the intended purpose, as the agreement between fitted curve and measurement is of similar quality to the one presented in figure 6.2.

The aSi2 devices suffered in the delivered state from a very low shunt resistance, which has an influence on other parameters as well, as indicated in figure 6.4. In this graph, the values extracted for the diode ideality factor and the shunt resistance are plotted against each other for different cells. For one device, aSi2-2, it is shown that heating the devices has a very positive influence on the overall device behaviour. This fact will become more apparent in the investigation of the hysteresis effects in section 6.4.

The measurements for this graph were produced using the measurement equip-

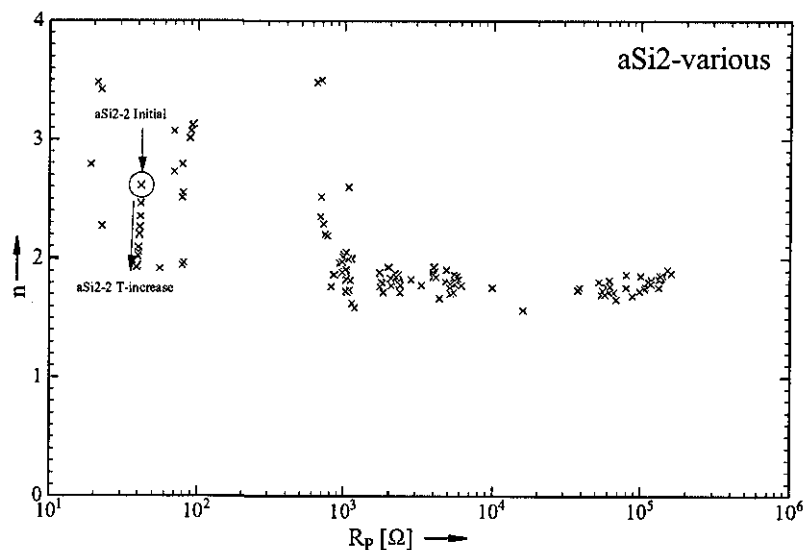


Figure 6.4: *Plot of Fitted Diode Ideality Factor Against Fitted Shunt Resistance.* It is becomes apparent that a low shunt resistance is a possible cause for a high diode ideality factor.

ment at the University of Erlangen at the Chair of Electron Devices. The cells with a significantly increased shunt resistance presented in figure 6.4 were produced by etching the edges of the samples, the low shunt resistances are 'as delivered' devices. It is clear from this graph that a low shunt resistance can cause an increased diode ideality factor. The theory predicts a value of less than two, hence the low shunt resistance apparently changes the device behaviour more than simply reducing the fill factor (in the illuminated case). Having said that, the device behaviour is described very well by the fits if one is prepared to accept the fact that the diode ideality factor is above two.

The reason for the low shunt resistance of the aSi2 devices is most likely the method of their production, as they are produced from larger modules. Cutting samples out of a larger device will create shunt paths at the cut edge. It was shown by Breitenstein and Iwig [Breitenstein 95] that shunts can be stress induced. Furthermore, applying too much pressure to the device can cause shunting of the

i layer. Thus it can be expected that the shunt resistance for a full module will be higher.

The repeatability of the measurements is very high as well, as shown in figure 6.5, where in total 10 measurements conducted at the same temperature at different stages of the measurement cycle are shown. Measurements marked "I" were the initial measurements conducted during the heating of the devices, the measurements marked "S" are the second set of measurements carried out during the cooling of the devices.

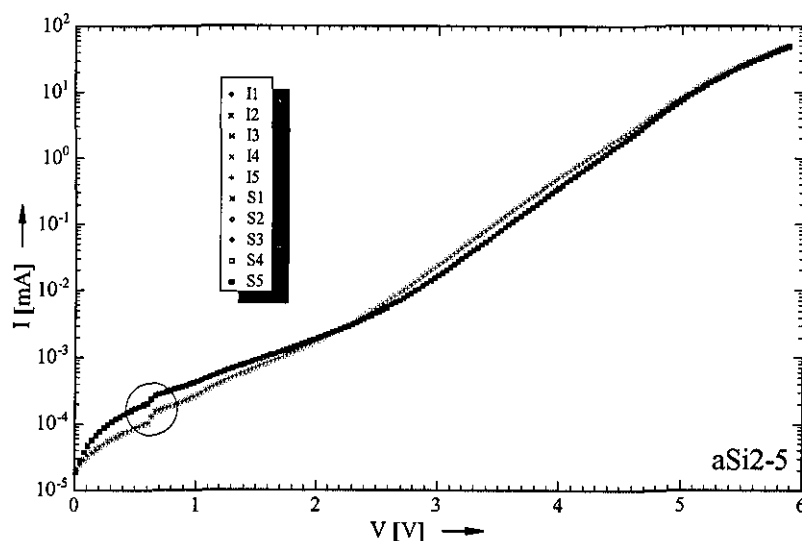


Figure 6.5: *Hysteresis of Measurements as Measured on Cell aSi2-5 at 25°C.* The initial measurements (I1 - I5) in the warming up period are significantly different from the second set of measurements (S1 - S5), which are taken in the cooling down period.

There is, however, an apparent hysteresis between the initial measurements taken during the warming up period and the measurements conducted when cooling down again. This effect is investigated in more detail in section 6.4. A further idiosyncrasy, is marked by the circle in figure 6.5, where a near step change in the I-V characteristic occurs. This step change is neither limited to this particular device, this technology nor the CREST measurement system. A similar effect

was found in measurements carried out at Imperial College, London, as shown in figure 6.6, which indicates that this is not an artifact of the measurement system used at CREST.

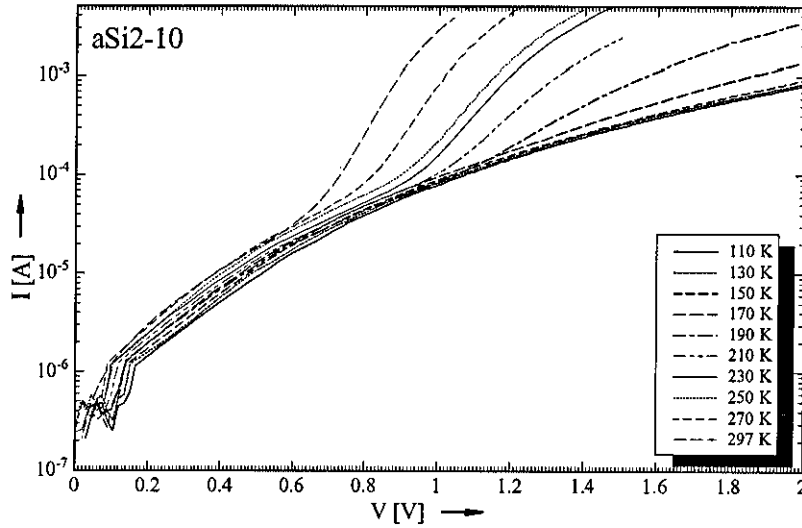


Figure 6.6: *Measurement of an aSi2 Device at Low Temperatures.* A single cell was produced and measured at very low temperatures.

The cell shown in figure 6.6 was etched prior to the measurements in order to increase the shunt resistance. The size of the device as well as the number of cells in series is different from the *aSi2*-5 device shown in figure 6.5, but nevertheless it exhibits this step change in the current. The phenomenon appears to be mainly influenced by the current passing through the device, as the onset is always at roughly the same current level, with varying voltages. This effect was also found for *aSi4* devices, but not as pronounced. This effect, however, will not contribute significantly to the overall power production and thus a further investigation in its physical origins is not carried out.

The measurements of the commercially available polycrystalline devices did not reveal any significant back diode. When fitting with the back diode model, the back diode height was used as a non-sensical adjusting parameter and no clear

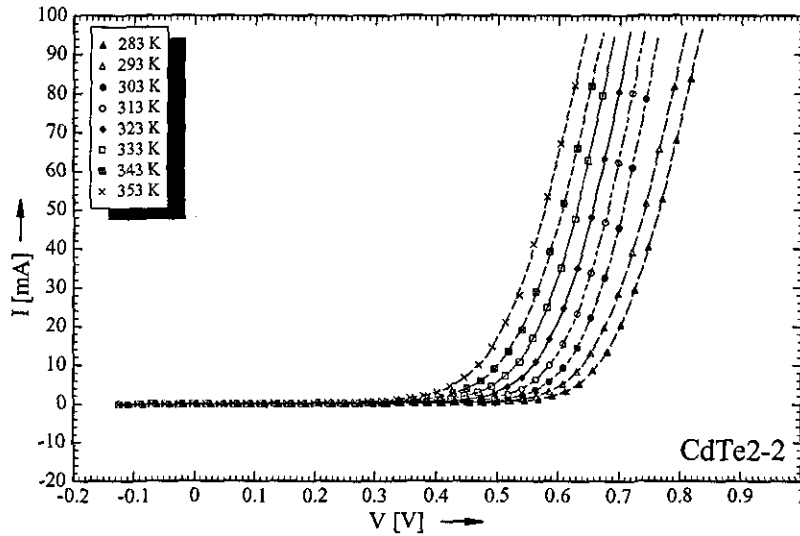


Figure 6.7: *Agreement Between Fit and Measurement for a CdTe2 Device.* This device does not exhibit any back diode behaviour and was thus fitted using the one diode model. The agreement between measurement and fit is very good.

trend was apparent from the results. Hence these devices were also fitted using the one diode model. The agreement between fit and measurements is very good, as illustrated in figure 6.7. One device exhibited the influence of a back diode (CdTe1), and is examined in section 6.6.

6.3 Thermal Variation of Parameters

6.3.1 Series Resistance

It is difficult to predict how the resistance terms vary with temperature. Semiconductor intrinsic resistances typically decrease exponentially with increasing temperature until the temperature is sufficient to change their properties to those of a conducting material, which exhibits a linear increase with temperature. However, this point will not be reached in a solar cell, as it signifies the fact that the band gap was eliminated by the increase in temperature and the apparent band

gap is zero, which would mean that one could not generate any power with this device any more. The semiconductor properties are not the only contribution to the resistance terms, making it difficult to predict exactly the behaviour of these parameters for the whole ensemble.

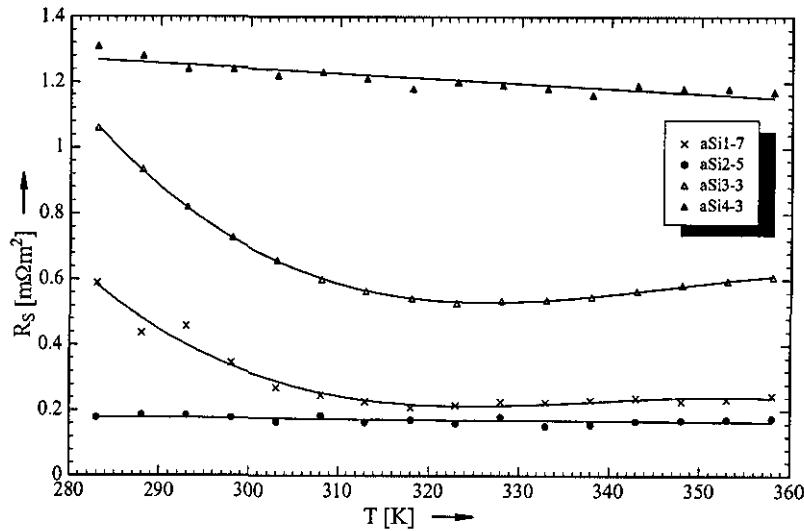


Figure 6.8: *Thermal Variation of the Series Resistance of the a-Si Samples.* The graph compares the variation of the resistances for four different technologies. The curves used for modelling purposes are given for visual guidance.

The thermal behaviour of the a-Si technologies is illustrated in figure 6.8. For the sake of comparability, the series resistance for the double junctions was normalised to single cells, i.e. the voltage per cell was halved during the fitting process. This assumes the cells to be identical, an assumption which certainly is not true for the a-Si/a-SiGe double junction aSi1 but allows a comparison of the devices.

There is a very obvious difference in the magnitude of the series resistance of the different technologies. It appears that the single junction aSi4 device has by far the highest series resistance, followed by the aSi3 double junction device. Both devices were obtained without any leads fitted and the connection was established prior to measurement, i.e. a significant time after procurement. That possibly

allowed the build up of an oxide layer on the contact points which might have increased the series resistance of the device. It is important to remember that not only the device itself, but the whole circuit up to the measurement device contributes to the overall series resistance and thus these things will contribute to the determined series resistance. It is not intuitive that the single junction device has the highest series resistance, especially as aSi3 and aSi4 were obtained from the same source. This is, however, an artifact of considering single cells rather than looking at the whole stack of cells, at least in this case of high contact resistance. The contact resistance affects the whole cell in a single junction, while only half of it contributes to each of the double junction cells. Hence, the result could be expected in this case.

A second difference transpires when investigating the shapes of the curves for the single junction (aSi2, aSi4) and double junction (aSi1, aSi3) devices. The thermal variation of the single junction is well described with a linear fit, while the double junctions need a higher polynomial to describe their behaviour. This difference is most likely due to the internal contacting of the stack, which normally uses a tunnelling contact. Such a tunnelling contact will have an exponential temperature dependence. The lines describing the double junctions are generated using a third order polynomial, purely for the reason that they exhibit the best correlation coefficient R^2 . A second or fourth order polynomial or an exponential decline described the overall behaviour significantly worse, the R^2 values were in the 70 percent range compared to the high nineties obtained by using a third order polynomial. The formulae used for describing the behaviour of the series resistance are summarised in table 6.1.

The series resistance of the polycrystalline devices did not follow the linear behaviour. This could be expected, as there is a small back diode or a contribution from grain boundaries. Both effects, as explained in chapter 3, will be reduced

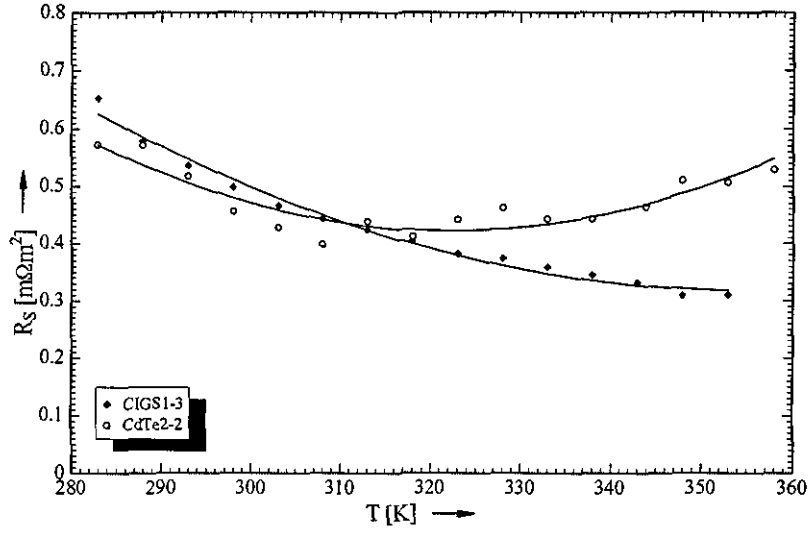


Figure 6.9: *Thermal Variation of the Series Resistance of Polycrystalline Devices.* The graph compares the variation of the series resistance for two technologies. The curves used for modelling purposes are included as a visual guide.

with temperature. The relationship of the CdTe device is more scattered, indicating that the device is less well suited for the single diode model. Both devices could, however, be sufficiently well described by a second order polynomial, as given in table 6.1.

The behaviour of the series resistance of the devices can be described well by polynomials, as indicated by the R^2 given in table 6.1. The obvious exception is the aSi2 sample, in which the fitting algorithm had some problems in finding

Technology	Fit Formula	R^2
aSi1	$R_S = 9.91 \cdot 10^{-2} - 8.79 \cdot 10^{-4}T + 2.60 \cdot 10^{-6}T^2 - 2.56 \cdot 10^{-9}T^3$	0.96
aSi2	$R_S = 2.35 \cdot 10^{-4} - 1.94 \cdot 10^{-7}T$	0.51
aSi3	$R_S = 1.13 \cdot 10^{-1} - 9.83 \cdot 10^{-4}T + 2.85 \cdot 10^{-6}T^2 - 2.74 \cdot 10^{-9}T^3$	0.999
aSi4	$R_S = 1.7 \cdot 10^{-3} - 1.54 \cdot 10^{-6}T$	0.78
CdTe2	$R_S = 1.06 \cdot 10^{-2} - 6.33 \cdot 10^{-5}T + 9.82 \cdot 10^{-8}T^2$	0.82
CIGS1	$R_S = 7.82 \cdot 10^{-3} - 4.23 \cdot 10^{-5}T + 5.96 \cdot 10^{-8}T^2$	0.99

Table 6.1: Formulae Describing the Series Resistance.

stable values. This was apparent because the fitting algorithm frequently jumped from one set of parameters to another. There are apparently two mathematical solutions for the fitting process which are equally good. Hence there is a higher scatter than for the other devices.

There is, however, one very significant observation for double junction as well as for polycrystalline devices. The results presented here dispute the general assumption that the series resistance is constant for all operating temperatures. The series resistance for the double junction a-Si devices is highest for the lowest temperature of 283K and has about half its initial value at 358K. The variation of the series resistance of the CIGS device is similarly significant as for the double junction a-Si devices. Hence it will be important to include this into a modelling package.

6.3.2 Parallel Resistance

Prediction of the variation of the shunt resistance is no less problematic than for the series resistance. In the case of a-Si devices, the thickness of the i-layer appears to have an influence on the apparent parallel resistance [Lord 94]. In some cases metastable shunt paths have been observed for a-Si [McMahon 94], which possess a memory of previous biasing. These things are difficult to include in a model and, depending on their magnitude, might not contribute significantly to the overall power production.

The variation of the shunt resistance of the a-Si devices is investigated in figure 6.10. It is apparent that the aSi3 and aSi4 devices lose their shunt resistance exponentially, while the aSi1 and aSi2 devices appear to be nearly constant in the logarithmic plot, i.e. they have a linear relationship on the operating temperature. The immediate question is if the exponential decline in the shunt resistance of aSi3 and aSi4 is an artefact of the measurement equipment used at CREST, especially

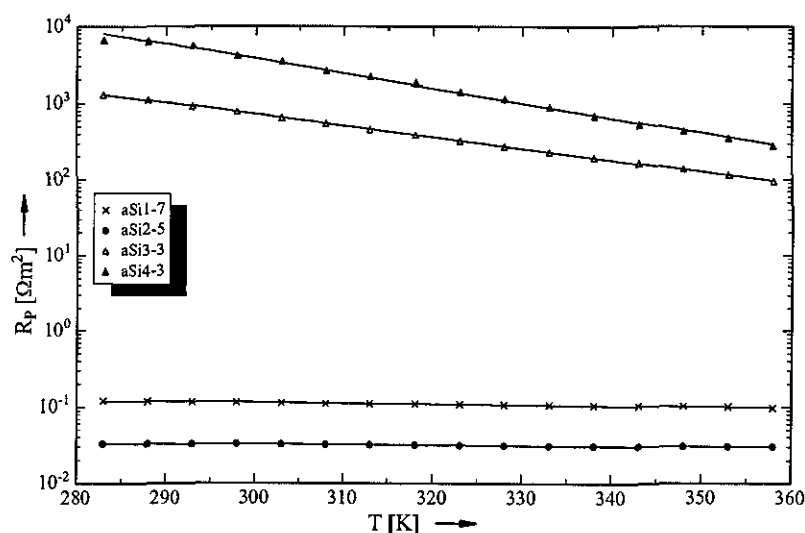


Figure 6.10: *Thermal Variation of the Shunt Resistance of the a-Si Devices.* A fitted line is given as a visual guide, their calculation is described in the text.

as the behaviour reported for c-Si is linear [Veissid 91]. Thus a number of devices were measured at the Chair of Electron Devices in Erlangen and analysed. Results obtained from measurements of four devices are shown in figure 6.11, indicating that the exponential decline is not an artefact of the CREST measurement system. The devices were contacted using 4 spring loaded needles, which exerted less strain on the device than the soldering carried out at CREST, explaining the higher overall values. It is interesting to note that the values for all devices converge for higher temperatures. The achievable temperature range is lower than the one used at CREST, but still, for the higher temperatures, the shunt is nearly identical for all devices.

This exponential decline in shunt resistance indicates that the main shunting path is a tunnel diode or something similar and not due to any ohmic contacts.

Another observation from figure 6.10 is that the shunt resistance of the aSi3 and aSi4 devices is about 4 orders of magnitude larger than for the other two devices. However, comparing figure 6.3 with the extracted shunt resistance magnitudes

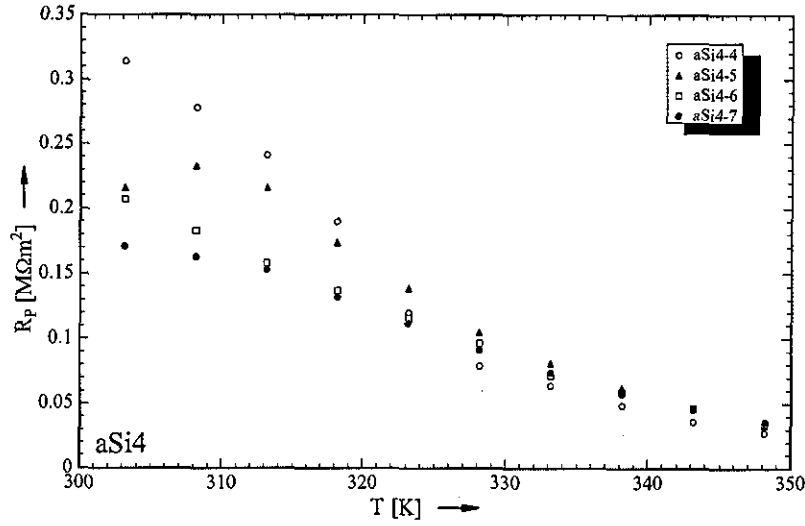


Figure 6.11: *Comparison of the Shunt Resistance Determined Using the Measurement System at the Chair of Electron Devices in Erlangen.* The figure compares the thermal variation of the shunt extracted from measurements of several cells.

of the aSi1 device indicates that the fitting underestimates this property, mainly because the fitting algorithm compensates for the idiosyncratic shape of the I-V characteristic. This compensation occurs because the characteristic can only be described satisfactorily when the model parameters are not necessarily the real physical values. Thus one has the choice of using the realistic shunt resistance, which is an order of magnitude higher and thus incurring an inaccuracy in the modelling or accepting the reduced value given in figure 6.10. For modelling purposes, it appears to be sensible to use the lower value, especially as the maximum error in this fit is below 10^{-4} A for the whole range, with this maximum deviation occurring well after the knee of the curve.

When considering that the aSi3 and aSi4 samples are double and single junction devices respectively, which were obtained from the same source, it is apparent that the double junction aSi3 has a shunt resistance of nearly one order of magnitude lower than the single junction. This result is not surprising, as the results given in figure 6.10 are for a single junction, reducing the overall shunt resistance by

a factor of two. Furthermore, double junction devices are more complicated and thus it is more difficult to eradicate all shunt paths.

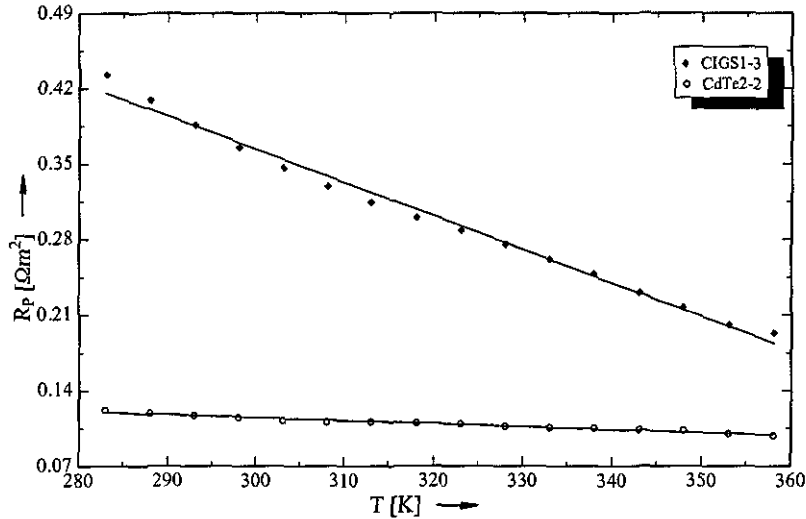


Figure 6.12: *Thermal Variation of the Shunt Resistance of the Polycrystalline Devices.* A fitted line is given as a visual guide, their calculation is described in the text.

The variation of the shunt resistance of the polycrystalline devices is investigated in figure 6.12. The overall behaviour is linear, with the obtained values being in the range of the aSi1 device. The overall decline appears to be steeper for the CIGS device than for the CdTe device, but as the overall shunt resistance is higher anyway, this is no cause for concern. The values given here are not necessarily technology specific, as it is apparent from the discussion of the a-Si samples that these values can vary from cell to cell as well as from manufacturer to manufacturer. It is however apparent that the assumption of a linear decline in shunt resistance models the behaviour of these devices well.

The parallel resistance varies significantly over the tested range of operating temperatures for the majority of the investigated devices. The simple assumption of a linear dependency is a good approximation for all devices except for aSi3 and aSi4, as shown in table 6.2. It appears that it is important to model the variation,

Technology	Fit Formula	R ²
aSi1	$R_P = 2.46 \cdot 10^3 - 1.38 \cdot 10^{-2}T$	0.98
aSi2	$R_P = 1.71 \cdot 10^3 - 7.32 \cdot 10^{-3}T$	0.99
aSi3	$R_P = 2.52 \cdot 10^7 \exp(-3.48 \cdot 10^{-2}T)$	1
aSi4	$R_P = 2.16 \cdot 10^9 \exp(-4.42 \cdot 10^{-2}T)$	0.996
CdTe2	$R_P = 1.98 \cdot 10^{-1} - 2.78 \cdot 10^{-4}T$	0.97
CIGS1	$R_P = 1.29 - 3.09 \cdot 10^{-3}T$	0.9

Table 6.2: Formulae Describing the Shunt Resistance.

especially in the case of the exponential decline of the aSi3 and aSi4 samples. The model parameters used for generating the trend lines in figures 6.10 and 6.12 are summarised in table 6.2. It is apparent from the R² values, that the overall agreement between trend lines and extracted parameters is excellent.

6.3.3 Diode Ideality Factor

The diode ideality factor is normally assumed to vary linearly with temperature in the case of c-Si devices [Veissid 91]. It was reported that this approximation does not hold for a-Si devices because the recombination in these devices is due to an energetic distribution of recombination centres, and not, as in the case of c-Si, via distinct energy levels. The influence of an energetic distribution of recombination centres can, according to Birkmire et al. [Birkmire 95], be modelled as:

$$n(T) = 2 \frac{T^*}{T + T^*} \quad (6.9)$$

Here T* is the characteristic temperature of the device (expected to be of the order of several hundred K). This formulation implies that the diode ideality factor is always smaller than 2. The value for T* can be determined by plotting the inverse of the diode ideality factor versus temperature. When investigating the values obtained for the devices tested, which are shown in figure 6.13, this imme-

diately highlights a problem: the values are frequently larger than this theoretical boundary.

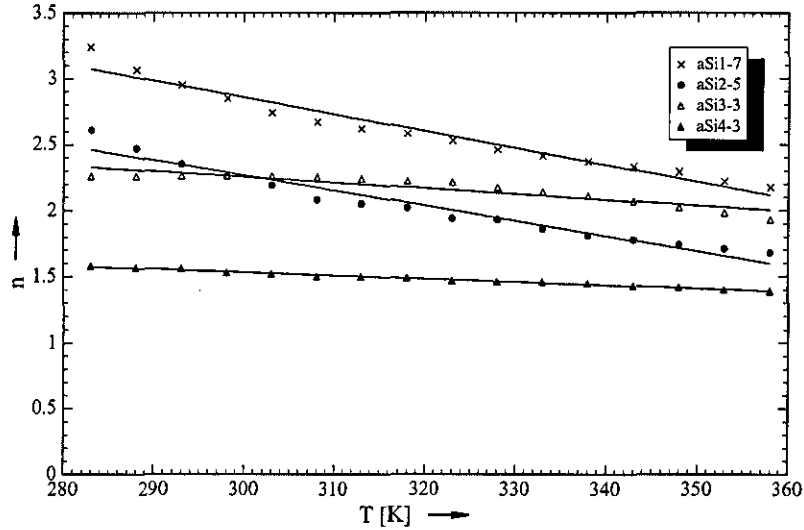


Figure 6.13: *Thermal Variation of the Diode Ideality Factor of the a-Si Devices.* A fitted line is given as a visual guide, their calculation is described in the text.

Values above this limit are not uncommon, see e.g. [Hegedus 97, Alonso 92]. According to Eisgruber and Sites [Eisgruber 94], a possible explanation for diode ideality factors greater than two is that the distributed series resistance of the front and the back contact can lead to deviations in the apparent series resistance, which can in turn affect the diode ideality factor. Thus the geometry of thin film devices can have an influence on the extracted parameters, although this is probably not sufficient to explain the observations found here.

A possible explanation for the high values obtained for the aSi2 device is given above, based on its shunt resistance. Even allowing for any geometrical factor does not really allow the modelling of the behaviour of the aSi2 devices with equation 6.9, as e.g. the Z value obtained for this particular aSi2 device is negative and subsequently the characteristic temperature is negative as well. Another problem for this model is presented by the aSi3 device, where the curvature is actually

opposite to the one predicted by equation 6.9. Thus it appears that the simple linear approximation is better in most cases. The R^2 value has the same order of magnitude for the linear approach as when using the model given in equation 6.9, in the case of aSi3 it is even reduced. Hence, as there is no statistical need for using a model allowing for an energetic distribution of recombination centres and such a model introduces additional problems, it was decided to use a linear fit for all a-Si devices.

The diode ideality factors extracted for the single junction aSi4 are well below the expected limit of two. The values for the double junction aSi3, which was obtained from the same source and employs the same manufacturing technology, are slightly above two. This indicates that the connection of the two junctions introduces a slight non-ideality. This appears to be even stronger in the aSi1 device, where two different materials (a-Si:H and a-SiGe:H) are joined. The high diode ideality, and thus the non-ideal behaviour, were expected from the visible shape of the curve, as shown in figure 6.3 and are explained in the discussion of this figure.

The thermal variation of the diode ideality factor of the polycrystalline devices is investigated in figure 6.14. Both devices shown exhibit a diode ideality factor of well below two, as it could be expected. It appears as if the CIGS device would be better modelled by a relation like equation 6.9, and the R^2 value indeed increases to 0.95 when doing so. The difference is, however, not so significant that it would justify to model the device as the only one using a different approach. Both devices are reasonably well described by a linear approximation. It is surprising, though, that the R^2 value for the CdTe2 device is as low as 0.82, as listed in table 6.3, because the data seems to be described very well indeed. An even lower value was obtained when applying the energetic distribution model, thus it was not used for this device either.

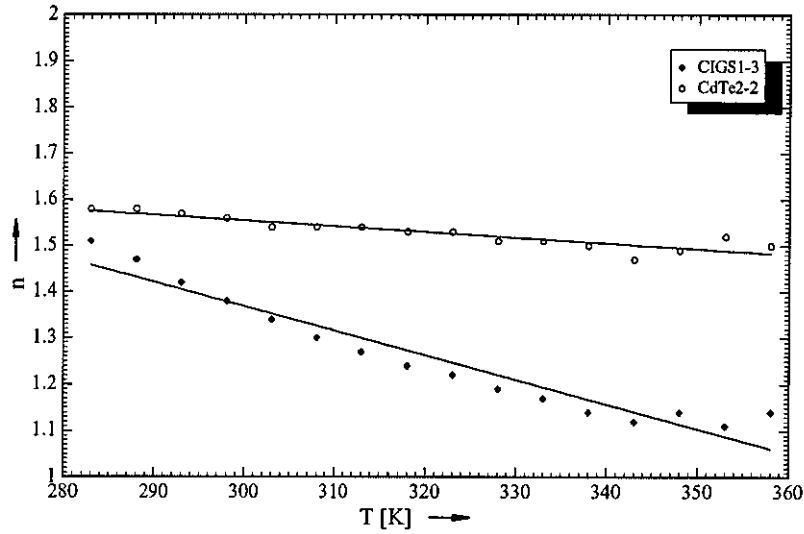


Figure 6.14: *Thermal Variation of the Diode Ideality Factor of the Polycrystalline Devices.* A fitted line is given as a visual guide, their calculation is described in the text.

Technology	Fit Formula	R^2
aSi1	$n = 6.69 - 1.28 \cdot 10^{-2}T$	0.96
aSi2	$n = 5.71 - 1.15 \cdot 10^{-2}T$	0.95
aSi3	$n = 3.56 - 4.34 \cdot 10^{-3}T$	0.86
aSi4	$n = 2.27 - 2.45 \cdot 10^{-3}T$	0.99
CdTe2	$n = 1.92 - 1.23 \cdot 10^{-3}T$	0.82
CIGS1	$n = 2.95 - 5.28 \cdot 10^{-3}T$	0.93

Table 6.3: Formulae Describing the Diode Ideality Factor.

The shape of the thermal variation is very device specific and should not be generalised to other devices of the same technology. Seifert [Seifert 96] showed that in the case of CIGS devices, the diode ideality factor can exhibit everything from a strong decrease with temperature to an increase with temperature, depending on their sodium and sulfur content. Thus, the values given in table 6.3 can only be seen as being valid for the devices tested in this chapter and not as general values for the whole technology.

The thermal behaviour of the diode ideality factor for all devices is summarised in table 6.3, together with the R^2 values obtained for each trend line. Statistically,

the fit is very good for all devices with the exception of the CdTe device which shows a slightly worse correlation coefficient than the other devices. The only device which showed a significant improvement when applying model using an energetic distribution of recombination centres is the aSi2 device, which showed an correlation of 0.98. It was decided for the sake of uniformity to model the behaviour of all devices in this chapter using linear relations.

The intercept of the devices depends strongly on their slope, even the very well behaved aSi4 device shows an intercept larger than two. The devices with an apparently non-linear behaviour have significantly elevated intercepts. This emphasises the fact that the model is valid only in the thermal range investigated. It is obvious from figure 6.14 that e.g. the CIGS device would exhibit a significant deviation from the value calculated with the model given in table 6.3 when operating at temperatures above 100°C. Keeping this in mind, the overall agreement between the model and the derived values is sufficiently good for the application to modelling codes.

6.3.4 Diode Saturation Current

As reviewed above, the recombination current of a thermally activated process be modelled as:

$$I_1 = C_{01} T^{\frac{6+\gamma}{2}} \exp\left(\frac{-E_G}{kT}\right) \quad (6.10)$$

Allowing for a more general formulation, an ideality factor is included, similar to the diode ideality factor in the I-V characteristic. This yields the general formulation as given by Fan [Fan 86]:

$$I_{01} = C_{01} T^{\frac{6+\gamma}{2}} \exp \left(-\frac{E_G}{mkT} \right) \quad (6.11)$$

This essentially requires three empirical parameters to be determined, C_{01} , γ and m , resulting in a large number of parameters which are necessary for the description of the thermal behaviour. One has to be aware that E_G and m are mathematically inseparable and have to be extracted as one parameter. It shows clearly, though, that the value to be expected should be lower than the band gap. This expresses the physical fact that, due to impurities, not all of the band gap is thermally activated.

It is clear from the values extracted, which are given as symbols in figures 6.15 and 6.16, that the model is not always suitable. The fitted lines presented in these figures were generated in two steps using the program TechPlot3.0. First, a general fit was used in order to estimate the rough order of magnitude of the γ parameter and then in a second step the two closest integer values were tested. The curves plotted in the figures correspond to the values given in table 6.4, which presented the highest R^2 value in the fit and best fit on a χ^2 basis.

It is clear that the model in equation 6.11 will not be perfect, as the double junctions especially will also have additional effects due to their internal contacting, as already apparent from the thermal variation of their series resistance shown in figure 6.8. This unusual behaviour also transpires in the thermal variation of the diode saturation current, as apparent from figure 6.15. Both double junctions show deviations from the predicted behaviour for lower temperatures, interestingly in opposed directions. The aSi1 device exhibits a nearly constant behaviour at low temperatures, while the aSi3 device shows an increased slope. The aSi1 device also presents a second challenge, which could be the reason for the different

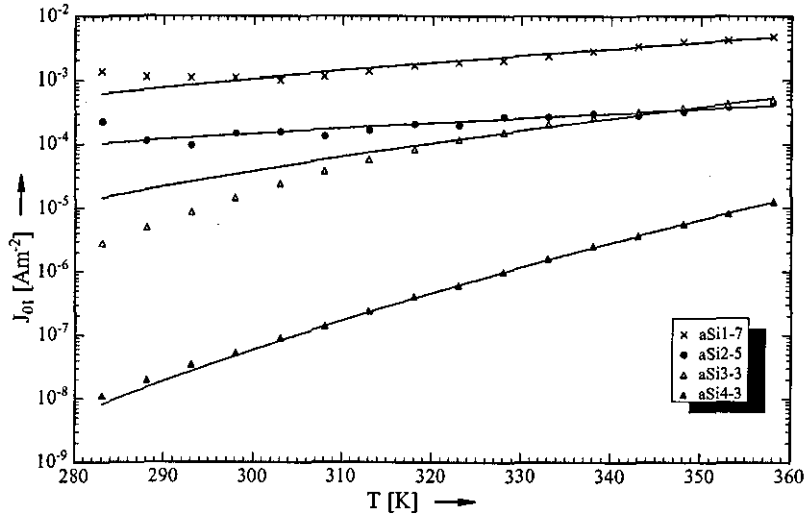


Figure 6.15: *Thermal Variation of the Diode Saturation Current Density of the a-Si Devices.* A fitted line is given as a guide for the eye, their calculation is described in the text.

behaviour from the aSi3 device. The aSi1 technology employs an aSi-aSiGe dual band gap double junction, thus there will be two different band gaps involved in these devices.

These two different band gaps will result in an overall lower m factor, as the band gap for aSiGe is in the range of 1.0-1.72 eV [Wagemann 94], depending on the amount of germanium present in the material. This also means that different temperatures will cause contributions of different magnitudes in the top and the bottom cell, which will have an effect on the overall impact of the temperature.

These deviations in the double junction explain the inability of the model to describe the behaviour at low temperatures to the same quality as in the case of the single junctions. The behaviour of the single junctions is indeed described well by the values extracted.

The behaviour of the polycrystalline devices is investigated in figure 6.16. The model exhibits problems describing the lower temperatures of the CdTe device well. This is most likely due to a non-ohmic back contact, as such an effect will

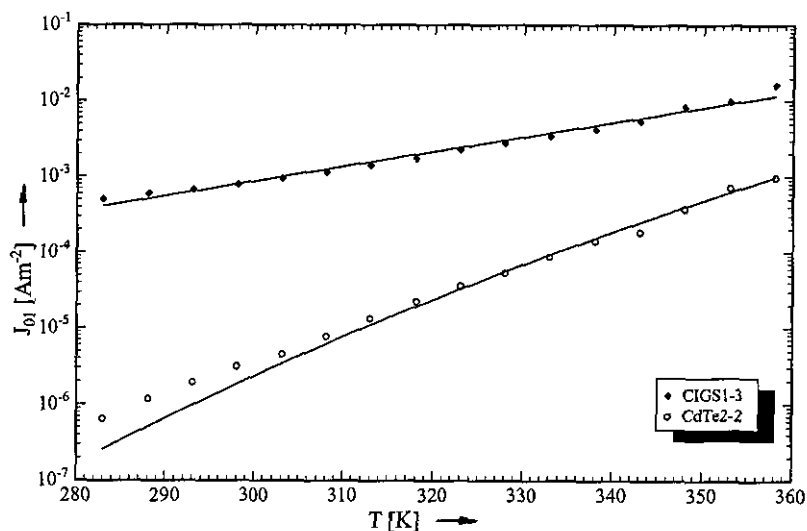


Figure 6.16: *Thermal Variation of the Diode Saturation Current Density of the Polycrystalline Devices.* A fitted line is given as a visual guide, their calculation is described in the text.

increase with decreasing temperature. The contact is not visibly non-ohmic and thus it can be assumed that the effect is not dominant at the temperature range investigated. Nevertheless, this deviation from the model indicates that such a contact is present.

The difference between devices employing the same production technology is given in figure 6.17, where the results of four devices measured at the Chair of Electron Devices at the University of Erlangen are compared with one another. There is an apparent difference in the magnitude of the empirical parameter C_{01} as defined in equation 6.11. The thereby defined minimum saturation current varies from cell to cell, but the thermal variation appears to be very similar for all devices. This indicates that for a given technology the γ and m values are constants, while C_{01} will vary from device to device. The C_{01} constant could thus be used as a measure for the quality of the device, while γ and m are more related to the device physics. The values extracted from the fit results are summarised in table 6.4. The band gaps used for the calculation of the m -value are (based on values given by Wage-

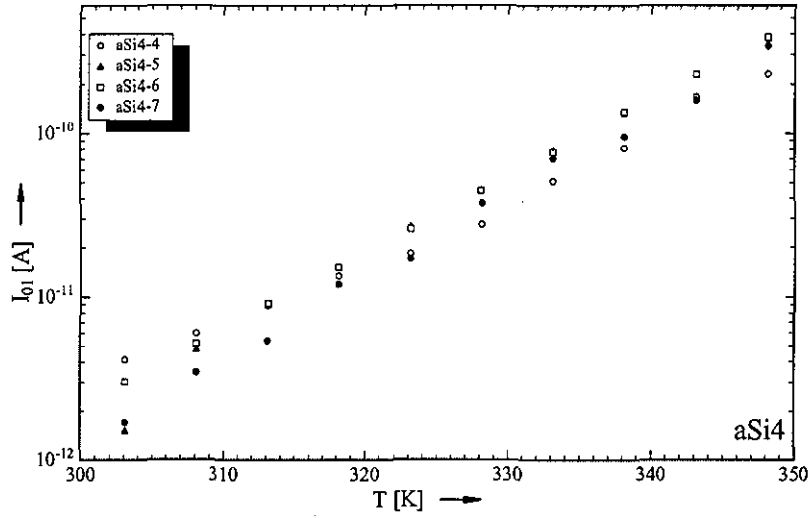


Figure 6.17: Comparison of the Diode Saturation Current of Devices Employing the Same Technology. The results for four devices measured at the Chair of Electron Devices, Erlangen, are presented.

Technology	C_{01}	m	γ	R^2
aSi1	$4.13 \cdot 10^{-7}$	10.36	-1	0.95
aSi2	$3.13 \cdot 10^{-9}$	19.41	-1	0.84
aSi3	$1.88 \cdot 10^{-5}$	4.99	-1	0.99
aSi4	$4.99 \cdot 10^{-1}$	2.24	-1	0.999
CdTe2	$6.8 \cdot 10^{-5}$	1.76	1	0.98
CIGS1	$9.72 \cdot 10^{-9}$	2.18	1	0.98

Table 6.4: Values Describing the Diode Saturation Current.

mann [Wagemann 94]) 1.72 eV for the a-Si devices and 1.02 eV for the CIGS device. The value used for CdTe is 1.45 eV, as given in chapter 3.

The values obtained for the description of devices vary significantly, especially the C_{01} parameter which spans many orders of magnitude. The factor C_{01} depends on different calculations for the various materials, in each it is case a conglomerate of different effects, which are all lumped together in one single parameter. The variation between the technologies should thus not be considered. Within the aSi group it is interesting to note that there are significant differences. It was apparent from the slope that the base value is very different for the different materials, as

well as the parameters describing its slope in the logarithmic plot. It is apparent that the effective barrier in the aSi2 device is by far the lowest, followed by the aSi1 device. The result for the aSi1 device should however not be taken as a physical description of the behaviour of the cell, as it was stated before that it is a lumped parameter for two different materials. If the value for the band gap had been estimated at 1.0 eV, which is essentially the lowest possible band gap when adding large amounts of germanium, the value for m would be identical to the parameter of the second double junction. Similarly, the result for the double junctions are not a physical property in the sense that it allows an insight into the device physics, it is a physical property of the lumped device, including effects at the tunnel junction between the two stacked cells. These parameters are, however, very useful for modelling the device performance as the thermal behaviour of the diode saturation current is exponential and thus (apart for the shunt resistance of the aSi3 and aSi4 samples) the device parameter varying the strongest. The main difference between the technologies lies in the γ -factor, which is -1 for all a-Si devices and 1 for the polycrystalline devices.

6.4 Hysteresis Effects

It was shown in figure 6.5 that the aSi2 sample exhibited an hysteresis for measurements taken in the initial warming up period and measurements taken in the subsequent cooling down period. This was generally observed for a-Si samples, while the polycrystalline samples did not show a visible difference. This effect is shown for a sample of the aSi3 technology in figure 6.18.

It is clear that this is a more general effect, as it affects all a-Si devices across all technologies investigated in this study. It cannot be included in a model at this stage, as it might very well be that this effect is reversible when under illumination.

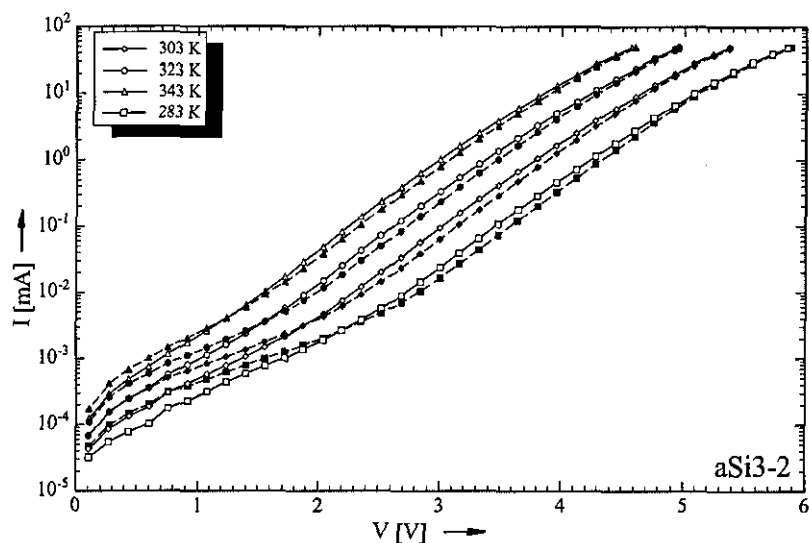


Figure 6.18: *Difference between Measurements at Different Points in the Measurement Cycle.* The solid lines with the empty symbols are taken during the heating up period, i.e. the initial measurements, the dashed lines with the solid symbols are taken at the same temperature in the cooling down period.

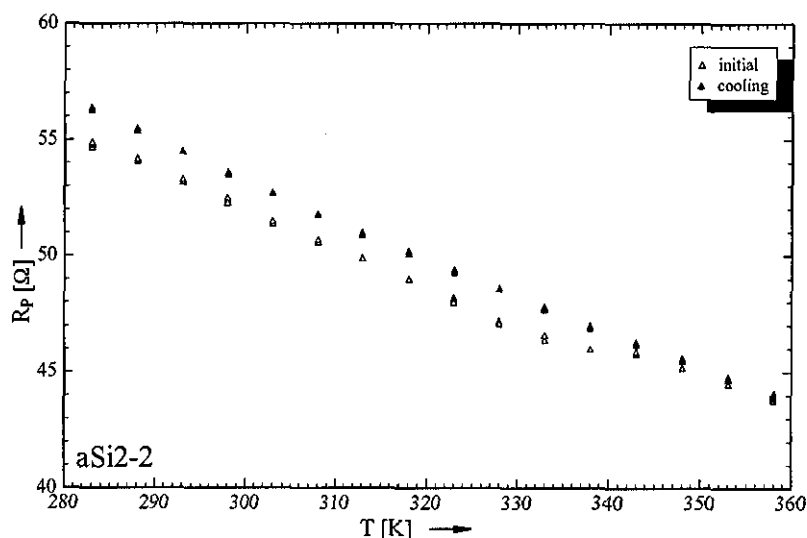


Figure 6.19: *Comparison of Shunt Values Extracted for the Initial Measurements and the Measurements in the Cooling Down Period.* It is apparent that the shunt changes as soon as a certain temperature is reached and stays afterwards on this higher, annealed value.

The behaviour again seems to be similar for all technologies investigated. There is a noticeable improvement in the shunt resistance for all samples. The onset is, as seen in figure 6.19, a rather sudden one. The graph presents the initial measurements as empty triangles and the measurements in the cooling down period as solid triangles. All 5 measurements taken at each thermal step are presented, no averaging was carried out.

The behaviour of the shunt resistance of the shown device is linear up to 338 K and then an annealing process occurs and the shunt resistance is shifted to slightly higher values. Further heating does not appear to make any further difference, nor does the time at this point, as all values are nearly identical and the time between each measurement was 5 minutes, i.e. the difference between the initial measurement at a temperature setting and the last point at this setting is 20 minutes. It took this sample roughly 25 minutes to achieve a stable temperature, hence the time of the heating up period and the constant period are of similar magnitude. There is a minor effect of the time at a measurement point, as it can be seen at the 358 K measurements, where the device improves slightly with time, but the main impact appears to be the maximum temperature achieved.

It appears from figure 6.18 that there is also a change in the diode behaviour of the device. There is, however, no significant difference in the diode saturation currents that could be generalised. In contrast, there is a visible effect on the diode ideality factor, as shown in figure 6.20.

The evolution of the diode ideality factor shown in figure 6.20 is seen to a varying degree with all a-Si devices. It appears again, that there is a thermal threshold up to which the diode ideality factor is not influenced significantly by the operating temperature. When this threshold is reached, in the shown case somewhere between 328 and 333 K, the cell is transformed and no further changes can be observed subsequently. In the cooling period, the diode ideality factor is then slightly

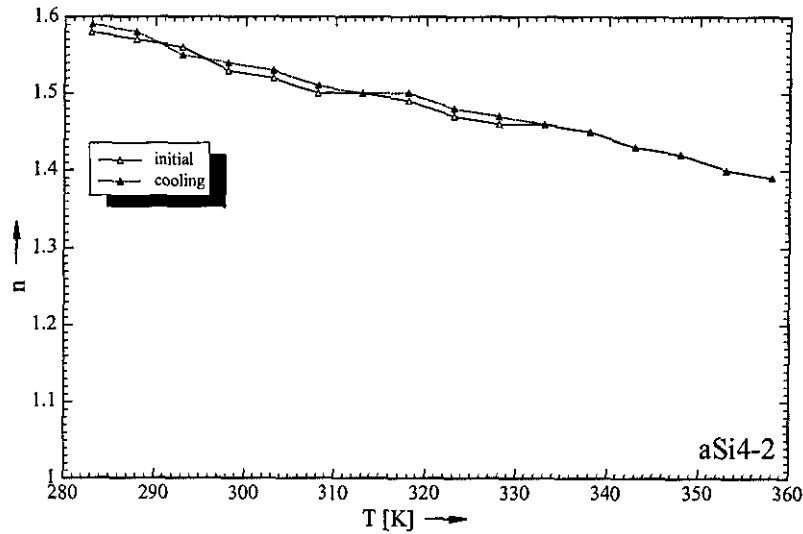


Figure 6.20: *Comparison of Diode Ideality Factors Extracted for the Initial Measurements and the Measurements in the Cooling Down Period.* It is apparent that the diode ideality factor changes as soon as a certain temperature is reached and stays afterwards on this higher, annealed value.

larger than in the heating period (with exception of the 293 K measurements in the example shown).

There is not a sufficient amount of data to investigate whether these changes are reversible. Thus these observations are only mentioned and no attempt at modelling them is made.

6.5 Repeatability of Measurements

The discussion so far is based on the assumption that the methodology is stable and the delivered values are not arbitrary. A significant effort was put into developing a stable algorithm, as described in chapter 4. There is, however, still a significant amount of scatter occurring. This section aims at investigating the stability of the methodology. To this end, 250 measurements were taken after the initial heating up and cooling down period. The temperature of these measure-

ments was 298.15 K, with a variation of less than 0.01 K during the time for the 250 measurements. A five minute settling time was introduced after every single measurement in order to ensure that the measurements are independent from each other and not influenced by the previous measurement. Thus the measurements are taken over a period of time of nearly 21 hours.

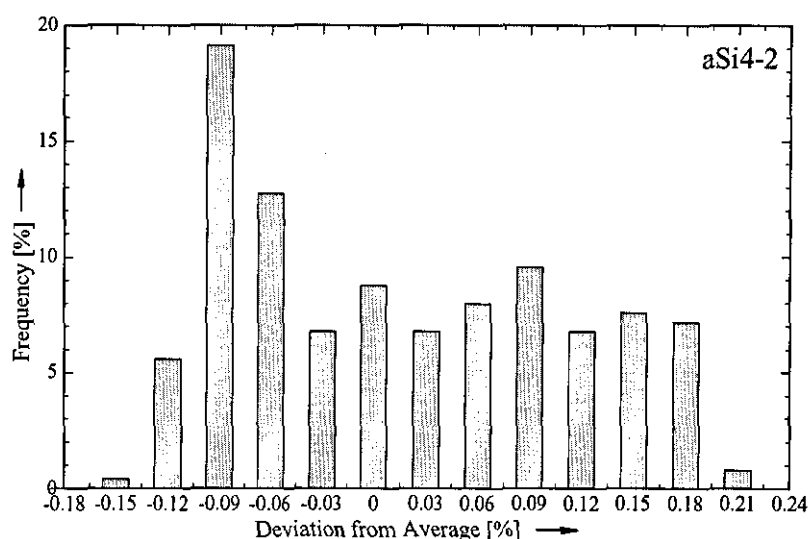


Figure 6.21: *Deviation of Series Resistance from the Average Measurement.* The value 0 indicates the average over all measurements. No results were obtained outside the range shown.

The data was then fed into the fitting algorithm without any user interaction. The parameters were estimated independently from the previous measurement, i.e. all fits were conducted as individual measurements. Then, the deviations from the average values of the parameters were determined and the spread of the results around the average was calculated. The results obtained are shown in figures 6.21, 6.22, 6.23 and 6.24.

It can be seen from figure 6.21, that the maximum deviation in the series resistance around the average is in the range of $\pm 0.2\%$. The distribution does not really have a specific shape, it appears to be relatively arbitrary. This can be attributed to the

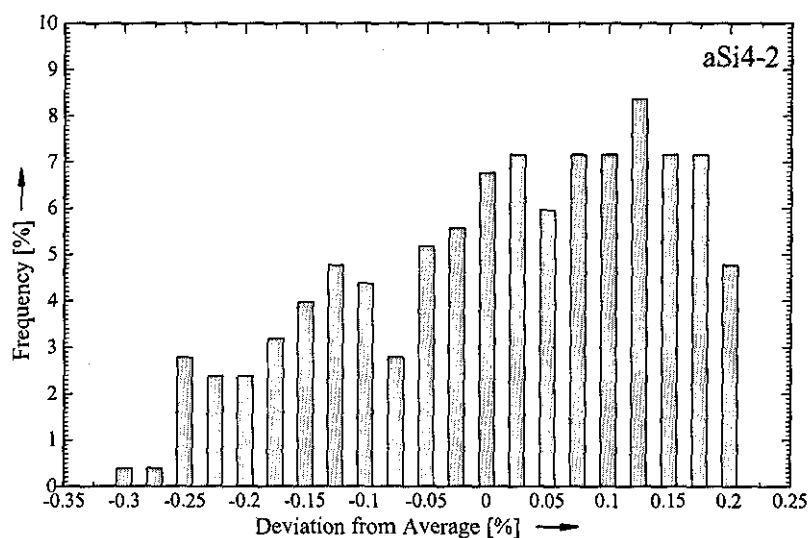


Figure 6.22: *Deviation of Diode Ideality Factor from the Average Measurement.* The value 0 indicates the average over all measurements. No results were obtained outside the range shown.

stopping criteria in the fitting process and indicates that an even narrower margin could have been achieved if the fitting accuracy would have been increased. The fitting accuracy was chosen in order to reflect the accuracy of the measurement and thus simply increasing the fitting accuracy would not have helped, an increase in the measurement accuracy would also have to be achieved. However, a variation of $\pm 0.2\%$ can in any case be considered to be a near perfect result.

The variation of the diode ideality factor is of a similar quality, as apparent from figure 6.22. The variation is in the range of -0.3% to $+0.2\%$ around the average. There appears to be a slight increase in the frequency of the extracted diode ideality factor towards higher values, with a rather sudden cut-off. There were no values retrieved outside the range shown in figure 6.22. Similarly to the series resistance, the result is certainly accurate enough for modelling purposes and the scatter occurring in the models of the thermal behaviour of the parameters cannot be attributed to inaccuracies in the method.

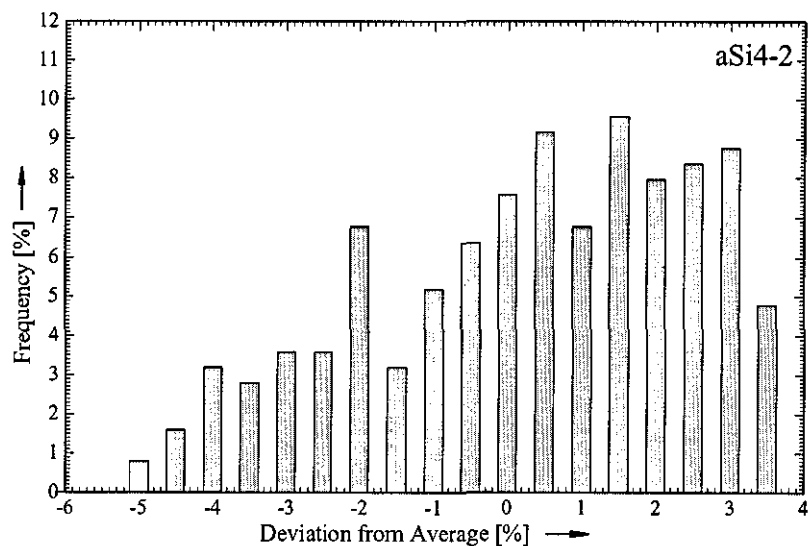


Figure 6.23: *Deviation of Diode Saturation Current from the Average Measurement.* The value 0 indicates the average over all measurements. No results were obtained outside the range shown.

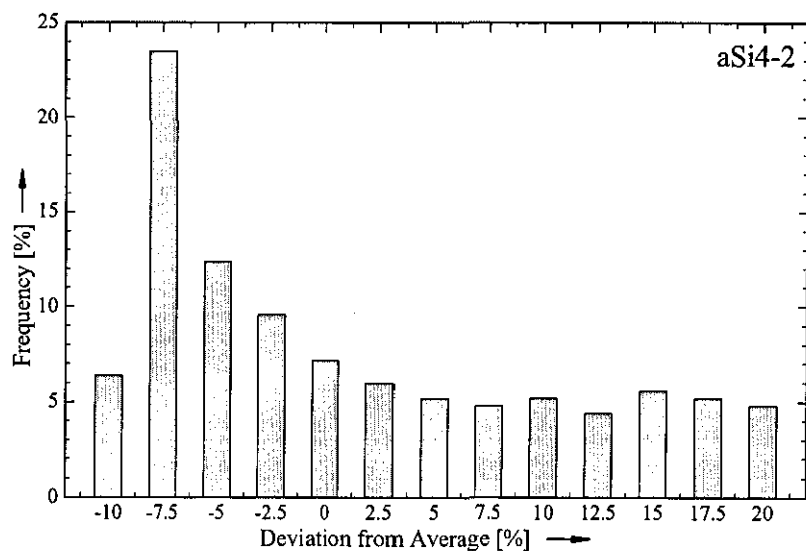


Figure 6.24: *Deviation of Shunt Resistance from the Average Measurement.* The value 0 indicates the average over all measurements. No results were obtained outside the range shown.

The diode saturation current shows a significantly higher spread for the given measurements, as shown in figure 6.23. The variation ranges from -5 to +3.5% for all measurements. There appears to be a distribution which is very similar to the distribution of the diode ideality factor shown in figure 6.22. This can be expected, as both parameters are intimately linked and thus a change in one will certainly cause an adjustment in the other. The overall accuracy achieved is still acceptable.

The shunt resistance, as shown in figure 6.24, exhibits the most significant changes. However, one has to keep in mind the absolute magnitude of the value and the resulting insignificance of the shunt current on the overall shape of this particular I-V characteristic, as discussed in section 6.3.2. For cells with a higher shunt current distribution, e.g. the aSi2 devices, the spread is significantly less. Thus the inaccuracy in this parameter should not be overestimated. It is interesting to note, though, that the shunt resistance showed a significant influence with regard to the time of operation, as illustrated in figure 6.25.

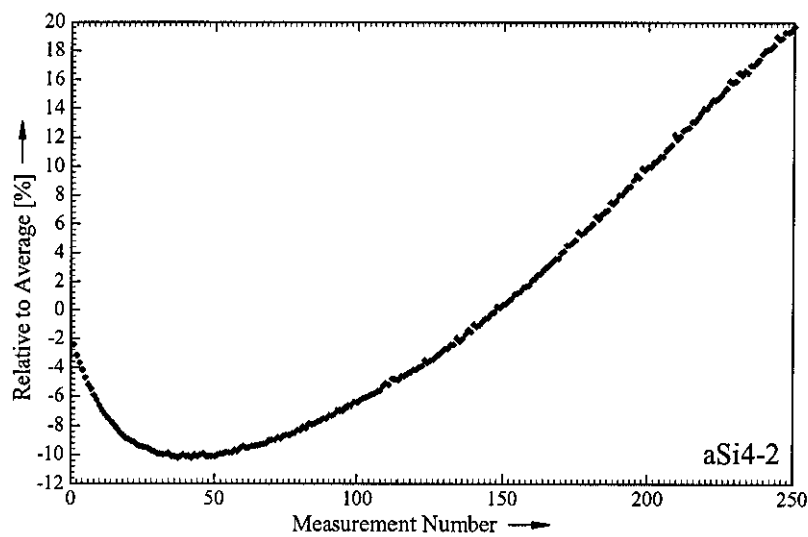


Figure 6.25: *Stability of the Shunt During the Measurements.* There appears to be a clear trend over time. There is no temperature variation detectable during this period.

Curiously, the shunt first deteriorates about 8% with respect to the average of all measurements and then starts recovering. The deterioration lasts about 40 measurements or roughly 3.5h until recovery. This certainly is no temperature effect, as there is no detectable variation of the temperature.

The other parameters showed a similar evolution with time of operation, albeit not in this order of magnitude. It is not a current strain, which has been reported by other researches, e.g. [Asaoka 94], as this tends to result in a deterioration of the shunt and not an increase. Hence the reasons for this phenomenon are not quite clear and should be investigated in more detail in a later study.

6.6 Devices with Back Diode

An idiosyncrasy of CdTe devices is shown in figure 6.26, where the squares highlight the points at which the 50 point limit of the interim storage was reached and a short break in the measurement sequence is needed for downloading the values measured so far to the PC. When starting again with the measurements, this small step occurs. These points were removed for the fitting. The effect, however, increases with temperature.

This effect also occurred for sample CdTe1-1, as shown in 6.27, again increasing in the magnitude with increasing temperature. It appears that the capacity of the system increases with increasing temperature, an effect, that could cause problems when measuring these devices very quickly, e.g. using a flash simulator.

The investigation of devices with a noticeable back diode, as shown in figures 6.27 and 6.28 also illustrate some of the problems of the models reviewed in chapter 3. These problems manifest when fitting the measurements: the algorithm finds sensible values for higher temperatures only. This allows the conclusion that the model is only applicable for higher operating temperatures. For lower temper-

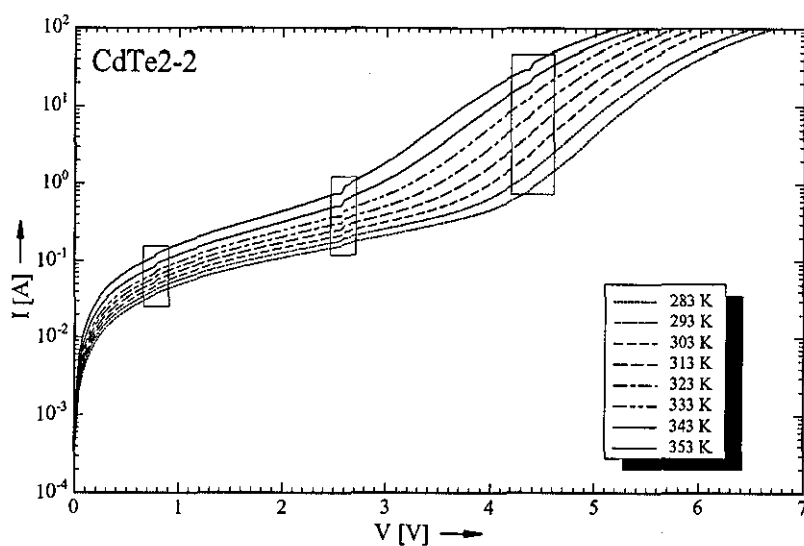


Figure 6.26: *Measurement Artifacts of Sample CdTe2-2.* The squares mark an area in which the measurement is interrupted for downloading points to the PC.

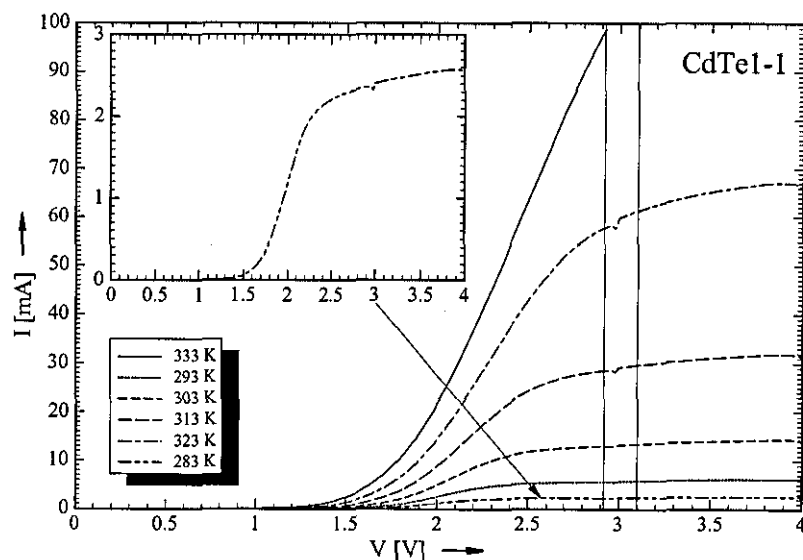


Figure 6.27: *Linear Plot of Measurements of Sample CdTe1-1.* The measurement artifact observed for the CdTe2 sample occurs as well but with significantly reduced magnitude. The measurement taken at the lowest temperature (283 K) is plotted again in the inset for the discussion in the text.

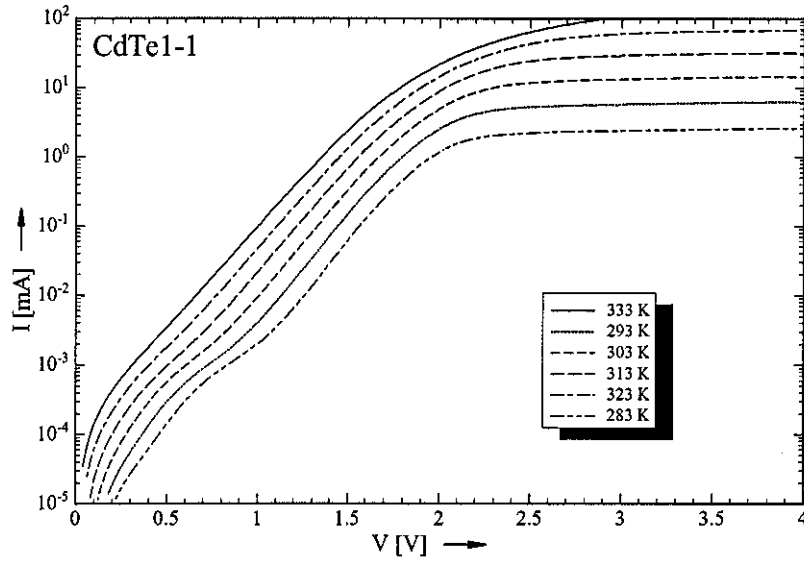


Figure 6.28: *Logarithmic Investigation of the Effect of the Back Diode on Sample CdTe1-1.* The sample exhibits a clear influence of the back diode, the effects on the I-V characteristic are explained in the text.

atures, the reduction in the fill factor is not as significant as predicted either, as apparent from the inset in figure 6.27. One would also expect a reduction in the shunt current and not an increase as apparent from figure 6.28. The levels of the shunt resistance cannot be represented with the given model, because the best values found manually or by the fitting algorithm do not match this. Furthermore, a significant series resistance is extracted by the fitting algorithm, that does not agree with the measured slope in the centre of the rise in the I-V characteristic before the back diode becomes noticeable. This discussion implies that the current mechanism, that was assumed to be thermionic emission in chapter 3, is changing with temperature and that thermionic emission is not dominating in lower temperatures. The thermionic emission appeared simplified, as a reverse current through a metal-semiconductor contact typically exhibits a Schottky barrier lowering which is voltage dependent. Sze [Sze 81] suggests a formula for the current through a reverse biased metal-semiconductor contact as:

$$J_R = A^{**}T^2 \exp\left(\frac{-e\phi_{B0}}{kT}\right) \exp\left(\frac{+e\sqrt{\frac{e\zeta}{4\pi\epsilon_s}}}{kT}\right) \quad (6.12)$$

with

$$\zeta = \sqrt{\frac{2eN_D}{\epsilon_s} \left(V + V_{bi} - \frac{kT}{e} \right)} \quad (6.13)$$

where A^{**} is the effective Richardson constant, ϕ_{B0} is the asymptotic value of the barrier height of the metal-semiconductor barrier at zero electric field, ϵ_s is the permittivity of the semiconductor, N_D is the donor impurity density and V_{bi} is the built-in potential as defined in figure 6.29. The property $\Delta\phi$ is the barrier lowering which occurs across the interface of the metal and the semiconductor, which is in the order of the atomic distance.

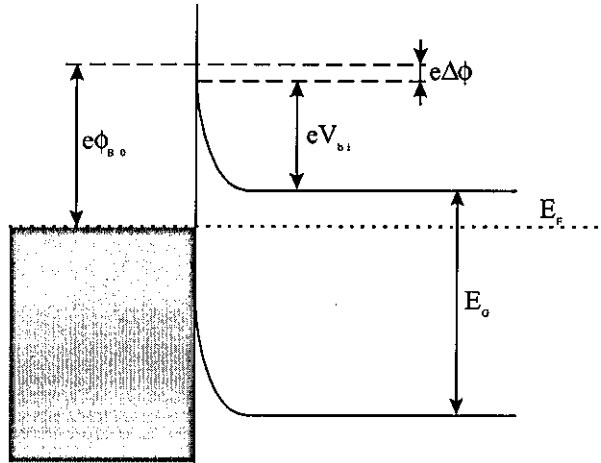


Figure 6.29: *Band Structure of a Metal-Semiconductor Contact.* The figure illustrates the properties used in the text.

The modelling of the device behaviour becomes even more complicated, as it can be expected that there is a significant component due to tunnelling. The

doping concentration of the CdTe is typically below 10^{17}cm^{-3} [Niemegeers 97]. Sze [Sze 81] presents the example of an Au-Si barrier, for which the ratio of tunnelling to thermionic emission is one for a doping concentration of 10^{17}cm^{-3} and temperatures around 260 K with the ratio increasing for higher doping levels and lower temperatures. Obviously, the ratio might be very different when using CdTe, but still, it is an indication that tunnelling might be significant in the measured cell.

Another deviation of devices with a significant back diode is the very pronounced separation of the I-V characteristics for low voltages. This is apparent when comparing figure 6.26, where no pronounced back diode effect occurs, and figure 6.28, where this separation is well observable.

This indicates that the modelling of a cell with a back diode with a simple parametric model might not be possible, as the number of parameters to be fitted increases significantly. There are 3 unknowns in equations 6.12 and 6.13 describing the thermionic emission (A^{**} , ϕ_{B0} and V_{bi}). Further unknowns will be introduced for the tunnelling component, which makes the case too complicated for the approach given here. It will be better to ignore the current in the first quadrant and model only the I-V characteristic in the power producing quadrant of the illuminated characteristics. This might result in empirical parameters which do not show the predicted behaviour but should be good enough for system modelling.

6.7 Conclusions

A methodology was established in this chapter that can be used for the modelling of thin film photovoltaic devices under conditions where the operating temperature varies. It is clear from the results obtained that the thermal behaviour of the parameters has to be included in any modelling approach, especially if a large

temperature range is to be considered or a system analysis is to be performed.

The thermal variation of the extracted parameter varies in some examples significantly from the variation reported for c-Si, depending on the device material and device structure. The series resistance of the a-Si devices showed a relatively small linear variation for the single junctions but a much more pronounced variation for the double junction devices, that could only be reproduced with a third order polynomial. The series resistance of the polycrystalline devices was described with a second order polynomial. The reasons for these higher order polynomials are found in the limited applicability of the single diode model for these cells.

The thermal behaviour of the parallel resistance is very dependent on the device manufacturer. The devices of one manufacturer showed an exponential decline of the parallel resistance with temperature while all the other devices exhibited a linear decline. However, the exponential decline can be expected to make a low impact on the overall performance, as the absolute value of the shunt resistance is several orders of magnitude higher than for the other devices.

The diode ideality factor could in some cases be reproduced with a model derived for a thermal distribution of recombination centres, but in general, the behaviour appears to be described better by a linear approach. The diode ideality factor is very stable for good natured devices, i.e. devices which follow the one diode model well. For devices with behaviour deviating from the one diode model, the fitting algorithm will compensate for this deviation with variations in the diode ideality factor. These extracted in this case do not always agree with values derived from the theory.

The model used for the description of the thermal behaviour of the diode saturation current appears to be applicable to the majority of devices in the temperature range investigated. Problems occur only when it is apparent that the one diode model is a significant oversimplification.

The repeatability of the method applied for the parameter extraction is shown to be very high, with the maximum variation occurring in the parameters having the lowest influence on the overall shape in the I-V characteristic, which is the shunt resistance in the example shown in this work. This variation is, however, demonstrated to be due to an effect occurring during the measurement period and not due to the applied methodology. It is also shown that there is a significant impact of the operating history on the behaviour of a-Si devices. Another problem for the presented method is posed by devices with a significant back diode. This is attributed to the complicated current transport in the back diode.

Overall, the behaviour of the curves can be described very well with the model given in this chapter.

Chapter 7

Spectral Effects for Outdoor Operations

7.1 Introduction

Photovoltaic systems are often designed on the basis of standard meteorological data. Modern thin film devices, however, have a band gap significantly different from that of standard c-Si devices, and thus exhibit a different spectral response. This chapter examines the importance of this factor for the three thin film technologies investigated in this work.

Spectral information is not included in standard meteorological data which usually give only the absolute total irradiance incident (i.e. integrated across all wavelengths) on a horizontal plane. The significance of neglecting the spectral effects with respect to the device performance of thin film devices will depend on the particular technology used since each technology has a characteristic spectral response, and associated with this, an effective spectral range. These ranges are illustrated in figure 7.1 against the standard AM1.5 spectrum. The importance of spectral effects has been demonstrated by several authors on the basis

of computer simulations [Kleiss 92, Martin-Chivelet 97] reflecting a relatively low number of measurements. There is little reliable data covering bad weather conditions as the spectroradiometers used to conduct these measurements are usually not environmentally sealed.

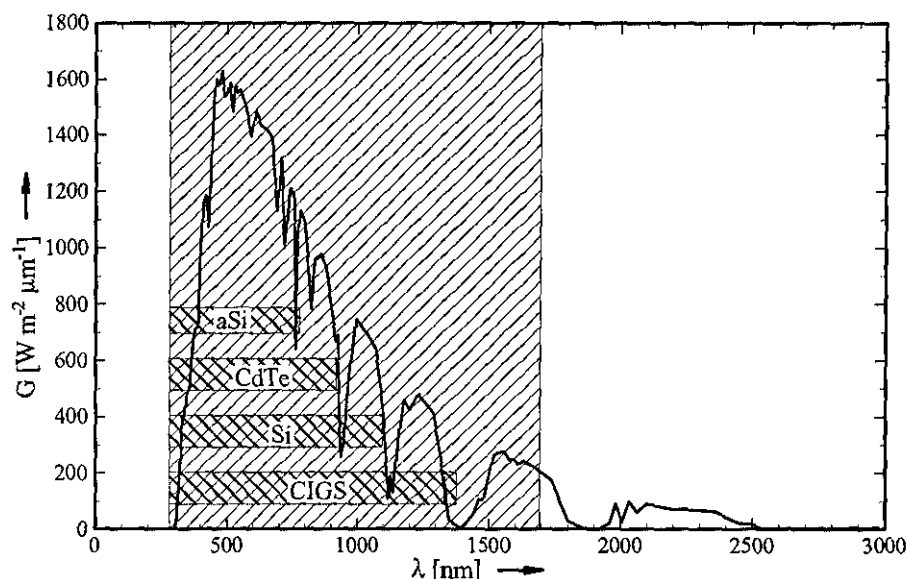


Figure 7.1: *AM1.5 Spectrum and Corresponding Spectral Response of Different Solar Cell Materials.* The measurement range of the spectroradiometer used in this work is indicated by the larger hatched area. The spectral response of various materials is indicated by the boxes.

Solar cells are normally tested under the agreed Standard Test Conditions, which specify the AM1.5 spectrum. There is only limited knowledge about the influence of the seasonal variation of the incident spectrum, and even less for a maritime climate such as the UK's. Investigations have been undertaken for Southern Germany and the US by Nann [Nann 92a] and Nann and Emery [Nann 92b]. Parretta [Parretta 97] investigated this effect at Portici, Italy, on the basis of measurements taken during good weather conditions. Berman et al. [Berman 99] have investigated spectral effects in the Negev desert, Israel. The different weather conditions between the desert climate investigated in this work [Berman 99] and the

maritime climate of the UK becomes very apparent when comparing the dependence of their spectral factor (which is defined similarly to the useful fraction used in this work) on the air-mass with the dependence found in this work: Berman et al. [Berman 99] report a linear relationship, a fact that most certainly is not found in the UK as shown in figure 7.2.

Fabero and Chenlo [Fabero 91] and Merten [Merten 96] model the spectral mismatch with a spectral mismatch factor for the short circuit current of crystalline and amorphous silicon devices. A more comprehensive approach was taken by Hirata and Tani [Hirata 95], who use a pyranometer and 6 filters up to a maximum spectral irradiance of 1200 nm and investigate the effect of the spectral changes on a-Si and c-Si devices.

However, all these investigations were undertaken in climates distinctly different from the UK's (and similar maritime climates) and thus specific investigations need to be undertaken to underpin thin film performance estimations appropriate to these locations. Only a limited amount of spectral data was available for the UK, prior to the Loughborough installation, since there are no spectroradiometer installations that could operate on a continuous basis. Moreover, to the author's knowledge no data has been presented to date describing the influence of daily variations in incident spectra nor on the influence of the detector used. The present work helps to address the lack of data available to the community, and uses this to examine the impact of spectral variation on device performance.

This chapter presents the analysis of the measurements of the spectral irradiance. The measurement procedure and analysis are outlined in chapter 5.

7.2 Spectral Effects of Weather and Air Mass

The effects of the spectral variation on thin film devices have been investigated on the basis of the useful fraction for a given technology. This is defined to be the ratio of the spectral irradiance in the useful spectral range to the total irradiance. The upper wavelength boundaries for useful irradiance of different technologies were identified from the literature as 1360 nm for CIGS [Gay 96], 1100 nm for Si [Emery 86], 900 nm for CdTe [Bonnet 94] and 780 nm for a-Si [Emery 86]. For a-Si, it was decided to consider only single junction a-Si devices. The effect of seasonal spectral variations on multi-junctions cannot be modelled with the simple useful fraction model used here, as it will be shown in chapter 8. Any shift in the spectrum results in mismatch of the series connected cells in the multijunction, hence significant non-linear effects occur. This will also impact on the fill factor of a device [Rüther 01]. This effect is thus very different to spectral effects of a single junction where the impact is seen solely in the short circuit current.

There are two main influences on the incident spectrum: air mass and weather. The influence of the weather on the useful fraction is mainly due to increased cloud cover which can be described, in a simplified manner through the clearness index k_t . The impact of the two factors is illustrated for a-Si in figure 7.2. In order to generate this graph, the data collected during the measurement period was binned. Averaged bin values are presented in figure 7.2 as a surface plot.

Due to their effect on the spectral composition of the incident radiation, it is clear from figure 7.2 that both the air mass and the clearness index have a distinct influence on the spectral composition of the incident radiation, here represented by the useful fraction for the case of a-Si devices. Care is needed, though, as the clearness index and the air mass are not completely independent from each other: a higher air mass will normally result in a lower clearness index, because of the absorption occurring during the passage of the light through the atmosphere.

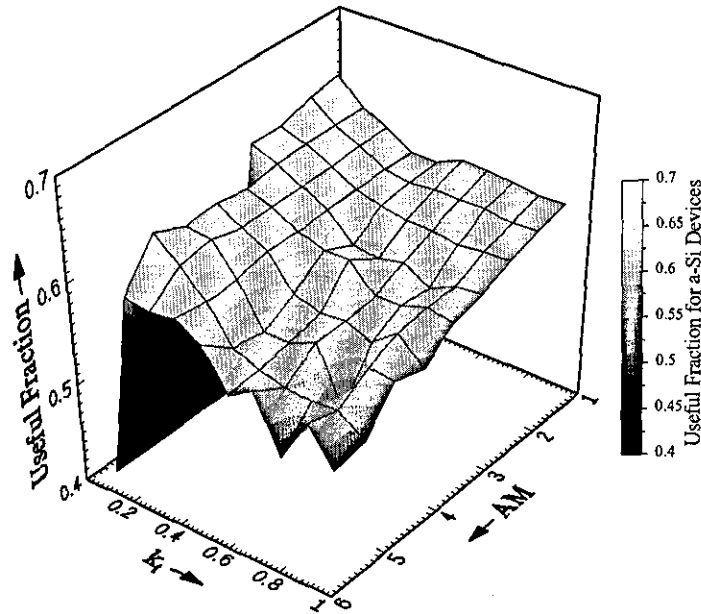


Figure 7.2: *Influence of the Weather and the Air Mass on the Useful Fraction for a-Si.* The influence of the weather can be expressed using the clearness index k_t .

Figure 7.2 also implies a seasonal and daily variation of the useful fraction, as the air mass will be higher in winter and during the morning and evening. However, lower k_t values (i.e. measurements with higher cloud cover) tend to have a higher useful fraction.

This effect is well documented [Landsberg 75, R  ther 99] and depends to a large extent on the band gap on the material under investigation. The results for a-Si are shown above, because it has the largest band gap and thus the effect will be more pronounced than for other materials. Typically, the diffuse component of the irradiation has a higher component of 'blue' light. This means that nearly every solar cell, depending on the spectral response of these devices, will perform with a higher efficiency in diffuse light, although the absolute energy production is obviously reduced. Those cells with band gaps larger than c-Si especially benefit from this spectral shift [Landsberg 75]. The exact magnitude of the effect can be

easily calculated for single junctions if the spectral response is known.

The spectral shift can be understood as follows. The scatter within the Atmosphere can be simplified into scatter at smaller scatter centres (such as molecules) and at larger centres (e.g. aerosols). The incident wavelength will excite the dipole in a molecule to an oscillation of rotational frequency $\omega=2\pi c/\lambda$. The molecule behaves as a Hertz-dipole, emitting with an energy P and absorbing the intensity I from the incident irradiation. The scatter diameter s can be calculated for particles smaller than 0.1 of the wavelength as [Gerthsen 89]:

$$\sigma = \frac{P}{I} \approx \frac{8V^2\pi^3}{3\lambda^4} \quad (7.1)$$

Thus blue light is scattered significantly stronger than red light, this process is called Rayleigh scattering. The light has, however, a strong directionality, roughly half the light is scattered forward and half the light is scattered backwards. This can be observed on clear days at very steep angles of incidence, when the blue light is scattered away nearly completely, while red light is still reaching the observer. This higher susceptibility to scattering also creates the blue sky, as the light which is scattered once, might activate another dipole which then can emit to the observer. This explains the influence of the AM on the UF. The step from the UF to the actual device is then a relatively simple multiplication with the spectral response of the device, thus small differences will occur between devices produced from the same material, depending on their spectral response.

Aerosols are small particles with a diameter in the range of 0.001 to 100 μm ; thus they can be of the order or larger than the wavelength of the light. For the larger particles, the wavelength dependence is not as strong as the Rayleigh scatter, it can be approximated in a parametric form for a given aerosol as [Nann 92a]:

$$\delta_A(\lambda) = \beta \left(\frac{\lambda}{1\mu m} \right)^{-\alpha_A} \quad (7.2)$$

where δ_A is the wavelength dependent optical thickness of the aerosol, which is calculated at an optical thickness β of 1mm. This case is called Mie scattering, and it is much less wavelength dependent than Rayleigh scatter.

Additionally to the scattering processes mentioned above, gases exhibit a selective absorption. With the exception of a small amount of light which is absorbed by O_3 in the UV region, this typically happens at wavelengths larger than 700 nm, i.e. in the red part of the spectrum. If there is a sufficient optical thickness in the path of the incident light, there will be no spectral irradiance in the absorption band and the band will widen with increased amounts of light. Thus, in a sufficiently thick cloud cover, the spectral irradiance beyond 700 nm will be absorbed nearly completely, thus the UF will increase.

This explains why Berman et al. [Berman 99] found a linear relationship in their spectral factor, as they worked in a very dry climate and thus the AM dependence will dominate. The question to be addressed in this chapter is the magnitude of these effects for thin film devices in a maritime climate.

It has to be emphasised, though, that the Rayleigh scattering and the absorption of molecules will affect all technologies, depending on their spectral response. The variation for *a*-Si was chosen as an example, as its maximal spectral response of up to 780 nm will make it quite susceptible to these changes. This effect has been shown e.g. by Nann [Nann 92a] for c-Si and GaAs, thus it is not specific to thin film devices.

7.3 Daily Cycle

Variation of the useful fraction for different technologies during the course of particular sunny days in winter and summer is presented in figures 7.3 and 7.5 respectively. In both graphs, the useful fraction and the total irradiance is plotted against the time of the day.

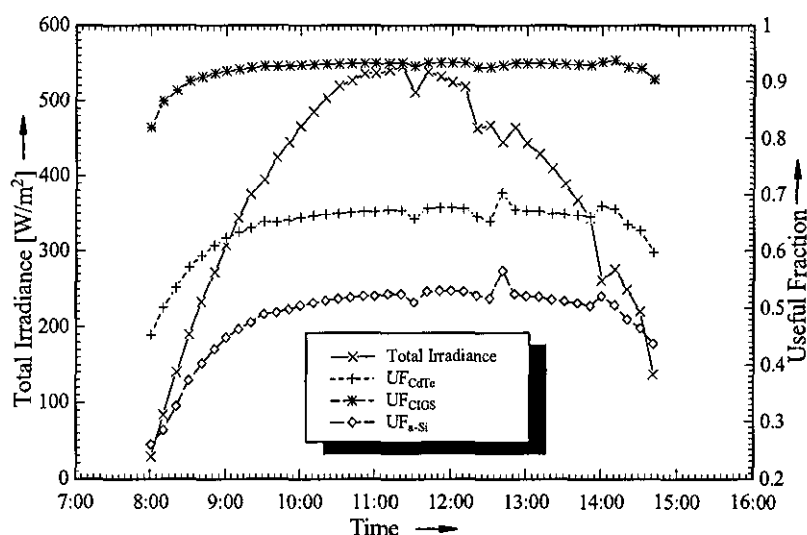


Figure 7.3: Variation of Useful Fraction over a Clear Winter Day. The useful fraction for the different materials is compared with the total irradiance.

A winter day (figure 7.3) shows a small increase of the useful fraction over the day (ignoring the flanks in the morning and the evening). This is due to the increase of water vapour in the atmosphere and the subsequent improved absorption of radiation at the higher end of the spectrum. It seems to be a general phenomenon, occurring also at other sites. Researchers, e.g. R  ther [R  ther 99], have reported an increased performance of a-Si systems in the afternoon. Figure 7.4 presents data collected by R  ther in Brazil illustrating the increase in system performance in the afternoon, which can not be attributed to any other environmental effect. This data was collected soon after commissioning, prior to any significant light-

induced degradation, and thus excluding any thermal annealing effects.

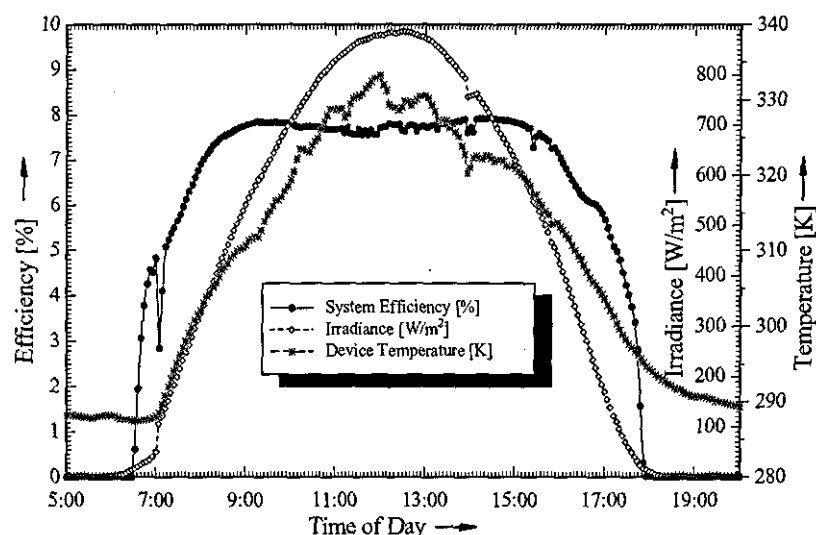


Figure 7.4: *Variation of the Daily Efficiency of an a-Si PV System in Brazil.* The figure shows the variation of the system efficiency, device temperature and irradiance in the plane of the system over the day. It features an improved performance in the afternoon that cannot be explained by magnitude of irradiance and temperature alone.

The system operated by Rüther [Rüther 99] uses same band gap, double junction a-Si modules and is installed in Florianopolis, Santa Catarina, Brazil. The relatively low system efficiencies in the morning (before 8:30) and the evening (after 16:30) can be attributed to the low levels of irradiance. The maximum efficiency of around 7.5 percent, reflects the undegraded state of the system. The efficiency dip at noon can be attributed to increased device temperature. In the afternoon, however, the system performs better at similar device temperatures and identical irradiance levels than in the morning. This can only be attributed to a shift in the solar spectrum, especially when considering that the devices used in this system are employing aSi3 devices, which have a minimal temperature coefficient, as shown in chapter 8. The improvement of system efficiency in the afternoon is a consistent feature, with a magnitude consistent with the increase in the useful

fraction for a-Si illustrated in figures 7.3 and figure 7.5. The traces shown in figure 7.4¹ are for a spring day in the middle of September, though the effect is not restricted to any particular month.

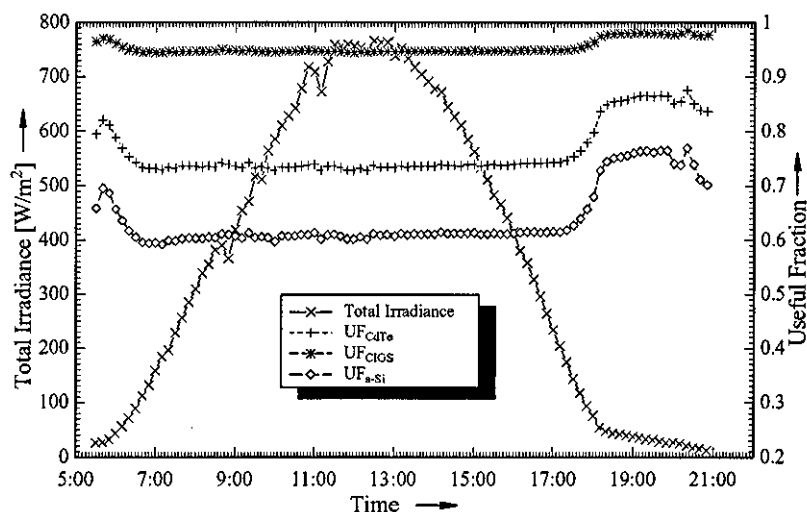


Figure 7.5: *Variation of Useful Fraction over a Clear Summer Day.* The useful fraction for the different materials is compared with the total irradiance.

An interesting effect is apparent from the graph of the sunny summer day shown in figure 7.5. The flanks in the morning are the other way round, i.e. the useful irradiance does not increase, it appears to decrease in the morning around 6:00 and increases again in the afternoon at 18:00. The latter time coincide with the time the sun vanishes behind the input optics, i.e. the incident irradiance changes from a mixture of beam, diffuse and albedo to a mixture of diffuse and albedo irradiance only. This has a beneficial effect in the sense that the useful fraction of the incident irradiance increases. Obviously, the blocking of the beam irradiance results in a strong attenuation of the overall radiation so that the energy production of the device will suffer despite the shift. In the morning the shift in the UF is caused by the Sun appearing from behind the optics.

¹Data courtesy to R. R  ther, Labsolar, Florianopolis, Brazil

The shift towards the blue of diffuse radiation is a more general feature [Green 92]. It explains, for example, why there are reports of a-Si systems in the UK which seem to show a better performance ratio when facing north (although clearly they produce less overall energy). The Solar Century demonstration house in Richmond, London, on a north facing aspect², produces around 64% of the output of the south facing aspect, whereas a simulation using local (Sutton Bonington) data showed that it should only produce around 61% [Gottschalg 01]. This calculation is based only on the total irradiance available and does not include low light efficiencies of the devices. It can be questioned whether other materials would exhibit such a feature, since a-Si has a particularly good low light response. Furthermore, for a-Si, lower levels of irradiance may lead to reduced degradation, hence improving the performance ratio further.

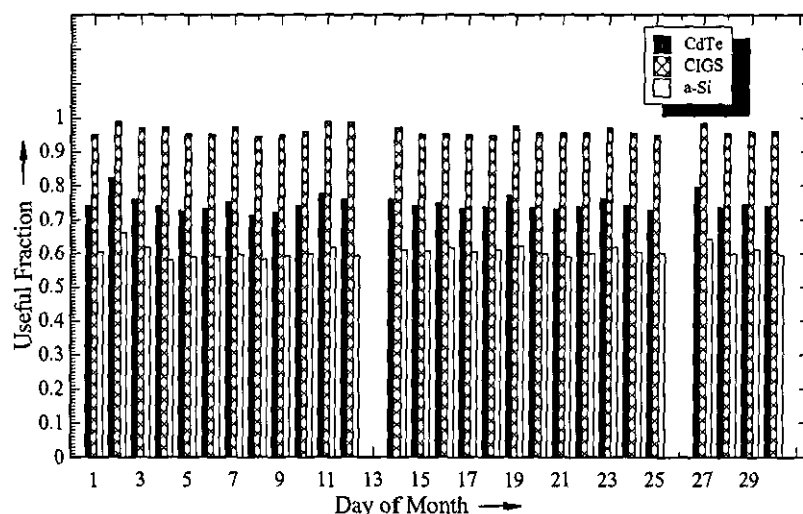


Figure 7.6: *Variation of the Daily Useful Fraction in June 1999.* The graph plots the useful irradiance for each day and thus includes the weather dependence of this measure on a day in summer.

²Data courtesy of K. Stevenson, Solar Century, London, UK

7.4 Seasonal Variations

The impact of the weather can be identified by looking at the variations of the daily integrated useful fraction, as shown for a summer month in figure 7.6 and for a winter month in figure 7.7. There is only a minor weather influence for the summer days, partially due to the fact that the weather was relatively stable during this period. The lacking data points are due to a system failure.

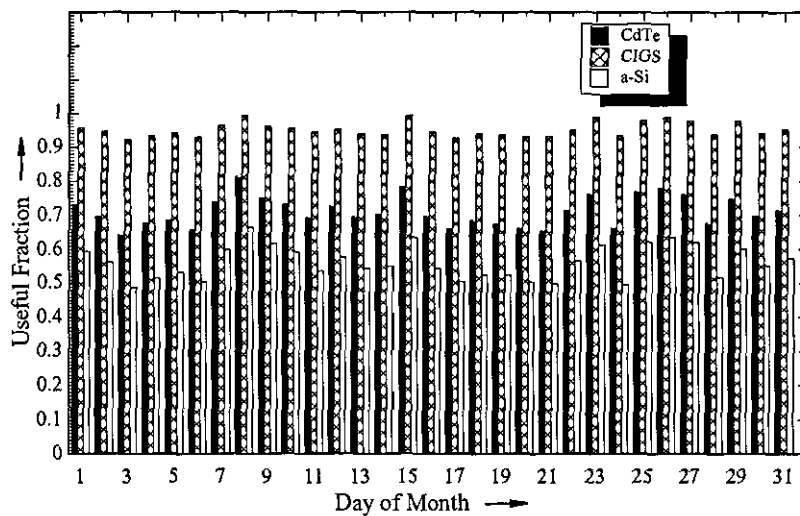


Figure 7.7: *Variation of the Daily Useful Fraction in December 1999.* The graph plots the useful fraction for each day and thus includes the weather dependence of this measure on a day in winter.

A much more pronounced variation can be observed in December with some very cloudy days showing a higher useful fraction. The average air mass apparent in the course of a month does not vary dramatically. The main difference between the sunny and cloudy days is in the absolute irradiance received by any solar collector. In the case of the data presented in figure 7.7, there were days with a maximum irradiance as low as 45 W/m^2 as well as days with a maximum irradiance of around 600 W/m^2 . This large variation in the cloud cover is reflected in the large variations in the useful fractions observed during these different days. Again, this

shift in the spectrum could be one of the reasons for the often reported good low light response of a-Si, the photovoltaic material most susceptible to spectral variation.

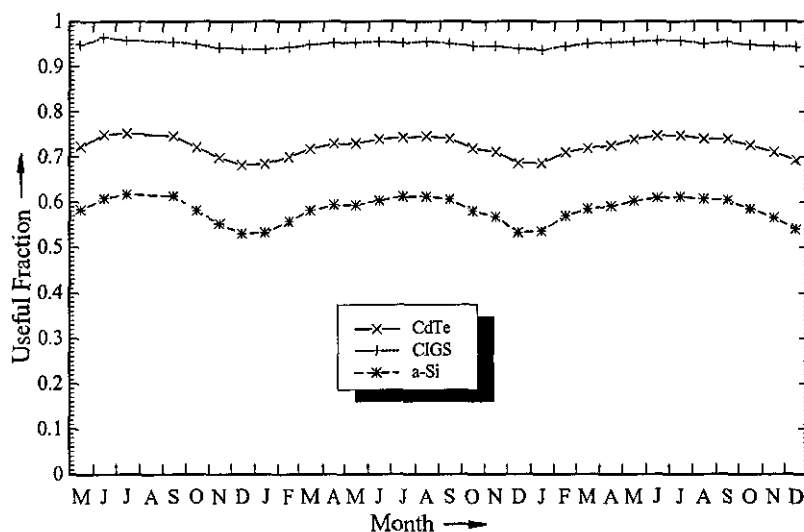


Figure 7.8: *Seasonal Variation of the Useful Fraction when Considering the Whole Spectrum.* The fraction of the irradiance, which is in the useful range for the given type of devices is plotted for each month.

Finally, the effect on the annual performance of thin film devices is investigated. Two common irradiance monitoring arrangements are considered in the following discussion, which will yield different results. Firstly, a system measuring the total global irradiance with a thermopile is considered (figure 7.8) and then the effect of replacing this thermopile with a silicon detector is investigated (figure 7.9). The difference is that, whilst a silicon detector responds only to spectral irradiance up to 1100 nm, a thermopile integrates over the complete spectrum.

It is apparent that the spectral effect for CIGS is negligible while it is strongest for a-Si, with CdTe being somewhere in between. All devices show an improvement of the useful fraction throughout the summer months. It is interesting to note that CIGS shows an inverted spectral effect when measuring with a Silicon detector as

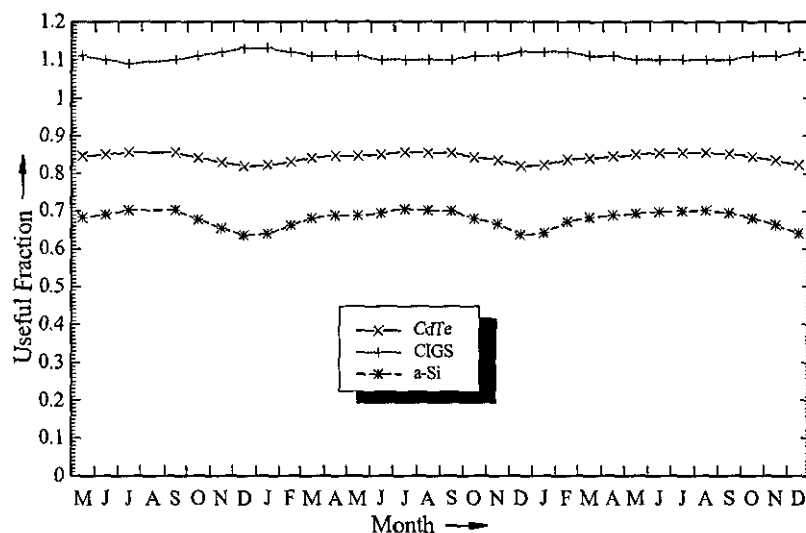


Figure 7.9: *Seasonal Variation of the Useful Fraction when Measuring with a Silicon Detector.* The percentage of the irradiance, which is in the useful range for the given type of devices is plotted for each month.

shown in figure 7.11. This emphasises the importance of appropriate measurement devices for PV system monitoring.

The reason that no seasonal improvement was reported except for a-Si devices, is due to the other materials being more susceptible to thermal effects. There are two reasons for this: firstly, the band gap of a-Si is larger than the ideal band gap of 1.4 eV calculated for terrestrial applications under AM1.5G [Green 92]. An increase in temperature will decrease the apparent band gap and thus the theoretical efficiency of the devices improves. Second, for good material properties, it can be expected that the effect of the degradation in electronic properties of a-Si devices with increased temperature is attenuated by the device structure, i.e. because they are drift driven devices, they can cope better with decreased electronic properties. Neither of the other thin films has a drift driven current and thus the effect of increased device temperature which goes along with increased irradiance levels will counteract this improved performance.

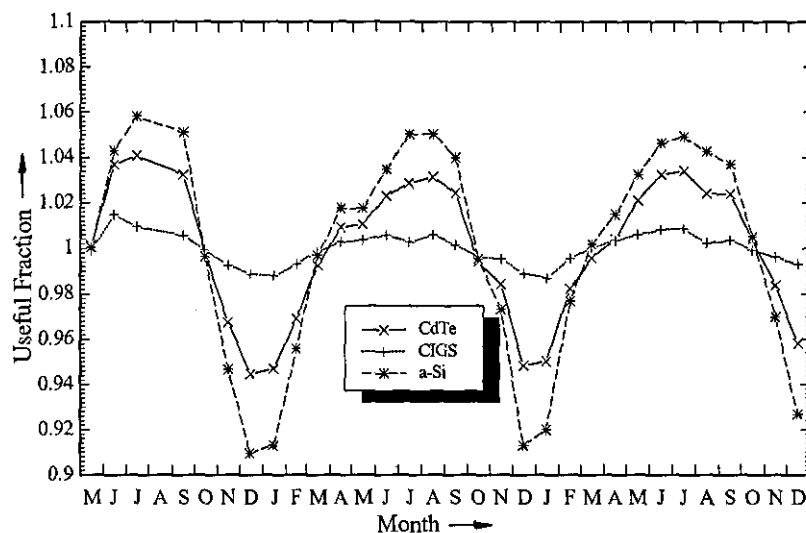


Figure 7.10: *Relative Seasonal Variation of the Useful Fraction when Measuring the Whole Spectrum.* The fraction of the irradiance in the useful range for the given devices is plotted for each month.

The magnitude of the useful fraction when measuring with a thermopile is plotted in figure 7.10. The effect for CIGS is less than $\pm 1.5\%$ with respect to the annual average. The spectral effect is more pronounced for CdTe, as could be expected from the band gap and the spectral responsivity shown in figure 7.1. The effect ranges from $+4\%$ to -6% around the annual average. The seasonal variation of useful fraction is strongest for a-Si where it ranges from $+6\%$ to -9% .

There is an apparent difference between measurements taken with a thermopile and a silicon detector, as can be seen from figure 7.11. As expected, the spectral effect is inverted for CIGS, thus the relative efficiency for CIGS would, compared with a silicon diode, increase in winter time. Interestingly, the seasonal spectral effect is even stronger than for measurements with a thermopile, only it is inverted with an increased useful fraction in winter time. This is down to the fact that c-Si devices are also prone to seasonal variation and are more affected than CIGS. The effect for CdTe and a-Si is less pronounced when measuring with a c-Si detector

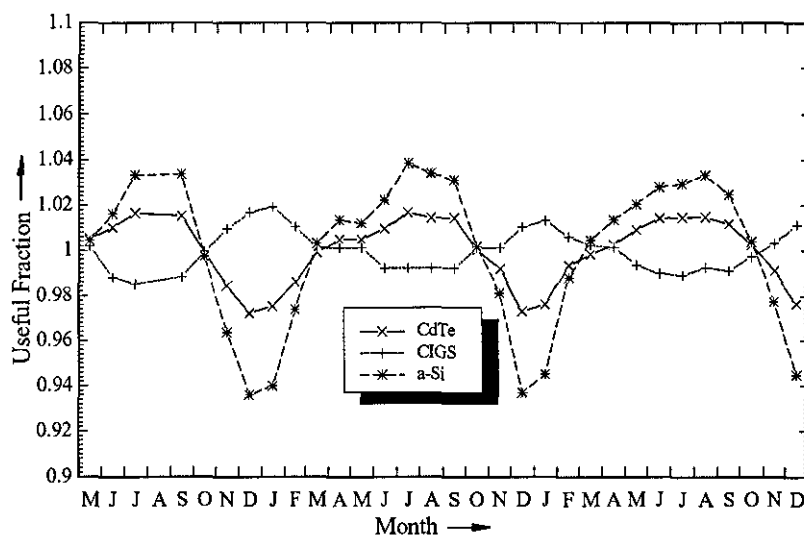


Figure 7.11: *Relative Seasonal Variation of the Useful Fraction when Measuring with a Silicon Detector.* The fraction of the irradiance in the useful range for the given type of devices is plotted for each month.

(reduced by roughly 30%).

7.5 Conclusions

It is clear from the presented results that the performance of thin film solar cells will be, to a varying degree, influenced by daily and seasonal variations in the incident solar spectral content. The change in the useful fraction is more influenced by the weather than by the air mass. In the course of the day, the spectrum shifts towards the blue because of increased absorption (probably due to increased water vapour in the atmosphere) and thus the useful fraction tends to increase. The variation of the useful fraction can be used to explain some of the unusual effects identified, particularly for a-Si systems.

On an annual basis, the most affected thin film material is a-Si. It is estimated that the useful irradiance for a-Si varies from +6% to -9% with respect to the annual average. CdTe and CIGS vary in the range of +4% to -6% and $\pm 1.5\%$ respectively

around the annual average. The effect is only fully apparent if the total irradiance is measured with a thermopile. Measurements with a silicon detector will not only reduce the apparent magnitude of the effect for CdTe and a-Si, it will even inverse the effect for CIGS. The variation of the spectral irradiance could also explain some seasonal effects reported on CdTe, e.g. by del Cueto [Cueto 98].

This chapter has shown the importance of considering the seasonal variation of the spectral irradiance, although this is not done to date for normal system sizing approaches.

Chapter 8

Outdoor Performance

8.1 Introduction

The outdoor performance of thin film solar cells can be very different to the performance of conventional devices. A-Si in particular exhibits a peculiar performance characteristic, as shown in figure 8.1. The graph shows the efficiency of two systems operating at LEEE-TISO in Canobbio in Switzerland¹. The maximum efficiency of the a-Si system is seen in summer rather than in winter, and this is so far not completely understood. The behaviour of c-Si devices, which exhibits the highest efficiencies in winter, when the operating temperature is low, is included for comparison. The magnitude of the effect of the c-Si system appears to be larger than for the a-Si system, but that might be a device specific behaviour. It was shown by Eikelboom and Jansen [Eikelboom 00] that different a-Si modules show a very different response to environmental conditions and thus the magnitude of the effects shown in figure 8.1 should not be taken as definite for all devices within the respective technology groups (i.e. a-Si and c-Si). It is, however, clear that there are significant differences between technologies.

¹Data courtesy of N. Cereghetti, TISO

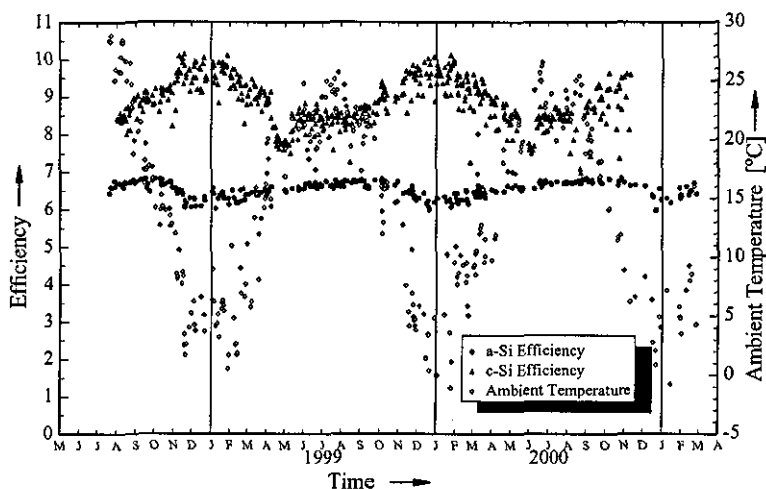


Figure 8.1: *Seasonal Variation of the Noon Time Efficiency of an a-Si and a c-Si System.* The shown systems are both installed at LEEE-TISO in Canobio, CH. Days with conditions close to STC are chosen.

This chapter aims to illustrate these by analysing the data collected during the measurement period from October 1999 to July 2000. The analysis presented here differs from analysis presented by other authors (e.g. del Cueto [Cueto 98], Strand et al. [Strand 95] or Chenlo and Vela [Chenlo 91]) in that it also considers spectral effects. This chapter is restricted to the discussion of the performance parameters of the different devices, a modelling approach is given in chapter 9. The variation of the performance indicators is not fully understood, as different researchers present different results. Again, a-Si has had the majority of the attention to date, as it is the most common thin film material.

The study most similar to the work presented in this chapter was carried out by Hirata et al. [Hirata 95, Hirata 98], who observed the performance of a-Si, CdTe and c-Si devices in Japan. They also reported the spectrum being a significant contributor to higher summer efficiencies of a-Si, despite the fact that the elevated operating temperature during the summer months. The magnitude of the effect is

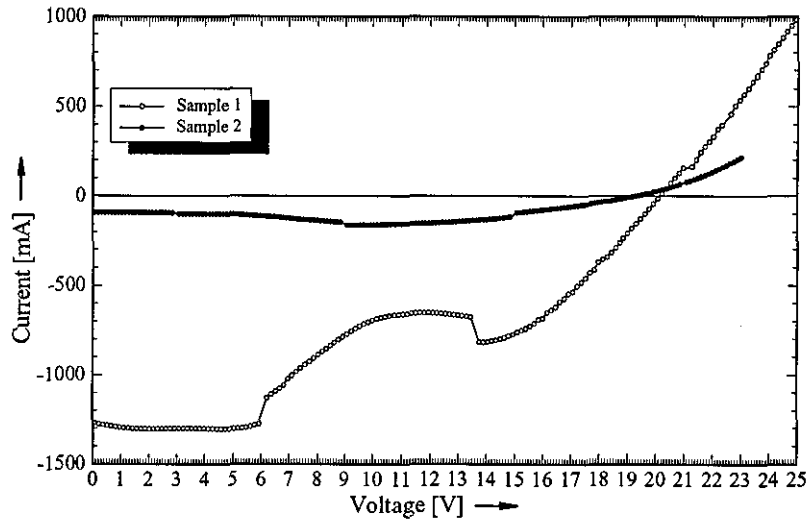


Figure 8.2: *Influence of Moving Clouds.* The graph shows two measurements in the same timestep influenced by moving clouds.

similar to the magnitude found in this study, but the explanation given in this work will be different, mainly based on the higher resolution of the spectral irradiance and different climate in the UK. Furthermore, it will be shown in section 8.4 that using only the availability of spectral irradiance for investigating spectral effects, as done by Hirata et al. [Hirata 98], is not applicable for double junction devices. As with all outdoor measurements, the conditions vary during the measurement process. The variation during a measurement period was restricted to a maximum of 5% from the average irradiance at the given time step, which was determined by the measurements taken before and after measuring a sample. This reduces the scatter but is not necessarily perfect. Figure 8.2 shows two examples of the influence of a passing cloud in the same time step. Sample 1 experienced a brighter spell in the middle of the 5 seconds measurement time. Towards the end, another cloud was moving in and, by chance, the irradiance at the end of the measurement period is nearly exactly the same as in the beginning. This behaviour could not be detected with the simple scatter limitation implemented and would have gone

unnoticed in the curve analysis. Another interesting curve was recorded in the same time step as shown by sample 2. The variation in the irradiance would have been strong enough to be detected by the scatter limitation but this would not have indicated the severity of the distortion of the curve. The distortion in the middle part of the curve is due to a cloud moving over the measurement setup. The discontinuity is due to the power supply sending data to the PC in 50 points intervals, thus having a short interruption in the measurement procedure. Despite this being less than half a second, it has an obviously significant impact on the overall measurement accuracy.

The problems of the setup are, however, evened out by the large number of measurements taken for each sample. There will be some scatter, but general trends are well described as shown below.

8.2 Measurement Environment

The measurement environment is of immense importance when investigating the performance of solar cells. Thin film solar cells especially are prone to spectral influences and to a varying degree to other environmental effects, as shown in the previous chapters of this work. Thus, an overview of the environmental conditions experienced during the measurement campaign is given in figure 8.3. The data shown here is for the aSi5 sample, as it was a sample operating during the whole measurement campaign. The bin size was 50 W/m² global irradiance, 5 K device temperature and 0.05 % for the useful fraction.

The data presented in figure 8.3 confirms some of the prejudices about the weather in the UK. More than 25% of the measurements were conducted at irradiance levels of less than 100 W/m². The frequency of high irradiances is relatively low but all levels of irradiance observable at other test centres were experienced. There is a

notable reduction in the number of measurements below 50 W/m^2 , where other groups typically report an increase of the number of measurements. The reason for this is the exclusion of all measurements below 10 W/m^2 , as done in the previous chapter for the exclusion of possibly erroneous spectral readings. Furthermore, many of these measurements would occur during sunset or sunrise, i.e. at times when the 5% scatter minimum is often breached due to fast changing irradiance conditions.

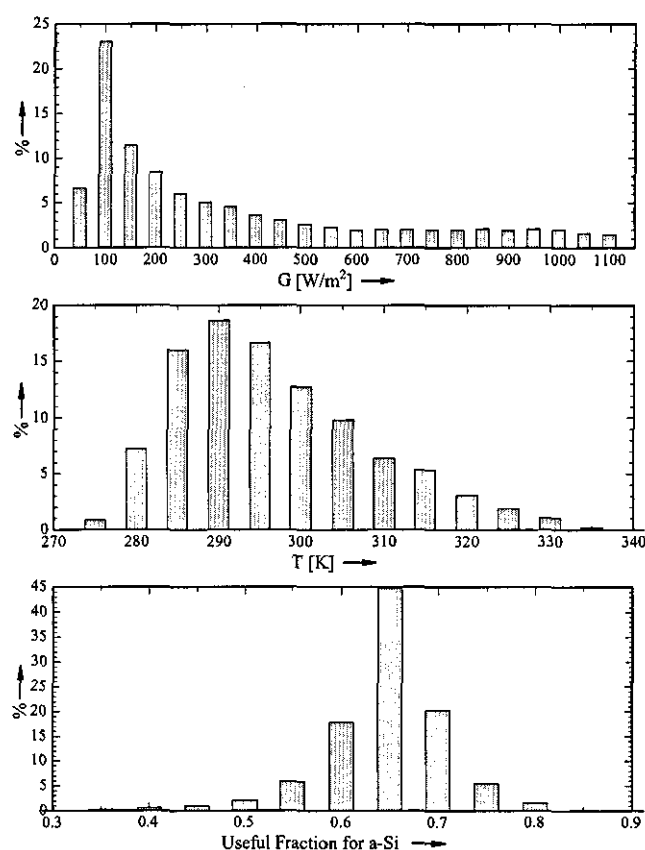


Figure 8.3: *Histograms of the Environmental Conditions.* The graph shows the relative number of measurements conducted in the given range. The useful fraction is given for an a-Si device.

The temperature range is rather limited and without extremes. It is neither very cold nor very hot. Temperatures of less than 2°C (275 K) are very rare indeed as are operating temperatures of more than 60°C (333 K). The vast majority of the

measurements in this campaign was conducted in the range 280 - 300 K, which is relatively cool compared to data presented by other researchers (e.g. [Rüther 99]). The variability of the spectrum is shown in the last plot in figure 8.3. The useful fraction is defined in chapter 7, as the ratio of irradiance in the spectrally active region over the total irradiance in the measurement range. It is emphasised again, that the maximum wavelength in this system is 1700 nm. The ratio for a-Si (max. wavelength of 790 nm) is about 63% for the standard AM1.5 spectrum as given in [Wenham 94]. Thus 45 % of the measurements are conducted at conditions very close to it. There is, however, a significant variation in the spectrum, as shown in figure 8.3. This allows an investigation of the influence of the spectrum on the overall performance, as done below.

8.3 Stability of Measurements

The first question to be investigated was the stability of the devices, as this has a significant bearing on the overall results. The variation of the efficiency of the devices is shown in figures 8.4 and 8.5. No selection criteria such as minimum irradiance levels or maximum device temperatures were applied, hence a large scatter can be expected. The specific reasons for the scatter will be investigated in the following sections.

It showed that the method used at CREST for encapsulation was not appropriate for the OEM modules. Nearly all of them suffered from contact with the environment. The worst affected sample is the CIGS1 sample, which immediately exhibited signs of degradation. Looking at the development of the shape of the curve, as shown in figure 8.6, it is apparent that the shunt resistance increases continuously and thus the problems can most likely be attributed to water ingress shunting out the device. This is unfortunate, especially as it was not immedi-

ately obvious and was only discovered at a later stage in the monitoring process. The modules aSi3 and aSi4, which were encapsulated by this method showed a rather sudden onset of the problem. Module aSi5 is the only fully manufacturer encapsulated device and did not show any signs of failure during the measurement campaign.

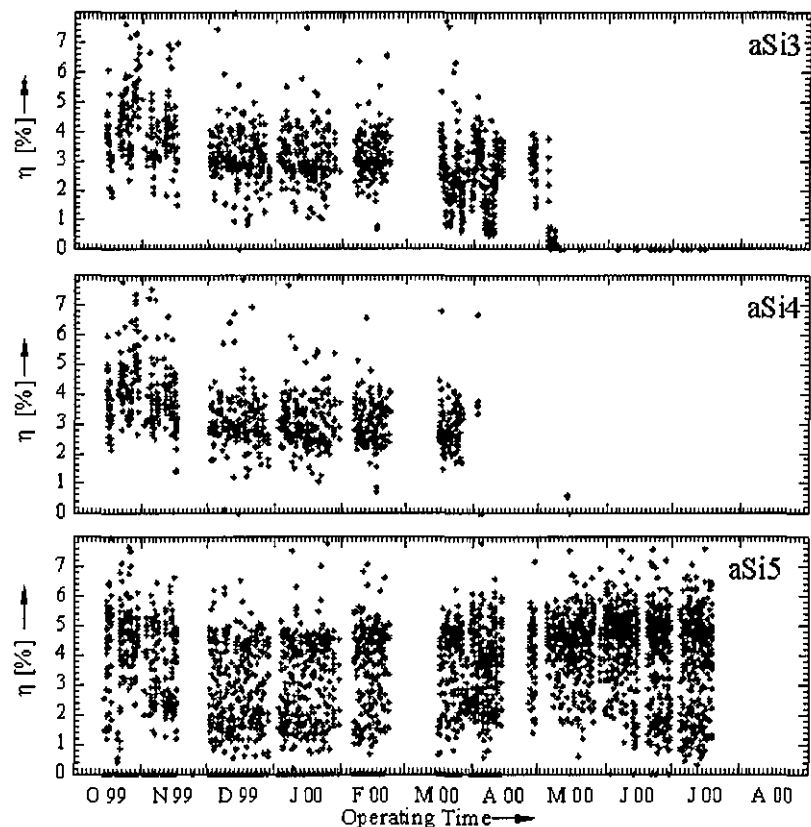


Figure 8.4: *Time Development of the Efficiency of the a-Si Modules.* The figure shows the variation of efficiencies during the measurement campaign, illustrating the relatively large band width which is investigated in this section.

Some seasonal trends can be identified for the a-Si samples from the data presented. All samples show some degradation in the initial period, however with different magnitudes. The mini-modules aSi3 (double junction) and aSi4 (single junction) exhibit the strongest degradation but performance is relatively stable after 3 months of operation. It is interesting to note that there is no notice-

able difference between the two samples. The lack of difference is in accordance with results presented by von Roedern et al. [Roedern 95], who found that the degradation depends more strongly on the manufacturing process than on the device structure. Both samples were produced by the same manufacturer and thus employ the same manufacturing technology. Unfortunately, an extension of the measurement campaign was not feasible, as the small samples failed and data collection could not be continued. Sample aSi5 is produced by another manufacturer and apparently was predegraded and did not show such a pronounced degradation in the beginning. Seasonal effects are apparent for the aSi5 sample as reported e.g. by Camani et al. [Camani 98] or R  ther [R  ther 99]. The aSi3 double junction exhibits the onset of the seasonal recovery pattern, while the single junction aSi4 does not show this recognisably. This highlights the differences between different materials and that it is not possible to make general statements to date. However, a continued degradation after the initial degradation period as reported by Mrig et al. [Mrig 87] could not be identified. All modules show a wide spread in their efficiencies, which is due to the environmental conditions discussed in the following sections. Sample aSi5 shows an especially significant range, which will be explained in section 8.5. These kinds of effects are, however, not unique to thin film solar cells, they are also observed for commercially available crystalline devices.

The polycrystalline devices did not show as clear a trend as the a-Si devices, as apparent from figure 8.5. Both devices tested exhibited degradation during their operation, which can be attributed to insufficient sealing. The CIGS sample exhibits the most pronounced deterioration, completely unrelated to the technology and contrary to findings of Strand et al. [Strand 95]. It is purely related to the contacts being too exposed and a shunt current building up over time. This can be seen from the change in the shape of the I-V characteristic depicted in figure

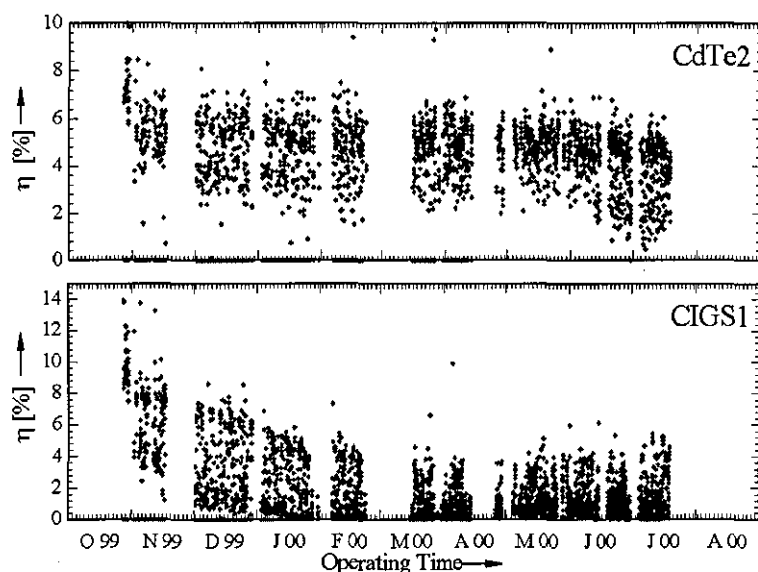


Figure 8.5: *Time Development of the Efficiency of the Polycrystalline Modules.* The figure shows the variation of efficiencies during the measurement campaign, and the influence of insufficient sealing.

8.6. It is supported by the fact that the short circuit current was relatively stable over the time of measurements, as shown in section 8.4.

The CdTe2 device showed a very stable operation in the initial time of the measurements reported here, at a later stage it also suffered environmental degradation. It is also apparent that there are no significant seasonal variations in the behaviour of the device, it performed at similar efficiency levels in summer as well as in winter. Again a significant spread of the operating efficiencies is seen.

The reasons for the degradation and/or device failure can be identified by investigating the shape of the I-V curve at different stages of the life of the sample. The I-V curves measured at noon time at the beginning of the measurement period are compared with measurements towards the end of the period of operation in figure 8.6. Figure 8.6 does not show any curves for the aSi3 sample, as the variation is very similar to the aSi4 sample. No particular care was taken to find

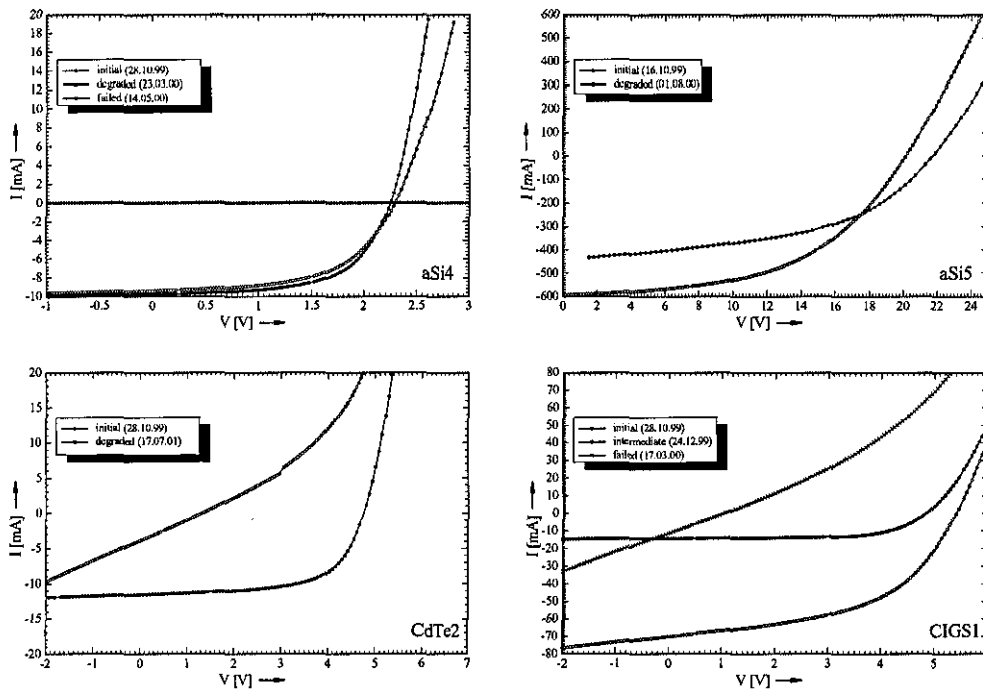


Figure 8.6: *Variation of the Shape of the I-V Characteristic with Time.* The figure shows the change of the form of the I-V characteristic for all 4 technologies investigated.

identical irradiances, as the aim of this graph is simply the identification of the reasons for failure. It is also nearly impossible to find matching spectral irradiances for a similar time of the day in a short period of time at the beginning or end of the measurement periods. The a-Si mini-modules aSi3 and aSi4 showed a flattening of the curve which can be observed by investigating the fill factor, as done in section 8.5. However, the overall performance was very good up to the point when the devices failed abruptly and completely. The final failure was intermittent in the beginning, in the sense that it appeared as an on/off switch, either the measurement was very good and the device showed a good performance or the measurement failed completely. The failure mode can be attributed to a loss of contact at the terminal. In the given case it is most likely due to ingressing water dissolving the water soluble solder. This solder was used because of a

recommendation of the manufacturer of these specific devices.

The problems with the CdTe and the CIGS devices could be due to similar problems, although the solder was not water soluble and thus no complete loss of contact occurred. The effect of the invading water most likely became apparent by building up a shunt path, apparent from the decreasing shunt resistance of the devices. This shunting could have occurred either across the contacts or across the sides of the device. This shows in the significantly increased slope at I_{SC} . The onset in all devices was rather sudden (with the exception of the CIGS sample), which leads to the belief that the initial sealing was appropriate but the silicon sealant used did not withstand the climate sufficiently. Future experiments should either use a better method of sealing or rely on manufacturer sealed devices.

8.4 Short Circuit Current

The short circuit current of a device is directly linked to the irradiance and can be calculated as:

$$I_{SC} = \int_{\lambda=0}^{\lambda_{\max}} E(\lambda) S(V=0, T, \lambda) d\lambda \quad (8.1)$$

where E is the energy of the incident light and S is the spectral response at the given wavelength. This implies a linear relationship with irradiance. The temperature variation is device dependent, namely on the variation of the band gap and the spectral response with temperature. This is normally simplified by the assumption of a linear temperature coefficient. The relation commonly used for modelling the I_{SC} is thus:

$$I_{SC} = (C_0 + C_1 T) G \quad (8.2)$$

where C_0 in $\left[\frac{m^2}{V}\right]$ and C_1 in $\left[\frac{m^2}{VK}\right]$ are empirical parameters. The parameters C_0 and C_1 must be positive to make sense physically. They can be determined by dividing the measured short circuit current by the incident irradiance and fitting a straight line to the resulting points. This is done here for the total irradiance (marked "total" in the following plots) using the irradiance measured with the Kipp and Zonen thermopile as well as using the radiation in the useful spectral range (marked "spectral" in the following plots). The number of points in the plots presented in the following was reduced by only plotting every fourth point, in order to make the graphs easier to visualise.

The general influence of considering only the irradiance in the useful spectral range is illustrated in figure 8.7, where data is plotted versus the data measured with the thermopile (left) and versus the spectrally useful irradiance as measured with the spectroradiometer (right). The larger scatter in the spectrally corrected measurements is due to the operating time of the spectroradiometer, which is much more prone to the influence of moving clouds as illustrated in figure 8.2. There is, however, a large enough number of data points to give a good illustration of the effects observed.

Figure 8.7 shows an increased slope for the data of a CdTe₂ sample measured with the spectroradiometer compared to the data measured with the pyranometer. Furthermore, the maximum irradiance is significantly less for the data measured with the spectroradiometer. This can be expected, as only a certain percentage of the light is considered when correcting for the spectrum.

Equation 8.2 implies that plotting $\frac{I_{SC}}{G}$ against the device temperature and least

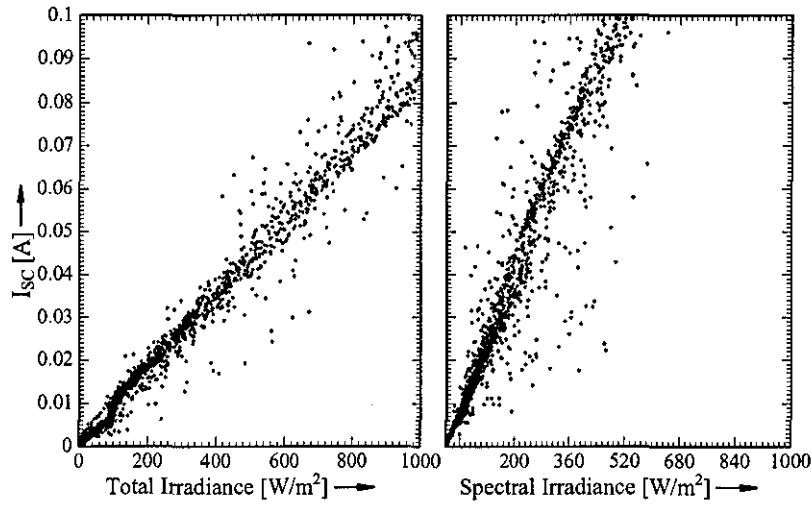


Figure 8.7: *Influence of Spectral Correction.* The graph shows the influence of correcting the incident spectrum for the useful incident irradiance for the CdTe2 sample.

square fitting a line should result in the coefficients. This plot is shown for the CdTe2 sample in figure 8.8. It is apparent that the slope of the global plot is negative, a result which appears to be unintuitive at first sight and is investigated further. This would imply a negative temperature coefficient C_1 with increasing temperature, which would correspond to an increase in the band gap with temperature, clearly not the result expected from physics.

A negative temperature dependence of the short circuit current is also not reported in the literature. Hence, the negative slope must be the result of some other effect. This is used in the following to emphasise the superposition of the different environmental effects on the device performance.

The negative slope in figure 8.8 could be due to a degradation in time or a non-linearity of the photocurrent with irradiance. Measurements started, as apparent from figure 8.5, in October 1999. Thus high temperatures will be experienced in the later stages of its operating life and thus degradation could be a factor. High temperatures are also invariably linked with high irradiances levels and thus a

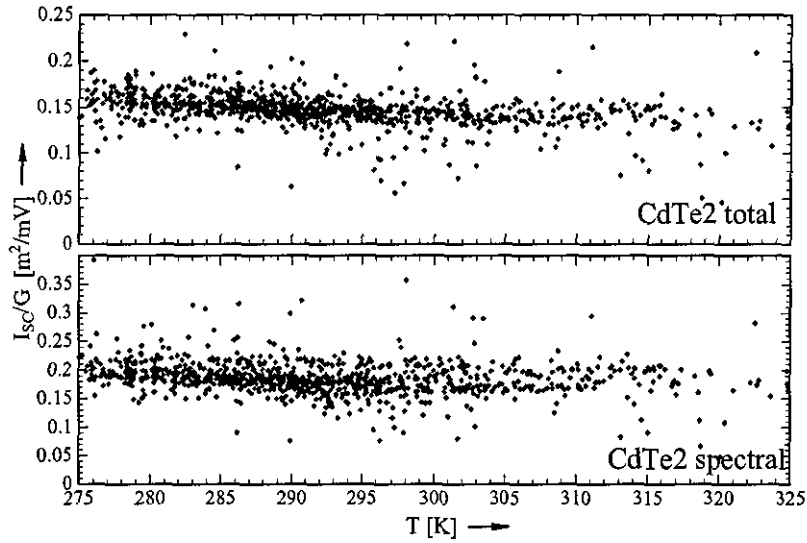


Figure 8.8: *Temperature Dependence of I_{SC} of the CdTe2 Device.* The trend is clearly negative, which is not physical.

current limiting effect could result in a negative slope in figure 8.8.

The variation of the $\frac{I_{SC}}{G}$ fraction with irradiance is investigated in figure 8.9. The ratio of $\frac{I_{SC}}{G_{glob}}$ exhibits a strange hook shaped dependence for irradiances up to 150 W/m^2 . A higher point number would show this region as a cloud of measurements. Beyond the 150 W/m^2 , there appears to be a small negative trend in the short circuit current. The widening for lower irradiance levels was also reported by del Cueto [Cueto 98], but he found a small dip in the short circuit current around 200 W/m^2 and a constant photocurrent afterwards. The large amount of scatter for lower irradiances is due to the fact that the incident spectrum is more variable for lower irradiances. As shown in chapter 7, a low clearness index increases the content of high energy (blue) light but on the other hand, a high air mass reduces the amount of blue light available. Both effects can be responsible for low irradiance levels and thus cause the increased scatter. The spectral analysis exhibits a negative trend for increasing irradiance. This slight reduction in the $\frac{I_{SC}}{G}$ ratio is one of the reasons for the negative temperature coefficient. Indeed, using

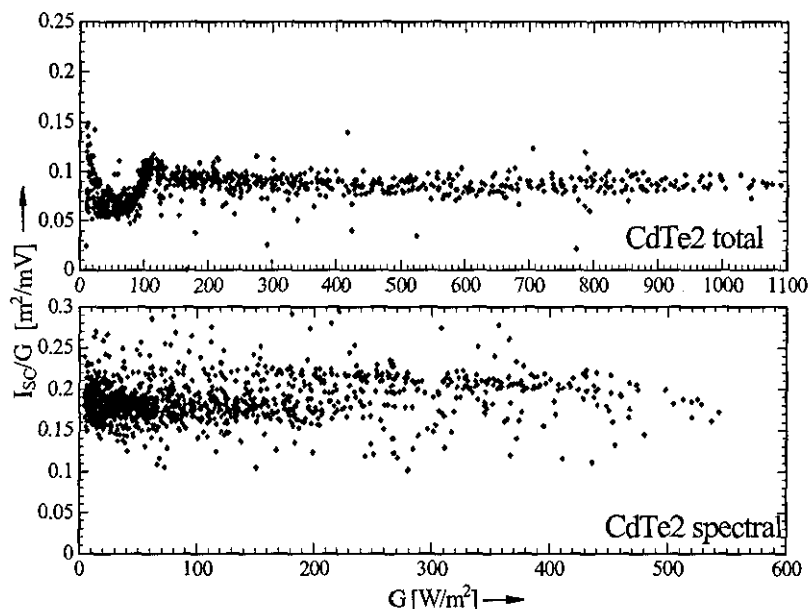


Figure 8.9: *Behaviour of I_{SC} with Irradiance.* There appears to be a spectral effect for lower irradiances, which is explained in the text.

binned radiation gives a positive temperature coefficient in an analysis analogous to figure 8.8.

The influence of the spectrum goes even further, it can explain the negative slope shown in figure 8.8. It was shown in chapter 7 that there is a daily and seasonal cycle in the useful fraction of irradiance for the different devices. It will be later shown that this negative slope observed in figure 8.8 is unique to the CdTe sample, hence a look is taken at the absorption properties of the different materials. Figure 8.10 compares the quantum efficiency, i.e. the number of electrons generated for each incident photon, for different materials.

There is a significant difference between the CdTe device and the other devices under investigation, which is apparent in wavelengths below 600 nm. This explains the negative temperature effect demonstrated in figure 8.8. High temperatures tend to occur in conjunction with high irradiances, typically around noon time. It was shown in chapter 7 that a low air mass causes a "bluer" light, i.e. shifting the

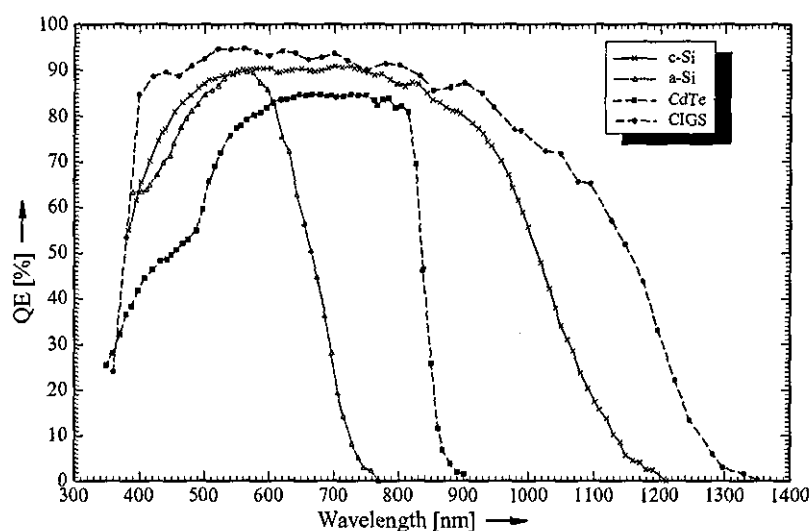


Figure 8.10: *Quantum Efficiency of Common Photovoltaic Devices.* The graph compares the region of useful irradiance to illustrate the explanation of material differences given in the text.

spectral distribution of the irradiance towards the spectrally less efficient region of the CdTe device. The air mass will be at its minimum in the daily cycle at the solar noon, which coincides with higher temperatures. This effect is not apparent for other devices, as they do not exhibit such a significant loss in collection efficiency at the blue end of the spectrum.

The other possibility for a negative temperature coefficient of the $\frac{I_{sc}}{G}$ ratio is its stability. This is investigated in figure 8.11. Here, spectral effects become apparent, because the ratio based on total irradiance shows an improvement during summer time which is not apparent in the plot using the spectral irradiance. On the contrary, the spectral plot reveals, after an initially stable performance, a slight degradation. This will to some extent contribute to the negative temperature coefficient found, as higher irradiance levels are typically associated with the summer months, when degradation is already apparent from the spectral plot. This trend could also be found by a drift in the instrumentation but following

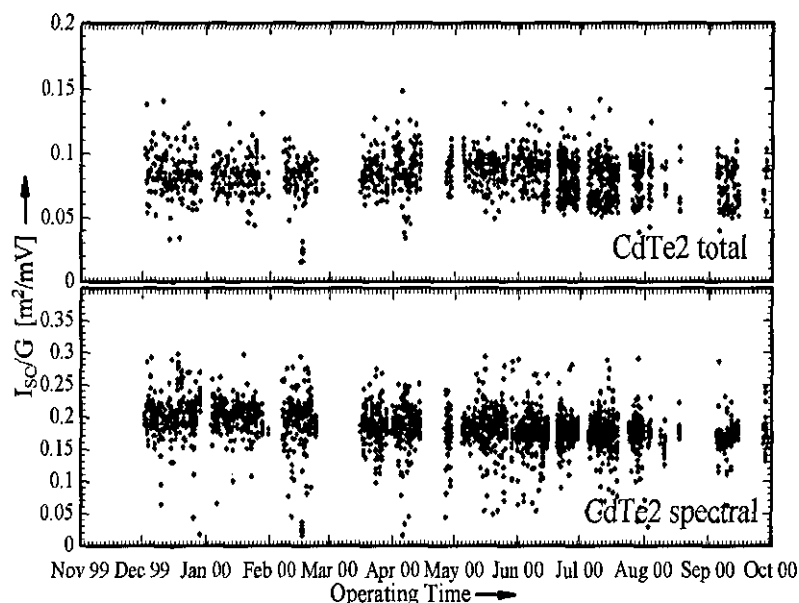


Figure 8.11: *Stability of $\frac{I_{sc}}{G}$ with Time Considering Total and Spectral Irradiance.* The global plot exhibits a seasonal pattern, while the spectral plot reveals a slight degradation.

tests, this can be excluded. Furthermore, a similar trend was observed by other researchers [Jardine 01] for this particular device, reducing the possibility of this being a measurement artifact of the system used for this work. Hence there is a slight degradation with time for the investigated sample, which is not necessarily due to our encapsulation method, as the samples tested by Jardine [Jardine 01] are full size modules. Further tests with additional samples will have to investigate the reasons for this. The slight improvement in the summer time, when considering total irradiances was predicted in chapter 7 and is thus expected, albeit the magnitude is much less severe than suggested. The larger scatter when considering the global variation is also to some extent expected, as cloud cover will change the spectrum significantly. The relatively narrow width of the spectral plots also indicates that there are no further spectral effects, as e.g. shown below for multi-junction devices.

The degradation in the spectral plot will be the cause of the negative temperature dependence shown in figure 8.8. It would not be apparent if the spectrum had not been determined, as seasonal changes in the spectrum mask the reduction in the collection efficiency.

The stability of $\frac{I_{SC}}{G}$ for the other devices in the outdoor test is visualised in figure 8.12. It shows that the global and spectral collection efficiency of the CIGS1 sample is relatively stable over time. This emphasises the fact that the problems were not material dependent. There is hardly any seasonal variation, as predicted in chapter 7. The widening of the scatter towards the end of the measurement period indicates that there seems to be a progression in the deterioration in the shunting problem and some improvements in a daily cycle, which would be consistent with the suggested water ingress. At high temperatures any water might be heated out and the device performance improves. In rainy days or at cold temperatures, this is not the case and thus the device performance worsens.

All amorphous samples show a seasonal variation in their global $\frac{I_{SC}}{G}$ ratio, as predicted in chapter 7. Unfortunately the single junction aSi4 sample failed at an early stage so the recovery cannot be observed. The recovery is very pronounced in the aSi5 sample, and consistent with changes in the spectrum. When considering the spectral irradiance the seasonal improvement is either ameliorated or completely gone. Comparing the spectral results of the single junction device (aSi4) with those obtained for double junction devices (aSi3, aSi5) shows that the simple picture of using irradiance in the spectral range is more appropriate for the single junction as the amount of apparent noise is significantly less for this type of device. This shows that for double junctions there is an even stronger dependence on the spectrum than the variation in the useful fraction.

This spectral effect is investigated in figure 8.13. Here the average $\frac{I_{SC}}{G_{spec}}$ ratio was determined by the ratio of the sum of all measured $\frac{I_{SC}}{G_{spec}}$ values to the number of

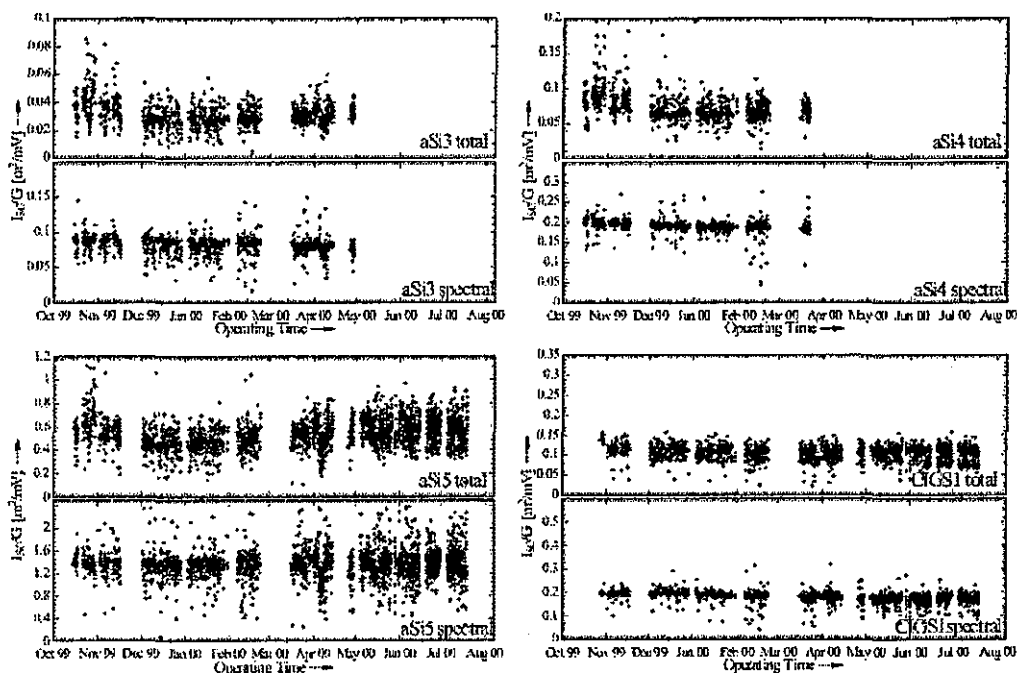


Figure 8.12: *Stability of the Short Circuit Current of the Tested Samples.* The graph compares the behaviour in time of the spectrally corrected and the global short circuit current.

measurements. The relative value of the fraction is then plotted against the useful fraction apparent during the measurement, which can be seen as a measure of the variation in the incident solar spectrum. The devices compared in figure 8.13 are a double junction (aSi3) and a single junction device (aSi4), both produced by the same supplier, thus employing the same manufacturing technology. There is hardly any variation in the relative $\frac{I_{SC}}{G_{spec}}$ ratio for the single junction device, across the whole range. A significant spectral effect as suggested by R  ther et al. [R  ther 01] as an explanation of the behaviour of the fill factor cannot be observed. The difference for the centre values can be attributed to variations in the device temperature and different degradational states.

In contrast to this, the double junction exhibits a visible slope towards lower "blueness" of the light, a plateau around the useful fraction of 65% and then a slight

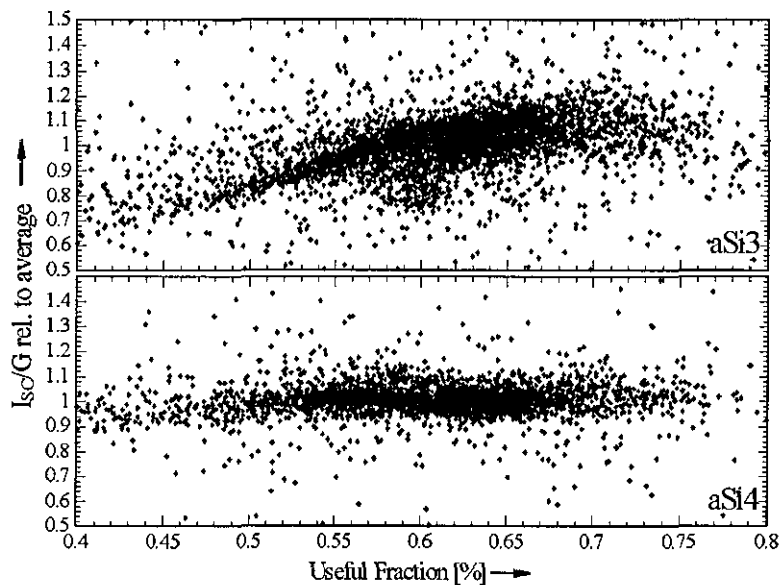


Figure 8.13: *Influence of the Spectrum on the $\frac{I_{sc}}{G_{spec}}$ Ratio.* The graph compares the variation of the $\frac{I_{sc}}{G_{spec}}$ ratio with respect to its average for a single and a double junction device in dependence from the spectrally useful fraction of the irradiance.

decline again for very red irradiance. This is a secondary spectral effect, which is due to the cell structure. It can be understood when considering the double junction as two cells connected in series with one another. The current through both cells will, according to Kirchhoff's law, have to be identical. Hence the short circuit currents of both devices are matched, normally for AM1.5 conditions.

A variation in the spectral composition will change the absorption of the light in the stack of cells that the light generated current in one cell will be larger than the light generated current of the other cell in this stack. The currents are no longer matched. A shift towards the blue will cause the upper cell of the stack having a higher short circuit current than the lower one, a shift towards the red will result in a higher short circuit current in the lower cell. The cells are mismatched and the excess energy will have to be dissipated and thus the overall short circuit current is reduced. This explains the slope for lower useful fractions of the double junction.

The wide scatter in the middle range can be explained in that the mismatch is not large for these spectra and thermal effects will also contribute to the magnitude of the effect. It is, however, clear that the modelling of the performance of double junction devices will need more sophistication than the suggested simple useful fraction model.

The variation of the short circuit current with incident irradiance is shown in figure 8.14. All amorphous silicon devices show a slight increase of the $\frac{I_{sc}}{G_{glob}}$ ratio towards higher irradiance levels. This can be expected, as these are typically associated with summer months and thus with a low air mass. It was shown in chapter 7 that a low air mass results in very "blue" irradiance. The scatter towards the lower end of the irradiance levels can be expected again due to the variation in atmospheric conditions discussed already. It is interesting to see, though, that the hook shape at the very low end gets masked by a bend in the samples aSi3 and aSi4. Those two samples also exhibit the strongest degradation, as shown in figure 8.4 and thus this bend might be due to the degradation in the short circuit current. The double junction a-Si devices show a small change in slope at around 600 W/m^2 . This bend is not a spectral effect, as it also occurs in the spectral plot to some degree. It occurs, however, only for the double junctions and hence it can be assumed that it is an effect due to variations in the absorption behaviour as shown in figure 8.13.

There is a small reduction in the short circuit current of the CIGS1 device but that is most likely due to the degradation of the short circuit current shown in figure 8.12. All samples show this hook shape for low irradiance levels.

The description using the spectrally useful fraction does work to a varying degree for the samples shown in figure 8.14. It works best for the single junction a-Si which shows a nearly straight line. The positive slope towards higher irradiance levels, as exhibited by the plot using the total irradiance, is not apparent any more,

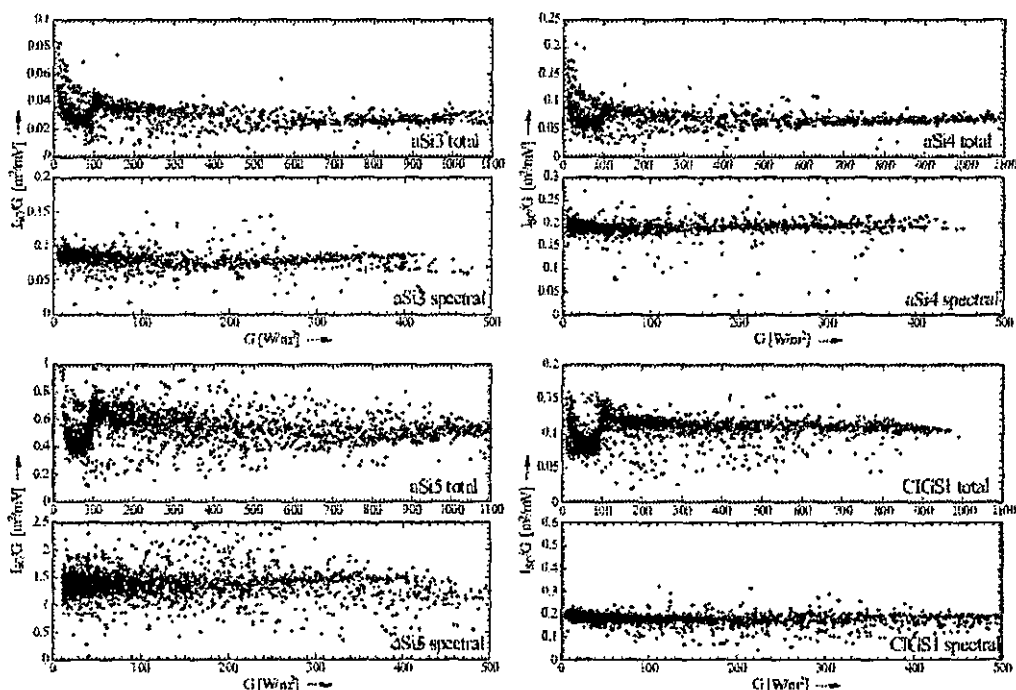


Figure 8.14: *Irradiance Dependence of the Short Circuit Current of the Tested Samples.* The graph compares the variation with irradiance of the spectrally corrected and the total short circuit current.

confirming that this is a spectral effect. The agreement for the double junction devices is not as good, resulting in a slightly negative slope for high irradiance levels, rather than a positive slope. This can be understood when associating the higher irradiances with low air mass conditions, where the incident irradiance is "bluer" than AM1.5 used for the current matching of the devices. It is noticeable that all a-Si devices show a slightly negative slope for low irradiance conditions, before recovering at the knee at around 600 W/m^2 . This trend can be associated with the irradiance, on average, being "bluer" because clouds act as an infrared filter. The trend is not completely eradicated for the double junction devices but significantly ameliorated. The remaining influence is most likely an effect of the current matching of these devices.

The spectral plot for the CIGS1 device depicts a relatively large amount of scatter,

which is most likely due to the fact that CIGS has the largest spectral range and thus the measurement of the spectral irradiance is most affected by the time it takes to record the spectroradiometer data. Furthermore, it is the only device that uses spectral irradiance beyond the 1100 nm range and thus the detector in the spectroradiometer has to be changed during the measurement, increasing the measurement time even further. This may give rise to increased cloud effects, thereby explaining the scatter.

From the data shown in figures 8.12 and 8.14 there are many influences and modelling the short circuit current using the simple formula given in equation 8.2 will not necessarily involve positive coefficients as other effects such spectrum, irradiance level and degradational state are inseparably linked to the short circuit current. The plot of the $\frac{I_{sc}}{G}$ ratios for the different samples is shown in figure 8.15. Using the spectral plots sometimes reveals a very different picture to the global plots. The double junctions aSi3 and aSi5 show a significant scatter of the $\frac{I_{sc}}{G}$ ratio for the lower levels of irradiance, indicating that the temperature most likely is not the main influence here. This is confirmed by the spectral plots, where the scatter is largely reduced, despite the otherwise larger scatter of the spectral plots. The scatter towards lower irradiances determines the overall slope and that might very well be negative. The aSi3 sample additionally suffers from the lack of high irradiance measurements as it failed in April 2000. A higher number of high irradiance measurements might have changed the slope slightly.

The CIGS1 sample exhibits a negative slope which again is marked by the scatter at the low end of the irradiance scale. There even appear to be two lines (and a lot of scatter in between), indicating that there was an influence in time, which reduced the overall $\frac{I_{sc}}{G}$ ratio, which is due to the progressing degradation shown in figure 8.5.

The spectral plots provide additional information. The slope here is for all devices

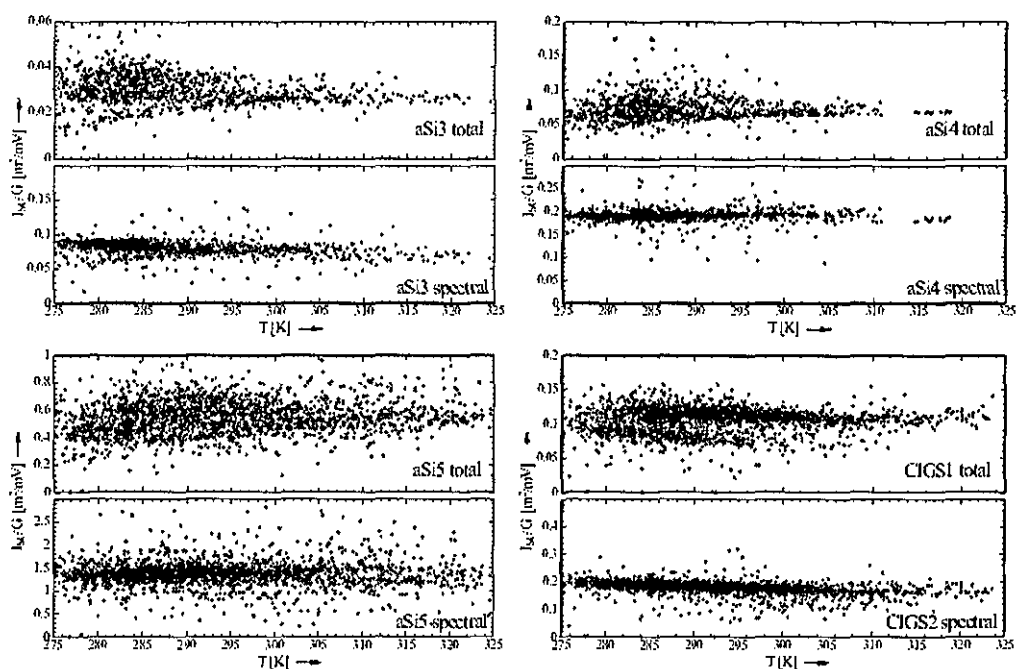


Figure 8.15: *Temperature Dependence of the Short Circuit Current of the Tested Samples.* The graph compares the variation with temperature of the spectrally corrected and the global short circuit current.

except for the single junction aSi4 device, negative. It is surprising that even the double junction devices exhibit a significant reduction in scatter-width of the plot. The difference between the single junction and the double junction devices is most likely due to current mismatch effects which are a result of different spectral conditions. The negative slope is most likely a result of negative dependence on the spectral irradiance shown in figure 8.14 for lower irradiances, keeping in mind that the majority of measurements were, as shown in figure 8.3, conducted at low irradiance levels.

The parameters for equation 8.2 are summarised in table 8.1. The negative parameters were explained previously and should be accepted as a result of an empirical model which is too simple to model all the different effects.

The global coefficients in table 8.1 show mostly positive values. The value for

Cell Type	$C_{0t} \left[\frac{m^2}{V} \right]$	$C_{1t} \left[\frac{m^2}{VK} \right]$	$C_{0s} \left[\frac{m^2}{V} \right]$	$C_{1s} \left[\frac{m^2}{VK} \right]$
aSi3	5.12E-05	7.36E-08	1.57E-04	-2.65E-07
aSi4	2.36E-05	1.69E-07	1.45E-04	1.61E-07
aSi5	3.42E-05	1.73E-06	1.61E-03	-8.509E-07
CdTe2	2.47E-05	-2.09E-07	4.56E-04	-8.84E-07
CIGS1	8.151E-05	8.07E-08	4.5E-04	-9.27E-07

Table 8.1: Coefficients of the Short Circuit Current of Different Devices.

the CIGS1 sample would have been negative if it had not been for low intensity effects. A similar behaviour was reported by Strand et al. [Strand 95]. It was, however, shown that these parameters strongly depend on the measurement environment and are not really suitable for the calculation of the short circuit current at different locations in the world. They are applicable as long as there are no significant effects of the irradiance intensity and no noticeable spectral effects. Neither is the case for thin film solar cells and thus these parameters using the total irradiance should not be used for site specific performance calculations, as they depend strongly on the local conditions. The spectral values initially appear to be surprising because of the negative slopes but these are the result of effects of irradiance dependence and stability of the collection efficiency, which is not apparent when looking at total irradiance only. These spectral parameters are significantly less site specific than the ones referring to total irradiance and thus should be used for the investigation of the performance at different sites.

8.5 Fill Factor

The fill factor is an important physical property of the device and it will be clear from the discussion in this section that it determines the device performance to a large extent. It is defined in chapter 2 as:

$$FF = \frac{V_{MPP} I_{MPP}}{V_{OC} I_{SC}} \quad (8.3)$$

The dependence of this is very material specific, as I_{MPP} depends strongly on the recombination current, shunt and series resistance. Predicting V_{MPP} is similarly difficult and thus no precise predictions can be made on the dependence of the fill factor on the environmental conditions. It does, however, give an indication of the performance of a device.

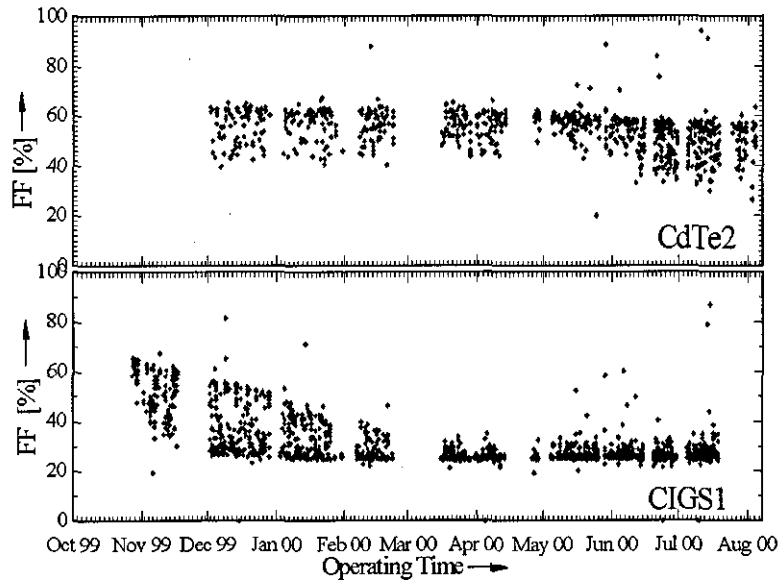


Figure 8.16: *Variation of the FF of the Polycrystalline Devices.* The figure depicts the variation of the FF with time.

The FF can give an indication of problems with devices. This can be seen in figure 8.16, where the evolution of the fill factor with time is plotted for the polycrystalline devices. The range of the daily FF variation is due to other environmental factors and is similar to the variation in the efficiency, but it is clear that for both samples the maximum achievable fill factor is reduced towards the end of

the operation of the devices. In the case of the CIGS device it even collapses on a daily basis, until it is as low as 20%. The CdTe sample operates in a relatively stable manner, but towards the end of the period, a deterioration is observable. There is no pronounced seasonal variation, which agrees with the findings of del Cueto [Cueto 98]. The reason for this reduction in the fill factor becomes apparent when studying the evolution of the shunt resistance, as shown in figure 8.17.

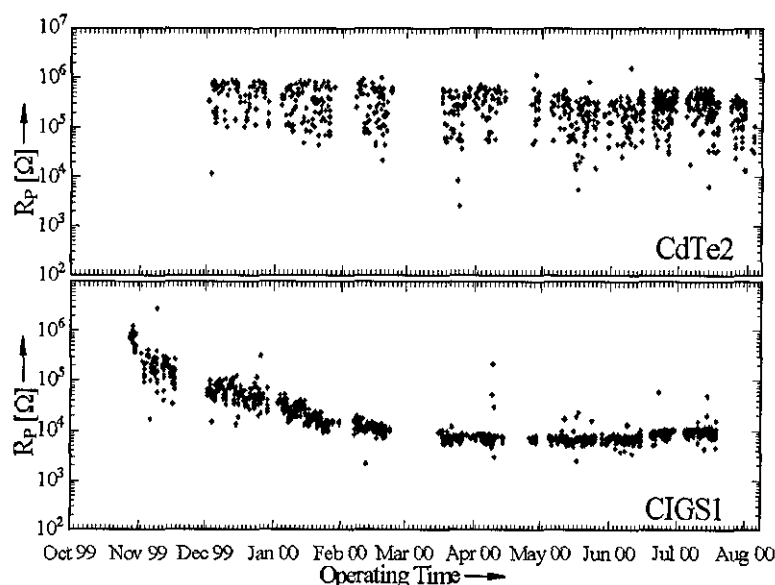


Figure 8.17: *Variation of the Shunt Resistance of the Polycrystalline Devices with Time.* The graph illustrates the relative reduction of shunting resistance of the devices over the operating time.

There is a significant daily variation for the shunt resistance of the CdTe2 device, an indication that there is an intensity or temperature dependence of this resistance, which would be consistent with the presence of a non-ohmic back contact. The daily variation of the CIGS device is significantly lower, but the evolution in time shows the reason for the problems of the device: The shunt resistance is reduced on a daily basis, indicating an increase in shunting, which in return causes the reduction in the fill factor observed in figure 8.16. The most likely

reason for this rapid loss of shunt resistance is the accumulation of dirt and salts due to ingressing water. The shunt resistance is reduced by nearly three orders of magnitude, which explains the rapid degradation of the device performance.

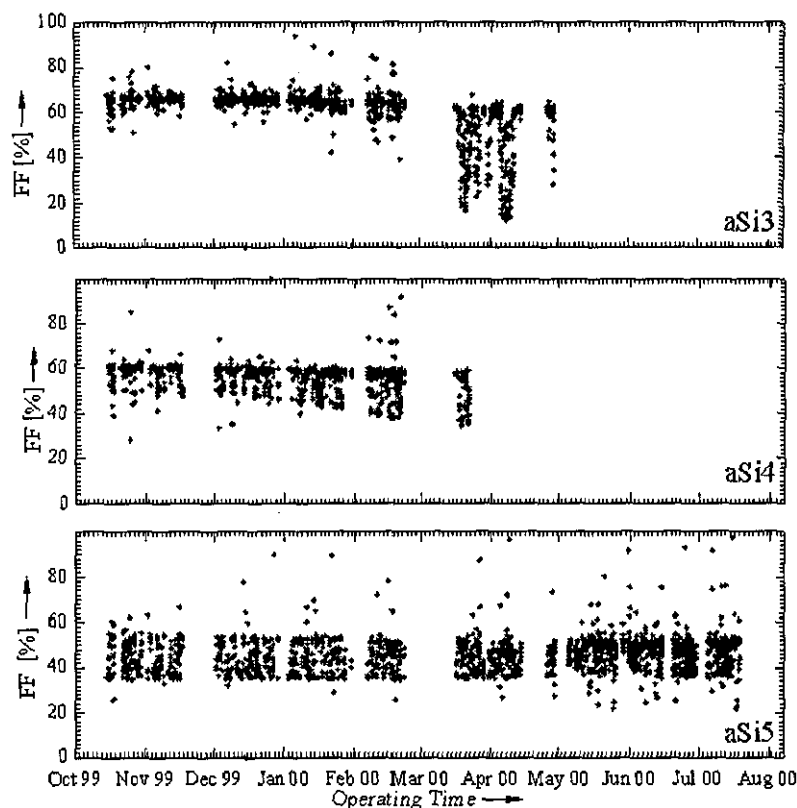


Figure 8.18: *Evolution of the FF with Time of the aSi Devices.* The fill factor is rather stable in the time of operation for all devices. The dependence on environmental conditions is significantly stronger than any influence of degradation.

The amorphous devices show a very stable fill factor during the measurement campaign, as illustrated in figure 8.18. There is a small increase in the FF in the winter months, which will be investigated further.

The FF analysis of aSi3 shows the onset of the water ingress, which is linked to a significant decrease in shunt resistance, as shown in figure 8.19. Samples aSi4 and aSi5 show a stable seasonal behaviour. The width of the daily variation is due to the daily variation in irradiance and temperature. The lack of significant

seasonal changes in the FF was also reported by Merten and Andreu [Merten 98a] and Ichikawa et al. [Ichikawa 87]. Thus, this appears to be a general feature, indicating that the seasonal changes are mainly due to the variation in the short circuit current shown in section 8.4. These findings correlate well with work carried out by Rüther and Livingstone [Rüther 94] or Vela et al. [Vela 94], who report the lack of a seasonal change in efficiency when measuring the devices in a simulator rather than in outdoor conditions.

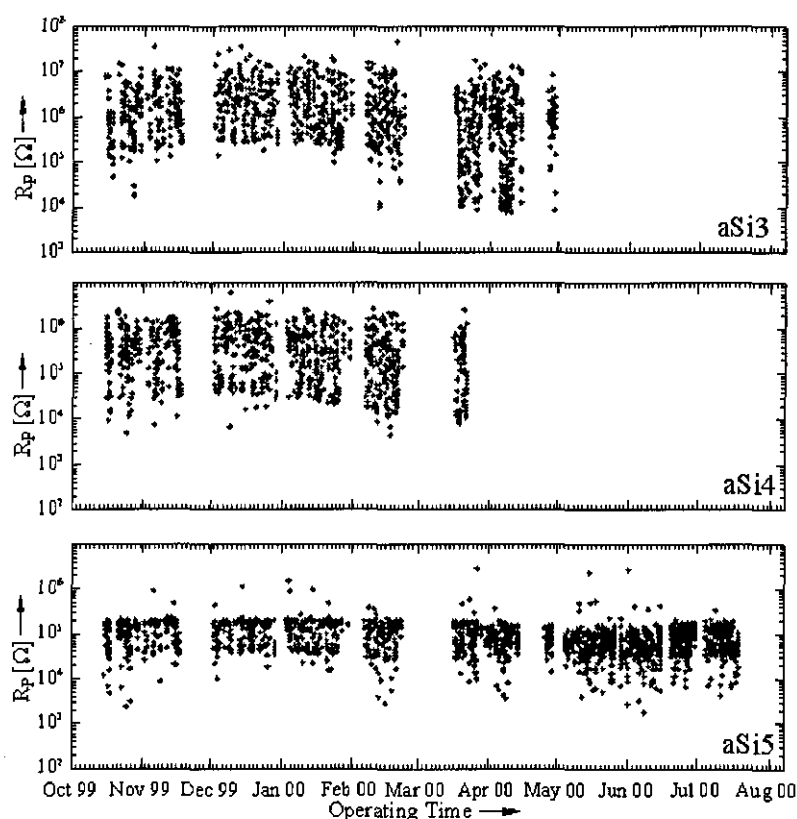


Figure 8.19: *Evolution of the Shunt Resistance with Time of the a-Si Devices.* The width of the band indicates that there is a significant environmental influence. The behaviour of R_P mirrors that of the FF.

There is, however, a significant difference between the polycrystalline devices shown in figure 8.16 and the a-Si devices shown in figure 8.18. While there is only a minimal seasonal variation in the FF, there is an appreciable seasonal vari-

ation of the shunt resistance, as shown in figure 8.19. All tested samples show that the shunt resistance is higher in winter than in summer time. This means that there must be an environmental influence on this property, which might not result in an appreciable variation in the FF. This can be attributed to the exponential decrease of the shunt resistance with increasing temperature, as shown for these devices in chapter 6.

There are three possible environmental influences on the FF, namely temperature, irradiance and spectrum. The spectral influence can be excluded when referencing to the short circuit current rather than to the irradiance, as it was shown in section 8.4. This does not fully exclude any secondary effects, but the primary effects, which are based purely on the available amount of light, are excluded.

The seasonal variation in figure 8.18 suggests that there is an influence of either irradiance or temperature on the overall FF. The presence of a voltage dependent photocurrent in a-Si suggests that, at least for these samples, the irradiance might have a larger influence. Thus, this is investigated first.

There are three main device specific influences on the fill factor: the shunt resistance, the series resistance and recombination processes. The shunt determines the slope around I_{SC} , as long as the principle of superposition holds. If there is an additional influence on the photocurrent which breaches this principle, this will have an additional influence on this slope. In a very simplistic way, the shunt resistance is determined as the slope of the I-V characteristic at short circuit conditions. In the case of a-Si, this is an approximation only, as a-Si does not have a constant photocurrent and the voltage dependence of the photocurrent will also have an influence on this resistance. A non-ohmic back contact, as reported for CdTe in chapters 3 and 6, will also affect this slope. The series resistance, depending on the level of irradiance, influences strongly the behaviour at V_{OC} . Thus the resistance R_{OC} at V_{OC} can give some indications of the underlying reasons for the

device behaviour. The evolution with increasing short circuit current is shown for all devices in figure 8.20.

There is an apparent difference between the behaviour of aSi3 and aSi4 with respect to the other devices. These devices do not show a pronounced knee in the FF for low light intensities. These devices also have the highest shunt resistance while the behaviour of the resistance at V_{OC} is similar for all devices, hence it appears that the main reason for this exceptionally good low light behaviour is the high shunt resistance. It is not a technology specific feature, as the other a-Si sample in the test exhibits a knee towards low intensities. Thus it is mainly dependent on the manufacturing process and the elimination of shunt paths..

Both samples, aSi3 and aSi4, are produced using the same technology but are double and single junctions respectively. Both devices show a similar behaviour in the first month of operation but a marked difference in their FF after 6 months of operation. While the original FF is reduced by roughly 10% (from 70% to 60% in the case of aSi3 and 65% to 55% for aSi4), there appears a significant reduction with irradiance for degraded modules, as much as 18% for the single junction sample aSi4.

A reduction of the FF with irradiance is a commonly reported feature, it was reported for a-Si by R  ther [R  ther 01] and Merten [Merten 96]. The reduction of the FF is due to an increasing influence of the shunting, as seen in figure 8.18. This increase in the shunt current can be expected when investigating the voltage dependent photocurrent as detailed in chapter 3. The voltage dependence of the photocurrent will have a stronger influence for higher levels of irradiance and thus the apparent shunt resistance will decrease. Furthermore, higher irradiance levels are inseparably linked with higher operating temperatures and these also result in a reduction of the shunt resistance, as shown in chapter 6. Thus this general reduction in the FF is explained by this model. The behaviour of the devices aSi3

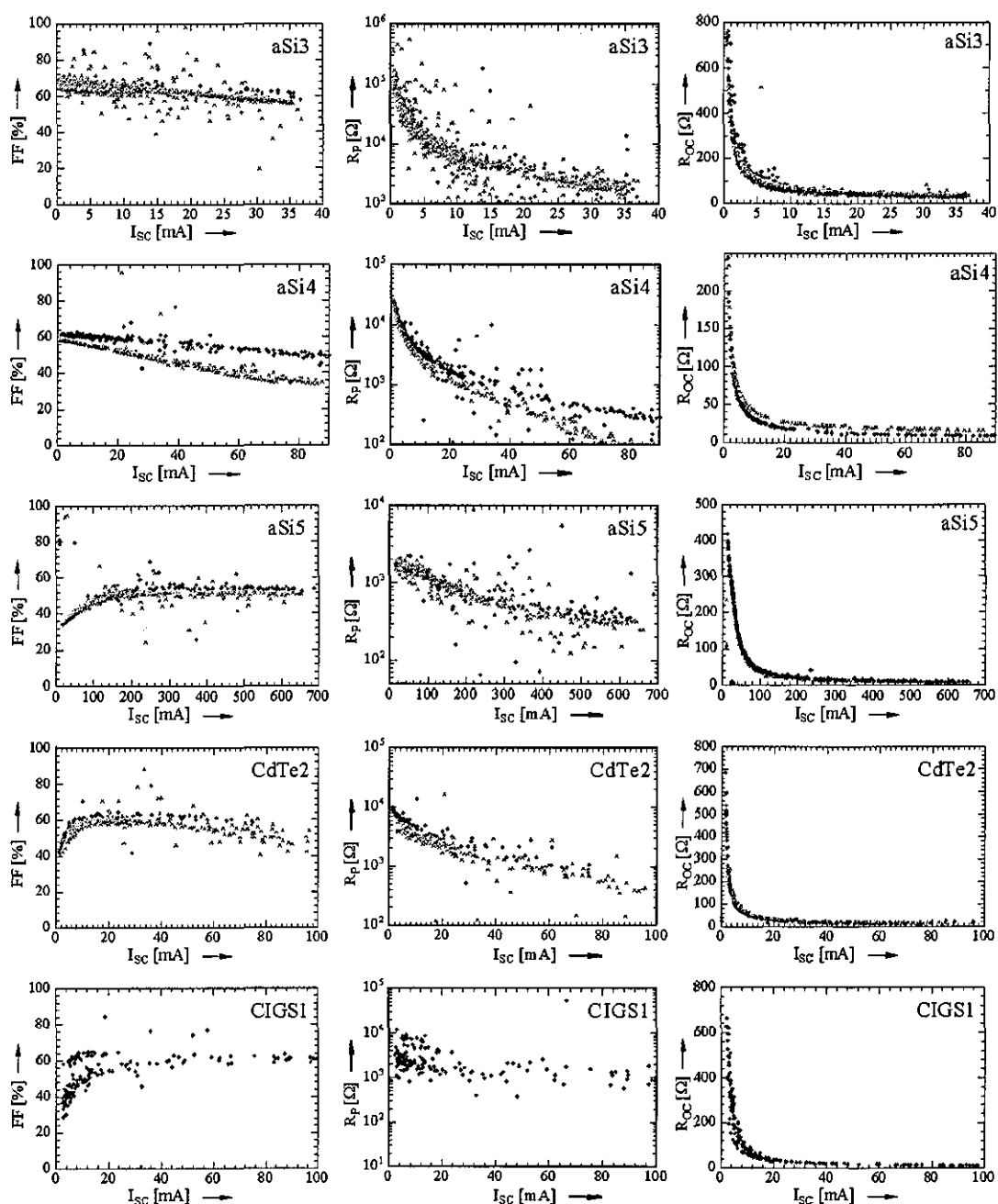


Figure 8.20: *Influence of Irradiance on the FF, R_P and R_{OC} .* The variation of the FF with irradiance is illustrated together with the influencing resistances. Data collected in the installation month is indicated by a diamond, data after 6 months of operation is marked with crosses.

and aSi4 is thus dominated by the voltage dependent photocurrent, as apparent from the very rapid reduction in the shunt resistance. The FF is not significantly influenced yet, which explains the lack of a knee in the FF-G relation, mainly due to the very high initial values. In fact, the knee does occur, but only at very low irradiances (3-7 W/m²), which are filtered out in this analysis.

Merten and Andreu [Merten 98a] suggest that the behaviour at I_{SC} is entirely dominated by the material properties. They suggest a model as:

$$R_P = I_{ph} \frac{\mu\tau}{d_i^2} V_{bi}^2 \quad (8.4)$$

The assumptions are reasonable as long as the influence of the parallel resistance is negligible, i.e. the parallel resistance is very large. This is true for the majority of irradiance levels, but strongly influenced by the operating temperature. This gives an explanation for the behaviour of the a-Si modules shown in figure 8.20. The influence of Staebler-Wronski degradation will manifest as a reduction of the lifetime-mobility product, which will cause a stronger voltage dependence of the photocurrent, thus the reduction of the FF will be reduced. This trend is generally observed, as it is a direct result of a decrease in the lifetime-mobility product, as illustrated e.g. by Coors et al. [Coors 98]. This explanation is supported by the reduction in R_P shown in figure 8.20.

These considerations show that the lower fill factors in figure 8.18 are linked to high irradiance levels. It also explains the widening of the range achieved during the course of the day, as apparent from figure 8.18. The comparison of the samples shows that the reduction of the fill factor of the aSi3 sample is the lowest, while the aSi4 sample suffers more from degradation. The sample aSi5 is somewhere in between. The effect is crucial, as the reduction of the FF is highest for the highest

irradiance levels, i.e. the operating points where the device would produce the most power.

The indicator R_{OC} will be identical to R_P for dark measurements, which is immediately apparent, as V_{OC} is zero in this case. For infinite irradiance levels, R_{OC} will be identical with the series resistance. In the intermediate region, there is an influence of the diode current, which decreases with increasing irradiance. Thus the shape of R_{OC} exhibited by all devices in figure 8.20 is as could be expected. It is interesting to note, though, that the a-Si samples show an increase of the R_{OC} with time. This could indicate a slight deterioration of the contacting or, and this is more likely, an increase in the voltage dependence of the photocurrent.

The behaviour of the other a-Si device in the test is slightly different. This is due to a significantly lower shunt resistance, which incurs an increased shunt current. For low irradiance levels, the influence of the shunt resistance causes a significant reduction in the FF. This results in a reduction of the influence of the shunt current with increasing irradiances and thus an improved FF with increasing irradiance. The onset of the voltage dependent photocurrent is not as pronounced as in the samples aSi3 and aSi4. The sample aSi5 is the largest device in the test and thus effects such as inhomogeneities during the production process will have a significantly larger influence as well as the higher number of interconnected cells, which will to some extent mask the expected increase of R_{OC} .

There is, however, a difference between the irradiance dependence of R_{OC} of the different materials. The value for the a-Si samples appears to fall more slowly than the value for the polycrystalline samples. This can be understood by assuming that the end of the knee in the R_{OC} plots signifies that the knee of the corresponding I-V characteristic is now below zero (i.e. in the power producing quadrant of the I-V relationship). In a very simplified picture we have a nearly rectangular connection of the shunt resistance dominated part of the curve at I_{SC}

and the series resistance dominated part at high voltages.

Moving beyond the knee in the I-V characteristic generally signals that one is moving into series resistance dominated part of the curve. The difference between polycrystalline and amorphous samples is that the voltage dependent photocurrent of a-Si effectively increases the slope of the I-V characteristic at short circuit conditions. By doing so, the point where the series resistance starts dominating is moved towards higher currents in the forward biased region of the I-V characteristic and thus a higher irradiance is needed to shift this point of the curve into the power producing quadrant. Thus the point when the series resistance starts to dominate the R_{OC} is achieved for higher irradiance levels, the reduction in the R_{OC} values is slower for the a-Si devices. It appears that the CdTe sample exhibits the fastest drop in the R_{OC} value. This appears to be surprising, as it was stated earlier that a non-ohmic back contact will impact more strongly for higher irradiances and hence it should drop slower than the CIGS sample. One has to keep in mind, though, that the overall current around V_{OC} is rather small, hence the impact of a non-ohmic back contact is not too significant. This does not explain the relatively slow drop in R_{OC} , compared to the CIGS sample, yet. The behaviour of this value can be understood when associating higher temperatures with higher irradiance levels, as it is nearly always the case in outdoor operation. Having a limited impact of a non-ohmic back contact in the first place means that temperature induced changes will have a significant impact. It was shown in chapter 3 that the influence of a non-ohmic contact is reduced more than exponentially for increasing temperatures, i.e. the impact on the FF will reduce similarly. Putting this together with the low initial impact at V_{OC} explains the comparatively slow decrease in the R_{OC} value of the CdTe device.

The behaviour of the FF with irradiance of the polycrystalline devices is as expected. For low irradiance levels, the influence of the shunt resistance causes a

decrease in the fill factor. With increasing irradiance, the FF increases. The reduction in the fill factor of the CdTe sample can be attributed to the non-ohmic back contact, as higher currents will incur a higher voltage drop and thus a larger reduction in the fill factor. A similar behaviour was reported by del Cueto [Cueto 98] for a CdTe module, albeit without the knee at low irradiance levels. There is a slight deterioration of the FF in time, which could be a seasonal effect as reported by del Cueto [Cueto 98] or a sign of a small degradation as reported by Jardine [Jardine 01]. An investigation of the FF after six months for the CIGS sample was not carried out.

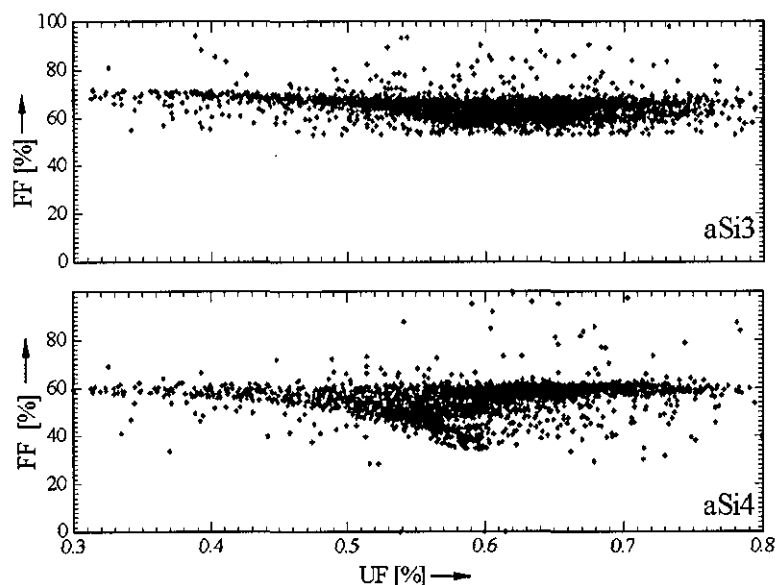


Figure 8.21: *Influence of the Useful Fraction on the FF of Two a-Si Devices.* The graph compares the different behaviour of a double and a single junction device.

In section 8.4 it was shown that different spectra have a significant influence on the short circuit current. In some cases, this can also be visible, as shown by R  ther et al. [R  ther 01], in the FF. Figure 8.21 shows the FF against the useful fraction of the incident spectrum. There is a significant difference between the behaviour of the aSi3 and aSi4 device. Only these two devices are considered here,

as they incorporate the same manufacturing technology. It is apparent from the analysis so far, that different technologies cannot be compared that easily. The calculation of a trend line for a-Si gives a correlation between the fill factor of this double junction FF_{dj} and the useful fraction UF as:

$$FF_{dj} = 70.03 - 10.15 \cdot UF \quad (8.5)$$

This means that the fill factor is reduced by 14.4% from a UF of zero to a UF of one. This is intended as a guide for the eye only, as significant scatter occurs towards higher useful fractions. However, contrary to this, the correlation for the fill factor of the single junction FF_{sj} is calculated as:

$$FF_{sj} = 41.93 + 22.06 \cdot UF \quad (8.6)$$

The positive coefficient is due to the bulging of the curve for mid range UF values. This is most likely due to other effects such as irradiance intensity and degradation, which affect this sample more than the aSi3 sample, as shown in figure 8.20. A reduction to a lower number of points would reduce the width of the useful fraction significantly and thus all points were used, and no filtering was carried out for irradiance levels or degradational state. However, regarding the shape of this curve as a triangle appears to be more appropriate, as it was shown in figure 8.20 that high irradiance levels are associated with low fill factors. This does not mean that high irradiances are associated with high useful fractions, because, as shown in chapter 7, a low clearness index can result in a high useful fraction. Thus it makes sense to consider the hypotenuse of the triangle only. This is essentially parallel to the axis, so the values for high and low UF values

are nearly identical. This signifies that there are hardly any effects observable for the single junction aSi4 while there is a pronounced effect for the double junction aSi3. Even considering only the upper boundary will result in a reduction in the FF with increasing "blueness" of the spectrum. Hence, there is a secondary spectral effect that does not only affect the I_{SC} but also affects the FF. This now poses the question as to why there are no steps in the I-V characteristic, as typically exhibited by mismatched cells. This is not detectable in the curves. An explanation would be that the high shunt resistance causes the step to be so close to the short circuit point that it is not recognisable in the measurements. Another possibility is that a-Si devices tend to exhibit a different reverse characteristic than c-Si devices [Alonso 98]. Furthermore, it could be possible that the change in the electron density within the device causes a change in the absorption profile that in return is responsible for a smoother curve. Hence the lack of an observable step does not disprove the existence of two mismatched cells, it just emphasises the problem of observing it experimentally.

The influence of temperature on the FF is illustrated in figure 8.22. It is apparent that a higher device temperature is nearly always associated with a higher irradiance level. It is also shown that a linear fit of the variation with irradiance of the FF results in a very good agreement with the measurements ($R^2=0.98$). This indicates that the irradiance dependence dominates the device behaviour. It is possible to correct for this irradiance dependence and then consider the scatter as being caused by the thermal variation. This does, however, not yield a sensible variation. The thermal variation will nearly vanish in the outdoor measurements, as the variation reported from laboratory measurements (see e.g. Eikelboom and Jansen [Eikelboom 00]) is below 2% of the FF, a value that is not measurable in outdoor arrangements.

Thus, the main impact on the FF of devices with a reasonable shunt resistance is

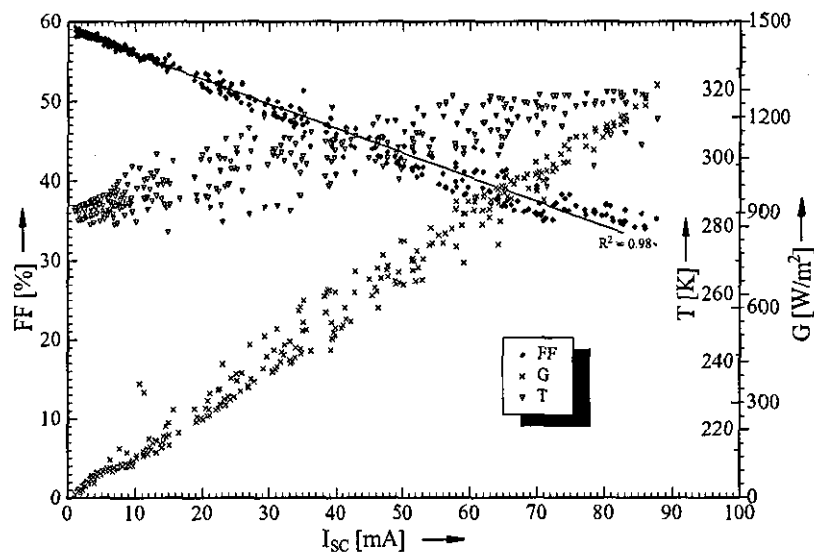


Figure 8.22: *Relation Between Device Temperature, Irradiance and Fill Factor.* The graph illustrates the behaviour of these variables for the aSi4 sample in March 2000.

the irradiance, as could be expected. The device physics determines the behaviour of this property as well as the manufacturing quality. Multijunctions exhibit a secondary spectral effect that is masked to some extent by the irradiance dependence but are also governed by the intensity of the irradiance. An outdoor variation is not measurable.

8.6 Open Circuit Voltage

The open circuit current depends on irradiance and temperature. This can be seen most easily when ignoring the losses due to the shunt resistance. For a good cell this is reasonable because the magnitude of the shunt current is marginal compared to the diode and the photo currents. The equation can then be written as:

$$I = -I_{ph} + I_{01} \left(\exp \frac{V_j}{nV_T} - 1 \right) \quad (8.7)$$

where V_T is the thermal voltage ($= \frac{kT}{e}$) and I_{ph} is the photocurrent in a general formulation. Neglecting the shunt current, a link between the short circuit current and the open circuit voltage can be established as:

$$I_{SC} = I_{01} \left[\exp \left(\frac{V_{OC}}{nV_T} \right) - 1 \right] \quad (8.8)$$

The open circuit voltage can then be calculated as:

$$V_{OC} = nV_T \ln \left(\frac{I_{SC}}{I_{01}} + 1 \right) \approx nV_T \ln \left(\frac{I_{SC}}{I_{01}} \right) \quad (8.9)$$

As it was shown earlier, I_{SC} depends linearly on the incident spectral irradiance. Hence, the dependence of V_{OC} increases with $\ln G$. This is true if there is no voltage dependent photocurrent, as this would introduce an additional voltage dependent term in equation 8.9. This behaviour is the basis of the varied irradiance measurements suggested by Merten et al. [Merten 97], which gives a very good approximation of the variables for constant temperatures. For very low irradiance levels, the V_{OC} is nearly exclusively dominated by the parallel resistance. The other extreme, very high irradiance levels, is nearly exclusively determined by the series resistance. In both cases the I-V characteristic will resemble a straight line in the power producing quadrant (although the current levels necessary to see the R_S domination are at a level that will cause significant current degradation). In between these extremes, the diode saturation current and, in the case of a-Si,

the voltage dependent photocurrent, will dominate the device behaviour. Equation 8.9 also gives an approximation for the temperature dependence. The temperature dependence should be linear if photocurrent and diode saturation current are temperature independent, which unfortunately is not the case. It also shows, however, that the thermal variation depends on the irradiance, therefore a clear separation is not possible and thus only data bins are investigated in the following.

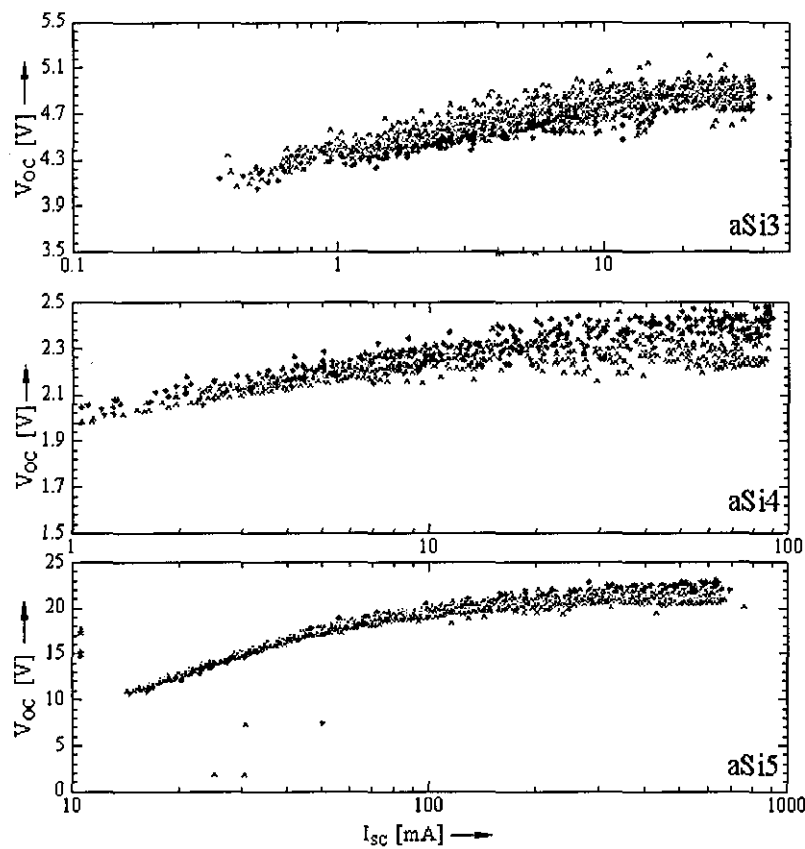


Figure 8.23: *Variation of the Open Circuit Voltage with Irradiance.* The logarithmic plot is used to identify the applicability of the model given in the text. The diamonds represent data collected in the first six month of operation, the crosses signify data collected after six months of operation.

Figure 8.23 shows the behaviour of the samples measured at CREST for irradiances above 10 W/m^2 in the first month of operation (diamonds) and after six

months of operation (crosses). All devices show a bending for higher irradiance levels, which is due to a more pronounced influence of the series resistance and the increasing influence of the voltage dependent photocurrent. Sample aSi5 especially shows the bending away from the logarithmic dependency relatively pronounced at short circuit currents around 30 mA. The reason for this is the more pronounced influence of the voltage dependent photocurrent and the higher series resistance which is shown in figure 8.20. Both effects are due to the size of the module and number of cells in series. The device also exhibits the largest variation in relative terms. This is most likely due to the higher shunting resistance exhibited by the device, which again can be attributed to the larger size of the sample. The size matters, as the lifetime-mobility product varies over a larger area and thus a larger area will nearly always have a lower effective lifetime-mobility product. The region of the V_{OC} - I_{SC} relation in which this bending occurs for all devices indicates that this is the influence of the voltage dependent photocurrent. The influence of the series resistance should, according to Merten et al. [Merten 97], dominate at higher levels of the curve.

Both double junction devices (aSi3 & aSi5) show a slight improvement in the open circuit voltage for lower irradiance levels with progressing degradation, an effect which was observed e.g. by Isomura et al. [Isomura 98]. However, the authors did not report an irradiance dependence of this phenomenon as apparent from figure 8.23. Following the arguments of these authors would indicate an increase in the flatband voltage due to the degradation. The irradiance dependence could then be explained by offsetting this with a decrease in the lifetime-mobility product which would result in a more pronounced reduction of the open circuit voltage at higher irradiance levels. It is apparent, however, that for irradiance levels above 100 W/m^2 , the open circuit voltage is reduced for all samples with the exception of the aSi3 sample, where V_{OC} is similar to undegraded values at high irradiance

levels. This highlights the difference between aSi5 and aSi3, which are both double junction devices. It also highlights that the device behaviour is not only governed by the structure but also by the manufacturing process, as also shown by von Roedern [Roedern 91]. The effect of degradation on the open circuit voltage of a single junction is, however, more pronounced than for a double junction. This is due to a larger impact of a reduction in the lifetime-mobility product. It was shown in chapter 3 that the photocurrent of a-Si devices can be modelled as:

$$I_{ph} = (C_0 - C_1 T) G \left(\frac{1}{\frac{\mu\tau}{d_i^2} (V_{bi} - V_j)} - 1 \right) \quad (8.10)$$

Assuming that the degradation of the lifetime-mobility product is the same for single as well as double junctions and that there is no appreciable change in the built-in potential shows that the impact of the degradation on a double junction will be roughly half that of a single junction, as the built-in potential is twice as high. This is, however, an estimation only, as there is an appreciable influence of the lifetime-mobility product on recombination as well.

The behaviour of the polycrystalline devices does not exhibit a bend as pronounced as the V_{OC} - I_{SC} relation of the a-Si devices. This is due to the absence of the voltage dependent photocurrent. The deviation from the predicted straight line at lower I_{SC} levels for the CIGS is due to the increasing shunt resistance. The CdTe device shows the onset of the influence of the series resistance at short circuit values around 60 mA. There is, however, a visible deterioration for the CdTe device, which occurs after 6 months of operation. The reason for this is a difference in the operating temperature. This is because the month of installation was December and thus the month ending the first six months of outdoor operation is May. Thus, due to seasonal effects, one can expect higher operating temperatures and thus a

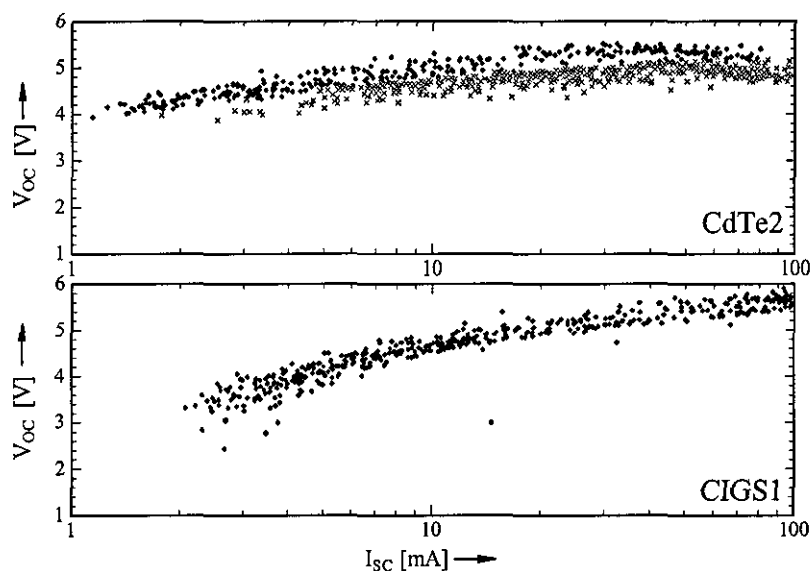


Figure 8.24: *Variation of the Open Circuit Voltage with Irradiance of Polycrystalline Samples.* The logarithmic plot is used to identify the applicability of the model given in the text. The diamonds represent data collected in the first month of operation, the crosses signify data collected after six months of operation.

lower open circuit voltage. The effect of operating temperature is discussed in the following.

It is clear from equation 8.9 that the influence of irradiance and temperature on the short circuit current are inexorably linked. This expresses itself in figure 8.25, where the influence of the operating temperature on the open circuit voltage is investigated. For this purpose, the data was binned according to month of operation and irradiance levels. The bins shown in figure 8.25 are data from the months 1&2 and 5&6 of operation, for irradiance levels of $1000 \pm 50 \text{ W/m}^2$ and $500 \pm 50 \text{ W/m}^2$. The two samples shown are produced by the same manufacturer and are single (aSi4) and double junction (aSi3) devices. There is a significant difference between the devices with regard to the data at the second point of time, as the aSi4 sample exhibits a significantly stronger influence of the degradation. It is apparent, however, that the variation with temperature (i.e. the slope of the

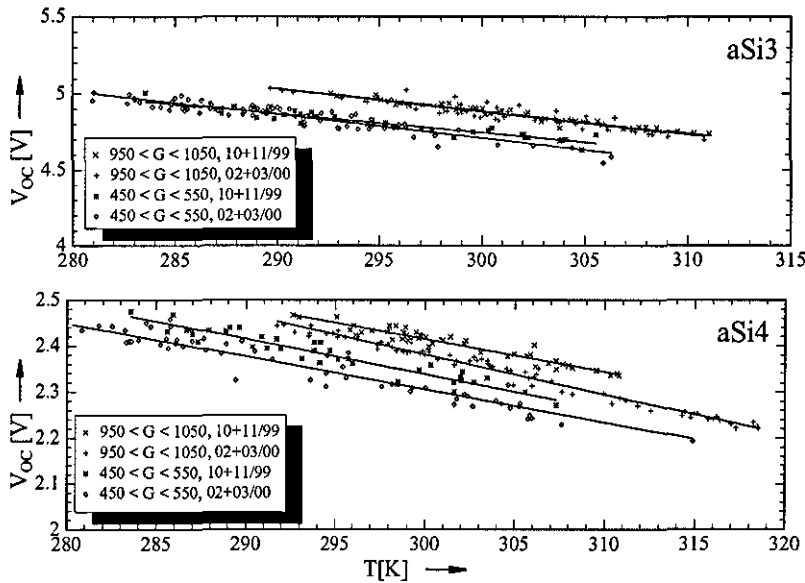


Figure 8.25: *Influence of the Operating Temperature on the Performance of a-Si Devices.* The graph shows the behaviour for the months 1&2 and 5&6 of the operation of the devices. The data shown is binned according to irradiance levels, the irradiance bins shown are $1000 \pm 50 \text{ W/m}^2$ and $500 \pm 50 \text{ W/m}^2$. As a guide for the eye, linear trendlines are included.

trend line) appears to be nearly identical during the measurement campaign, at least within the accuracy of our experimental arrangement. The influence of the irradiance is illustrated by the variation of the magnitude of V_{OC} between the different irradiance bins. Again, the magnitude might change, but the thermal variation does not change significantly. There are some minor variations in the slopes of the trend lines but this may very well be due to scatter introduced by short term variation in the environmental conditions during a single measurement. The bins for the first two months of operation were used for the determination of the temperature coefficients of the different devices. The data resulting from irradiance levels of $1000 \pm 50 \text{ W/m}^2$ is given in table 8.2. There was, unfortunately not enough data for the CIGS device to obtain a reliable result.

The thermal variation of the open circuit voltage is given on a per cell basis. There

Device	$\frac{d}{dT} V_{OC}/\text{Cell}$ $\frac{V}{K}$
aSi3	$-5.01 \cdot 10^{-3}$
aSi4	$-2.92 \cdot 10^{-3}$
aSi5	$-3.95 \cdot 10^{-3}$
CdTe2	$-2.04 \cdot 10^{-3}$

Table 8.2: Temperature Coefficients of Open Circuit Voltage.

appears to be a relationship between the band gap and the thermal variation of the devices. The device with the smallest band gap (CdTe, 1.45 eV) also exhibits the smallest thermal variation. The device with the next largest band gap, the single junction a-Si device (aSi4), exhibits the second lowest thermal variation. The two double junction devices show a stronger relationship, which is most likely due to the effects of interconnection, and that these devices essentially have twice the built in potential of a single junction device. Such a relationship could be expected from the simple model given in equation 8.9. The band gap dependence of the influence of the operating temperature can be derived when considering the logarithmic term only, which is approximately $\ln \left(\frac{I_{SC}}{I_{01}} \right)$. Considering that I_{01} has a temperature dependence which depends exponentially on the band gap, i.e. a pre-factor times $\exp \left(\frac{-E_G}{kT} \right)$, indicates that larger band gaps will have a larger impact. There is, however, no exact relation, as this also depends on the manufacturing process, as can be seen when considering both double junction devices, which have significantly different values. This band gap dependence might, however, be crucial when using thin film devices for the monitoring of irradiance. Most data acquisition makes use of voltage signals rather than current signals. Thus it may lead to significant errors using the open circuit voltage of, say, a double junction a-Si device for monitoring the irradiance relevant for an a-Si system.

In the last part of this section, a look is taken at the seasonal variation of the open circuit voltage. It was shown before that increasing irradiance generally increases the open circuit voltage while an increase in temperature decreases this property.

In general, high irradiance is linked to higher temperatures and thus there will be an overall influence on the open circuit voltage, which could change seasonally.

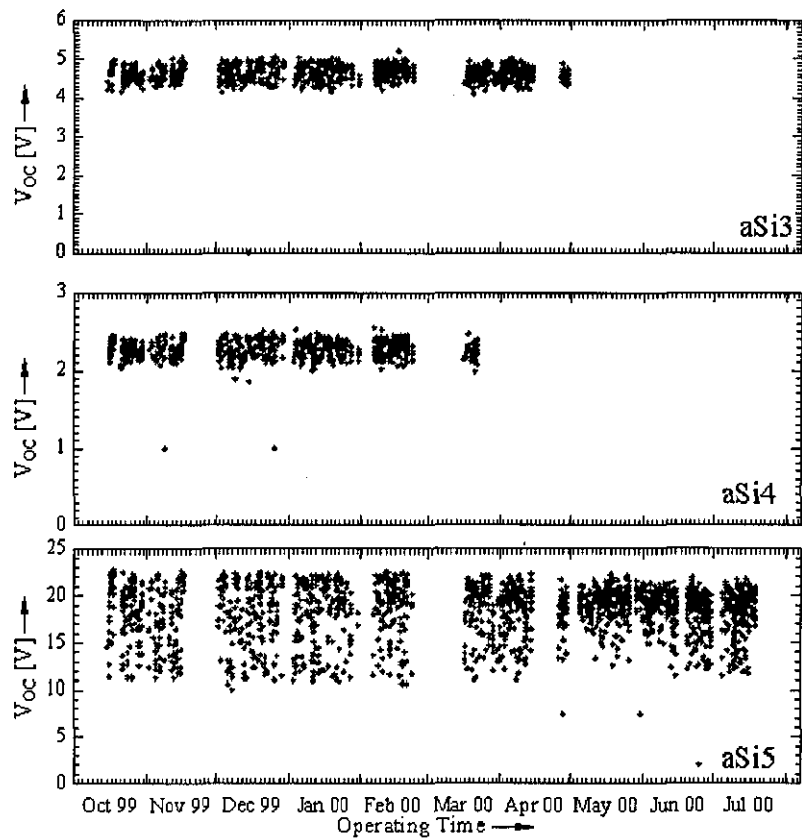


Figure 8.26: *Seasonal Variation of the Open Circuit Voltage of the a-Si Devices.* No normalisation was carried out, the reasons for the occurring scatter are investigated in the text.

The variation of the open circuit voltage is outlined in figure 8.26. There is a small seasonal variation apparent for all devices. There seems to be a maximum of V_{OC} around March. The irradiance already reaches significant levels while the ambient temperature is still relatively cold. Hence this is consistent with one's expectations. The large scatter on the aSi5 module is a direct result of the larger irradiance dependence of its open circuit voltage as shown in figure 8.23. All three devices show nearly stable behaviour of V_{OC} in the beginning,

which is mainly due to the degradation, which reduces the open circuit voltage [Takahisa 94], offsetting the possible gains due to increasing irradiance levels. Towards the summer months, the maximum V_{OC} achieved is reduced, as the temperature is higher, thus reducing the open circuit voltage.

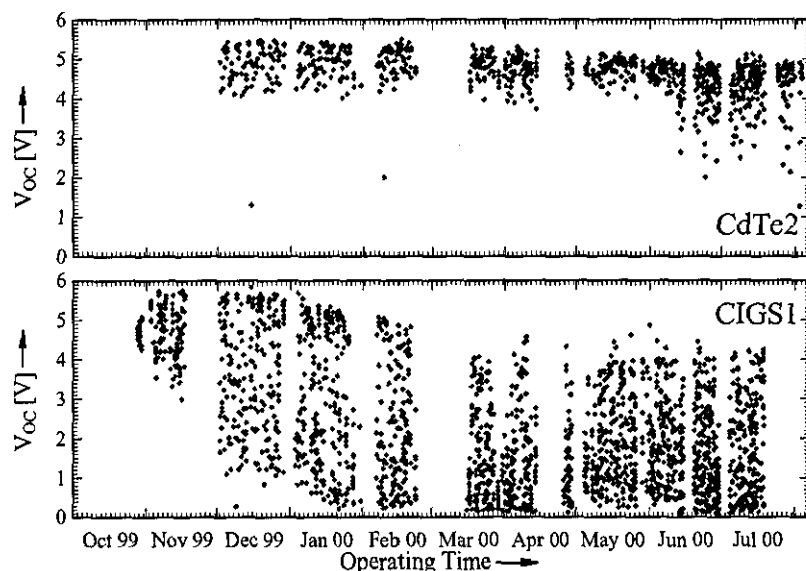


Figure 8.27: *Seasonal Variation of the Open Circuit Voltage of the Polycrystalline Devices.* No normalisation was carried out, the reasons for the occurring scatter are investigated in the text.

The CdTe sample, as shown in figure 8.27, is very stable over the year, it follows to some extent the trend reported by del Cueto [Cueto 98], with a reduction in the summer months. However, due to the limited period of operation, this cannot be confirmed. There is no maximum in March time, as is apparent for the a-Si devices. This is a result of the smaller band gap, and the resulting lower temperature dependence of the open circuit voltage.

The variation exhibited by the CIGS sample is a direct result of the decreasing shunt resistance and thus does not agree with a common model. There is an increasing irradiance dependence due to the increasing shunt current, reducing the V_{OC} at lower irradiances significantly.

It is clear from the discussion in this chapter that the common method of correcting for different irradiances and temperatures as given e.g. the NREL approach by Anderson [Anderson 96] or the approach used as European standard [Krebs 89], which are based on the behaviour of I_{SC} and/or V_{OC} will not work well for thin film solar cells. Indeed, work carried out at JRC-Ispra [Anderson 00] using the European standard for the translation of laboratory measurements to outdoor conditions was not entirely satisfactory albeit yielding very good results for polycrystalline silicon devices. The NREL method presented by Anderson [Anderson 96] may be even more prone to errors, as it uses the approximation of a logarithmic behaviour of the open circuit voltage, which is, following the discussion in this section, not truly applicable. It will thus be beneficial to investigate the behaviour of the open circuit voltage in more detail in order to implement it in an empirical translation procedure. The thermal variation of thin films appears to be described well by the normally applied simplifications, although the voltage dependent photocurrent in the case of a-Si does have some impact.

8.7 V_{MPP} to V_{OC} Ratio

The ratio between V_{MPP} and V_{OC} is very important where maximum power point tracking is concerned. Some inverters use a maximum power tracking method which disconnects in given time steps, measures the open circuit voltage and uses 78% of the measured open circuit voltage as the operating voltage. This percentage was shown to be a good approximation for many c-Si devices but might not be applicable for thin film cells. As shown in figure 8.28, this is not a good approximation for thin film solar cells. There the data is plotted against the short circuit current, which again is used to exclude spectral effects. The CIGS1 sample is not included in the following discussion, as the progressing shunting

made the analysis questionable.

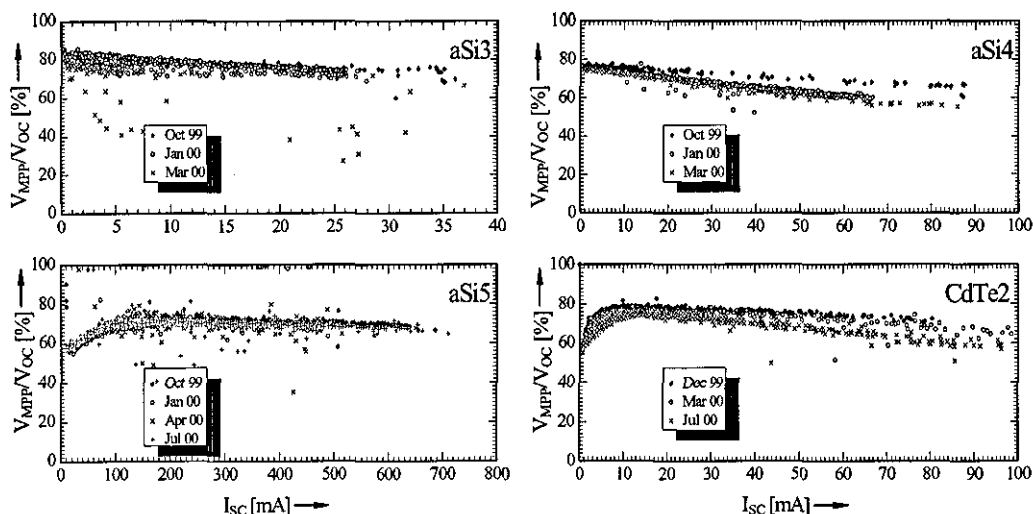


Figure 8.28: *Irradiance Dependence of $\frac{V_{MPP}}{V_{OC}}$ in Three Monthly Intervals.* It is apparent that the time of exposure has an influence for aSi4 and CdTe2, while it is nearly independent for the double junction a-Si devices. The shape of the relationship is nearly identical to the FF.

The ratio shows a dependency on the irradiance that closely mirrors the shape of the FF for higher irradiances (short circuit currents). It can thus be concluded that $\frac{V_{MPP}}{V_{OC}}$ determines the behaviour at low irradiance levels and is nearly constant for higher irradiance levels. This is the case, as shown as an example for the aSi5 and the CdTe2 devices in figure 8.29. Both devices show a decline in $\frac{I_{MPP}}{I_{SC}}$ ratio for low irradiance levels but then are relatively constant. The constant behaviour is reached when the series resistance dominates the device performance, as shown in figure 8.20.

This finding is, however, expected, as both devices exhibited a slightly higher influence of the shunting resistance, as shown in figure 8.20. Thus this is dominant for lower irradiance levels. The influence of the reduction in shunt resistance is more apparent in the aSi5 sample, as the overall shunting resistance is lower and thus the contribution at the MPP is higher. $\frac{I_{MPP}}{I_{SC}}$ is nearly completely stable

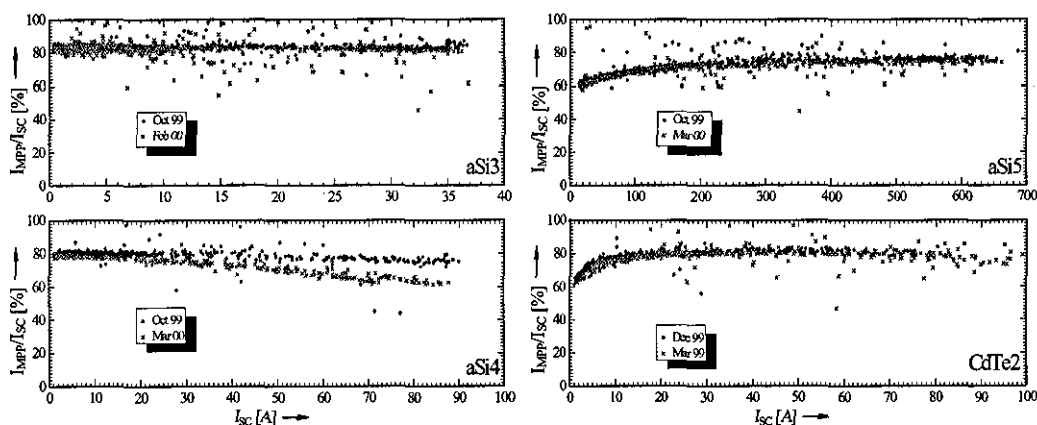


Figure 8.29: Variation of $\frac{I_{MPP}}{I_{SC}}$ with Irradiance for Samples. It is shown that the ratio is nearly constant for higher intensity levels, but can vary significantly for lower intensities.

when the shunt resistance is high, as apparent from figure 8.29.

There is a slightly negative slope for the single junction aSi4 device, while $\frac{I_{MPP}}{I_{SC}}$ hardly changes for the aSi3 device. This can again be expected from the behaviour of the shunt resistance in figure 8.20. The absolute value of the I_{MPP} is a device specific number, which is determined by the recombination. Its variation with intensity is, however, apparently mainly dependent on the shunt resistance and voltage dependent photocurrent.

The figure also shows the variation of $\frac{I_{MPP}}{I_{SC}}$ after six months of operation. The double junction devices do not show a marked influence. There is no change apparent in the aSi3 sample and only a small change towards larger irradiances for the aSi5 sample. There is, however, a marked change for the single junction aSi4 device. The fact that there is only a small change at low irradiance levels while there is a large change for high irradiance levels indicates that the main reason for this is not found in the recombination, but in a change in the photocurrent. This can be expected as a reduction of the lifetime-mobility product associated with degradation of devices. The influence of the voltage dependent photocurrent is

stronger for a reduced lifetime-mobility product [Coors 98]. It is also responsible for a reduction in V_{OC} , which was demonstrated in section 8.6, and a minor reduction in I_{SC} . The difference between a single and a double junction is that a double junction has effectively twice the built in potential and thus the variation of the lifetime-mobility product is less significant. Thus the findings shown in figure 8.29 agree well with the expectations. An irradiance dependent effect as in the aSi4 sample is apparent with a smaller magnitude for aSi5. It appears, though, that the performance at low irradiance levels is slightly higher than in the undegraded state. This is not an effect of degradation, it can be attributed to seasonal spectral effects on double junctions. This indicates that the overall effect should be stronger if similar times of the year would have been chosen.

The $\frac{V_{MPP}}{V_{OC}}$ is more dependent on the slope at the open circuit voltage, which is influenced by the series resistance, voltage dependent photocurrent (for a-Si) and a non-ohmic contact (for CdTe). Thus an exact mathematical relation is not available. It appears, however, that there is a change of this behaviour over time. The samples CdTe2 and aSi4, especially, exhibit a reduction in time, the sample aSi4 even shows a change in the slope with irradiance. This is, however expected in case of the aSi4 sample. The progressing Staebler-Wronski degradation reduces the lifetime-mobility product and thus the impact of the voltage dependence of the photocurrent. This effect is also evident when investigating the apparent shunt resistance of this device in figure 8.20. This effect is less pronounced for the double junctions, hence their variation is not really distinguishable from the initial irradiance influence. The CdTe device shows no reduction after three months of operation. A change is apparent after 6 months of operation, which can be seen as an early sign of contact problems. Thus, the $\frac{V_{MPP}}{V_{OC}}$ ratio could be a method for condition monitoring without any additional equipment, as most inverters track the MPP, can open-circuit the system and can measure voltages. This possibility

is further explored in figure 8.30, where the variation of the $\frac{V_{MPP}}{V_{OC}}$ ratio with time is plotted.

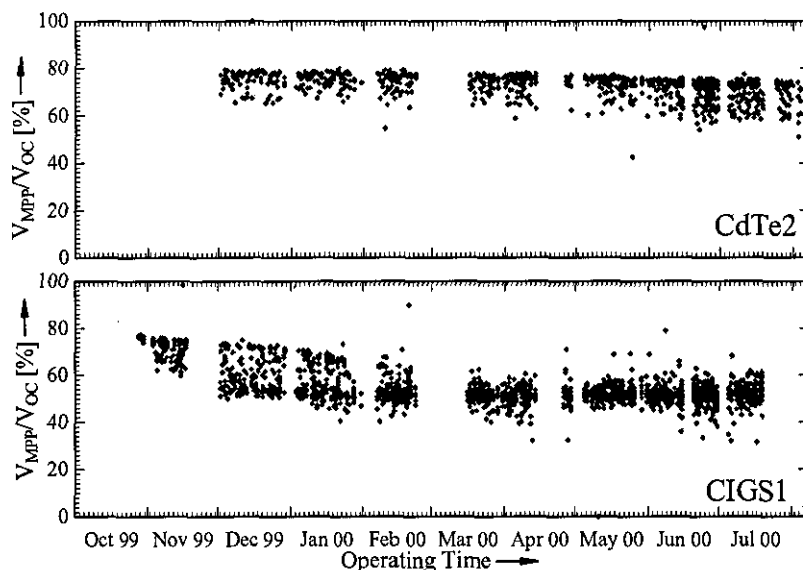


Figure 8.30: Variation of the $\frac{V_{MPP}}{V_{OC}}$ Ratio with Time for the Polycrystalline Devices. It appears that for correct operation, the ratio is relatively constant within a narrow band width while failing devices show marked reduction or widening of the band width.

The impact of device problems on the $\frac{V_{MPP}}{V_{OC}}$ ratio is illustrated by the behaviour of the CIGS device. Initially (last week of October 99) it is limited to a very narrow band width. The ingressing water starts to make an impact and the band width widens. This effect is accompanied by a slight decrease of the ratio (early November 99). The widening of the band width as well as the decrease in the ratio accelerate until reaching a stable plateau in March/April 2000. It is also apparent that the lowest value achieved in the course of the day reduces during the whole process. Thus a simple condition monitoring method would be to check the ratio on an hourly basis and raise an alarm when the determined value falls short of a technology-specific limit. The minimum is technology specific, and varies possibly seasonally, as can be seen for the *a*-Si devices shown in figure

8.31. The CdTe device does not exhibit any seasonal variation until the very end of the measurement period, where a widening and a slight reduction in the ratio are apparent, indicating that the device develops problems. Indeed, soon after the end of the period reported here, the device started shunting and its performance is significantly reduced today, as apparent from figure 8.6. The open circuit voltage might be used for condition monitoring as well, but due to the irradiance influence, monitoring V_{OC} would require a light sensor, while the $\frac{V_{MPP}}{V_{OC}}$ ratio can be generated nearly as easily without any additional equipment. It appears to be a very robust method to monitor the $\frac{V_{MPP}}{V_{OC}}$ ratio, which is not overly dependent on irradiance or temperature, albeit being sensitive to possible device problems.

The variation for the a-Si devices shown in figure 8.31 again emphasises the sensitivity to possible device problems, e.g. in the case of the aSi3 sample. The possible failure did show up in the investigation of the fill factor only, where a similarly large variation is apparent. It was not observable in any other property investigated so far. The variation in the fill factor could, however, be due to technology specific effects, as the aSi5 sample (the other double junction in the text) has a similar band width of the fill factor as the aSi3 sample close to its failure. Overall, the $\frac{V_{MPP}}{V_{OC}}$ indicates the possibility of a problem much more reliably.

It is apparent from figure 8.31 that different devices will typically operate at slightly different ratios, an indicator that the fixed ratio used for MPP-tracking is not a good method for thin film devices. There is, as shown before, a possible influence of the irradiance level, which determines the band width to some extent. It is clear from figure 8.28 that there is a reduction of the ratio for lower irradiance levels, but that can be allowed for when using the $\frac{V_{MPP}}{V_{OC}}$ ratio for condition monitoring. The a-Si samples also seem to exhibit a small seasonal variation, which is again device specific. This does not, however, reduce the suitability of the $\frac{V_{MPP}}{V_{OC}}$

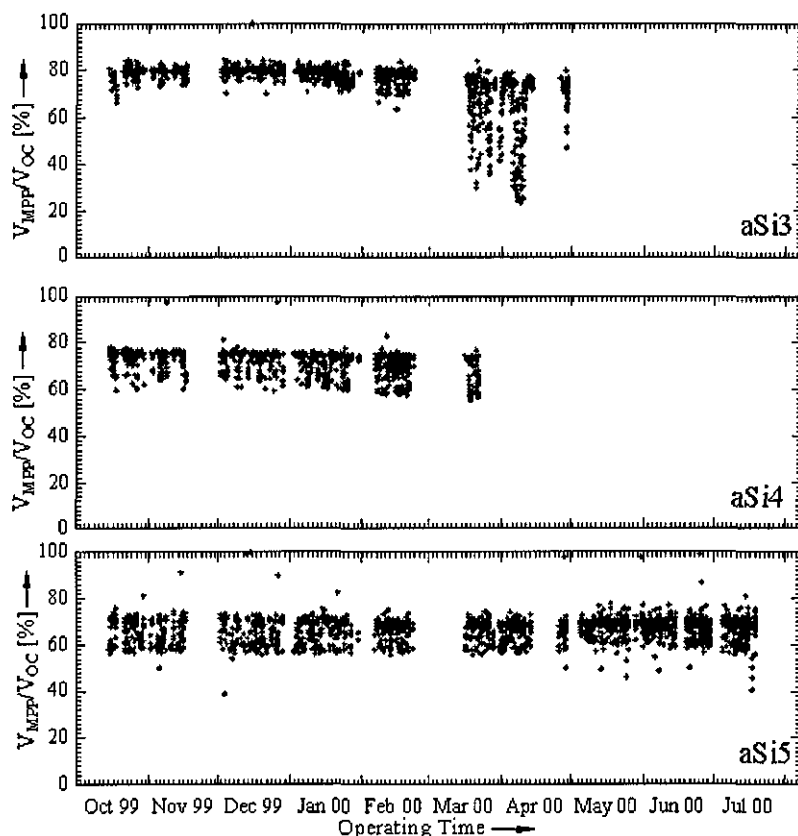


Figure 8.31: Variation of the $\frac{V_{MPP}}{V_{OC}}$ Ratio with Time for the a-Si Devices. The band width is wider than for the CdTe device but relatively stable, until the early signs of failure occur.

ratio for condition monitoring.

8.8 Efficiency

The efficiency is the most important factor of the photovoltaic device. The seasonal behaviour of the efficiency was already discussed in section 8.3. In this section, a look is taken at the influence of the environmental conditions on the efficiency η . The efficiency used here is related to the aperture area, i.e. the area of the overall device including any inactive areas. This favours larger modules, as they typically have a higher ratio of active material to device size. It avoids,

however, the problem of how to count the last cell in a thin film device, which typically is made up as a whole cell but used for contacting purposes only, i.e. it does not contribute to the overall electrical generation. Hence it was decided to use aperture efficiency, which is not necessarily a very meaningful number, but as the interest here is in the variation of the efficiency and not in the absolute value this is an acceptable definition. Furthermore, the efficiency is related to the useful irradiance, i.e. irradiance which is in the spectral range in which the device is responsive to illumination. This will increase the efficiency, as e.g. a-Si devices can typically use only 65% of the AM1.5 spectrum used for laboratory calibrations. Due to the relatively slow measurement speed of the spectroradiometer, the amount of scatter is significantly more than found when plotting against the total irradiance but the information is much more site independent compared to the use of total irradiance. The absolute irradiance values used in this section are, if not mentioned otherwise, always the irradiance within the spectrally active area. The efficiency can be linked to the parameters of the devices investigated so far through a simple relation:

$$\eta = \frac{V_{OC} \cdot I_{SC} \cdot FF}{G \cdot A} \quad (8.11)$$

with A being the area of the device and G being either spectral or total irradiance. The short circuit current went up nearly linearly with irradiance, although there was a small reduction in the ratio $\frac{I_{SC}}{G}$. The open circuit voltage exhibited a roughly logarithmic increase with irradiance. There was, however, a reduction in the fill factor with irradiance for all devices except for the aSi5 sample. The magnitude of this reduction will thus determine the behaviour of the device. This is apparent when comparing the CIGS and the CdTe sample in figure 8.32.

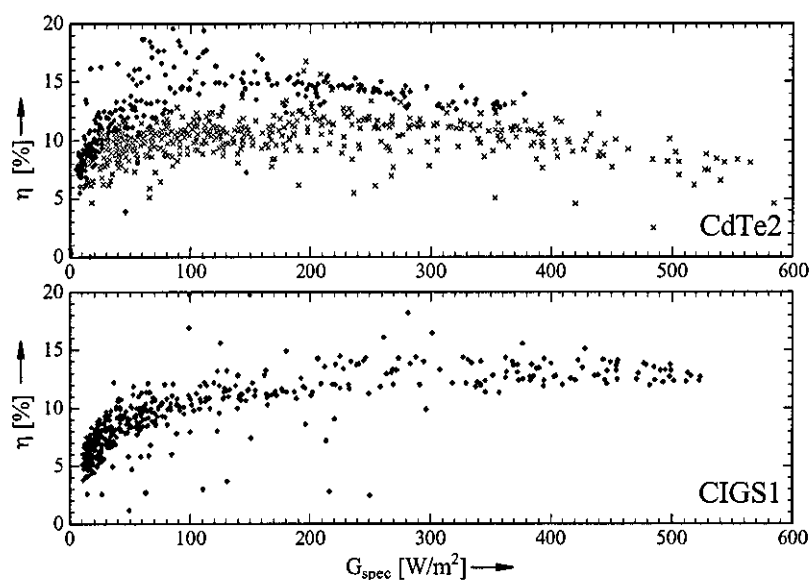


Figure 8.32: *Variation of the Efficiency with Irradiance for the Polycrystalline Devices.* The relation is plotted for the first month of operation (diamonds) and the sixth month of operation (crosses).

The fill factor of the CIGS device showed a slight improvement in figure 8.20 and thus the overall efficiency goes up with increased irradiance. The CdTe device on the other hand showed a reduction of the FF with higher irradiance values, a fact which also shows in the efficiency of the device. One has to keep in mind here that higher irradiance levels are inevitably linked to higher operating temperatures. This will enhance any effect. A slight decrease for CdTe devices was also reported by del Cueto [Cueto 98], albeit of smaller magnitude. This might be very device specific and a spectral effect was considered by del Cueto [Cueto 98] only by calculating a clear sky efficiency, hence an underlying spectral effect could not have been detected. It was shown in section 8.4 that there is an underlying spectral effect on the short circuit current, which will enhance the reduction of efficiency. Hence, our findings are not contradicting this work. It appears from the shape of the relation plotted in figure 8.32 that the fill factor determines the overall irradiance-efficiency relation. Considering that the factor is very dependent

on the $\frac{V_{MPP}}{V_{OC}}$ ratio, this emphasises the appropriateness of this ratio for condition monitoring.

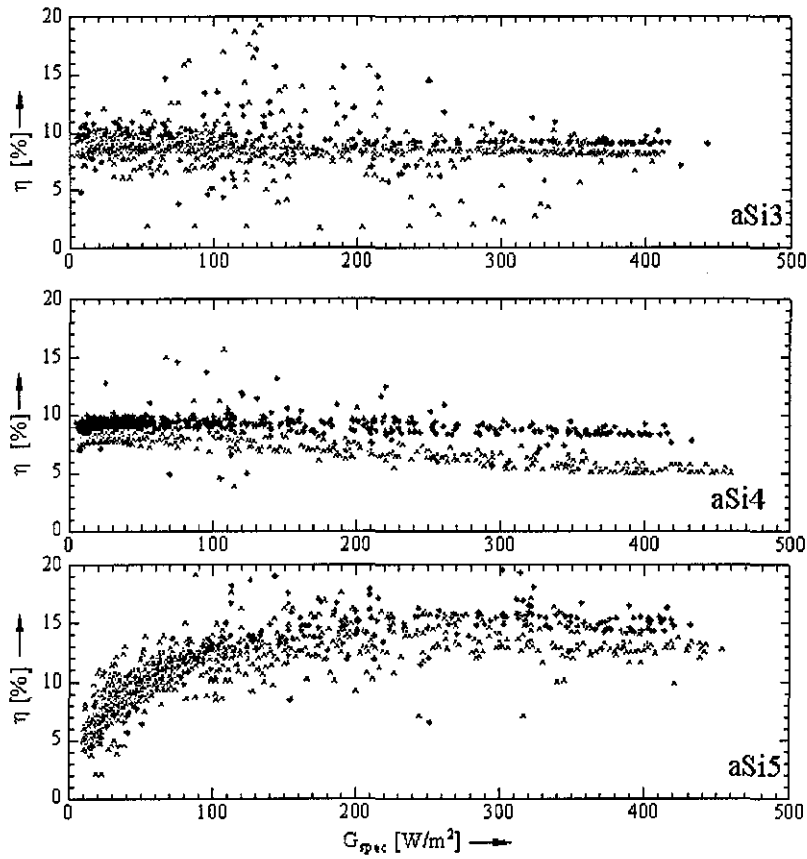


Figure 8.33: *Variation of the Efficiency with Irradiance for the a-Si Devices.* The relation is plotted for the first month of operation (diamonds) and the sixth month of operation (crosses).

The influence of the FF is also apparent for the a-Si devices shown in figure 8.33. The efficiency reproduces in all cases the behaviour of the fill factor shown in figure 8.20. It also reflects the influence of degradation on the a-Si devices, as apparent from the different slopes most obvious for the aSi4 sample.

This relation with the FF also highlights the importance of a high shunt resistance of the devices as it was shown in section 8.5 that the FF depends strongly on the shunt resistance. This means that in a country such as the UK, where the irradi-

Device	$\frac{d}{dT} \eta_{spec} \left[\frac{\%}{K} \right]$
aSi3	$-2.22 \cdot 10^{-2}$
aSi4	$-2.13 \cdot 10^{-2}$
aSi5	$-7.68 \cdot 10^{-2}$
CdTe2	$-1.42 \cdot 10^{-1}$

Table 8.3: Thermal Efficiency Coefficients.

ance is for the majority of the time around 100 W/m^2 , it is crucially important to have devices with a very high shunt resistance, such as aSi3 and aSi4. The importance of this is highlighted in chapter 9, where it is shown that for certain samples the losses at low irradiance levels determine the overall performance ratio of these devices.

It was shown in figures 8.32 and 8.33 that there is an irradiance dependence of the efficiency. Hence, the thermal effect on the efficiency was investigated for irradiance levels of $1000 \pm 50 \text{ W/m}^2$ only. The coefficients for the spectral efficiency are given in table 8.3.

It is apparent from table 8.3, that the temperature coefficient of the tested a-Si devices is lower than for the tested CdTe sample, which is roughly twice as high as for the aSi5 sample, the a-Si sample with the highest temperature coefficient. The CIGS sample did not accumulate enough measurements at high levels to allow a sensible analysis.

It is interesting to note that the temperature coefficient for the single junction aSi4 and the double junction aSi3, both manufactured by the same source, is nearly identical and significantly lower than for the other a-Si sample in the test. This indicates that the manufacturing method is more important for the temperature response than the device structure. Otherwise the two double junctions should exhibit a closer relationship.

The literature reports positive temperature correlations (e.g. Carlson et al. [Carlson 00]) and negative temperature correlations (e.g. Schade et al. [Schade 98]).

This could well be due to different locations and materials. However, commonly, a negative coefficient is found [Schade 98].

The overall effect is for all tested devices significantly smaller than the one reported for c-Si devices, which is typically in the region of 0.4%/K [Schade 98]. This effect can be understood easily by considering the band gap of the different materials. There is a well known relationship between the band gap and the maximum efficiency, which has a maximum around band gaps of 1.4 eV. Crystalline silicon has a band gap of 1.12 eV hence the band gap is lower than the maximum. An increase in operating temperature will reduce the apparent band gap and thus the maximally achievable efficiency is reduced. This effect is enhanced by the increase in recombination. Amorphous silicon and CdTe on the other hand have band gaps larger than the maximum, hence the theoretically achievable efficiency increases for higher temperatures, albeit this effect is counteracted by the increased recombination. If the increase in recombination is now less than the gains due to a better match of the band gap to the apparent spectrum, a positive temperature correlation will result. On the other hand, if the recombination increase is stronger than the gains due to a better match of spectrum and band gap, a negative coefficient will result. Either way, a lower thermal coefficient will result. Amorphous silicon is further away from the possible maximum than CdTe, hence a small increase will make a larger impact on the possible efficiency improvements than in the case of the CdTe device and thus the thermal effect is smaller.

It is clear from the discussion above that a-Si has a significantly lower temperature coefficient than all other materials and thus will be well suited for operation in hot environments. The influence of the irradiance is less clear, its behaviour is mainly determined by the variation of the fill factor. It can, however result in an increased efficiency for lower irradiance conditions.

An interesting aspect comes to light when investigating the impact of the spec-

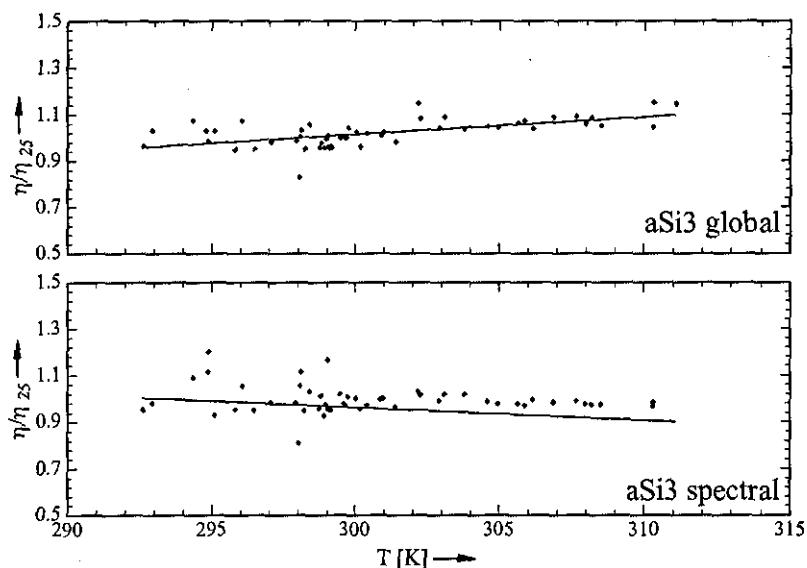


Figure 8.34: *Influence of the Spectrum on the Temperature Coefficient of the aSi3 Device.* It is that the spectrum can have a major influence on the thermal coefficient, it can even change the sign of the coefficient.

trum on the temperature coefficient, as done in figure 8.34. This graph depicts the temperature coefficient calculated for irradiance levels of $1000 \pm 50 \text{ W/m}^2$, once spectrally corrected and once using the total irradiance. A trend line was determined and the values in figure 8.34 are given relative to the value at a temperature of 25°C as calculated by this trend line. It becomes apparent that changes in the spectrum can be the reason for positive temperature coefficients as reported by Carlson et al. [Carlson 00], while a spectrally corrected irradiance will result in a negative temperature coefficient. This is apparent when considering that higher temperatures normally occur during summer, a time when typically the air mass is relatively low and thus the useful fraction for a-Si devices is very high.

8.9 Conclusion

This section highlighted the importance of the environmental variations under realistic operating conditions. Some lessons were learned for future measurement arrangements, namely that a higher measurement speed is desirable. This could be achieved with a reduced measurement accuracy within the source-measure unit, which would allow one to measure faster and store more curves in the memory of the SMU. Secondly, it highlighted the difficulties of sealing the devices and future investigations will have to apply a more appropriate sealing procedure. It is shown that the possible failure of the devices is always expressed by a significant reduction in the minimum $\frac{V_{MPP}}{V_{OC}}$ ratio. As this ratio can be determined without any additional equipment, it lends itself to condition monitoring the state of a PV device.

It is shown that the UK environment differs from other places with a more continental climate in operating temperature, irradiance level and spectral composition of the light. The data is then analysed for effects of degradation, temperature, irradiance and incident spectrum. It is shown that the spectrum has a significant influence on the short circuit current. The behaviour of thin film solar cells can generally be modelled with the simple equation 8.2 without any spectral correction, but this makes the data site specific. It is better to allow for negative coefficients (which are due to effects other than temperature) and use the spectral irradiance only for translation from one site to another. It is clear, however, that the spectrum has a major influence on the device performance. The variations of the short circuit current found in the course of this study are due to changes in the incident spectrum. The spectrum causes a secondary spectral effect on multi-junctions which is also seen in the fill factor.

The behaviour of the fill factor is determined by the intensity of the incident irradiance and, in the case of multijunctions, also by its spectral composition.

The variation of the FF is highly dependent on the manufacturing technology. A major influence on the low light behaviour is the shunt resistance. Amorphous silicon devices exhibit a reduction in the fill factor due to the voltage dependent photocurrent. A similar effect can be observed for CdTe devices, but it can be attributed to a non-ohmic back contact.

The open circuit voltage is shown to have a behaviour of irradiance dependence, which is not entirely described by the commonly applied logarithmic dependency, as other effects influence the open circuit voltage as well. This can pose problems for empirical translation procedures which partially make use of the behaviour of I_{SC} and V_{OC} . On the other hand, the influence of the operating temperature is well described by the common linear approximation. A band gap dependence is apparent, although material specific influences play an important role in this. The temperature variation of the open circuit voltage will increase with increasing band gap, although this does not necessarily mean it will influence the efficiency negatively.

The efficiency is shown to depend mainly on the variation of the fill factor with irradiance, which is in turn partially determined by the shunt resistance. This emphasises the importance of using devices with high shunt resistances in climates with low average irradiance conditions, as this regime tends to be dominated by the shunt resistance alone. The impact of higher operating temperatures is mainly linked to the band gap of the device, with larger band gaps resulting in smaller changes in the overall device efficiency.

Chapter 9

Simulation of the Outdoor Performance

9.1 Introduction

There is a significant interest in the modelling of photovoltaic systems as this technology matures. It is obviously important for economic reasons to predict the electric output of a system. Especially in the background of guaranteed results, i.e. that a manufacturer guarantees the output of a system, this becomes increasingly important. It is obvious, though, that any system model is only as good as its input, i.e. if the meteorological data is insufficient, no method will yield any sensible result. This should be kept in mind when considering the quality of different approaches for modelling PV systems.

To date, different methods have been used. They broadly can be categorised as methods using laboratory measurements and methods translating outdoor measurements from one location to another. The latter, as e.g. presented by Ransome and Wohlgemuth [Ransome 00], has the obvious advantage that effects such as spectrum and temperature are inextricably embedded in the model and the prob-

lem of separating the different effects, as attempted in chapter 8, does not arise. The disadvantage is that obviously a number of installations is necessary, which have to be modelled for a longer period of time, before being able to model the system. This will cause a problem for smaller and younger companies entering the market.

Methods using laboratory measurements have the advantage that they need significantly fewer measurements, but care has to be taken that the effects of irradiance level, spectrum and temperature are included. Thus conducting such an analysis is potentially cheaper and faster. There is, however, a significant potential for things to go wrong. Kroposki et al. [Kroposki 94] tested a number of methods which fall into this category using either manufacturers data or laboratory measurements. The results show that the highest errors occur on cloudy days, with differences between measured and calculated performance higher than 60% using some methods. The application of such a method would result in disastrous accuracy in countries such as the UK, with prevailing high cloud cover. The method which performs best in the study of Kroposki et al. [Kroposki 94] is the RRC method developed by Raicu [Raicu 93]. The RRC method uses laboratory measurements of I-V curves at different irradiance and temperature levels and applies them to meteorological data which is binned according to temperature and irradiance. If the number of measurements is not sufficient to cover all bins, this data is extrapolated using the two diode model described in equation 3.11. This is in principle not different from the time-step based approaches used in simulation codes such as PVSyst. The RRC method has the advantage that it requires a low number of calculations while time-step based approaches are more computationally intensive. The latter can, however, implement effects such as shading in their calculations, while methods such as the RRC concentrate on the efficiency only. The RRC method as tested by Kroposki et al. [Kroposki 94] exhibits its highest

inaccuracies for the thin film technologies in the test, clearly indicating the need for development work in this area.

Anderson et al. [Anderson 00] presented a method using tabulated data, but applying the IEC904 standard, as first published by Krebs [Krebs 89], for the interpolation of points. They show a generally very good agreement, but indicate problems for CdTe and a-Si devices. This could be due to the translation procedure, as this certainly is not aimed for thin film technologies. Another possibility for the reported deviations is that they use a flash solar simulator, which could show capacitive effects at higher temperatures, as shown in chapter 6 or that the spectrum is not fully considered.

Recently, Eikelboom and Jansen [Eikelboom 00] presented a model using simulator measurements. They applied a Dutch meteorological year for calculating the annual performance ratio. They report that the performance ratio for a-Si devices is the highest, followed by crystalline devices. The worst results were obtained for CIGS devices. Similar findings for a-Si are reported by Conibeer et al. [Conibeer 01], who actually monitored systems for 18 months in two different climates. Conibeer et al. [Conibeer 01] also show a strong dependence on the material, as a-Si devices represent the best as well as the worst performers, an effect that did not show up in this magnitude in the Eikelboom and Jansen study [Eikelboom 00]. Furthermore, CIGS devices (of the same manufacturer) are producing nearly as much as a-Si, with c-Si devices generating less electricity. One reason for the divergence between the two studies is that Eikelboom and Jansen [Eikelboom 00] neglect spectral effects, while they clearly have a significant influence, as shown in chapter 8.

This highlights the importance of including a spectral model into any investigation of the seasonal effects on devices. This was done by Kleiss [Kleiss 97] who extended the RRC method for thin film technologies. The seasonal degradation

and recovery pattern is implemented in this work using a stretched exponential model, as suggested by Nakamura et al. [Nakamura 90]. From chapter 8 it is however questionable how much seasonal annealing occurs, as the majority of the effects can be explained simply by changes in the spectrum.

A different approach will be presented in this chapter, which does not consider any seasonal recovery pattern but attributes these effects solely to changes in the spectrum. It will be shown that in principle it is able to model the performance of thin film devices. The model was partially implemented by Holley [Holley 99]. The final form presented here, however, uses solely the thermal model implemented in Holley's work.

9.2 Model

A model was developed for simulating the performance of thin film photovoltaic devices. A time-step based approach was chosen, as the long-term aim is to understand the device performance including shading effects, and this can only be done accurately by such an approach.

An overview of the algorithm employed is given in figure 9.1 and illustrates the three main contributions to the overall model: the thermal model, the optical model and the cell model. All components are equally important, although it appears that the cell response is the least understood element in this assembly.

The elements are linked by the irradiance, as apparent from figure 9.1. The simulation code here does not use a spectral model as it uses measurements conducted in Loughborough. The spectral distribution will, however, have an influence on the device temperature as well, as it determines the amount of thermalised energy which contributes to the heating of the devices. The three parts of the model are discussed below and further information on them can be found in the appendices.

The meteorological input for the model was data collected at CREST. The system inclination was taken as 52° , which equals the latitude of Loughborough and is the inclination of the roof mounted system at CREST.

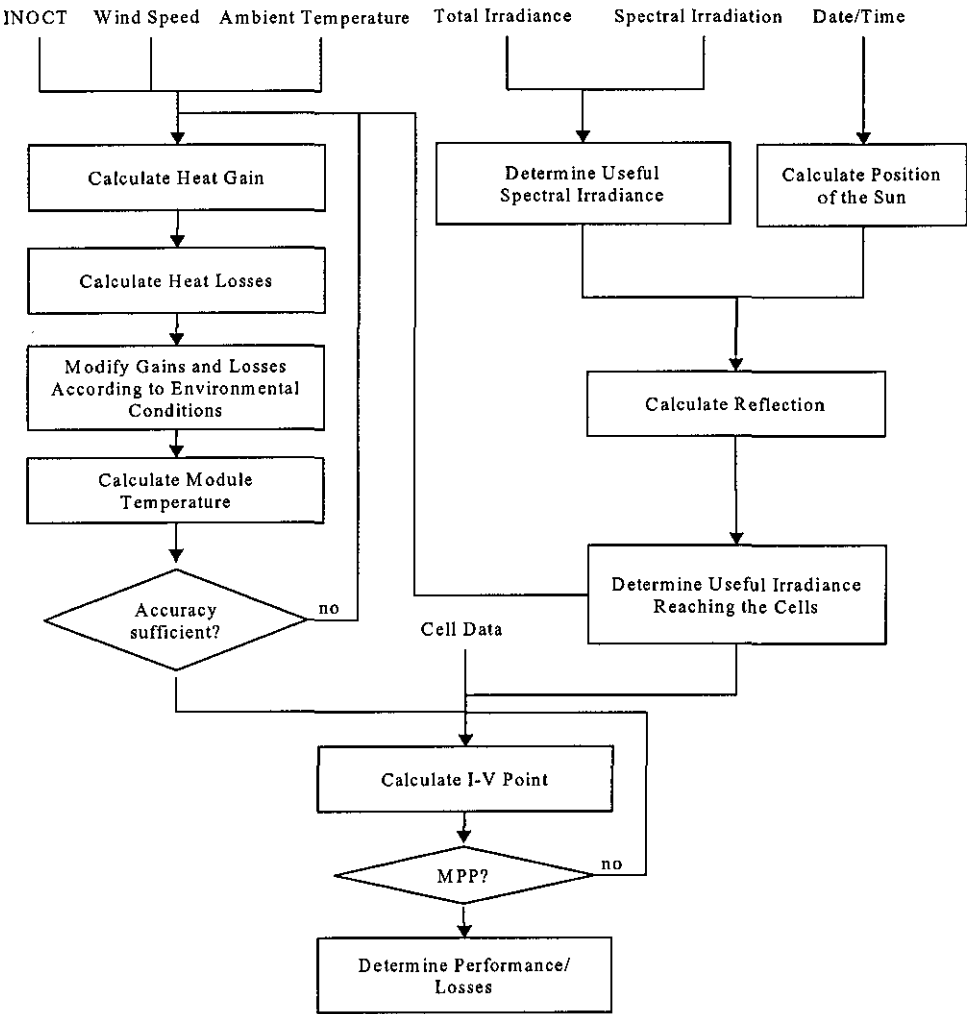


Figure 9.1: *Flowchart of the Algorithm.* The graph visualises the three main parts of the simulation, the thermal model, the optical model and the cell model, which are performed in the order shown in the graph.

9.2.1 Thermal Model

The thermal model used was originally developed by Fuentes [Fuentes 87] and predicts the average module temperature according to local environmental conditions, it is given in more detail in appendix B.4. Wind speed, plane-of-array irradiance, ambient temperature and Installed Nominal Operating Cell Temperature (INOCT) are used as input parameters. The environmental data used in the simulation are measurements carried out with the CREST environmental monitoring system.

INOCT is defined as the cell temperature of an installed array at NOCT conditions (800 W/m² irradiance, AM1.5G spectrum, 20°C ambient temperature and 1 m/s wind speed) [JPL 81] and therefore takes into account the module mounting configuration. For example, stand-alone rack-mounted modules will clearly possess different heat flow characteristics from those designed for building integrated installations. The Fuentes [Fuentes 87] model initially uses INOCT to estimate heat gain and convective/radiative heat losses from both top and bottom module faces at NOCT conditions. These values are then modified according to the local environmental conditions. Thermal capacitance of the module is also incorporated to account for the natural temperature lag.

The model used in this work was slightly modified in order to account for the specific geographical location. A new tilt angle was incorporated for calculating the convective coefficient of the module top surface. Additionally, the actual clearness index is included for each data point while Fuentes assumes a single average clearness index value. This might be important, as the UK is prone to fast changing cloud cover which will affect the temperature of a PV device significantly.

Any PV device will operate at elevated temperatures compared to the ambient temperature, largely depending on the irradiance level. This is apparent from the

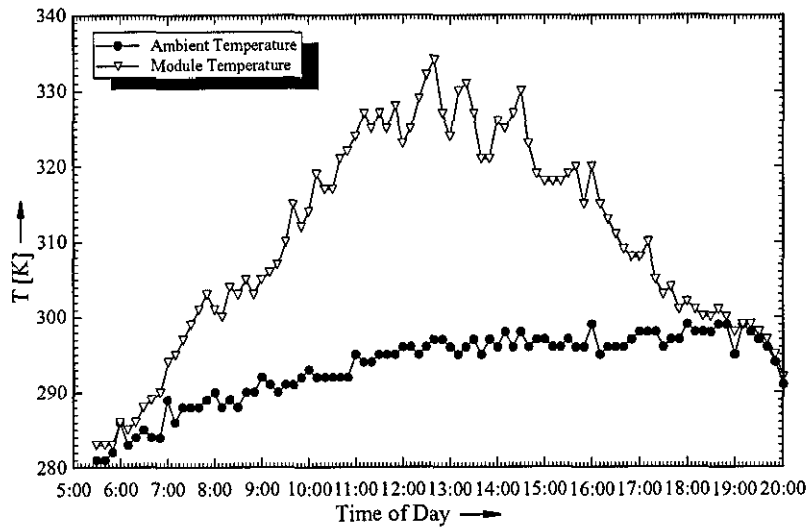


Figure 9.2: *Variation of Module Temperature in Summer.* The graph illustrates the relation of the ambient temperature and the module temperature for a rack mounted system on a sunny day in summer 1999.

thermal model as shown in figure 9.2 for a sunny summer day. Figure 9.2 illustrates the results for irradiance values above 10 W/m^2 , values below this irradiance level were not considered in this graph. In the morning and evening, the ambient temperature and the module temperature are nearly identical. Indeed, they are identical during the night. With the onset of the irradiance, the temperature increases and peaks around about 1 pm. The time of the peak largely depends on the inclination, because the irradiance received by inclined systems tends to be larger in the afternoon. The ambient temperature did show a steady increase during this day, which appears to be unusual, as one would expect the temperature to peak in the early afternoon. This is due to the fact that a relatively cold day is depicted in figure 9.2 and the following day was warmer, i.e. the UK was experiencing an influx of warm air. The data was checked against data collected by the meteorological department and no significant deviations were observed. The accuracy of this model was validated against the a-Si array installed at

Property	Value
INOCT	325K
Thermal Mass	11000 Jm ⁻² K ⁻¹
Emissivity	0.84

Table 9.1: Values Used for the Thermal Model.

CREST by Holley [Holley 99] for conditions in Loughborough. It showed a reasonable agreement with a maximum deviation of 5°C for any given time step, even when using device unspecific values as given by Fuentes [Fuentes 87] describing the thermal properties averaged over the samples investigated by Fuentes. Thus, these values, which are summarised in table 9.1, were taken without any adjustments for the simulation. Considering a full scale system, it is advisable to determine the exact values for the parameters describing the thermal lag of the system more precisely, e.g. by means of fitting measured operating temperatures to the model temperatures. The achievable agreement between prediction and measurement should be in the range of one or two degrees, and thus should certainly be sufficient for modelling a free standing system.

9.2.2 Optical Model

The optical model has to perform two tasks: it has to calculate the reflection occurring and adjust for the seasonal and daily spectral variations. These variations are important because it changes the useful percentage of the incident energy drastically, as shown in chapter 7 and is one of the most likely causes for problems in other models published to date.

The approach chosen for including the spectral effect is to scale the incident total irradiance. This is done by comparing the energy in the useful range and calculating the total irradiance (with AM1.5 global spectrum) that contains the same amount of energy in the useful range. This can, as is illustrated in figure 9.3, have a beneficial effect but can also have a detrimental effect. This model will only

allow the estimation of primary spectral effects but secondary spectral effects as shown e.g. in figure 8.13 will need additional work to be included.

The spectral content depends, as shown in chapter 7 on air mass and content of the atmosphere, with diffuse irradiance typically being 'bluer'. This effect becomes apparent from figure 9.3, where the simulated irradiance is compared with the spectral measurements and the scaled irradiance.

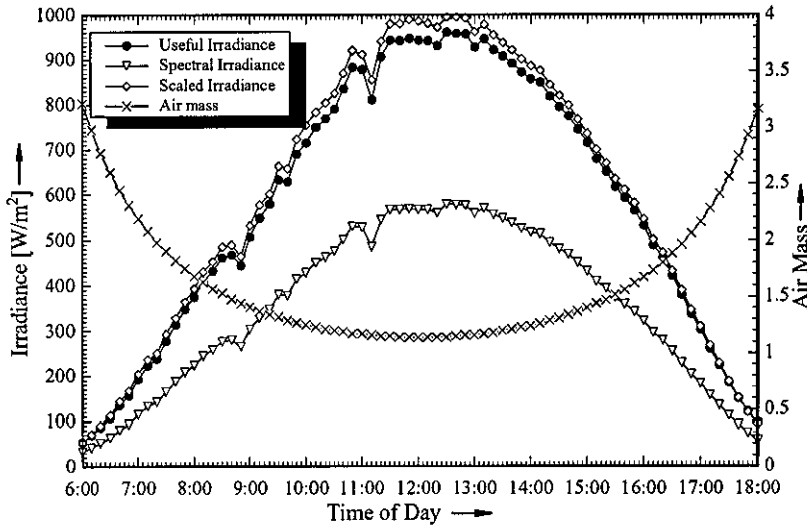


Figure 9.3: *Incorporation of the Spectral Variation.* The graph illustrates the effect for June 18th in 1999, and yields a beneficial result.

Furthermore, the reflection needs to be considered for a non-tracking system. The model implemented to do this uses the model presented by Erbs et al. [Erbs 82] for the separation of diffuse and beam irradiance. The details of this model are given in appendix B.2.

This model is used for determining the beam irradiance on the elevated surface, based on the global irradiance measured by the CREST measurement system. The beam radiation is then subjected to reflection occurring on the glass cover. This reflection is calculated following the Fresnel model as given by Duffie and Beckman [Duffie 74] and described in appendix B.3. Doing so is a significant over-

simplification, as not only the beam irradiance will be reflected but also the diffuse irradiance. It would, however, involve a very significant computational effort to calculate the reflection of the diffuse irradiance, as firstly the distribution over the sky would have to be calculated and secondly the reflection would have to be integrated over the whole sky distribution. Another simplification is neglecting the reflection on the semiconductor surface, but as the majority of manufacturers uses an anti-reflective coating, this is difficult to include without having any further information on this.

The reflection is obviously dependent on the angle γ between module and the beam direction, which is calculated for a module facing due south as [Gottschalg 01]:

$$\cos \gamma = \sin \delta \sin (\phi - \alpha) + \cos \delta \cos (\phi - \alpha) + \cos \omega \quad (9.1)$$

where δ is the declination of the Sun, ϕ is the latitude, α is the elevation of the module and ω is the hour angle of the Sun.

The calculation of this angle thus requires the calculation of the position of the Sun. A model claiming to give an accuracy of 0.01 degrees was presented by Walraven [Walraven 78] and is used for this calculation. The method itself is reviewed in appendix B.1.

9.2.3 Cell Model

The simulation carried out in this chapter focuses on the simulation of a single junction a-Si sample, but could be carried out for any other device in principle. A complete investigation of all samples in this study was not carried out due to the lack of a complete set of simulator data, dark and illuminated. Estimates had to be made which might slightly change the results and for reaching hard

Parameter	Base Value	Thermal Correction
A	100 cm ²	-
I _{ph}	1.1·10 ⁻³ A	9.9·10 ⁻⁷ A/K
E _G	1.7 eV	-
Z	1.77	-
T*	1.8·10 ⁴ K	-
$\frac{\mu\tau}{d_s^2}$	1·10 ⁷ V ⁻¹	3.8·10 ⁴ V ⁻¹ K ⁻¹
V _{fb}	1.1 eV	-
R _S	5.25·10 ⁻² Ω	4·10 ⁻⁴ Ω/K
R _P	1.14·10 ⁴ Ω	1.95·10 ² Ω/K

Table 9.2: Cell Parameters and Their Thermal Variation Used in the Model.

conclusions on the comparative performance analysis of devices, accuracy is of utmost importance. Thus it was decided to simulate a single device as a proof of concept and investigate if the challenges for modelling thin film devices as set out in section 9.1 have been fulfilled in principle.

The cell simulated here is the aSi2-1 cell, which is not significantly different from the devices of the aSi2 technology reviewed throughout this work. The dark characteristics of the cell were measured at the Chair of Electron Devices at the university of Erlangen and the thermal variation of the parameters was determined as described in chapter 6. It was found that the thermal behaviour of the diode ideality factor could be modelled well with the model given for an energetic distribution of recombination centres, as given in equation 6.9 as:

$$n(T) = 2 \frac{T^*}{T + T^*} \quad (9.2)$$

The multiplier was changed from the theoretical value of two, which is given in this equation, to a variable factor Z which allows to include the different effects, which have an impact on this factor, as shown in chapter 6. The model applied is the model of Hubin and Shah [Hubin 95] in the form presented by Merten et al. [Merten 98b], as described in chapter 3.

The thermal variation of the short circuit current was generated using data published by the manufacturer and scaling them so that they match the area of the tested cell. All parameters used in the simulation are summarised in table 9.2.

9.3 Seasonal Performance

It was explained in section 9.1, that the first challenge for the developed simulation code has to be that the seasonal performance pattern observed by researchers in the field is reproduced. This is the case, as can be seen in figure 9.4, where a normalised daily efficiency is presented. In order to validate the seasonal trends, the daily efficiencies were averaged for both months investigated and all values were normalised with respect to this average. The simulation is based on a ten minute time step throughout the day, simply because that is the measurement frequency of the CREST data logging equipment.

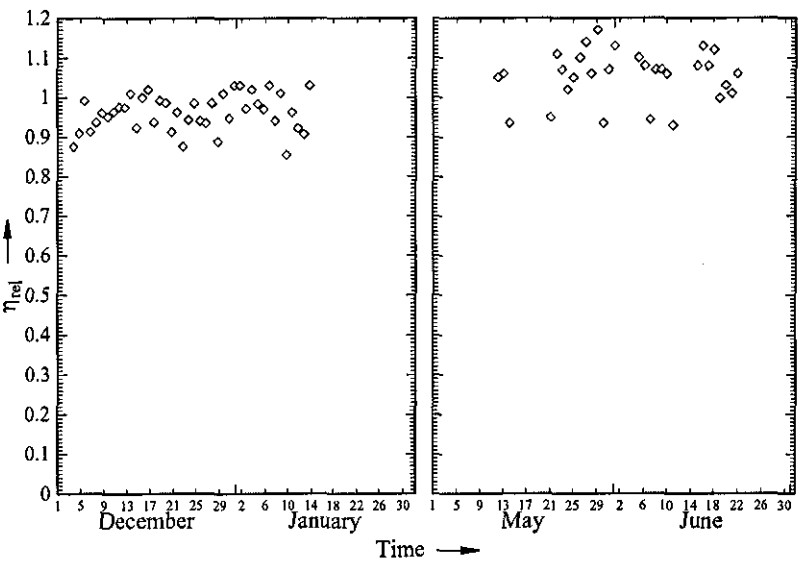


Figure 9.4: *Seasonal Variation of the Relative Efficiency.* The figure shows the efficiency with respect to the total global irradiance. The value 1 indicates the average of all simulation points.

The seasonal performance variation is well observable without considering any degradational effects. This agrees with the findings of Merten and Andreu [Merten 98a] or R  ther and Livingstone [R  ther 94], who claim that degradation plays an insignificant role after the initial degradation period of 6 months.

The performance in the summer months is, generally speaking, higher than in the winter months, emphasising the importance of the inclusion of a spectral model. No seasonal annealing process is necessary and thus the reasons for the use of the stretched exponential suggested by Nakamura et al. [Nakamura 90] are not given. It is however questionable if there is any significant seasonal annealing in countries like the UK, where the operating temperatures seldom top 50  C (as shown in figure 8.3), as it was shown that the annealing is temperature dependent [Nakamura 98]. The situation might be different for building integrated systems, though. There are, however, some days where an overall low efficiency is achieved by the simulated system. These are mainly due to low irradiance losses, as shown in section 9.4. In a monthly calculation they would hardly show up, as a much larger amount of energy is generated on sunny days.

9.4 System Losses

There was significant amount of scatter observed in figure 9.4 and the reasons for this should be investigated, as this might indicate problems with the suggested methodology. This section investigates the losses due to different environmental effects in order to determine their magnitude and investigate the feasibility of the given simulation approach. The term loss here signifies a reduced energy production due to deviations from STC, the detailed calculation of these deviations is described below.

The losses investigated in this section are presented as daily averages. These values

were calculated with respect to STC conditions, by determining the electricity generated in the course of the day and calculating the electricity generated if the corresponding STC condition would have prevailed throughout the day. In the case of the temperature, for example, the generated energy was calculated for each time step of the day, first with the apparent temperature and then with the corresponding STC temperature of 25°C. This was done for all time steps of the whole day and the generated energy was calculated for both cases. The daily losses presented in figure 9.5 are then based on the ratio of the energy generated in the realistic case with respect to the energy generated applying the corresponding STC condition, i.e. the STC condition is one and the loss presented in figure 9.5 is the reduction in this value due to the environmental conditions. This method would, however, result in extremely high numbers when carried out for the irradiance level, and these numbers will not be meaningful either as it would depend nearly exclusively on the apparent irradiance. Hence the approach chosen here was slightly different. The values for each time step were calculated as for every other property, but instead of calculating the ratio directly, the efficiency achieved for the STC condition (i.e. 1000 W/m²) was calculated. The energy generated in this time step at STC was then calculated by multiplying the efficiency at STC with the irradiance apparent at this time step in order to generate a meaningful difference between STC and realistic conditions. Finally, the ratio was calculated as for the temperature.

The results of the simulation shown in figure 9.5 illustrate the impact of the apparent environmental conditions on the electrical output of the device, not the losses of the input, i.e. it shows how much current is lost due to reflection rather than how much light is reflected.

An expected result is that the variation of the operating temperature leads to gains in efficiency in winter time and losses in the summer. The small impact

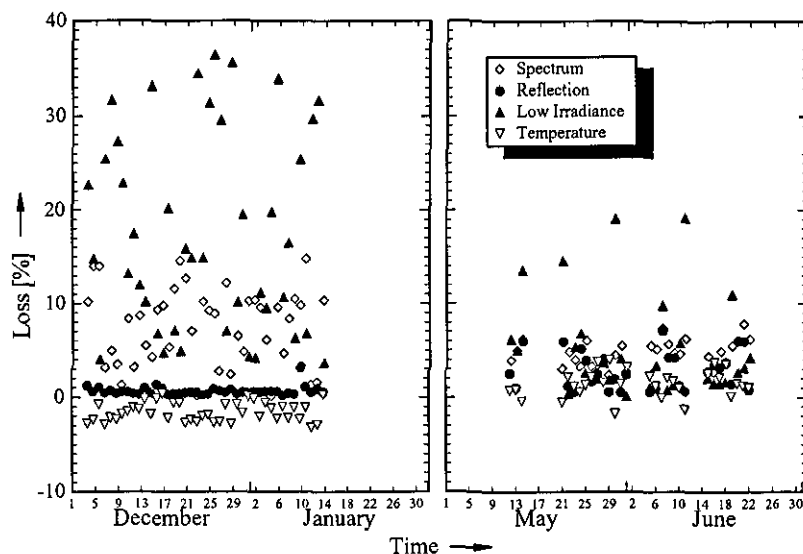


Figure 9.5: *Investigation of the Losses of an a-Si Module.* The graph compares the significance of different loss mechanisms in winter and summer.

of these variations could be expected because of the good thermal stability of a-Si devices. Overall, the magnitude of the losses is significantly lower than for conventional devices, an outcome which is expected from the previous chapters of this work and thus a confirmation of the validity of the chosen approach.

It appears surprising that the reflection losses in summer are higher than in winter. This is because the days are much longer and thus steeper angles are achieved in the course of a single day in summer, reaching a point where the Sun vanishes behind the module. These losses are lumped together with the reflection, despite strictly speaking not being reflection losses. The reasoning is that they are losses that would occur on any non-tracking system and are due to the same reason (i.e. movement of the Sun) and thus including them in this section is justified. The low value of the reflection in winter time is also due to the inclination of 52° of the simulated modules which equals the inclination of CREST's a-Si array.

It is clear from figure 9.5 that spectral losses have a significant impact on the seasonal performance. This again fits in with the findings reported in earlier

chapters of this work and thus can be seen as a confirmation of the applicability of the chosen modelling approach. It has to be emphasised, however, that the values presented here are for a whole day. It is obvious that during certain hours of the day a net gain might be achieved, but that is offset at other times of the day. The rather large scatter in the winter is explained by the influence of the weather as shown in chapter 7.

The low irradiance losses appear to be excessive in the winter months. However, this appears reasonable considering the level of irradiance. On some days, the condition of a minimum irradiance of 10 W/m^2 might lead to significant errors. For the worst day during the simulated period, the 26.12.98, only 2-3 hours around lunch are considered (out of the 6 hours daylight). The maximum irradiance on 26.12.98 is below 50 W/m^2 , emphasising the significant low irradiance losses. This low value of irradiance appears to be very low indeed, but was checked against CREST's thermopile, the integrated irradiance of the spectroradiometer and the meteorological station operated on the campus of Loughborough University. It is apparent that even in summer there are losses due to decreased irradiance, as apparent for sub-average days.

It is apparent from the simulation that low illumination losses determine the performance of a device in the UK. This emphasises the importance of a low shunt resistance as discussed in chapter 8. It is important to remember in this context that the aSi2 technology was suffering from a significant shunt resistance, as shown in chapter 6. The simulation of e.g. the aSi4 technology would have shown significantly reduced low irradiance measurements.

9.5 Conclusions

The simulation shows that by using an appropriate equivalent circuit and modelling the appropriate operating conditions a seasonal change is observed in the range as expected from the literature. In the given climate of the United Kingdom, it can be concluded that the developed model is sufficient to adequately model the output of thin film devices, provided that a device specific translation procedure is used and the changes in the spectrum are considered. It appears from the simulation carried out, that there is no need to consider a stretched exponential model for a-Si devices, the seasonal variation in the efficiency can be explained by solely considering spectral changes.

There is further work needed to simulate a system based on a complete set of laboratory measurements. This work is ongoing and will be completed in the near future. The simulation will then be able to deal with single junction thin film devices. Double junction devices will need an extended model that can account for secondary spectral effects demonstrated in chapter 8.

Chapter 10

Conclusions and Recommendations for Future Work

10.1 Conclusions

Prior to this work, the understanding of the performance of thin film photovoltaic devices was relatively poorly developed. To improve this understanding was the aim of this work. This was achieved by designing high quality measurement arrangements for indoor and outdoor calibration.

The modelling of I-V curves was achieved through appropriate modification of standard approaches used for c-Si devices. All the features observed with thin film technologies to date could be reproduced; effects such as cross-over or roll-over of curves did not pose a problem. This is a significant improvement, as some earlier approaches had to filter out points in a certain region because the methods were not able to reproduce the intersection of measurements at different light levels. In order to achieve this, an improved algorithm for the extraction of the

underlying parameters was developed. This algorithm compared well when tested against other approaches, allowing a confident extraction of parameters. Applying this algorithm also shows a good agreement for outdoor measurements. Thus the method developed for modelling the I-V characteristics represents an important advance for system modelling.

The monitoring of the environment and outdoor calibration of devices showed that the spectrum has a significant influence on the overall performance of thin film devices, depending upon their band gap and their device structure. There are two spectral effects reported in this work, a primary and a secondary effect. The first depends only on the availability of spectral irradiance, while the second also depends on the spectral composition of the useful irradiance.

The primary spectral effect exists, in principle, for all solar cells, including c-Si. However, this work adds information to a previously poorly investigated environment, a maritime climate, to the locations investigated elsewhere. The magnitude of this primary effect was investigated for Loughborough, showing significant seasonal variations of the useful fraction. Indeed, using the spectral irradiation allows resolving a number of questions under discussion, such as a positive temperature coefficient for a-Si devices or the seasonal performance variation.

The secondary effect occurs mainly for double junction devices and is due to the stacked cells being mismatched. Double junctions to date are mainly for space applications and as such optimised for AM0. In recent times, devices made from amorphous silicon alloys were produced for terrestrial use, which are all optimised for AM1.5. The demonstration of this secondary spectral effect indicates that matching to AM1.5 might not be a good approach universally and local climatic conditions will have an influence on this. The demonstration also contradicts the common statement that increasing the number of junctions will result in better cell performance. Increasing the number of junctions might increase the AM1.5

efficiency of devices, but almost certainly not the annual energy production.

It is also shown in this work that the STC efficiency rating is not always a good method for predicting energy yield of any device. There are differences in the response to changes in the environmental conditions compared to c-Si that make some of the generalisations applied questionable. It is shown specifically that some parameters vary strongly with temperature, i.e. the shunt resistance. This might have to be included in a modelling approach. Furthermore, the variation of efficiency with temperature and irradiance is different to c-Si devices. The losses due to elevated temperature are shown to be band gap dependent, with larger band gap devices having lower thermal effects. The dependence on the level of irradiance is very cell specific. It depends on a number of factors resulting often in a reduction of efficiency with increasing irradiance, something which is uncommon for c-Si devices in unconcentrated sunlight. For low irradiances, the behaviour is also different from c-Si, depending on the shunt resistance of the particular device. This behaviour also changes with time of operation. These properties will have a significant influence on the annual yield of thin film devices and a further understanding is desirable.

The work also shows that extending the common diode model to allow for the idiosyncrasies of thin film devices (by applying the specific thermal variations and accounting for the spectral effect) allows for better modelling of the seasonal device performance. Investigating a larger number of devices will allow a more accurate picture, but a proof of the methodology is given for a certain a-Si device. The modelling of fully degraded a-Si appears to be possible based on the methodology given in the work.

10.2 Recommendations for Future Work

The natural extension of this work is the investigation of the irradiance dependence of the parameters and the understanding of performance surfaces, i.e. the performance in relation to the irradiance level and device temperature. This should then be used to derive a complete model for the translation of laboratory measurements to a realistic operating environment. This might need some simplification of the model presented in this work. The degree of simplification should be determined by investigation of the impact of the parameter variations on the ability to reproduce the performance surface and on the calculated annual yield, in a given environment. Work covering this will be undertaken at CREST as soon as the necessary equipment is commissioned.

The investigation of spectral effects on devices needs to be broadened to secondary spectral effects as they do present an interesting challenge for some technologies, e.g. triple junction devices which are optimised for AM1.5 spectra. The magnitude of this effect is currently being investigated and work on deriving a model has indeed started at CREST.

Extending the model to include degradational effects is an important step, which is needed for future developments, mainly for a-Si devices. This will need an advanced understanding of the influence of the operating history on the immediate performance of these devices.

Finally, the model should be tested and validated against outdoor measurements using complete I-V characteristics, as this allows for the investigation of system specific effects such as mismatch. The final system model should allow the investigation of effects such as interconnection, by-pass diodes, mismatch in the MPP-tracker of the inverter and mismatch due to shading and variations within the production process.

Appendix A

Mathematical Formulae for the Fitting

The Marquardt-Levenberg algorithm used needs the first derivation of the basic equation for each parameter. Additionally, the derivations needed for the error propagation are given in this appendix. The basic equation, without any modification, is given as:

$$I = -I_{ph} + I_{01} \left[\exp \left(\frac{eV_j}{n_1 kT} \right) - 1 \right] + \frac{V_j}{R_P} \quad (\text{A.1})$$

It is important to note that the function is given implicitly, which complicates the derivation significantly. This is taken into account by the γ_i used in the following. The abbreviation V_j used in this section is given as:

$$V_j = V - IR_s \quad (\text{A.2})$$

A.1 One Diode Model

$$\gamma_1 = \frac{eR_s I_{01}}{n_1 kT} \exp\left(\frac{eV_j}{n_1 kT}\right) + \frac{R_s}{R_p} + 1 \quad (\text{A.3})$$

$$\frac{\partial I}{\partial I_{ph}} = -\frac{1}{\gamma_1} \quad (\text{A.4})$$

$$\frac{\partial I}{\partial I_{01}} = \left[\exp\left(\frac{eV_j}{n_1 kT}\right) - 1 \right] / \gamma_1 \quad (\text{A.5})$$

$$\frac{\partial I}{\partial n_1} = -I_{01} \exp\left(\frac{eV_j}{n_1 kT}\right) \left(\frac{eV_j}{n_1^2 kT}\right) / \gamma_1 \quad (\text{A.6})$$

$$\frac{\partial I}{\partial R_p} = -\frac{V_j}{R_p^2 \gamma_1} \quad (\text{A.7})$$

$$\frac{\partial I}{\partial R_s} = -\frac{I \frac{\gamma_1 - 1}{R_s} + 1}{\gamma_1} \quad (\text{A.8})$$

$$\frac{\partial I}{\partial V} = \left[\frac{eI_{01}}{n_1 kT} \exp\left(\frac{eV_j}{n_1 kT}\right) + \frac{1}{R_p} \right] / \gamma_1 \quad (\text{A.9})$$

$$\frac{\partial I}{\partial T} = \left[\frac{\partial I_{ph}}{\partial T} - I_{01} \frac{eV_j}{n_1 k T^2} \exp \left(\frac{eV_j}{n_1 k T} \right) \right] / \gamma_1 \quad (\text{A.10})$$

$$\frac{\partial I}{\partial G} = - \frac{I_{ph}}{G \gamma_1} \quad (\text{A.11})$$

A.2 Two Diode Model

The terms for the parameters I_{ph} , I_{01} , n , R_p and R_s are similar to the equations A.4-A.8 for the one diode model if the factor γ_1 is exchanged to γ_2 . The additional equations for I_{02} , n_2 and the changed formulae for the error propagation are given.

$$\gamma_2 = \frac{R_s I_{01}}{n_1 k T} \exp \left(\frac{eV_j}{n_1 k T} \right) + \frac{R_s I_{02}}{n_2 k T} \exp \left(\frac{eV_j}{n_2 k T} \right) + \frac{R_s}{R_p} + 1 \quad (\text{A.12})$$

$$\frac{\partial I}{\partial I_{02}} = \left[\exp \left(\frac{eV_j}{n_2 k T} \right) - 1 \right] / \gamma_2 \quad (\text{A.13})$$

$$\frac{\partial I}{\partial n_2} = -I_{02} \exp \left(\frac{eV_j}{n_2 k T} \right) \left(\frac{eV_j}{n_2^2 k T} \right) / \gamma_2 \quad (\text{A.14})$$

$$\frac{\partial I}{\partial V} = \left[\frac{e I_{01}}{n_1 k T} \exp \left(\frac{eV_j}{n_1 k T} \right) + \frac{e I_{01}}{n_2 k T} \exp \left(\frac{eV_j}{n_2 k T} \right) + \frac{1}{R_p} \right] / \gamma_2 \quad (\text{A.15})$$

$$\frac{\partial I}{\partial T} = \left[\frac{\partial I_{ph}}{\partial T} - I_{01} \frac{eV_j}{n_1 k T^2} \exp\left(\frac{eV_j}{n_1 k T}\right) - I_{02} \frac{eV_j}{n_2 k T^2} \exp\left(\frac{eV_j}{n_2 k T}\right) \right] / \gamma_2 \quad (\text{A.16})$$

A.3 Crandall Model

The difference between the basic one diode model (equation A.1) and Crandall's model is the photocurrent. It is given as:

$$I_{ph,g} = I_{ph} (V_0 - V_j) \frac{\mu\tau}{d_i^2} \left[1 - \exp\left(-\frac{1}{\frac{\mu\tau}{d_i^2} (V_0 - V_j)}\right) \right] \quad (\text{A.17})$$

the parameters μ , τ and d_i are not linearly independent from each other and are thus treated as a single parameter μ' in the following. The equations describing the diode and the shunt resistance are identical to A.5 - A.7 as long as the factor γ_1 is changed to γ_3 . The derivations for the change I_{ph} , μ' , V_{bi} , R_S and the changed error propagation are given as:

$$\gamma_3 = -I_{ph} R_S \mu' \left(1 - \left(1 + \frac{1}{\mu' (V_{bi} - V_j)} \right) \exp\left(-\frac{1}{\frac{\mu\tau}{d_i^2} (V_0 - V_j)}\right) \right) \quad (\text{A.18})$$

$$\gamma_3 = \gamma_3 + \frac{R_S I_{01}}{n_1 k T} \exp\left(\frac{eV_j}{n_1 k T}\right) + \frac{R_s}{R_p} + 1 \quad (\text{A.19})$$

$$\frac{\partial I}{\partial I_{ph}} = -\frac{\mu' (V_{bi} - V_j)}{\gamma_3} \left[1 - \exp \left(\frac{-1}{\mu' (V_{bi} - V_j)} \right) \right] \quad (\text{A.20})$$

$$\frac{\partial I}{\partial \mu'} = -\frac{I_{ph} (V_{bi} - V_j)}{\gamma_3} \left[1 - \left(1 + \frac{1}{\mu'^2 (V_{bi} - V_j)} \right) \exp \left(-\frac{1}{\frac{\mu\tau}{d_i^2} (V_0 - V_j)} \right) \right] \quad (\text{A.21})$$

$$\frac{\partial I}{\partial V_{bi}} = \frac{I_{ph}\mu'}{\gamma_3} \left[1 + \left(1 - \frac{1}{\mu' (V_{bi} - V_j)} \right) \exp \left(-\frac{1}{\frac{\mu\tau}{d_i^2} (V_0 - V_j)} \right) \right] \quad (\text{A.22})$$

$$\frac{\partial I}{\partial V} = I_{ph}\mu' \left[1 - \left(1 + \frac{1}{\mu' (V_{bi} - V_j)} \right) \exp \left(-\frac{1}{\frac{\mu\tau}{d_i^2} (V_0 - V_j)} \right) \right] \quad (\text{A.23})$$

$$\frac{\partial I}{\partial G} = -\frac{I_{ph,G}}{G\gamma_3} (V_0 - V_j) \frac{\mu\tau}{d_i^2} \left[1 - \exp \left(-\frac{1}{\frac{\mu\tau}{d_i^2} (V_0 - V_j)} \right) \right] \quad (\text{A.24})$$

A.4 Merten Model

The photocurrent of the one diode model is modified to:

$$I_{ph,g} = I_{ph} \left(\frac{1}{\frac{\mu\tau}{d_i^2} (V_{bi} - V_j)} - 1 \right) \quad (\text{A.25})$$

As in the case of Crandall's model, the parameters μ , τ and d_i are not linearly independent from each other and are thus in the following treated as a single

parameter μ' . The equations describing the diode and the shunt resistance are identical to A.5 - A.7 as long as the factor γ_1 is changed to γ_4 . The modified equations for I_{ph} , μ' , V_{bi} , R_s and the changed error propagation are given as:

$$\gamma_4 = -\frac{I_{ph}R_s}{\mu'(V_{bi}-V_j)^2} + \frac{eI_{01}R_s}{n_1kT} \exp\left(\frac{eV_j}{n_1kT}\right) + \frac{R_s}{R_p} + 1 \quad (A.26)$$

$$\frac{\partial I}{\partial I_{ph}} = \left(\frac{1}{\frac{\mu\tau}{d_i^2}(V_{bi}-V_j)} - 1 \right) / \gamma_4 \quad (A.27)$$

$$\frac{\partial I}{\partial \mu'} = -\frac{I_{ph}}{\mu'^2(V_{bi}-V_j)} / \gamma_4 \quad (A.28)$$

$$\frac{\partial I}{\partial V_{bi}} = -\frac{I_{ph}}{\gamma_4 \mu' (V_{bi}-V_j)^2} \quad (A.29)$$

$$\frac{\partial I}{\partial R_s} = \left[\frac{I_{ph}I}{(V_{bi}-V_j)^2 \mu'} - \frac{eI_{01}I}{n_1kT} \exp\left(\frac{eV_j}{n_1kT}\right) - \frac{I}{R_p} \right] / \gamma_4 \quad (A.30)$$

$$\frac{\partial I}{\partial V} = \left[\frac{-I_{ph}}{(V_{bi}-V_j)^2 \mu'} + \frac{eI_{01}}{n_1kT} \exp\left(\frac{eV_j}{n_1kT}\right) + \frac{1}{R_p} \right] / \gamma_4 \quad (A.31)$$

$$\frac{\partial I}{\partial T} = \left[\frac{\partial I_{ph,G}}{\partial T} - I_{01} \frac{eV_j}{n_1 k T^2} \exp \left(\frac{eV_j}{n_1 k T} \right) \right] / \gamma_4 \quad (\text{A.32})$$

$$\frac{\partial I}{\partial G} = \frac{I_{ph}}{\gamma_4 G} \left(\frac{1}{\frac{\mu\tau}{d_i^2} (V_{bi} - V_j)} - 1 \right) \quad (\text{A.33})$$

A.5 Backdiode Model

Here the voltage at the junction is modified to:

$$V_j = V - IR_s + \frac{kT}{e} \ln \left(1 - \frac{I}{I_{BD}} \right) \quad (\text{A.34})$$

In principle this leads to the same equations as A.4 - A.7 using the factor γ_5 instead of γ_1 . The difference to the derivations needed for the one diode model are the derivation after I_{BD} and the different thermal influence:

$$\gamma_5 = \frac{eI_{01}}{n_1 k T} \left(R_s - \frac{\frac{kT}{e}}{I_{BD} - I} \right) \exp \left(\frac{eV_j}{n_1 k T} \right) + \left(R_s - \frac{\frac{kT}{e}}{I_{BD} - I} \right) \frac{1}{R_p} + 1 \quad (\text{A.35})$$

$$\frac{\partial I}{\partial I_{BD}} = \left[\frac{I_{01} I}{n_1 I_{BD} (I_{BD} - I)} \exp \left(\frac{eV_j}{n_1 k T} \right) + \frac{k T I}{e R_p I_{BD} (I_{BD} - I)} \right] / \gamma_5 \quad (\text{A.36})$$

$$\frac{\partial I}{\partial T} = \left[-\frac{\partial I_{ph,G}}{\partial T} - \frac{eI_{01}(V - IR_S)}{n_1 k T^2} \exp\left(\frac{eV_j}{n_1 k T}\right) - \frac{\frac{k}{e} \ln\left(\frac{I}{I_{BD}} + 1\right)}{R_P} \right] / \gamma_5 \quad (\text{A.37})$$

Appendix B

Simulation of Environmental Conditions

There is a necessity for the simulation of the environmental conditions when predicting the outdoor performance of photovoltaic devices. This is taken from the literature and was thus not included in the main body of the work. This appendix gives an overview of the methods used and their implications.

B.1 Position of the Sun

In various parts throughout this work, the position of the Sun is calculated, mainly for the investigation of reflection on the solar cell or the calculation of the air mass. This calculation is normally carried out in the horizontal system in spherical coordinates. This system describes the position of the Sun with two angles, the azimuth Z and the elevation β , using the perspective of an observer on Earth's surface as illustrated in figure B.1. Due south is given by an azimuth of zero, the notation adopted for this work notes angles east with a positive sign. It is important to note, though, that this notation is not standardised and different researchers use different notations. This notation assumes the observer to be fixed,

while the Sun moves across the celestial sphere, thus simplifying the calculations significantly.

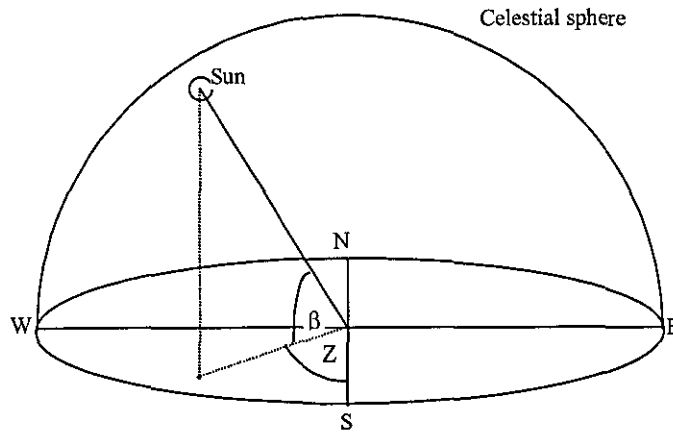


Figure B.1: *The Horizontal System for Describing the Position of the Sun.* The graph illustrates the azimuth Z and the elevation β , from the perspective of an observer.

Using this notation means that sunrise and sunset are described by elevation angles of zero, while the solar noon is described by an azimuth of zero.

There are several methods available, ranging from very simple textbook models as given e.g. in [Gottschalg 01]. A very standard way of performing this calculation is using the formulae adopted for the calculation of the Nautical Almanac. The problem with this method is that it uses a very complicated algorithm. Walraven [Walraven 78] published an algorithm that is much simpler, claiming an accuracy of 0.01° . This was doubted by other researchers (e.g. [Wilkinson 81]), because the refraction of the atmosphere of the Earth has to be taken into account to reach the desired accuracy. These corrections are included in the method adopted in this work.

The main reason for the relative simplicity of Walraven's [Walraven 78] algorithm is that the time calculations are based on noon on January 1st, 1980 instead of 1900 as the Nautical Almanac does. This shift of the point of reference allows

to use fewer correction terms. Additionally some of the minor corrections made in the original algorithm are neglected because they have no effect at the desired level of accuracy.

B.1.1 Notation

The algorithm determines positions on the Earth's surface by two spherical coordinates: the longitude α and the latitude Φ . The reference plane is the equatorial plane, perpendicular to the rotation axis and intersecting the surface of the Earth along the equator. Circles intersecting Earth's surface parallel to the equator determine the latitude. Latitude is defined as the angle between the equatorial plane and a line from the Earth's centre to a location on the surface of the Earth. By definition the latitude is positive in the northern hemisphere, negative in the southern one. For the determination of the longitude one needs a plane perpendicular to the equator including the rotational axis. This plane will create a circle of intersection, or two half circles going from one pole to the other named meridians. The zero longitude is by definition the meridian passing through Greenwich, UK. The longitude of any location is determined by the angle between the zero meridian and the meridian passing through the location. In this work positive values for longitudes west of Greenwich are used.

All calculations are based in an equatorial coordinate system and then are translated to the given location. The rotational axis intersects the celestial sphere in the celestial North Pole and the celestial South Pole. Again, two angles are sufficient to determine the position of any object on the celestial sphere.

The first of these angles is the declination. This angle is equivalent to the elevation in the horizontal system. It ranges from -90° to $+90^\circ$, positive in the northern hemisphere. The second coordinate is the right ascension α . The reference direction is the vernal equinox, the day in spring when the Sun crosses the equatorial

plane.

The movement of the Sun in this system is a circle on the celestial sphere with a tilt angle of approximately 23.5° , called the ecliptic. The Sun makes one revolution along the ecliptic per year in the direction opposite to the Earth's daily rotation. This is the cause of the seasons and the different noon time elevation of the Sun on different days.

B.1.2 Solar Time

The rotation of the Earth around its own axis has so far been neglected in this simple model, but it explains how the Sun describes its daily path over the celestial sphere. For calculating the exact position in the horizontal frame it is not sufficient to determine only the position of the Sun in the celestial sphere. Additionally the position of the celestial sphere with respect to the equatorial system must be known. These two positions are interconnected through the sidereal time. A sidereal day is the time between two successive transits of the hour circle of the vernal equinox across the celestial meridian, i.e. the time it takes the Sun to make a full circle on the celestial sphere and reach the reference point again. Due to the counter-rotational movements of the Sun and the Earth a sidereal day is slightly shorter than a standard day D_{st} [Walraven 78]:

$$D_{st} = 1.0027379 D_{sidereal} \quad (\text{B.1})$$

The sidereal time at Greenwich can be described as [Walraven 78]:

$$ST = 6.720165 + 24 \left(\frac{T_{1980}}{365.25} - Year - 1980 \right) + 0.000001411 T_{1980} \quad (\text{B.2})$$

Here T_{1980} is the time in days calculated from January 1st, 1980 and year is the actual year. In leap years after 1980 the value one should be subtracted from the day number if it is before March 1st.

Greenwich time has to be adapted to the local time, giving the following relation:

$$S = ST + (T_{1980} * 15 - \alpha) \quad (\text{B.3})$$

B.1.3 Position of the Sun

In the first step the position of the Sun is calculated on the celestial sphere. Due to two effects the speed of travel of the Sun is not constant. The first effect is that the path of the Sun is an ellipse. According to Kepler's second law, the speed of travel of the Sun on its path must vary because the radius vector must sweep equal areas in equal amounts of time. The second reason for the deviation of a solar day from a real day is the inclination of the ecliptic of the Sun of 23.5° . This causes a half yearly deviation in the length of a solar day from the standard day of 15 minutes. These effects make it rather difficult to calculate the longitude of the Sun. Walraven [Walraven 78] gives the following formulae:

$$\Theta = 2\pi \frac{T}{365.25} \quad (\text{B.4})$$

$$g = -0.031271 - (4.53963 \cdot 10^{-7} T + \Theta) \quad (\text{B.5})$$

$$L = 4.900968 + 3.67474 \cdot 10^{-7} T + (0.033434 - 2.3 \cdot 10^{-9} T) \sin g + 0.000349 \sin 2g + \Theta \quad (\text{B.6})$$

In the next step the angle ε between the plane of the ecliptic and the plane of the celestial equator is calculated as:

$$\varepsilon = 23.442^\circ - 3.56 \cdot 10^{-7} T \quad (\text{B.7})$$

Now the right ascension α and the declination δ can be calculated. With spherical trigonometry it can be shown that:

$$\tan \alpha = \cos \varepsilon \tan L \quad (\text{B.8})$$

$$\sin \delta = \sin \varepsilon \sin L \quad (\text{B.9})$$

Having calculated the sidereal time, the right ascension and the declination of the Sun, and knowing the local latitude, makes it possible to determine the position of the Sun in the horizontal system.

The hour angle ω is simply the right ascension minus the sidereal time:

$$\omega = \alpha - S \quad (\text{B.10})$$

In the final step the azimuth Z and the elevation β are calculated as through:

$$\sin \beta = \sin \Phi \sin \delta + \cos \Phi \cos \delta \cos \omega \quad (\text{B.11})$$

$$\sin Z = \frac{\cos \delta \sin \omega}{\cos \beta} \quad (\text{B.12})$$

In order to reach the desired accuracy of 0.01° the refraction of the Earth's atmosphere has to be taken into account. The azimuth is not affected. The correction is given by Wilkinson [Wilkinson 81] as:

$$RC = \frac{1}{0.955 + 20.267 \sin \beta} - 0.047121 \quad (\text{B.13})$$

$$QRC = \sin \beta + (0.0083RC) \quad (\text{B.14})$$

$$\beta_{refrac} = \arcsin(QRC) \quad (\text{B.15})$$

Applying the given set of formulae yields for the location of Loughborough at noon time the angles shown in figure B.2. The difference of siderial and standard time is apparent in the slight variation of the azimuth angle over the year.

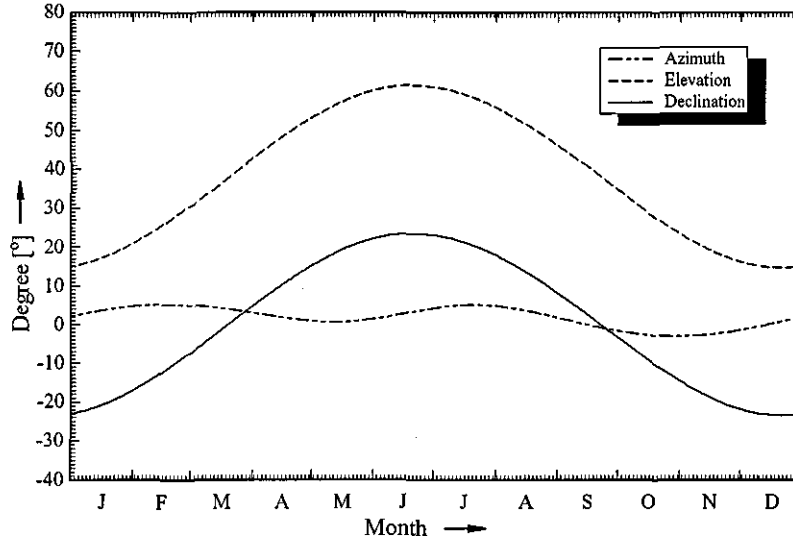


Figure B.2: *Angles Describing the Position of the Sun throughout the Year.* The graph shows the relevant angles of the Sun at noon of the corresponding day of the year for Loughborough.

B.2 Separation of Beam and Diffuse Irradiance

There are several empirical models available which are suitable for performing the task of calculating diffuse and beam irradiance. Nearly all of them are site specific. Each model is found to have an irradiance-dependent error pattern for different environments. There is no perfect model. One has to choose the model which performs best in the conditions of the investigated site. The model described in this section was originally published by Erbs et al. [Erbs 82]. This model is well suited for mid-range solar zenith angles (50-65°) [Skiba 96]. In this model the beam radiation G_{beam} is related to the global irradiance G_{glob} through:

$$G_{beam} = G_{glob} (1 - \Psi) \quad (B.16)$$

Here Ψ is an empirical function which depends on the clearness index k_t which has

to be calculated for the given conditions. The correlation between the clearness index and the beam radiation is calculated as [Erbs 82]:

$$\Psi = \begin{cases} 1 - 0.09k_t & k_t \leq 0.22 \\ 0.9511 - 0.1604k_t + 4.388k_t^2 - 16.638k_t^3 + 12.336k_t^4 & 0.22 < k_t < 0.8 \\ 0.165 & k_t \geq 0.8 \end{cases} \quad (\text{B.17})$$

The clearness index is the ratio of the percentage of extraterrestrial radiation reaching the surface of the Earth and thus is highly weather dependent. The above regions of the clearness index could be described as clear weather for the highest category (>0.8), overcast for the middle region and heavily clouded for the low region (<0.22). The clearness index is given as:

$$k_t = \frac{G_h}{G_{h,oa}} \quad (\text{B.18})$$

Here $G_{h,oa}$ is the irradiance on a horizontal plane outside the atmosphere and G_h the irradiance on a horizontal plane on the ground. $G_{h,oa}$ exhibits a seasonal variation, as illustrated in figure B.3.

Finally, the seasonal variation of the irradiance outside atmosphere is calculated. While G_h is given by meteorological data, $G_{h,oa}$ has to be calculated in dependence of the day of the year (DoY). To do this one first has to calculate the day angle Γ , which is given as:

$$\Gamma = 2\pi \frac{\text{DoY} - 1}{365} \quad (\text{B.19})$$

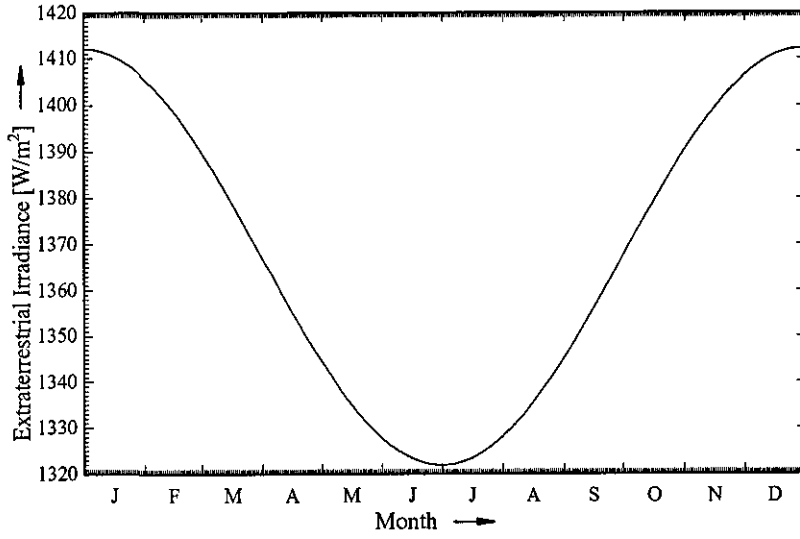


Figure B.3: *Variation of the Irradiance on a Horizontal Plane Outside Atmosphere.* The seasonal variation is shown calculated using the method given in the text.

Furthermore, the eccentricity factor E_0 of the Sun has to be calculated. This is done using Spencer's Fourier series as given in [Gottschalg 01]:

$$E_0 = 1.0001 + 0.034221\cos\Gamma + 0.00128\sin\Gamma + 0.000719\cos 2\Gamma + 0.000077\sin 2\Gamma \quad (\text{B.20})$$

The radiation outside the atmosphere is then calculated as:

$$G_{h,oa} = E_0 G_{SC} \sin\beta \quad (\text{B.21})$$

G_{SC} is the solar constant, given as 1353 W/m^2 .

The diffuse radiation G_{diff} is simply the difference between the global and the beam radiation:

$$G_{diff} = G_{glob} - G_{beam} \quad (B.22)$$

This model tends to underestimate the beam radiation slightly.

B.3 Reflection on the Surface of a PV Module

Radiation of interest for the performance of PV devices is the radiation transmitted to the main device. The transmitted light is that part which passes through a material, i.e. the incident beam less reflection and absorption. The relationship between incident beam, reflection and refraction is illustrated in figure B.4. Both effects cause the beam to change direction. When reflection occurs, the new direction is the incident direction mirrored at the perpendicular to the material. Thus, the angle of the reflected beam is the same as the incident beam, although with a negative sign, i.e. α equals $-\alpha$ ".

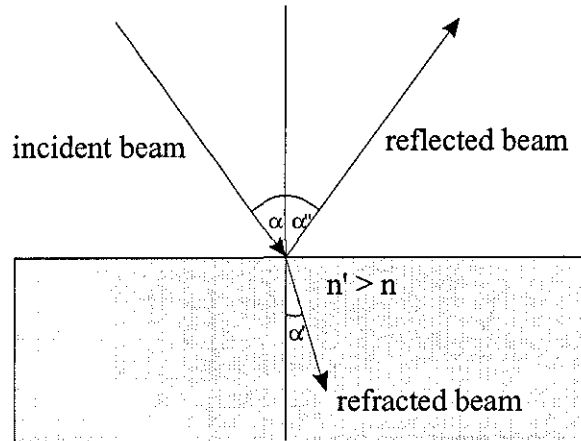


Figure B.4: *Illustration of Reflection, Refraction and Transmission.* The incident beam is refracted in the material and reflected by the material. The angle of reflection to the perpendicular is the same as the angle of the incident beam with a negative sign while the refraction changes the angle of incidence.

Material	Refractive Index
Vacuum	1
Air	1.0003
Water	1.333
Glass	~1.5
Diamond	2.419

Table B.1: Refractive Index for Some Materials.

Refraction causes a change in the angle of the beam. This change of angle depends on the optical density of the material, which is indicated by the refractive index. The angle of refraction α' can easily be calculated by the application of Snellius' law, which is given by:

$$n \sin \alpha = n' \sin \alpha' \quad (\text{B.23})$$

This links the optical density of the initial material, described by the refractive index n , and the incident angle to the same parameters for the second material, which are annotated by an apostrophe. Table B.1 gives some typical values for the refractive index of various materials.

The refractive index is also important for calculating the magnitude of the reflected beam, i.e. how much light actually reaches the solar system underneath its cover. This can be done using the Fresnel expression, which assumes unpolarised (i.e. random) light. The light is split into components: parallel polarised r_p and orthogonal polarised r_o . The overall reflection r is then given as:

$$r = \frac{1}{2} (r_o + r_p) \quad (\text{B.24})$$

The components are described as:

$$r_p = \frac{\sin^2(\alpha' - \alpha)}{\sin^2(\alpha' + \alpha)} \quad (\text{B.25})$$

$$r_o = \frac{\tan^2(\alpha' - \alpha)}{\tan^2(\alpha' + \alpha)}$$

This can very easily be linked to the refractive index, although the resulting formula is not as simple. The resulting reflection is illustrated in figure B.5. It is apparent that even minimal changes in the refractive index can have a significant effect for higher angles of incidence, as seen for the curve with n equal to 1.01, which is only 1% above the refractive index of a vacuum. On the other hand, high refractive indices will result in significant reflection of light even if the angle of incidence is zero.

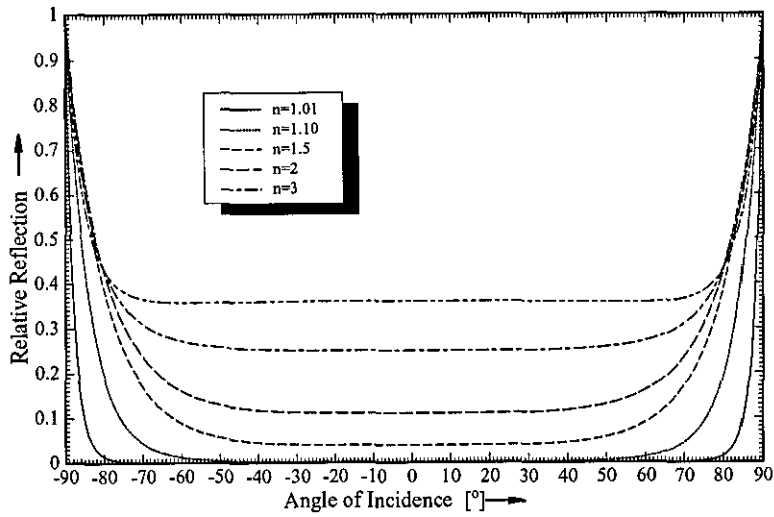


Figure B.5: *Illustration of Fresnel-Reflection.* It is apparent that even one percent change in the refractive index can have a significant impact for larger angles of incidence. High refractive indices will reflect significant amounts even at low angles of incidence.

Installation	INOCT
Rack Mounted	NOCT-3K
Direct Mount	NOCT+18K
Integrated	Dependent on Standoff

Table B.2: Influence of Mounting on the Operating INOCT Temperature.

B.4 Operating Temperature of the PV Module

The method used to calculate module temperature is based on the model presented by Fuentes [Fuentes 85]. Plane-of-array irradiance, ambient temperature and wind speed are used as inputs, along with the Installed Nominal Operating Cell Temperature (INOCT). This latter parameter differs from the JPL [JPL 81] standard NOCT value (NOCT = cell temperature at 800 W/m², 20°C ambient and 1 m/s wind speed) inasmuch as the mounting configuration is taken into account. Building-integrated modules, for example, will clearly have different thermodynamic properties from those which are rack mounted. Table B.2 shows a method based on empirical data for obtaining INOCT from the NOCT value and mounting configuration.

B.4.1 Energy Balance

The temperature calculation assumes an initial simplified energy balance in which the module receives heat in the form of irradiance and loses heat via convection to ambient and radiation to the sky and ground. This is given as:

$$hc(T_c - T_a) + \varepsilon\sigma(T_c^4 - T_g^4) - \alpha G + mc\frac{\partial T_c}{\partial t} = 0 \quad (\text{B.26})$$

Here hc is the overall convective coefficient of the module, T_c is the cell temperature, T_a is the ambient temperature, ε is the emissivity of the module, T_g is the ground temperature, α is the absorption of the module and mc is the thermal

mass per unit area.

The above radiation terms can be expanded and approximated in order to linearise the equation. As the product $(T_c^2 + T_s^2)(T_c + T_s)$ changes less than 5% for a 10°C variation in T_c , the product can be considered approximately constant. The radiation terms in equation B.26 then become linear:

$$(T_c^4 - T_s^4) = (T_c^2 + T_s^2) (T_c + T_s) (T_c - T_s) \quad (\text{B.27})$$

After solving for T_c , the value of this constant can then be re-evaluated and solved again for T_c . Thus, the heat balance can be iterated to any desired accuracy. The heat balance equation can be simplified by defining a radiation coefficient hr as:

$$hr_s = \epsilon \sigma (T_c^2 + T_s^2) (T_c + T_s) \quad (\text{B.28})$$

$$hr_g = \epsilon \sigma (T_c^2 + T_g^2) (T_c + T_g) \quad (\text{B.29})$$

Here hr_g is the radiative coefficient to the ground and hr_s is the radiative coefficient to the sky. The assumption can also be made that the irradiance varies between time steps in a linear fashion:

$$G = G_0 + \frac{\Delta G t}{\Delta t} \quad (\text{B.30})$$

The resulting heat balance results then in:

$$hc(T_c - T_a) + hr_s(T_c - T_s) + hr_g(T_c - T_g) - \alpha \left(G_0 + \frac{\Delta G t}{\Delta t} \right) + mc \frac{\partial T_c}{\partial t} = 0 \quad (\text{B.31})$$

Here G_0 is the irradiation in the last time step. This can be integrated to obtain an explicit expression for T_c :

$$T_c = \frac{(hcT_a + hr_sT_s + hr_gT_g + \alpha \frac{\Delta G}{L})(1 - e^L) + \alpha \Delta G}{hc + hr_s + hr_g} + T_{c0}e^L \quad (\text{B.32})$$

Where T_{c0} is the module temperature at the start of the time step. L is the reciprocal thermal capacity of the module and characterises the thermal lag. It is calculated as:

$$L = -(hc + hr_s + hr_g) \frac{\Delta t}{mc} \quad (\text{B.33})$$

The parameters in equation B.32 can now be applied to calculate an initial estimate of T_c . However, as the value of hr_s is dependent on T_c , the solution requires iterating.

B.4.2 Convective Coefficient of Module Top Surface

The convective coefficient is dependent on the profile of the air near the module top surface which may be laminar, turbulent, free or a combination of these conditions. Convective coefficients are therefore required for all considerations. For laminar, turbulent, free and mixed convection the following formulae are used:

$$\begin{aligned}
St \cdot Pr^{0.67} &= 0.86 Re^{-0.5} & Re < 1.2 \cdot 10^5 \\
St \cdot Pr^{0.4} &= 0.028 Re^{-0.2} & Re > 1.2 \cdot 10^5 \\
Nu &= 0.21 (Gr \cdot Pr)^{0.32} \\
h_{mixed}^3 &= h_{free}^3 + h_{forced}^3
\end{aligned} \tag{B.34}$$

The last line in equation B.34 applies to the transition region between free and laminar conditions. The transition region between laminar and turbulent conditions is modelled as an abrupt change at $Re = 1.2 \times 10^5$. A 0.3m x 1.2m module is assumed, giving a hydraulic diameter of 0.5m for the calculation of the Reynolds number.

B.4.3 Convective Coefficient of Module Bottom Surface

The effect of different mounting configurations on the convective coefficient is approximated by the use of INOCT. The ground (or roof) temperature is assumed to lie somewhere between ambient and that of the module. For a rack mount, the convective coefficient under the module is approximately equal to that on top and ground or roof temperature would be equal to ambient. It is obvious, that a rack mount would be the best case for maximum heat transfer and situations less than ideal are modelled by the assumption that the radiation and convection under the module would be penalised equally. This penalty is calculated by using the energy balance equation at NOCT conditions:

$$\alpha S - hcT(T_{INOCT} - T_a) - hr_s(T_{INOCT} - T_s) = hc_B(T_{INOCT} - T_a) + hr_g(T_{INOCT} - T_g) \tag{B.35}$$

Here hc_T is the convective coefficient of the top of the module and hc_B is the convective coefficient of the bottom of the module. The ratio of actual to ideal heat loss from the back of module convection and radiation is calculated as:

$$R = \frac{hc_B (T_{INOCT} - T_a) + \varepsilon \sigma (T_{INOCT}^4 - T_g^4)}{hc_T (T_{INOCT} - T_a) + \varepsilon \sigma (T_{INOCT}^4 - T_a^4)} \quad (B.36)$$

Combining equations B.35 and B.36 then yields:

$$R = \frac{\alpha S - hc_t (T_{INOCT} - T_a) + \varepsilon \sigma (T_{INOCT}^4 - T_g^4)}{hc_T (T_{INOCT} - T_a) + \varepsilon \sigma (T_{INOCT}^4 - T_a^4)} \quad (B.37)$$

This allows the calculation of the convective coefficient under the module and the ground/roof temperature:

$$hc_B = R \cdot hc_T \quad (B.38)$$

$$T_g = [T_{INOCT}^4 - R (T_{INOCT}^4 - T_a^4)]^{0.25} \quad (B.39)$$

These equations are valid for NOCT conditions only. The translation to other environmental conditions is done by scaling the bottom convective coefficient in proportion to the top coefficient. The overall convective coefficient is the sum of both, the top and the bottom convective coefficients.

Ground or roof temperatures are scaled with respect to the ratio of ambient and module temperatures, with the ratio R_g being constant for all environmental conditions:

$$T_g = T_a + R_g (T_c - T_a) \quad (\text{B.40})$$

$$R_g = \frac{T_g - T_a}{T_{INOCT} - T_a} \quad (\text{B.41})$$

As ground temperature varies with module temperature, an iteration is required to obtain an appropriate value.

B.4.4 Sky Temperature

The sky temperature T_s is calculated using Swinbank's equation for clear sky conditions:

$$T_s = 0.0552T_a^{1.5} \quad (\text{B.42})$$

Atmospheric conditions will, however, cause the sky temperature to approach that of ambient. Based on the assumption that a clear sky has a clearness index of 0.9, the sky temperature is then estimated as:

$$T_s = \frac{0.0552k_t}{0.9}T_a^{1.5} + T_a \left(1 - \frac{k_t}{0.9}\right) \quad (\text{B.43})$$

Appendix C

Publications and Presentations Arising from this Work

C.1 Conference Publications

R. Gottschalg, D.G. Infield and M.J. Kearney: *Influence of Environmental Conditions on Outdoor Performance of Thin Film Devices*. In: 17th European Photovoltaic Solar Energy Conference, Munich, 2001, to be published.

R. Gottschalg, D.G. Infield, H.G. Beyer and F. Jakobides: *Translation and Validation of Laboratory Measurements of Amorphous Silicon Devices to Real Operating Conditions*. In: 17th European Photovoltaic Solar Energy Conference, Munich, 2001, to be published.

R. Gottschalg, D.G. Infield and M.J. Kearney: *Performance of Thin Film Solar Cells under Real Operating Conditions*. In: IOP Thin Film Photovoltaic Materials and Devices Meeting, London, 2001, to be published.

R. Gottschalg, D.G. Infield and M.J. Kearney: *Influence of Environmental Conditions on Thin Film Photovoltaic Devices*. In: Proceedings of Renewable Energy

in Maritime Climates (REMIC) Conference, Belfast, 2001, pp 119-126.

M.J. Holley, **R. Gottschalg**, A.D. Simmons, D.G. Infield and M.J. Kearney: *Modelling the Performance of a-Si PV Systems*. In: Proceedings of the 16th European Photovoltaic Solar Energy Conference, Glasgow, 2000, pp. 2356-2359.

R. Gottschalg, G. Perentzis, D.G. Infield and M.J. Kearney: *Comprehensive Approach for the Estimation of Outdoor Degradation of Amorphous Silicon Photovoltaic Devices*. In: Proceedings of the International Solar Energy Society Conference, Jerusalem, 1999, pp 129-133.

R. Gottschalg, B.J. Elsworth, D.G. Infield and M.J. Kearney: *Investigation of the Back Contact of Cadmium Telluride Solar Cells*. In: Proceedings of the International Solar Energy Society Conference, Jerusalem, 1999, pp. 124-128.

R. Gottschalg, D.G. Infield and M.J. Kearney: *Spectral Losses on Thin Film Solar Cells in Loughborough, UK*. In: Proceedings of the UK- Solar Energy Society Jubilee Meeting, Brighton, 1999, pp. 35-41.

R. Gottschalg, M. Rommel, D.G. Infield and M.J. Kearney: *Applicability of Parametric Models for Amorphous Silicon Modules and Cells*. In: Proceedings of the 15th European Photovoltaic Solar Energy Conference, Vienna, 1998, pp. 990-993.

R. Gottschalg, D.G. Infield and M.J. Kearney: *Parametrisation of Thin Film Solar Cells*. In: Proceedings of the East Midlands Universities Renewable Energy Conference '98, Loughborough, 1998, pp. 49-54.

R. Gottschalg, M. Rommel, D.G. Infield and H. Ryssel: *Comparison of Different Methods for the Parameter Determination of the Solar Cells Double Exponential Equation*. In: Proceedings of the 14th European Photovoltaic Solar Energy Conference, Barcelona, 1997, pp. 321-324.

R. Gottschalg, M. Rommel and D.G. Infield: *Variation of Solar Cell Equivalent Circuit Parameters under Different Operating Conditions.* In: Proceedings of the 14th European Photovoltaic Solar Energy Conference, Barcelona, 1997, pp. 2176-2179.

C.2 Journal Publications

R. Gottschalg, D.G. Infield and M.J. Kearney: *Experimental Study of Spectral Variation of Relevance to Thin Film Solar Cells.* submitted to Solar Energy Materials and Solar Cells.

R. Gottschalg, M. Rommel, D.G. Infield, M.J. Kearney and H. Ryssel: *Influence of the Measurement Environment on the Extraction of the Physical Parameters of Solar Cells.* In: Journal of Measurement Science and Technology **10** (1999) 9 pp. 794-803.

R. Gottschalg, D. G. Infield and M. J. Kearney: *Parametrisation of Thin Film Solar Cells.* In: Journal of Ambient Energy **17** (1998) 3, pp. 135-142.

C.3 Oral Presentations

R. Gottschalg, D.G. Infield, H.G. Beyer and F. Jakobides: *Translation and Validation of Laboratory Measurements of Amorphous Silicon Devices to Real Operating Conditions.* In: 17th European Photovoltaic Solar Energy Conference, Munich, 2001.

R. Gottschalg, D.G. Infield and M.J. Kearney: *Performance of Thin Film Solar Cells under Real Operating Conditions.* In: Thin Film Photovoltaic Materials and Devices Meeting, London, 2001.

R. Gottschalg, D.G. Infield and M.J. Kearney: *Influence of Environmental Conditions on Thin Film Photovoltaic Devices.* Renewable Energy in Maritime Climates (REMIC) Conference, Belfast, 2001.

R. Gottschalg, G. Perentzis, D.G. Infield and M.J. Kearney: *Comprehensive Approach for the Estimation of Outdoor Degradation of Amorphous Silicon Photovoltaic Devices.* International Solar Energy Society Conference, Jerusalem, 1999.

R. Gottschalg, B.J. Elsworth, D.G. Infield and M.J. Kearney: *Investigation of the Back Contact of Cadmium Telluride Solar Cells.* International Solar Energy Society Conference, Jerusalem, 1999.

R. Gottschalg, D G. Infield and M.J. Kearney: *Parametrisation of Thin Film Solar Cells.* East Midlands Universities Renewable Energy Conference '98, Loughborough, February 1998.

Bibliography

- [Alonso 92] M.C. Alonso, F. Fabero & F. Chenlo. *Extrapolation of I-V Curves of Degraded and Undegraded a-Si Solar Cells to STC - Applicability of the one Exponential Model to a-Si*. In Proceedings of the 11th European Photovoltaic Solar Energy Conference, Montreux, pages 738-741, 1992.
- [Alonso 94] M.C. Alonso & F. Chenlo. *Validation of the One Exponential Model for Undegraded and Degraded a-Si Solar Devices - Comparison with other Models and with c-Si Solar Cells*. In Proceedings of the 12th European Photovoltaic Solar Energy Conference, Amsterdam, pages 176-179, 1994.
- [Alonso 98] M. C. Alonso & F. Chenlo. *Experimental Study of Reverse Biased Silicon Solar Cells*. In Proceedings of the 15th European Photovoltaic Solar Energy Conference, Vienna, pages 2376-2379. Stephenson, 1998.
- [Anderson 96] A.J. Anderson. Photovoltaic Translation Equations: A New Approach, Final Subcontract Report. NREL, Golden, 1996.
- [Anderson 00] D. Anderson, J. Bishop & E. Dunlop. *Energy Rating for Photovoltaic Modules*. In Proceedings of the 16th Euro-

pean Photovoltaic Solar Energy Conference, Glasgow, pages 2087–2091. James and James, 2000.

- [Appelbaum 93] J. Appelbaum, A. Chait & D. Thompson. *Parameter Estimation and Screening of Solar Cells*. Progress in Photovoltaics., vol. 1, pages 93–106, 1993.
- [Araujo 82] G.L. Araujo, E. Sanchez & M. Marti. *Determination of the Two-Exponential Solar Cell Equation Parameters from Empirical Data*. Solar Cells, vol. 5, pages 199–204, 1982.
- [Araujo 86] G.L. Araujo, A. Cuevas & J.M. Ruiz. *The Effect of Distributed Series Resistance on the Dark and Illuminated Current-Voltage Characteristics of Solar Cells*. IEEE Transactions on Electron Devices, vol. 33, no. 3, pages 391–401, 1986.
- [Asaoka 94] K. Asaoka, M. Izumina, Y. Tawada, T. Hama, M. Itoh, Y. Suzuki, M. Ohnishi & R. Shimokawa. *Current-Induced Degradation Method for Stabilization of a-Si Solar Cells*. Solar Energy Materials and Solar Cells, vol. 34, no. 1-4, pages 465–472, 1994.
- [Beier 92] J. Beier. Untersuchungen zur Anwendbarkeit des Superpositionsprinzips bei Silizium-Solarzellen, Dissertation. Fraunhofer ISE, Freiburg, 1992.
- [Berman 99] D. Berman, D. Faiman & B. Fahri. *Sinusoidal Spectral Correction for High Precision Outdoor Module Characterization*. Solar Energy Materials and Solar Cells, vol. 58, pages 253–264, 1999.

- [Birkmire 95] R.W. Birkmire, J.E. Phillips, W.A. Buchanan, S.S. Hegedus, B.E. McCandless & W.N. Shafaraman. Processing and Modeling Issues for Thin-Film Solar Cell Devices, Annual Subcontract Report 12.01.1994-15.01.1995, Report No.: NREL/TP-451-8017. NREL, Golden, 1995.
- [Bonnet 94] D. Bonnet. *Die Cadmium-Tellurid-Dünnschicht-Solarzelle*. In J. Schmid, editor, *Photovoltaik: Strom aus der Sonne. Technologie, Wirtschaftlichkeit und Marktentwicklung*, pages 49–64, Heidelberg, 1994. C.F. Müller.
- [Bowron 91] J.W. Bowron, S.D. Damaskinos & A.E. Dixon. *Characterization of the Anomalous Second Junction in Mo/CuInSe₂/(CdZn)/S/ITO Solar Cells*. *Solar Cells*, vol. 31, pages 159–169, 1991.
- [Breitenstein 95] O. Breitenstein & K. Iwig. *Forward Bias Shunt Hunting in Solar Cells by Dynamical Precision Contact Thermography*. In *Proceedings of the 13th European Photovoltaic Solar Energy Conference, Nice*, pages 145–149, 1995.
- [Bücher 90] K. Bücher & K. Heidler. *Photovoltaic Measurements and Calibration*. In *Technical Digest of the International PVSEC-5, Kyoto*, pages 489–492, Kyoto, 1990.
- [Burgers 96] A.R. Burgers, J.A. Eikelboom, A. Schönecker & W.C. Sinke. *Improved Treatment of the Strongly Varying Slope in Fitting Solar Cell I-V Curves*. In *Proceedings of the 25th IEEE Photovoltaic Specialists Conference, Washington DC*, pages 569–572. IEEE, 1996.

- [Caceci 84] M.S. Caceci & W.P. Cacheris. *Fitting Curves to Data. The Simplex Algorithm is the Answer*. Byte, vol. 05, pages 340–360, 1984.
- [Camani 98] M. Camani, N. Cereghetti, D. Chianese & S. Rezzionico. *How Long Will My PV Plant Last?* In Proceedings of the 15th European Photovoltaic Solar Energy Conference, Vienna, pages 2058–2061, Felmersham, 1998. Stephenson.
- [Carlson 00] D.E. Carlson, G. Lin & G. Ganguly. *Temperature Dependence of Amorphous Silicon Solar Cell PV Parameters*. In Proceedings of the 28th IEEE Photovoltaic Specialists Conference, Anchorage. IEEE, 2000.
- [Charles 81] J.P. Charles, M. Abdelkrim, Y.H. Muoy & P. Mialhe. *A Practical Method of Analysis of the Current-Voltage Characteristics of Solar Cells*. Solar Cells, vol. 4, pages 169–178, 1981.
- [Chen 94] M. Chen. *Spektrale Sonnenbestrahlungsstärke: Messungen, Modellrechnungen, aktinische Bewertung*. Verlag Dr. Köster, Berlin, 1994.
- [Chenlo 91] F. Chenlo & N. Vela. *Analysis of Different Commercial Technologies a-Si Submodules: Characterization and Short-Time Outdoor Degradation Test*. In Proceedings of the 10th European Photovoltaic Solar Energy Conference, Lisbon, pages 408–411, Felmersham, 1991. Stephenson.
- [Conibeer 01] G.J. Conibeer, C. Jardine & K. Lane. *PV-COMPARE: Direct Comparison of Eleven PV Technologies at Two Loca-*

tions in Northern and Southern Europe. In Proceedings of 17th European Photovoltaic Solar Energy Conference, Munich, page to be publ., 2001.

- [Coors 97] S. Coors & M. Böhm. *Validation and Comparison of Curve Correction Procedures for Silicon Solar Cells.* In Proceedings of the 14th European Photovoltaic Solar Energy Conference, Barcelona, pages 220–223, 1997.
- [Coors 98] S. Coors, B. Schneider & M. Böhm. *Towards an Analytic Model for Curve Correction Procedures for Amorphous Silicon a-Si:H Solar Cells.* In Proceedings of the 15th European Photovoltaic Solar Energy Conference, Vienna, pages 902–905, Felmersham, 1998. Stephenson.
- [Crandall 83] R.S. Crandall. *Modeling of Thin Film Solar Cells: Uniform Field Approximation.* Journal of Applied Physics, vol. 54, no. 12, pages 7176–7166, 1983.
- [Craparo 95] J.C. Craparo & E.F. Thacher. *A Solar-Electric Vehicle Simulation Code.* Solar Energy, vol. 55, no. 3, pages 221–234, 1995.
- [Cueto 98] J. A. del Cueto. *Review of the Field Performance of One Cadmium Telluride Module.* Progress in Photovoltaics: Research and Applications, vol. 6, no. 6, pages 433–446, 1998.
- [Cueto 99] J. A. del Cueto & B. von Roedern. *Temperature-Induced Changes in the Performance of Amorphous Silicon Multi-Junction Modules in Controlled Light Soaking.* Progress

in Photovoltaics: Research and Applications, vol. 7, no. 3, pages 101–112, 1999.

- [DeVos 84] A. DeVos. *The Distributed Series Resistance Problem in Solar Cells*. Solar Cells, vol. 12, no. 3, pages 311–327, 1984.
- [Duffie 74] J.A. Duffie & W.A. Beckmann. Solar Energy. Thermal Processes. Wiley, New York, 1974.
- [Eikelboom 00] J. A. Eikelboom & M. J. Jansen. Characterisation of PV Modules of New Generations. Results of Tests and Simulations. ECN, Petten, NL, 2000.
- [Eisgruber 94] I.L. Eisgruber & J.R. Sites. *Effect of Thin Film Module Geometry on Solar Cell Current-Voltage Analysis*. In Proceedings of the First World Conference on Photovoltaic Energy Conversion, Hawaii, pages 271–274. IEEE, 1994.
- [Elsworth 98] B. J. Elsworth. Investigation of the Back Contact of Cadmium Telluride Photovoltaic Cells, MSc Thesis. CREST, Loughborough, 1998.
- [Emery 86] K. A. Emery. *Solar Simulators and I-V Measurement Methods*. Solar Cells, vol. 18, pages 251–260, 1986.
- [Emery 87] K. A. Emery, C. R. Osterwald & C. V. Wells. *Uncertainty Analysis of Photovoltaic Efficiency Measurements*. Proceedings of the 20th IEEE Photovoltaic Specialists Conference, pages 153–159, 1987.
- [Enebish 93] N. Enebish, D. Agchbayar, S. Dorjkhanda, D. Baatar & I. Ylemj. *Numerical Analysis of Solar Cell Current-Voltage*

Characteristics. Solar Energy Materials and Solar Cells, vol. 29, no. 3, pages 201–208, 1993.

- [Engelhardt 96] F. Engelhardt. Elektrische Charakterisierung von polykristallinen Dünnschichtsolarzellen in Abhängigkeit von der Beleuchtungsintensität, Diplomarbeit. Universität Bayreuth, Lehrstuhl Experimentalphysik II, Bayreuth, 1996.
- [Erbs 82] D.G. Erbs, S.A. Klein & J.A. Duffie. *Estimation of the Diffuse Radiation Fraction for Hourly, Daily and Monthly-Average Global Radiation*. Solar Energy, vol. 28, pages 293–302, 1982.
- [Fabero 91] F. Fabero & F. Chenlo. *Variance in the Solar Spectrum with the Position of the Receiver Surface during the Day for PV applications*. In Proceedings of the 22nd IEEE Photovoltaic Specialists Conference, pages 812–817. IEEE, 1991.
- [Fan 86] J.C.C. Fan. *Theoretical Temperature Dependence of Solar Cell Parameters*. Solar Cells, vol. 17, pages 309–315, 1986.
- [Fischer 94] D. Fischer & A.V. Shah. *Compensation of the Dangling-Bond Space-Charge in Amorphous Silicon Solar Cells by Graded Low-Level Doping in the Intrinsic Layer*. Applied Physics Letter, vol. 65, no. 8, pages 986–988, 1994.
- [Fuentes 85] M.K. Fuentes. *Thermal Characterization of Flat-Plate Photovoltaic Arrays*. In Proceedings of the 18th IEEE Photovoltaic Specialists Conference, pages 203–207. IEEE, 1985.

- [Fuentes 87] M.K. Fuentes. A Simplified Thermal Model for Flat-Plate Photovoltaic Arrays. Sandia, Albuquerque, 1987.
- [Gay 96] R.R. Gay. *personal communication*, 1996.
- [Gerthsen 89] C. Gerthsen. Physik. Springer Verlag, Heidelberg, 1989.
- [Gottschalg 97] R. Gottschalg, M. Rommel & D. G. Infield. *Variation of Solar Cell Equivalent Circuit Parameters under Different Operating Conditions*. In Proceedings of the 14th European Photovoltaic Solar Energy Conference, Barcelona, pages 2176–2179. Stephenson, 1997.
- [Gottschalg 98] R. Gottschalg, M. Rommel, D.G. Infield & M.J. Kearney. *Applicability of Parametric Models for Amorphous Silicon Modules and Cells*. In Proceedings of the 15th European Photovoltaic Solar Energy Conference, Vienna, pages 990–993. Stephenson, 1998.
- [Gottschalg 01] R. Gottschalg. *The Solar Resource and the Fundamentals of Solar Radiation for Renewable Energy Systems*. Sci-Notes, vol. 1, no. 1, pages 1–64, 2001.
- [Green 92] M.A. Green. Solar Cells. Operating Principles, Technology and System Applications. University of New South Wales, Kensington, 1992.
- [Guha 00] S. Guha, J. Yang & A. Banerjee. *Amorphous Silicon Alloy Photovoltaic Research - Present and Future*. Progress in Photovoltaics, vol. 8, pages 141–150, 2000.

- [Hack 85] M. Hack & M.S. Shur. *Physics of Amorphous Silicon Alloy p-i-n Solar Cells*. Journal of Applied Physics, vol. 58, no. 2, pages 997–1020, 1985.
- [Hegedus 97] S.S. Hegedus. *Current-Voltage Analysis of a-Si and a-SiGe Solar Cells Including Voltage Dependent Photocurrent Collection*. Progress in Photovoltaics, vol. 5, pages 151–168, 1997.
- [Heidler 93] K. Heidler. *Photovoltaische Meßtechnik*. In Dieter Meissner, editor, Solarzellen. Physikalische Grundlagen und Anwendungen in der Photovoltaik, pages 184–217. Vieweg, Wiesbaden, 1993.
- [Herrmann 97] W. Herrmann, H. Becker & W. Wiesner. *Round Robin Test on Translation Procedures for Measured PV Generator Characteristics*. In Proceedings of the 14th European Photovoltaic Solar Energy Conference, Barcelona, pages 203–206, 1997.
- [Hirata 95] Y. Hirata & T. Tani. *Output Variation of Photovoltaic Modules with Environmental Factors - I. The Effect of Spectral Solar Radiation on Photovoltaic Module Output*. Solar Energy, vol. 55, no. 6, pages 463–468, 1995.
- [Hirata 98] Y. Hirata, T. Inasaka & T. Tani. *Output Variation of Photovoltaic Modules with Environmental Factors - II: Seasonal Variation*. Solar Energy, vol. 63, no. 3, pages 185–189, 1998.

- [Holley 99] M.J. Holley. Modelling the Seasonal Variations in Performance of Amorphous Silicon Photovoltaic Devices. MSc Thesis. CREST, Loughborough, 1999.
- [Hubin 95] J. Hubin & A.V. Shah. *Effect of the Recombination Function on the Collection in a p-i-n Solar Cell*. Philosophical Magazine B - Physics of Cond. Matter, Stat. Mechanics Electronic Optical and Magnetic Properties, vol. 72, no. 6, pages 589–599, 1995.
- [Ichikawa 87] W. Ichikawa, O. Nabeta, K. Maruyama, T. Ihara, T. Yoshida, H. Sakai & Y. Uchida. *Long Term Experimental Tests and Analysis of Single Junction a-Si PV System*. In Stability of Amorphous Silicon Alloy Materials and Devices. AIP Conference Proceedings 157, pages 318–325. AIP, 1987.
- [IEC 94] IEC, editor. Solar Simulator Performance Requirements, Draft Standard IEC 60904-9. International Electrotechnical Commission, Geneva, 1994.
- [Isomura 98] M. Isomura, H. Yamamoto, M. Kendo & K. Matsuda. *The Light-Induced Increase in Open Circuit Voltage of Amorphous Silicon Solar Cells*. In Proceedings of the 15th European Photovoltaic Solar Energy Conference, Vienna, pages 925–928. Stephenson, 1998.
- [Jardine 01] C. Jardine. *personal communication*, 2001.
- [Jia 87] Q.X. Jia & E.K. Liu. *A Method for the Direct Measurement of the Solar Cell Junction Ideality Factor*. Solar Cells, vol. 22, pages 15–21, 1987.

- [JPL 81] JPL, editor. Block V - Solar Cell Module Design and Test Specification for Residential Applications. Jet Propulsion Laboratory, 1981.
- [Kleiss 92] G. Kleiss, K. Bücher, A. Raicu & K. Heidler. *Performance of Thin Film Solar Cells under Realistic Reporting Conditions Including Degradation Effects*. In Proceedings of the 11th European Photovoltaic Solar Energy Conference, Montreux, pages 578–581. Harwood Academic Publishers, 1992.
- [Kleiss 94] G. Kleiss, K. Bücher, P. Ragot & M. Chantant. *Monitoring Outdoor Performance and Photodegradation of a-Si:H Modules by Evaluation of Continuously Measured I-V Curves*. In Proceedings of the First World Conference on Photovoltaic Energy Conversion, Hawaii, pages 531–534. IEEE, 1994.
- [Kleiss 97] G. Kleiss. Energetische Bewertung von Photovoltaischen Modulen auf der Grundlage der Jahreswirkungsgradmethode, Dissertation. Verlag Dr. Köster, Berlin, 1997.
- [Knaupp 97] W. Knaupp. Analyse und Optimierung von Photovoltaik-Modulen, Dissertation. Shaker Verlag, Aachen, 1997.
- [Koltay 98] P. Koltay, J. Wenk & K. Bücher. *Outdoor Measurements of NOCT and Simulations of its Influence on Energy Collection*. In Proceedings of the 15th European Photovoltaic Solar Energy Conference, Vienna, pages 2334–2337. Stephenson, 1998.
- [Kondo 97] M. Kondo, H. Nishio, S. Kurata, K. Hayashi, A. Takenaka, A. Ishikawa, K. Nishimura, H. Yamagishi & Y. Tawada.

Effective Conversion Efficiency Enhancement of Amorphous Silicon Modules by Operation Temperature Elevation. Solar Energy Materials and Solar Cells, vol. 49, no. 1, pages 1–6, 1997.

- [Krebs 89] K. Krebs. Standard Procedures for Terrestrial Photovoltaic Performance Measurements. Commission of the European Communities, Brussels, 1989.
- [Kroposki 94] B. Kroposki, K. Emery, D. Myers & L. Mrig. *A Comparison of Photovoltaic Module Performance Evaluation Methodologies for Energy Ratings*. In Proceedings of the First World Conference on Photovoltaic Energy Conversion, Hawaii, pages 858–862. IEEE, 1994.
- [Landsberg 75] P.T. Landsberg & J. Mallinson. *Determination of larger-than-silicon band gaps for optimal conversion of the diffuse component*. In Proceedings of 11th IEEE Photovoltaic Specialists Conference, Scottsdale, pages 241–242, 1975.
- [Lord 94] K.R. Lord, M.-R. Walters & J.R. Woodyard. *Investigation of the Shunt Resistance in Single Junction a-Si:H Alloy Solar Cells*. Materials Research Society Symposium Proceedings, vol. 336, pages 729–734, 1994.
- [Martin-Chivelet 97] N. Martin-Chivelet. *Analysis of the Spectral Factor of Different Commercial PV Modules Based on Measured Data*. In Proceeding of the 14th European Photovoltaic Solar Energy Conference, Barcelona, pages 282–283, 1997.

- [Matson 84] R.J. Matson, K.A. Emery & R.E. Bird. *Terrestrial Solar Spectra, Solar Simulation and Solar Cell Short-Circuit Current Calibration: A Review*. Solar Cells, vol. 11, pages 105–145, 1984.
- [McMahon 94] T.J. McMahon & M.S. Bennett. *Metastable Shunt Paths in a-Si Solar Cells*. In Proceedings of the First World Conference on Photovoltaic Energy Conversion, Hawaii, pages 449–452. IEEE, 1994.
- [Merten 96] J. Merten. *Photovoltaics with Amorphous Silicon: Aspects of Technology, Physics and Application*, Dissertation. University of Barcelona, Barcelona, 1996.
- [Merten 97] J. Merten, J.M. Asensi, J. Andreu & Shah. *Assessing Amorphous Silicon Solar Modules by Variable Illumination Measurements (VIM) of the I(V)-Characteristic*. In Proceedings of the 14th European Photovoltaic Solar Energy Conference, Barcelona, pages 260–263. Stephenson, 1997.
- [Merten 98a] J. Merten & J. Andreu. *Clear Separation of Seasonal Effects on the Performance of Amorphous Silicon Solar Modules by Outdoor I/V-Measurements*. Solar Energy Materials and Solar Cells, vol. 52, no. 1-2, pages 11–25, 1998.
- [Merten 98b] J. Merten, J.M. Asensi, C. Voz, A.V. Shah, R. Platz & J. Andreu. *Improved Equivalent Circuit and Analytical Model for Amorphous Silicon Solar Cells and Modules*. IEEE Transactions on Electron Devices, vol. ED-45, no. 2, pages 423–429, 1998.

- [Mrig 87] L. Mrig, S. Rummel & D. Waddington. *Long Term Stability Performance Testing of Amorphous Silicon Modules under Natural Sunlight*. In *Stability of Amorphous Silicon Alloy Materials and Devices*. AIP Conference Proceedings 157, pages 326–333. AIP, 1987.
- [Nakamura 90] K. Nakamura, S. Nakazawa, K. Takahisa & K. Nakahara. *A Prediction Method of Degradation of a-Si:H Solar Cells*. In *Technical Digest of the International PVSEC-5, Kyoto*, pages 359–362, 1990.
- [Nakamura 98] K. Nakamura, T. Koyanagi, T. Kojima, T. Yanagisawa & K. Takahisa. *Change of the Equivalent Circuit Constants Accompanied by the Degradation and Recovery of Efficiency on a-Si Solar Cells*. In *Proceedings of the 15th European Photovoltaic Solar Energy Conference, Vienna*, pages 652–653. Stephenson, 1998.
- [Nann 92a] S. Nann. *Variabilität der spektralen Bestrahlungsstärke der Sonneneinstrahlung und deren Einfluß auf den Wirkungsgrad von Solarzellen*, Dissertation. Universität Oldenburg, Oldenburg, 1992.
- [Nann 92b] S. Nann & K. Emery. *Spectral Effects on PV-Device Rating*. *Solar Energy Materials and Solar Cells*, vol. 27, pages 189–216, 1992.
- [Nguyen 82] P.H. Nguyen, B. Lepley, C. Boutrit & S. Ravelet. *Computer Aided Characterisation of the Illuminated and Dark Current Voltage Characteristics of Solar Cells*. In *Proceedings of the*

4th European Photovoltaic Solar Energy Conference, pages 492-497, 1982.

- [Niemegeers 97] A. Niemegeers & M. Burgelman. *Effects of the Au/CdTe Back Contact on IV and CV Characteristics of Au/CdTe/CdS/TCO Solar Cells*. *Journal of Applied Physics*, vol. 81, no. 6, pages 2881-2886, 1997.
- [Niemegeers 98] A. Niemegeers, M. Burgelman, R. Herberholz, U. Rau, D. Hariskos & H.-W. Schock. *Model for Electronic Transport in Cu(In,Ga)Se₂ Solar Cells*. *Progress in Photovoltaics: Research and Applications*, vol. 6, no. 6, pages 407-421, 1998.
- [Nishitani 98] M. Nishitani, N. Kohara, T. Negami, T. Wada, S. Igari & R. Shimokawa. *Analysis of Temperature and Illumination Dependencies of CIS Cell Performance*. *Solar Energy Materials and Solar Cells*, vol. 50, no. 1-4, pages 63-70, 1998.
- [Obst 94] C. Obst. *Kennlinienvermessung an installierten Photovoltaik-Generatoren und deren Bewertung*, Diplomarbeit. Universität Oldenburg, Oldenburg, 1994.
- [Overstraeten 86] R.J. van Overstraeten & R.P. Mertens. *Physics, Technology and Use of Photovoltaics*. Adam Hilger Ltd., Bristol, Boston, 1986.
- [Parretta 97] A. Parretta, A. Sarno, R. Schioppo, M. Zingarelli & L.R.M. Cicari. *Analysis of Loss Mechanisms in Crystalline Silicon Modules in Outdoor Operation*. In *Proceedings of the 14th European Photovoltaic Solar Energy Conference*, Barcelona, pages 242-245, 1997.

- [Phang 84] J.C.H. Phang, D.S.H. Chan & J.R. Phillips. *Accurate Analytical Method for the Extraction of Solar Cell Model Parameters*. Electron Letters, vol. 20, no. 10, pages 406–408, 1984.
- [Phang 85] J.C.H. Phang & D.S.H. Chan. *A New Curve Fitting Error Criterion for Solar Cell I-V Characteristics*. In Proceedings of the 18th IEEE Photovoltaic Specialists Conference, Las Vegas, pages 758–763, 1985.
- [Phang 86] J.C.H. Phang & D.S.H. Chan. *A Comparative Study of Extraction Methods for Solar Cell I-V Characteristics*. Solar Cells, vol. 18, no. 1, pages 1–12, 1986.
- [Polman 86] A. Polman, W.G.J.H.M. van Sark, W. Sinke & F.W. Saris. *A New Method for the Evaluation of Solar Cells Parameters*. Solar Cells, vol. 17, pages 241–251, 1986.
- [Press 89] W.H. Press, B.P. Flannery, S.A. Teukolsky & W.T. Vetterling. *Numerical Recipes in Pascal - The Art of Scientific Computing*. Cambridge University Press, Cambridge, 1989.
- [Protogeropoulos 91] C. Protogeropoulos, B.J. Brinkworth, R.H. Marshall & B.M. Cross. *Evaluation of Two Theoretical Models in Simulating the Performance of Amorphous-Silicon Solar Cells*. In Proceedings of the 10th European Photovoltaic Solar Energy Conference, Lisbon, pages 412–415, 1991.
- [Raicu 93] A. Raicu. *Entwicklung einer Bewertungsmethodik von Solarzellen unter realistischen Witterungsbedingungen*, Doktorarbeit. Albert-Ludwigs-Universität, Freiburg, 1993.

- [Ransome 00] S.J. Ransome & J.H. Wohlgemuth. *Predicting kWh/kWp Performance for Amorphous Silicon Thin Film Modules*. In Proceedings of the 28th IEEE Photovoltaic Specialists Conference, Anchorage. IEEE, 2000.
- [Roedern 91] B. von Roedern. *The Staebler-Wronski Effect - A Fresh Assessment*. In B.L. Stafford, editor, *Amorphous Silicon Materials and Solar Cells*, Denver, AIP Conference Proceedings, pages 122–129, New York, 1991. AIP.
- [Roedern 95] B. von Roedern, B. Kroposki, T. Strand & L. Mrig. *New Insights into the Staebler-Wronski Degradation Mechanism from Analyses of Solar Cell and Module Degradation*. In Proceedings of the 13th European Photovoltaic Solar Energy Conference, Nice, pages 1672–1676. Stephenson, 1995.
- [Rubinelli 98] F.A. Rubinelli & R.I.E. Schropp. *Sensitivity of the a-Si:H Based Solar Cell Current-Voltage Characteristics to the Model Adopted for the Density of Dangling Bonds*. In Proceedings of the 15th European Photovoltaic Solar Energy Conference, Vienna, pages 998–1001. Stephenson, 1998.
- [Rüther 94] R. Rüther & J. Livingstone. *Seasonal Variations in Amorphous Silicon Solar Module Outputs and Thin Film Characteristics*. *Solar Energy Materials and Solar Cells*, vol. 36, no. 1, pages 29–43, 1994.
- [Rüther 99] R. Rüther. *Demonstrating the Superior Performance of Thin-Film Amorphous Silicon for Building-Integrated Photovoltaic Systems in Warm Climates*. In *Solar World Conference 1999*, Jerusalem, pages 217–222. ISES, 1999.

- [Rüther 01] R. Rüther, G. Kleiss & K. Reiche. *Spectral Effects on Amorphous Silicon Solar Module Fill Factors*. Solar Energy Materials and Solar Cells, page accepted for publ., 2001.
- [Schade 98] H. Schade, P. Lechner, R. Geyer, W. Frammelsberger, H. Rübel, M. Schmid, H. Maurus & W. Hoffmann. *Application-Related Features of a-Si Based PV Technology*. In Proceedings of the 15th European Photovoltaic Solar Energy Conference, Vienna, pages 2054–2057. Stephenson, 1998.
- [Schiff 91] E.A. Schiff. *Photocarrier Drift Measurements and Solar Cell Models for Amorphous Silicon*. Solar Cells, vol. 30, pages 227–233, 1991.
- [Seifert 96] O. Seifert. *Temperaturabhängigkeit der elektrischen Transporteigenschaften von Chalkopyrit-Dünnschicht-Solarzellen*, Diplomarbeit. Universität Bayreuth, Lehrstuhl Experimentalphysik II, Bayreuth, 1996.
- [Shafarman 96] W.N. Shafarman & J.E. Phillips. *Direct Current-Voltage Measurements of the Mo/CuInSe₂ Contact on Operating Solar Cells*. In Proceedings of the 25th IEEE Photovoltaic Specialists Conference, Washington DC, pages 917–919, Piscataway, 1996. IEEE.
- [Sharma 93] S.K. Sharma, D. Pavithra, N. Srinivasamurthy & B.L. Agrawal. *Determination of Solar Cell Parameters: An Analytical Approach*. Journal of Physics D: Applied Physics, vol. 26, pages 1130–1133, 1993.

- [Shockley 49] W. Shockley. *The Theory of p-n Junctions in Semiconductors and p-n Junction Transistors*. Bell Syst. Tech. J., vol. 28, pages 475–489, 1949.
- [Skiba 96] M. Skiba, M. Mohr & H. Unger. *Comparative Assessment and Validation of Models Estimating Diffuse Irradiation on Inclined Planes*. In Proceedings of Eurosun '96, Freiburg. ISES, 1996.
- [Smeets 86] J. Smeets, M. van Roy & P. Nagels. *I-V Curve Fitting for a-Si:H Solar Cells*. In Proceedings of the 7th European Photovoltaic Solar Energy Conference, Sevilla, pages 539–543, 1986.
- [Stollwerck 95] G. Stollwerck. Quantitative Separation of Photon and Back-Contact Losses in CdTe Solar Cells - Where Have All the Photons Gone? Dissertation. Colorado State University, Fort Collins, Colorado, 1995.
- [Strand 95] T.R. Strand, B.D. Kroposki, R. Hansen & D. Willett. *Siemens Solar CIS Photovoltaic Module and System Performance at the National Renewable Energy Laboratory*. In Proceedings of the 25th IEEE Photovoltaic Specialists Conference, Washington DC, pages 965–968. IEEE, 1995.
- [Sze 81] S.M. Sze. *Physics of Semiconductor Devices*. Edition 2nd. Wiley, New York, 1981.
- [Takahisa 94] Kiyoshi Takahisa, Kuniomi Nakamura, Sigeji Nakazawa, Yoshinobu Sugiyama, Junta Nose, Sanekazu Igari & Tune-kichi Hiruma. *Long-term Reliability of Amorphous Silicon*

Solar Cells. Solar Energy Materials and Solar Cells, vol. 34, no. 1-4, pages 485–492, 1994.

- [Tarr 80] N.G. Tarr & D.L. Pulfrey. *The Superposition Principle for Homojunction Solar Cells*. IEEE Transactions on Electron Devices, vol. ED27, no. 4, pages 771–776, 1980.
- [Topic 97] M. Topic, F. Smole & J. Furlan. *Examination of Blocking Current-Voltage Behaviour Through Defect Chalcopyrite Layer in ZnO/CdS/Cu(In,Ga)Se₂/Mo Solar Cell*. Solar Energy Materials and Solar Cells, vol. 49, no. 1-4, pages 311–317, 1997.
- [Veissid 90] N. Veissid, M.T.F. da Cruz & A.M. de Andrade. *A Method for the Determination of the Standard Deviations of the Solar Cell I-V Characteristic Parameters*. Solar Cells, vol. 28, pages 351–357, 1990.
- [Veissid 91] N. Veissid & A.M. de Andrade. *The I-V Silicon Solar Cell Characteristic Parameters Temperature Dependence. An Experimental Study Using the Standard Deviation Method*. In Proceedings of the 10th European Photovoltaic Solar Energy Conference, Lisbon, pages 43–47, 1991.
- [Vela 94] N. Vela, F. Fabero & F. Chenlo. *Testing of Stability and Reliability of a-Si PV Modules. Long Term Life Time Prediction*. In Proceedings of the 12th European Photovoltaic Solar Energy Conference, Amsterdam, pages 1210–1213. Stephenson, 1994.

- [Wagemann 94] H.-G. Wagemann & H. Eschrich. *Grundlagen der Photo-voltaischen Energiewandlung*. Teubner, Stuttgart, 1994.
- [Wagner 95] H. Wagner. *Physical Aspects and Technological Realization of Amorphous Silicon Thin Film Solar Cells*. *Physical Status Solidi B - Basic Research*, vol. 192, no. 2, pages 229–239, 1995.
- [Walraven 78] R. Walraven. *Calculating the Position of the Sun*. *Solar Energy*, vol. 20, no. 5, pages 393–397, 1978.
- [Wenham 94] S.R. Wenham, M.A. Green & M.E. Watt. *Applied Photo-voltaics*. University of New South Wales, Kensington, 1994.
- [Wilkinson 81] B.J. Wilkinson. *An Improved Fortran Program for the Rapid Calculation of the Solar Position*. *Solar Energy*, vol. 27, pages 67–68, 1981.
- [Wolf 63] M. Wolf & H. Rauschenbach. *Series Resistance Effects on Solar Cell Measurements*. *Advanced Energy Conversion*, vol. 3, pages 455–479, 1963.
- [Wolf 77] M. Wolf, G.T. Noel & R.J. Stirn. *Investigation of the Double Exponential in the Current-Voltage Characteristics of Silicon Solar Cells*. *IEEE Transactions on Electron Devices*, vol. ED-24, no. 4, pages 419–428, 1977.
- [Zweibel 95] Ken Zweibel. *Thin Films: Past, Present, Future*. *Progress in Photovoltaics*, vol. 3, no. 5, pages 279–293, 1995.

